First principles study of the structural, electronic, elastic, mechanical, thermal, and vibrational properties in pyrochlores and temperature-dependent phonon properties in pyrochlores and $SrTiO_3$ perovskite

A Thesis

Submitted For the Degree of

Doctor of Philosophy

in the Faculty of Science

by

Pramod Kumar Verma

Department of Physics

Indian Institute of Science

BANGALORE – 560 012

2019

©Pramod Kumar Verma

2019

All rights reserved

Declaration

I hereby declare that the work reported in this thesis is original. The entire work is carried out by me during my tenure as a PhD student at the Department of Physics, Indian Institute of Science, Bangalore. This thesis has not formed the basis for the award of any degree, diploma, associateship, membership or similar title of any university or institution.

(**Pramod Kumar Verma**)

Department of Physics
Indian Institute of Science
Bangalore-560012
India

TO

My Parents

Acknowledgements

Many people have contributed directly or indirectly during this journey of my PhD thesis. First and foremost, I would like to thank my research supervisor, H R Krishnamurthy for all his guidance and support. My sincere gratitude to him for his patience and kindness. I can not imagine completing my thesis without his help. I sincerely thank my collaborator Umesh Waghmare for all his help, patience, and kindness. He and his group members extended all their support related to the technical details of the first-principles calculations. I extend my gratitude to my experimental collaborator, Ajay K Sood for his kindness and patience. His insights about the problems were always helpful. I thank my co-supervisor Manish Jain for all the discussions we had. It has been a great learning experience interacting with him.

I thank Subroto Mukerjee, Vijay Shenoy, Chandan Dasgupta, Prabal Maiti, Rahul Pandit for the physics they taught me in the classes. I thank all the Professors of the department for their support and kindness. I thank my past labmates and seniors: Sumilan Banerjee, Subhro Bhattacharjee, Samriddhi Sankar Ray, Srijan K Saha, Tathagat Avatar Tulsi, Ganapati Sahoo, Suropriya, Yogeshwar, and Manjari. I thank my batchmates: Kingshuk, Vishwanath, Rajany, Taraknath, Baban, Shreyas, Ashoka, Akshay, Atul, and Siddhesh. I thank my juniors: Aabhaas, Soumen, Gaurav, Gyan, Parth, Priyo, Soham, Swetha, Yogendra, Animesh, Surabhi, and Sibaram. I thank all other friends of the department whom I have forgotten to mention here.

I would like to thank the department office staff for all their support. We have been very lucky to have a very helpful office staff.

My stay at the institute has been of great experience from different points of view. I have been privileged enough to serve the student community as a chairman of the Students' council. I would like to thank the institute administrative staff for their support.

It is very hard to think to complete a PhD degree without financial support. I would like to thank the council of scientific and industrial research (CSIR) for providing me with the fellowship towards my research. I would like to thank Umesh Waghmare and particularly H R Krishnamurthy for further financial support after the stipulated time of my CSIR fellowship was over.

I would like to thank IISc's Supercomputer education and research centre (SERC) for giving me access to use its clusters, especially the CRAY supercomputer for my research projects. I would like to

thank the Department of Physics for giving me access to use its Rahman cluster. I thank Manish Jain and Umesh Waghmare for allowing me to use their clusters for my thesis work.

I would like to thank my friends from the Jawaharlal Nehru Centre for Advanced Scientific Research (JNCASR) for all the helpful discussions.

I would like to thank my A mess friends: Rishikesh, Bhawana, Ved, Durga, Sarada, Shreevalsa, Vasanth, and Kamana for the unforgettable company we had together. I extend my sincere thanks to Hindi Samiti, PDA, Students' Council, and ENTIISc teams for allowing me to serve them. I thank my yoga teacher, Mrs Karpagam for teaching me yoga and making life beautiful and healthy. Before joining the institute, I had no knowledge about the Hindustani classical music, so, I would like to thank my music teacher, Mrs Geetha for teaching me Hindustani classical music. I thank Kannada and Sanskrit committees for allowing me to learn Kannada and Sanskrit languages. I would like to thank the Gymkhana club for providing an opportunity to learn Chinese martial art- KUNG FU and swimming. I would like to thank the department cleaning staff for their love and blessings; the conversation with them in Kannada was helpful.

Today whatever I am is because of the love, patience, and hard work of my family. I thank my parents and brothers for all their support and love. I thank my wife Seema for all her support, love, and affection. Her contribution during my research journey can not be described in words. She has put a tremendous effort in helping me towards every aspect of life so that I could focus on my Research. Her company has been wonderful so far.

Last but not least, I thank everyone who has helped me towards my PhD thesis.

Publications based on this Thesis

None published yet.

In preparation

1. First principles study of elastic, mechanical, and thermal properties in the rare-earth $RE_2B_2O_7$ (RE = Sm, Gd, Tb, Dy, Ho, Er, Yb and Lu; B = Ti, Zr and Hf) pyrochlores
2. Experimental and theoretical study of the high pressure calculations of the structural, elastic, and vibrational properties in $Dy_2Ti_2O_7$ titanate pyrochlore
3. Theoretical study of temperature dependent phonon properties in $Y_2Ti_2O_7$ pyrochlore
4. Theoretical study of temperature dependent phonon properties in the antiferrodistortive (AFD) $SrTiO_3$ perovskite

Abstract

In this thesis work, we have employed density functional theory (DFT) calculations to study the structural, electronic, elastic, mechanical, thermal, and vibrational properties in pyrochlore materials. Using DFT and the Green's function formalism, we have also explored the temperature dependent phonon properties in some of the pyrochlores and $SrTiO_3$ perovskite.

Pyrochlores with the general formula $A_2B_2O_7$ (generally written as $A_2B_2O_6O'$) are quite fascinating from many different perspectives [Rev. Mod. Phys., **82** (2010), Prog. Sol. St. Chem. **15**, 55 (1983)]. The effect of pressure, at ambient temperatures, has been investigated for some of the titanate pyrochlores [Chem. Phys. Lett. **413**, 248 (2005), App. Phys. Lett. **86**, 181906 (2005)]. Recently, the vibrational properties of some of the pyrochlores have been investigated as a function of temperature by various groups. More specifically, the temperature-dependent phonon properties in pyrochlore titanates have attracted a great deal of attention experimentally as it has been found that some of the phonon modes in these systems show anomalous softening upon cooling [Phys. Rev. B **79**, 214437 (2009), J. Raman Spec. **39**, 537 (2008), Phys. Rev. B **78**, 214102 (2008)]. This phonon anomaly has been attributed to phonon-phonon anharmonic interactions.

Motivated by these temperature-dependent phonon studies in titanate pyrochlores, we have carried out temperature-dependent phonon calculations in some of the titanate pyrochlores using DFT and Green's function approach, to leading order in the third-order phonon-phonon interactions.

The elastic constants are directly related to the atomic bonding in materials and are of fundamental importance. They are closely connected to the thermodynamic properties of the materials such as the specific heat, the Debye temperature and the Grüneisen parameter, and also play a crucial role in structural phase transitions. In this thesis, we present a systematic study of the elastic, mechanical, and thermal properties in a series of pyrochlores.

A synoptic presentation of the content covered in each of the chapters in this thesis is given below:

In **Chapter 1**, we have introduced the pyrochlores and perovskites studied in this thesis, with a review of the literature about their structural, electronic, vibrational, and mechanical properties. Here, we have also performed the factor group analysis to characterize the symmetries of various phonon modes. We have briefly brought out our interests in these systems.

In **Chapter 2**, we have briefly described the theoretical background, i.e. density functional theory (DFT), lattice dynamics, density functional perturbation theory (DFPT), and phonon anharmonic theory. We have also discussed the importance of various contributions of phonon anharmonic theory. Furthermore, we have briefly discussed the elastic moduli and their importance in terms of the various physical properties.

In **Chapter 3**, we have presented DFT results of the structural, electronic, and vibrational properties in a series of rare-earth $RE_2B_2O_7$ (RE = Sm, Gd, Tb, Dy, Ho, Er, Yb, Lu and B = Ti, Zr, Hf) pyrochlores. We have performed a comparative analysis and showed how the structural, electronic, and vibrational properties of pyrochlore depend on the rare-earth and transition metal cations. The interesting findings in the pyrochlore titanate are anomalous dynamical charges and structural instabilities which manifest as imaginary phonon frequencies. We show that a small distortion of the atomic positions within the unit cell stabilizes the structure. We have briefly described how the local density approximation (LDA) works better than the generalized gradient approximation (GGA) for most of the pyrochlore materials, as found by other authors as well. We have briefly explored the contribution of the various force constants to the vibrational modes and have presented a comprehensive and comparative analysis of Raman and infrared active modes among various pyrochlore titanates.

In **Chapter 4**, we have carried out a comparative study of the elastic, mechanical, and thermal properties in rare-earth $RE_2B_2O_7$ (RE = Sm, Gd, Tb, Dy, Ho, Er, Yb, Lu and B = Ti, Zr, Hf) pyrochlores. We have shown the dependence of the bulk modulus, elastic constants, shear modulus, Young's modulus, Poisson's ratio, sound velocities, Debye temperature and the minimum thermal conductivity on the rare-earth and transition metal cations. In this chapter, we have also carried out a comparative analysis between the LDA and GGA methods.

In **Chapter 5**, motivated by the high pressure experimental study, we have performed first-principles calculations in $Dy_2Ti_2O_7$ to investigate the structural, elastic, and vibrational properties under the application of the hydrostatic pressure. Both experimental and theoretical results show that the cell-volume, internal structure parameter, elastic moduli, and the vibrational frequencies display a slope change around 9 GPa pressure. The space group remains invariant across the pressures studied, hence the slope change is most likely related to an isostructural phase transition.

In **Chapter 6**, we have examined the structural, electronic, vibrational, elastic, mechanical, and thermal properties in yttrium-based pyrochlores, i.e. $Y_2B_2O_7$ (B = Ti, Zr, and Hf). A large anomalous dynamical charge for Ti^{4+} ions is reported. The GGA calculations of $Y_2Ti_2O_7$ display large structural instabilities with respect to the phonon calculations, i.e. the frequencies of several of the optical modes are imaginary. A small distortion of the atomic positions in the primitive unit-cell stabilizes the structure in the sense that all the frequencies become real valued. When the lighter Ti^{4+} ions are replaced by the heavier ions like Zr^{4+} or Hf^{4+} ions, no structural instability is found in either of the approaches used.

As mentioned earlier, experimentally it has been found that several of the phonon modes in pyrochlore titanates show an unconventional behaviour with cooling, i.e. they display a redshift. It was suggested in these studies that phonon-phonon interactions are responsible for the anomalous nature of these phonon modes. Motivated by these studies, we have carried out temperature dependent phonon calculations in $Y_2Ti_2O_7$ using first principles density functional theory calculations and the many-body Green's function approach to see if we can theoretically capture these anomalies within a perturbative treatment of third-order an-harmonic interactions. These studies are reported in **Chapter 7**. More specifically, in this chapter we have reported the Grüneisen parameter values for various phonon modes, the temperature variation of the linear thermal expansion coefficient, and the temperature dependence of the quasiharmonic contribution to the various normal modes. A calculation of the contribution to the temperature dependent shifts in the phonon frequencies (and the phonon line-widths) arising from the third-order anharmonic interactions requires a knowledge of the third-order interatomic force constant matrix elements. The calculations presented in this chapter have been carried out by approximating these matrix elements in terms of an assumed form involving a single coupling constant, which is then used as a fitting parameter. Within this approximation, we have performed a comprehensive analysis of the two-phonon density of states, phonon linewidths, and frequency shifts for some of the phonon modes. We find that the results do not completely match experiments, in that while we do find anomalous temperature dependence, they happen only for two high frequency modes, and not for the low frequency modes as seen experimentally.

In **Chapter 8**, Motivated by the results of Chapter 7, we have reexamined the temperature-dependent phonon properties in $Y_2B_2O_7$ (B = Ti, Zr) pyrochlores using the same DFT plus Green's function approach, but this time calculating the third-order interatomic force constant matrix elements (IFC3s) ab initio, using the "$2n+1$" theorem, implemented within the density functional linear response theory [Phys. Rev. B **87**, 214303 (2013)]. The most interesting finding in our calculations in case of $Y_2Ti_2O_7$ is the anomalous behaviour of the same two modes as in the previous calculation. Among these two modes, we find that the F_{1g} mode shows a huge anomaly compared to the other anomalous mode, concurrent with the lowest lifetime found within our theoretical calculations. However, even these more sophisticated calculations are unable to reproduce the anomalies reported in experiments for the lower frequency modes. On the other hand, when Ti^{4+} ions are replaced by Zr^{4+} ions, no anomaly in any of the phonon modes is found, consistent with the experimental finding in $Sm_2Ti_{2-x}Zr_xO_7$ [J. Raman Spec. **43**, 549 (2012)], where the authors have found phonon anomalies in $Sm_2Ti_2O_7$, whereas $Sm_2Zr_2O_7$ showed no anomalous behaviour of any phonon modes.

In **Chapter 9**, we have investigated the temperature-dependent phonons in rare-earth $RE_2Ti_2O_7$ (RE = Dy, Lu) pyrochlores using the same procedure as in Chapter 7 to get a qualitative understanding of the behaviour of phonons as a function of temperature. We find that the third order anharmonic

shift in frequency for some of the phonon modes in these systems shows a positive contribution, which is a likely signature of phonon anomalous behaviour that one will find if one calculates the third order force constant matrix elements exactly.

In **Chapter 10**, we have explored the temperature-dependent phonons in tetragonal $SrTiO_3$ perovskite. We have also studied the vibrational properties in the high temperature cubic phase of $SrTiO_3$, which displays a strong structural instability as indicated by the imaginary frequencies for several of the optical modes. For the tetragonal structure, we have calculated the mode Grüneisen parameters, the temperature variation of the linear thermal expansion coefficient, and the quasiharmonic frequency shift. Here also we have used "$2n + 1$" theorem to calculate the IFC3s. Within the third-order anharmonic approach, we have studied the two-phonon density of states and temperature dependence of the phonon linewidths as well as the temperature dependence of the shift in frequency and the total frequency for some of the phonon modes. Here, we find that almost all the modes show a normal behaviour with temperature, i.e. frequency hardens with cooling, completely unlike the experiments.

In **Chapter 11**, we summarize our findings on the two different systems, namely, pyrochlores and $SrTiO_3$ and highlight a few possible theoretical calculations that may be undertaken in future to have a better understanding of these systems.

Contents

Acknowledgements **i**

Publications based on this Thesis **iii**

Abstract **v**

1 Introduction **1**
1.1 What are pyrochlores? . . . 1
1.1.1 Structural details . . . 1
1.1.2 Geometrical frustration . . . 4
1.1.3 Magnetic ground states . . . 5
1.1.4 Vibrational properties . . . 6
1.1.5 Phase stability and phase transitions . . . 6
1.1.6 Temperature dependent phonon studies . . . 7
1.1.7 Our interest . . . 9
1.2 $SrTiO_3$ perovskite . . . 10
1.2.1 The cubic STO perovskite . . . 11
1.2.2 The tetragonal STO perovskite . . . 12
1.2.3 Vibrational properties . . . 13
1.2.4 Temperature dependent phonon properties . . . 15
1.2.5 Our interest . . . 15

2 Theoretical background **16**
2.1 The Many body picture . . . 16
2.2 Independent-electron approximation . . . 18
2.2.1 Hartree approximation . . . 18
2.2.2 Hartree-Fock Approximation . . . 19
2.3 Density Functional theory . . . 20
2.3.1 The Hohenberg-Kohn Theorems . . . 20
2.3.2 The Kohn-Sham Formalism . . . 20
2.3.3 Approximations for the exchange-correlation functional . . . 22
2.3.4 Lattice periodicity . . . 23
2.3.5 Electron-ion interactions:Pseudopotential approximation . . . 24
2.3.6 Geometry optimization . . . 24
2.4 Phonon calculations . . . 25
2.4.1 Harmonic Approximation . . . 27
2.4.2 Thermodynamic potentials . . . 29
2.4.3 Limitations of the harmonic approximation . . . 30
2.5 Phonon dynamics in the presence of anharmonicity . . . 30
2.5.1 Quasiharmonic Approximation . . . 30
2.5.2 Anharmonic Lattice Dynamics . . . 32

2.5.3 Green's function method . . . 33
2.6 Density functional perturbation theory . . . 35
2.7 Elastic Constants . . . 36

3 Structural, electronic, and phonon properties of some $RE_2B_2O_7$ pyrochlores 37
3.1 Motivation . . . 37
3.2 Computational details . . . 38
3.3 Results and discussion . . . 39
3.3.1 Lattice parameters . . . 39
3.3.2 Oxygen parameter . . . 40
3.3.3 Bond distances . . . 42
3.4 Electronic properties . . . 44
3.4.1 Dynamical charges . . . 45
3.5 Vibrational properties; Structural instability analysis . . . 49
3.5.1 A detailed description of the structural instability in pyrochlores . . . 50
3.5.2 Description of Raman and Infra-red active modes . . . 53
3.6 Conclusions . . . 60

4 Elastic, mechanical, and thermal properties of $RE_2B_2O_7$ pyrochlores 63
4.1 Motivation . . . 63
4.2 Computational details . . . 64
4.3 Results and discussion . . . 65
4.3.1 Elastic properties . . . 65
4.3.2 Mechanical properties . . . 70
4.3.3 Thermal properties . . . 73
4.3.4 Minimum thermal conductivity . . . 76
4.4 Conclusions . . . 78

5 High pressure study of structural, mechanical, elastic, and vibrational properties in $Dy_2Ti_2O_7$ pyrochlore 80
5.1 Motivation . . . 80
5.2 Theoretical details . . . 81
5.3 Results and discussion . . . 81
5.3.1 Elastic properties . . . 82
5.4 Pressure dependence of the Raman and IR active phonon modes . . . 84
5.5 Conclusions . . . 85

6 Electronic, elastic, thermal, and vibrational properties of $Y_2B_2O_7$ pyrochlores 87
6.1 Motivation . . . 87
6.2 Computational details . . . 88
6.3 Structural properties . . . 88
6.4 Elastic, mechanical, and thermal properties . . . 89
6.5 Electronic properties . . . 91
6.5.1 Dynamical charges . . . 92
6.6 Vibrational properties; Structural instability analysis . . . 93
6.6.1 A detailed description of the structural instability . . . 93
6.6.2 Description of Raman and Infrared active modes . . . 97
6.7 Conclusions . . . 99

7 Temperature dependent phonon properties of $Y_2Ti_2O_7$ pyrochlore 101
7.1 Introduction . . . 101
7.2 Computational details . . . 103
7.3 Results and discussions . . . 103
7.3.1 Quasiharmonic results . . . 103
7.3.2 Anharmonic calculations . . . 105
7.4 Conclusions . . . 112

8 Temperature dependent phonon properties of $Y_2Ti_2O_7$ and $Y_2Zr_2O_7$ pyrochlores 113
8.1 Introduction . . . 113
8.2 Computational details . . . 114
8.3 Results and discussion . . . 115
8.3.1 Quasiharmonic results . . . 115
8.3.2 Anharmonic calculations . . . 119
8.4 Conclusions . . . 132

9 Temperature dependent phonon properties of $Dy_2Ti_2O_7$ and $Lu_2Ti_2O_7$ pyrochlores 133
9.1 Introduction . . . 133
9.2 Computational details . . . 134
9.3 Results and discussion . . . 134
9.3.1 Quasi-harmonic results . . . 134
9.3.2 Anharmonic calculations . . . 136
9.4 Conclusions . . . 142

10 Temperature-dependent phonons of tetragonal $SrTiO_3$ perovskite 143
10.1 Introduction . . . 143
10.2 Computational details . . . 144
10.3 Phonon symmetry in cubic and tetragonal phases . . . 144
10.4 Results and discussion . . . 145
10.4.1 Structural and vibrational properties . . . 145
10.4.2 Quasiharmonic calculations in tetragonal $SrTiO_3$ . . . 149
10.4.3 Anharmonic results . . . 151
10.5 Conclusions . . . 156

11 Summary and conclusion 158

A Linear thermal expansion coefficient 162

B Quasiharmonic shift in frequency 165

C Phonon-Phonon interactions 166
C.1 Non-zero Temperature Green's function formalism . . . 166
C.1.1 Matsubara Green's function . . . 167
C.1.2 Dyson's equation . . . 170
C.1.3 Frequency summations . . . 174

D Theory of elasticity in the cubic crystals 179
D.1 Stress-strain dependence . . . 179
D.2 The relation between elastic energy, strain and elastic constants within the harmonic approximation . . . 179
D.2.1 Further reduction in the number of independent elastic constants . . . 181
D.2.2 Elastic stiffness constants of cubic crystals . . . 182
D.3 Calculation of elastic constants . . . 184
D.3.1 Hydrostatic deformation of fcc lattice . . . 184

D.3.2 Uniaxial or tetragonal deformation 185
D.3.3 Shear deformation 186

List of Tables

1.1 Atomic positions in $A_2B_2O_6O'$ pyrochlore (space group: $Fd\bar{3}m$, No: 227). x is the fractional coordinate of oxygen at 48f. We denote N as the number of atoms per primitive cell . . . 2
1.2 Wyckoff positions for strontium titanate in the high temperature cubic phase (space group $Pm\bar{3}m$ O_h^1 (SG 221)). . . . 12
1.3 Wyckoff positions for strontium titanate in the low temperature tetragonal phase (space group I4/mcm D_{4h}^{18} (SG 140)). . . . 14

3.1 Calculated values of the lattice constants (Å), and displacement parameter x of $RE_2Ti_2O_7$ titanate pyrochlores. The results are compared with the available experimental data. . . 39
3.2 Calculated values of the lattice constants (Å), and displacement parameter x of $RE_2Zr_2O_7$ pyrochlores. The results are compared with the available experimental and theoretical data. . . . 39
3.3 Calculated values of the lattice constants (Å), and displacement parameter x of $RE_2Hf_2O_7$ pyrochlores. The results are compared with the available experimental and theoretical data. . . . 40
3.4 Ionic radii of rare earth ions. Ionic radii of O^{2-}, Ti^{4+}, Zr^{4+} and Hf^{4+} ions are 1.38, 0.605, 0.72 and 0.71 Å, respectively. . . . 40
3.5 Our calculated values of the bond distances (Å) in $RE_2Ti_2O_7$ titanate pyrochlores. The results are compared with the available experimental data. . . . 42
3.6 Our calculated values of the bond distances (Å) in $RE_2Zr_2O_7$ zirconate pyrochlores . . . 42
3.7 Our calculated values of the bond distances (Å) in $RE_2Hf_2O_7$ hafnate pyrochlores 43
3.8 Energy band gaps (eV) in $RE_2B_2O_7$ (RE = Sm and Lu, B = Ti, Zr and Hf) pyrochlores using both the LDA and GGA methods, along with the available experimental and theoretical data. . . . 44
3.9 Dynamical charge tensors of rare-earth, Ti, and oxygen elements in $RE_2Ti_2O_7$ calculated within LDA approach. The dynamical charges for any other atoms can be achieved by utilising the symmetry operations of the crystal. Eigenvalues of the symmetric part of the tensor are also given in the brackets. . . . 46
3.10 Dynamical charge tensors of rare-earth, Zr, and oxygen elements in $RE_2Zr_2O_7$ calculated within LDA approach. The dynamical charges for any other atoms can be obtained by applying the symmetry operations of the crystal. Eigenvalues of the symmetric part of the tensor are also given in the brackets. . . . 47
3.11 Dynamical charge tensors of rare-earth, Hf, and oxygen elements in $RE_2Hf_2O_7$ calculated within LDA approach. The dynamical charges for any other atoms can be obtained by applying the symmetry operations of the crystal. Eigenvalues of the symmetric part of the tensor are also given in the brackets. . . . 48
3.12 Structural stability analysis of LDA and GGA calculations. N_i stands for the number of imaginary phonon modes, ω_i represents the highest imaginary frequency. . . . 52

3.13 Amount of distortion(in Å) required to stabilize the structure of $Sm_2Ti_2O_7$ titanate pyrochlore. The results clearly show that the structure is highly unstable in GGA compared to LDA calculations. 53
3.14 Raman mode frequencies (cm^{-1}) of rare-earth pyrochlore titanates $RE_2Ti_2O_7$ with assignments along with the literature data. Modes with $\star$ indicate that they are experimentally observed, but not found from DFT. Frequencies with † implies that they are not assigned experimentally to any Raman-active mode, and with ‡ means they are assigned as overtones in experiments. Theory A shows results for other first-principles simulations. 56
3.15 Calculated Infra-red mode frequencies (cm^{-1}) of rare-earth pyrochlore titanates, $RE_2Ti_2O_7$ with assignments along with the literature data. Theory A shows results for other first-principles simulations. 57
3.16 Calculated Raman mode frequencies (cm^{-1}) of rare-earth pyrochlore zirconates, $RE_2Zr_2O_7$ with assignments along with experimental data. 58
3.17 Calculated infra-red mode frequencies (cm^{-1}) of rare-earth pyrochlore zirconates, $RE_2Zr_2O_7$ with assignments along with experimental data. 59
3.18 Calculated Raman mode frequencies (cm^{-1}) of rare-earth pyrochlore hafnates, $RE_2Hf_2O_7$ with assignments along with experimental data. 59
3.19 Calculated infra-red mode frequencies (cm^{-1}) of rare-earth pyrochlore hafnates, $RE_2Hf_2O_7$ with assignments along with experimental data. 60

4.1 Calculated elastic constants, Zener anisotropy factor, bulk, shear, and Young's moduli, Poisson's and Pugh's ratio of the rare-earth $RE_2Ti_2O_7$ pyrochlores, along with the available experimental data. 67
4.2 Calculated elastic constants, Zener anisotropy factor, bulk, shear, and Young's moduli, Poisson's and Pugh's ratio in the rare-earth $RE_2Zr_2O_7$ pyrochlores, along with the available literature data. Theory A, B, and C show results for other first-principles simulations. 68
4.3 Calculated elastic constants, Zener anisotropy factor, bulk, shear, and Young's moduli, Poisson's and Pugh's ratio in the rare-earth $RE_2Hf_2O_7$ pyrochlores, along with the available literature data. Theory A shows results for other first-principles simulations. 69
4.4 Calculated crystal density, sound velocities, Debye temperature, and the minimum thermal conductivity in the rare-earth $RE_2Ti_2O_7$ pyrochlores, along with the available experimental data. 74
4.5 Calculated crystal density, sound velocities, Debye temperature, and the minimum thermal conductivity in the rare-earth $RE_2Zr_2O_7$ pyrochlores, along with the available literature data. Theory A shows results for other first-principles simulations. 75
4.6 Calculated crystal density, sound velocities, Debye temperature, and the minimum thermal conductivity in the rare-earth $RE_2Hf_2O_7$ pyrochlores. 76

5.1 Calculated elastic constants (in GPa), and the anisotropy factor for $Dy_2Ti_2O_7$ pyrochlore. 83
5.2 Comparison of our calculated Raman mode frequencies (cm^{-1}) (at zero pressure and temperature) with the experimental values at room temperature and pressure. A mode with Superscript *a* means that it is experimentally observed but not found in theory, while frequencies with superscript *b* are overtones in experiments. 85

6.1 Calculated lattice parameters for $Y_2B_2O_7$ (B = Ti, Zr, and Hf) pyrochlores, along with the available theoretical and experimental data. Theory A and B show results for other first-principles simulations. 89
6.2 Calculated elastic moduli for $Y_2B_2O_7$ (B = Ti, Zr, and Hf) pyrochlores, along with the available literature data. Theory A, B, and C show results for other first-principles simulations. 90
6.3 Calculated crystal density, longitudinal, transverse, and mean sound velocities, Debye temperature, and the minimum thermal conductivity in $Y_2B_2O_7$ (B = Ti, Zr, and Hf). Results are compared with the available literature data. 91

6.4 Dynamical charge tensors of Y, B (B = Ti, Zr, and Hf), and oxygen elements in $Y_2B_2O_7$ calculated within the LDA approach. The dynamical charges for any other atoms can be achieved by utilizing the symmetry operations of the crystal. Eigenvalues of the symmetric part of the tensor are also given in the brackets. 94
6.5 Amount of distortion(in Å) required to stabilize the structure of $Y_2Ti_2O_7$ titanate pyrochlore. The results clearly show that the structure is highly unstable in GGA compared to LDA calculations. 95
6.6 Calculated Raman mode frequencies (cm^{-1}) in $Y_2B_2O_7$ (B = Ti, Zr, and Hf) pyrochlores with assignments along with the literature data. Modes with $\star$ indicate that they are experimentally observed, but not found from the DFT. Frequencies with † implies that they are not assigned experimentally to any Raman-active mode, and with ‡ means they are assigned as overtones in experiments. Theory A shows results for other first-principles simulations. 99
6.7 Calculated Infra-red mode frequencies (cm^{-1}) in $Y_2B_2O_7$ (B = Ti, Zr, and Hf) pyrochlores with assignments along with the literature data. Theory A shows results for other first-principles simulations. 99

7.1 Calculated values of the phonon frequencies and the mode Grüneisen parameters in $Y_2Ti_2O_7$. 104

8.1 Calculated values of phonon frequencies and mode Grüneisen parameters in $Y_2Ti_2O_7$ and $Y_2Zr_2O_7$, at $T = 0$ K. 116
8.2 Calculated values of phonon frequencies, FWHM, and lifetimes in $Y_2Ti_2O_7$, at $T = 0$ K. 123
8.3 Calculated values of phonon frequencies, FWHM, and lifetimes in $Y_2Zr_2O_7$, at $T = 0$ K. 124

9.1 Calculated phonon frequencies and mode Grüneisen parameters in $Dy_2Ti_2O_7$ and $Lu_2Ti_2O_7$ pyrochlores, along with the available experimental results. 135

10.1 Wyckoff positions and phonon symmetry in cubic and tetragonal AFD $SrTiO_3$ 146
10.2 Cubic STO basic properties. Theory A and B correspond to the other first-principles calculations. 146
10.3 Calculated phonon frequencies (cm^{-1}) in cubic STO, compared with the available literature data. 147
10.4 AFD STO structural properties. 148
10.5 Calculated LDA values of frequencies of Raman active, silent, and Infrared active modes in tetragonal STO structure, along with the available theoretical (Theory A[76] and Theory B[77]) and experimental results. 149
10.6 Calculated phonon frequencies, mode Grüneisen parameters, full width at half maximum at $\boldsymbol{q} = \mathbf{0}$, and phonon lifetimes of tetragonal $SrTiO_3$ perovskite. 152

List of Figures

1.1 Pyrochlore tetrahedra sublattices formed by A and B sites. Adapted from Ref.[1] 2
1.2 Octahedral and tetrahedral geometries of the pyrochlore lattice. An octahedron (i) is formed by B^{4+} and O_{48f} atoms such that six-octahedra make a puckered hexagonal ring (ii) sharing their corners. Four A^{3+} cations form a tetrahedron (iii) with an O_{8b} atom at its centre, which constitute the A-site tetrahedral network (iv). Finally (v), the puckered hexagonal ring bonds with the A_4O tetrahedron to provide the pyrochlore building block. Figure adapted from Ref.[5] 3
1.3 A schematic of magnetic frustration between antiferromagnetically coupled spins on a (a) triangular or (b) tetrahedral lattice. 4
1.4 Experimental result of temperature dependence of the different modes of $Dy_2Ti_2O_7$. The figure is taken from Ref.[54]. For more details see the reference. 8
1.5 Experimental result of temperature dependence of the different modes of $Lu_2Ti_2O_7$. The figure is taken from Ref.[54]. For more details see the reference. 9
1.6 Representation of ideal cubic $Pm\bar{3}m$ perovskite, B centred (left) and A centred (right). Polyhedra show the coordination of each cation, the colours of which relate to the cation inside. To represent STO, green, blue and red characterize Sr, Ti and O ions, respectively. Adapted from Ref.[66] 12
1.7 Representation of I4/mcm perovskite with two different types of cell: B centred with a $\sqrt{2} \times \sqrt{2} \times 2$ unit cell and selected octahedra drawn (left) and an A centred $2 \times 2 \times 2$ cell, with all octahedra drawn (right). Polyhedra show the coordination of each cation, the colours of which relate to the cation inside. To represent STO, green, blue and red represent Sr, Ti and O atoms, respectively. Adapted from Ref.[66] 14
1.8 Anharmonic phonon dispersion of cubic STO at 300 K. The dotted lines show the harmonic phonon dispersion and the open symbols are experimental values at room temperature. Figure adapted from Ref.[79] (for more details, see this reference and references therein) 14
1.9 Temperature dependence of the anharmonic phonon frequencies of two optical modes in cubic STO. Figure adapted from Ref.[79] (for more details, visit this reference and references therein) 15

2.1 An instantaneous position of an atom 26
2.2 Illustration of a) second and b) third order force constants on a lattice. The second order force constant $\Phi_{\alpha\beta}$ determines the coupling between atoms ls and $l's'$, with the strength of interaction determined by the length of displacements $\boldsymbol{u}$. The third order force constant involves the coupling between three atoms. 27
2.3 The lowest order terms of the phonon self energy 34

3.1 Variation of the lattice parameter of $RE_2B_2O_7$ (RE = Sm, Gd, Tb, Dy, Ho, Er, YB, Lu and B = Ti, Zr, Hf) as a function of RE^{3+} ionic radius. LDA and GGA results are compared. 41

3.2 Variation of the positional parameter of oxygen O_{48f} of $RE_2B_2O_7$ (RE = Sm, Gd, Tb, Dy, Ho, Er, YB, Lu and B = Ti,Zr, Hf) as a function of RE^{3+} ionic radius. LDA and GGA results are compared. 41
3.3 Variation of the bond distances of $RE_2B_2O_7$ (RE = Sm, Gd, Tb, Dy, Ho, Er, YB, Lu, and B = Ti, Zr, Hf) as a function of RE^{3+} ionic radius. LDA and GGA results are compared. 43
3.4 Electronic band structures of $RE_2B_2O_7$ (RE = Sm and Lu; B = Ti, Zr and Hf) within the LDA method. The valence band maximum is shifted to zero for our convenience. . . 44
3.5 Electronic band structures of $RE_2B_2O_7$ (RE = Sm and Lu; B = Ti, Zr and Hf) within the GGA method. The valence band maximum is shifted to zero for our convenience. . 45
3.6 Phonon band spectra of $RE_2B_2O_7$ (RE = Sm and Lu, B = Ti, Zr and Hf) calculated using LDA method. For more details see the text. 51
3.7 Phonon band spectra of $RE_2B_2O_7$ (RE = Sm and Lu, B = Ti, Zr and Hf) calculated using GGA method. For more details see the text. 51

4.1 Variation of the elastic constants in the rare-earth $RE_2B_2O_7$ (RE = Sm, Gd, Tb, Dy, Ho, Er, Yb, Lu, and B = Ti, Zr, Hf) pyrochlores as a function of RE^{3+} ionic radius. Both LDA and GGA results are compared. 70
4.2 Variation of the bulk modulus in the rare-earth $RE_2B_2O_7$ (RE = Sm, Gd, Tb, Dy, Ho, Er, Yb, Lu, and B = Ti, Zr, Hf) pyrochlores as a function of RE^{3+} ionic radius. Both LDA and GGA results are compared. 71
4.3 Variation of the shear and Young's moduli, Poisson's and B/G ratios in the rare-earth $RE_2B_2O_7$ (RE = Sm, Gd, Tb, Dy, Ho, Er, Yb, Lu, and B = Ti, Zr, Hf) pyrochlores as a function of RE^{3+} ionic radius. Both the LDA and GGA results are compared. 72
4.4 Variation of the crystal density, mean sound velocity, Debye temperature, and the minimum thermal conductivity in the rare-earth $RE_2B_2O_7$ (RE = Sm, Gd, Tb, Dy, Ho, Er, Yb, Lu, and B = Ti, Zr, Hf) pyrochlores as a function of RE^{3+} ionic radii. Both the LDA and GGA results are compared. 77

5.1 (Color online) The calculated volume of the unit cell as a function of pressure. The black solid circle symbols represent the calculated data while the blue and red solid lines are obtained from fitting the data to the BM EOS with two different parameter sets in the low and high-pressure regions respectively; Inset: The variation of the fractional coordinate of the oxygen O_{48f} ions with pressure. The vertical dashed line is placed at the position where the phase transition occurs. 82
5.2 (Color online) Pressure dependence of the elastic constants for the structure resulting in internal atomic relaxation. A linear fit below and above 8.5 GPa shows a clear slope change in the shear modulus C_{44}. The dashed vertical line is placed at the location where the slope change occurs. 83
5.3 Pressure dependence of the phonon frequencies of $Dy_2Ti_2O_7$ calculated using DFPT. The change of slope (numbers shown, in cm^{-1}/GPa), at around 8.5 GPa, of some of the phonon modes is in accordance with the changes of slopes as measured by the Raman data as a function of pressure reported earlier in this paper. Vertical dashed lines are placed at the positions where the change in slope is observed. 84
5.4 Experimental results for the cell volume as a function of pressure. Inset graph shows the pressure dependence of the fractional coordinate of oxygen 48f. 85
5.5 Experimental results for the elastic moduli as a function of pressure. A vertical line is marked at 9 GPa pressure where the slope change in the moduli occurs 86
5.6 Experimental results for the phonon frequencies as a function of pressure. A vertical line is marked at 9 GPa pressure where the slope change in the moduli occurs. 86

6.1 Electronic band structure of $Y_2B_2O_7$ (B = Ti, Zr, and Hf) calculated both within the LDA and GGA approaches. The valence band maximum is shifted to zero for our convenience. 92
6.2 Calculated partial density of states for $Y_2Ti_2O_7$ within LDA. 93

6.3 Phonon band spectra of $Y_2Ti_2O_7$ calculated using the LDA method. Left panel (in blue colour) is for the optimized structure, while the right panel (in red colour) is for the distorted structure. For more details see the text. 94
6.4 Phonon band spectra of $Y_2Ti_2O_7$ calculated using the GGA method. Left panel (in blue) is for the optimized structure, while the right panel (in red) is for the distorted structure. For more details see the text. 95
6.5 Phonon band spectra of $Y_2Zr_2O_7$ pyrochlore. Both the LDA (left panel) and GGA (right panel) spectra are shown. 96
6.6 Phonon band spectra of $Y_2Hf_2O_7$ pyrochlore. Both the LDA (left panel) and GGA (right panel) spectra are shown. 96
6.7 Electronic density of states (DOS) of $Y_2Ti_2O_7$ pyrochlore. Both the LDA (left panel) and GGA (right panel) results are shown. The DOS for the optimized (undistorted) and the distorted crystal structures are plotted together for the comparison. 97
6.8 The partial density of states (PDOS) of $Y_2Ti_2O_7$ calculated using the GGA method. The DOS for the optimized (undistorted) and the distorted crystal structures are plotted together for the comparison. 98

7.1 (Left panel) Variation of the mode Grüneisen parameters for the Raman active modes along the high symmetry directions in the first BZ; (Middle panel) Temperature dependence of the linear thermal expansion coefficient; (Right panel) Temperature dependence of the Quasiharmonic contribution to some of the optical modes. 105
7.2 Three-phonon interaction processes that may create or destroy the phonon $\boldsymbol{q}j$. 106
7.3 (Right panel) Two phonon density of states (TDOS) of $Y_2Ti_2O_7$. The broadening parameters (ϵ) are in cm^{-1}. (Left panel) The up and down conversion decay processes of TDOS are shown for two different temperature values and for $\epsilon = 3$ cm^{-1}. 110
7.4 Phonon linewidth as a function of frequency of $Y_2Ti_2O_7$. The broadening parameters (ϵ) are in cm^{-1}. The up and down conversion decay processes are shown for two different temperature values and for $\epsilon = 3$ cm^{-1}. 110
7.5 Temperature dependence of the cubic contribution to some of the modes in $Y_2Ti_2O_7$. $|C_j^{(3)}|^2 = 1.0 \times 10^{10}$ erg^{-1} was used for all the modes. 111
7.6 Experimental result of temperature dependence of the modes P_1, P_3, P_4, P_5, P_6, and P_8 of non-magnetic pyrochlore $Y_2Ti_2O_7$. Solid lines are quide to eye. The figure is taken from Ref.[5]. See the reference for more details about the assignment of different modes. . . . 111

8.1 Variation of the mode Grüneisen parameters for Raman active modes in $Y_2Ti_2O_7$ (left panel) and $Y_2Zr_2O_7$ (right panel), along the high symmetry directions in the BZ. 117
8.2 Temperature dependence of the linear thermal expansion coefficient in $Y_2Ti_2O_7$ (left panel) and $Y_2Zr_2O_7$ (right panel). 117
8.3 Temperature dependence of the Quasiharmonic contribution to Raman active(top left), IR active (top right), and silent modes(bottom) in $Y_2Ti_2O_7$ compound. 118
8.4 Temperature dependence of the Quasiharmonic contribution to Raman active(top left), IR active (top right), and silent modes(bottom) in $Y_2Zr_2O_7$ compound. 119
8.5 Temperature dependence of cubic contribution to Raman active(top left), IR active (top right), and silent modes(bottom) in $Y_2Ti_2O_7$. 125
8.6 Temperature dependence of cubic contribution to Raman active(top left), IR active (top right), and silent modes(bottom) in $Y_2Zr_2O_7$. 126
8.7 Temperature variation of phonon frequencies of Raman active(top left), IR active (top right), and silent modes(bottom) in $Y_2Ti_2O_7$. 127
8.8 Temperature variation of phonon frequencies of Raman active(top left), IR active (top right), and silent modes(bottom) in $Y_2Zr_2O_7$. 128
8.9 Temperature variation of the FWHM of Raman active(top left), IR active (top right), and silent modes(bottom) in $Y_2Ti_2O_7$. 130

8.10 Temperature variation of the FWHM of Raman active(top left), IR active (top right), and silent modes(bottom) in $Y_2Zr_2O_7$. 131

9.1 Variation of the mode Grüneisen parameters for Raman active modes in $Dy_2Ti_2O_7$ and $Lu_2Ti_2O_7$ pyrochlores, along the high symmetry directions in the BZ. 136
9.2 Temperature dependence of the linear thermal expansion coefficient of $Dy_2Ti_2O_7$ and $Lu_2Ti_2O_7$ pyrochlores. 137
9.3 Temperature dependence of the Quasiharmonic contribution to some of the modes in $Dy_2Ti_2O_7$ and $Lu_2Ti_2O_7$ pyrochlores. 137
9.4 Two phonon density of states (TDOS) of $Dy_2Ti_2O_7$ and $Lu_2Ti_2O_7$ pyrochlores. The up and down conversion decay processes of TDOS are shown for two different temperature values. 139
9.5 Temperature dependence of the full width at half maximum for some of the modes calculated at $\epsilon = 3.0$ cm^{-1}. 139
9.6 Temperature dependence of the cubic contribution to some of the modes in $Dy_2Ti_2O_7$. $|C_j^{(3)}|^2 = 1.0 \times 10^{10}$ erg^{-1} was used for all the modes. 140
9.7 Temperature dependence of the cubic contribution to some of the modes in $Lu_2Ti_2O_7$. $|C_j^{(3)}|^2 = 1.0 \times 10^{10}$ erg^{-1} was used for all the modes. 140
9.8 Temperature dependent contributions from different terms of third-order shift for an infrared active mode F_{1u} (188 cm^{-1}) and a high frequency Raman active mode F_{2g} (801 cm^{-1}) of $Dy_2Ti_2O_7$. 141
9.9 Temperature dependent contributions from different terms of third-order shift for an infrared active mode F_{1u} (164 cm^{-1}) and a high frequency Raman active mode F_{2g} (826 cm^{-1}) of $Lu_2Ti_2O_7$. 141

10.1 Phonon band dispersion of cubic $SrTiO_3$ calculated within the LDA framework. 147
10.2 Phonon band dispersion of Tetragonal $SrTiO_3$ calculated within the LDA framework. . 148
10.3 Temperature dependence of the linear thermal expansion coefficient of tetragonal STO. 150
10.4 Temperature dependence of the Quasiharmonic contribution to Raman active(top left), IR active (top right), and silent (bottom) modes in $SrTiO_3$ perovskite. 151
10.5 Temperature dependence of cubic contribution to Raman active(top left), IR active (top right), and silent (bottom) modes in $SrTiO_3$ perovskite. 153
10.6 Temperature variation of phonon frequencies of Raman active(top left), IR active (top right), and silent (bottom) modes in $SrTiO_3$ perovskite. 154
10.7 Temperature variation of full width at half maximum(FWHM) of Raman active(top left), IR active (top right), and silent (bottom) modes in $SrTiO_3$ perovskite. 156

C.1 Self energy diagram in second order perturbation theory 173
C.2 Contour of evaluation of frequency sums 175

D.1 Rotation by $2\pi/3$ about the axis marked 3 changes $x \to y; y \to z;$ and $z \to x$. 182

Chapter 1

Introduction

This thesis presents our endeavour to understand the structural, electronic, elastic, mechanical, and the phonon dynamics of pyrochlore systems and the phonon anharmonic effects in SrTiO3 perovskite material, using first principles DFT calculations. We, therefore, begin our thesis with this introductory chapter devoted to a detailed account of the pyrochlores, all of which have a chemical formula of the form - $A_2B_2O_7$, and perovskites with the chemical formula - ABO_3.

1.1 What are pyrochlores?

The name pyrochlore comes from the mineral $NaCaNb_2O_6F$ pyrochlore. The stoichiometry of the pyrochlore systems is $A_2B_2O_7$, a ternary metallic oxide where the cations A and B have charges of 3+ and 4+, respectively. However, another series of pyrochlores with A^{2+} and B^{5+} charge configuration also exists[1]. Due to their structure and wide compositional range, these materials offer different properties[1–3], and have been used in a wide variety of applications, e.g., as solid electrolytes (ionic conductors), electrodes for fuel cells, sensors, catalysts, materials for nuclear waste disposal, insulators, semiconductors, electrical conductors, superconductors, and also as dielectric, piezoelectric, ferroelectric, and colossal magnetoresistance (CMR)[4] materials. The magnetic properties in the pyrochlore materials have been studied extensively, especially of A^{3+} and B^{4+} type, where A^{3+} is a rare-earth ion and B^{4+} is usually a transition metal ion. This is because they exhibit geometric frustration (due to their special geometry-see below).

1.1.1 Structural details

The generic pyrochlore is written as $A_2B_2O_6O'$ with four distinct crystallographic sites, namely, A, B, O, and O′. The space group of the pyrochlores is $Fd\bar{3}m$ (SG No. 227) with eight formula units in a

conventional unit-cell and two formula units in a primitive cell. The B^{4+} cations occupy the origin at the 16c site, A^{3+} cations are at 16d, O are at 48f, and O′ are at the 8b sites, while the 8a site remains vacant. The site symmetry of the cations is D_{3d}, that of oxygen 48f is C_{2v} and that of oxygen 8b is T_d (see Table 1.1). The pyrochlore systems have only one internal parameter x which is related to the position of oxygen 48f. Both the cations individually form corner-sharing tetrahedral sublattices (see Fig. 1.1) thus giving rise to a geometrically frustrated lattice if any of the cations are magnetic.

Table 1.1: Atomic positions in $A_2B_2O_6O'$ pyrochlore (space group: $Fd\bar{3}m$, No: 227). x is the fractional coordinate of oxygen at 48f. We denote N as the number of atoms per primitive cell

Atom	N	Wyckoff position	Site symmetry	Coordinates
A	4	16d	$\bar{3}m(D_{3d})$	$\frac{1}{2}, \frac{1}{2}, \frac{1}{2}$
B	4	16c	$\bar{3}m(D_{3d})$	0, 0, 0
O	12	48f	$mm(C_{2v})$	$x, \frac{1}{8}, \frac{1}{8}$
O′	2	8b	$\bar{4}3m(T_d)$	$\frac{3}{8}, \frac{3}{8}, \frac{3}{8}$

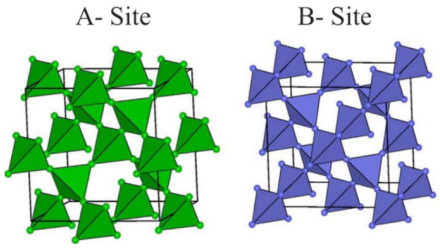

Figure 1.1: Pyrochlore tetrahedra sublattices formed by A and B sites. Adapted from Ref.[1]

Depending on the value of the oxygen x-parameter, the pyrochlore structure can be described from different perspectives, e.g. as an anion deficient fluorite lattice; as an interpenetrating network of BO_6 octahedra and AO'_2 chains; or as a network of A_4 and B_4 tetrahedra with appropriate locations of the oxygen anions inside or outside the tetrahedra. However, due to the uniqueness of pyrochlore structures, none of these aspects can define its structure entirely. The polyhedral geometry of the cations changes its form as the x parameter of oxygen O_{48f} is varied. Typically, x lies in the range 0.3125-0.375, though the extreme values have never been recognised experimentally[2]. For $x = 0.3125$, the B^{4+} cations have an octahedral geometry with six O ions, and the A^{3+} cations form cubic polyhedra with eight oxygen ions (6O+2O′) where six O ions form a puckered hexagonal ring with their average plane being perpendicular to the O′-A-O′ axis. However, for the extreme value of $x = 0.375$, eight oxygen atoms (6O + 2O′) form a regular cube wherein the cations A^{3+} reside at its centre, while the B^{4+} ions get placed at the centre of a highly distorted octahedron formed by six O atoms. Experimentally, the value of x lies in the range 0.320-0.345 and therefore, the polyhedra formed around the cations are distorted from their ideal shapes. Due to the site symmetry of $B^{4+}(D_{3d})$, the B-O bond distances are of the

same length in octahedral BO_6 (see Fig. 1.2). The octahedral O-B-O angle lies in the range 81-100° (different from the ideal value of 90°), while the B-O-B angle of two adjoining octahedra lies in the range 120-140°. The four B^{4+} cations in the primitive cell form a tetrahedron with an 8a-vacant site at its centre. As the value of x decreases from 0.375, the coordination polyhedra of A^{3+} sites get distorted from regular cubes to puckered hexagonal ring formed by the 48f oxygen ions with two apical 8b-O′ ions. The A-O′-A angle is always 109° 28′ (the tetrahedral angle). The A-O′ bond length ($\approx 2.2\mathring{A}$) is independent of the oxygen x-parameter and is always less than the A-O bond length ($\approx 2.4 - 2.5\mathring{A}$).

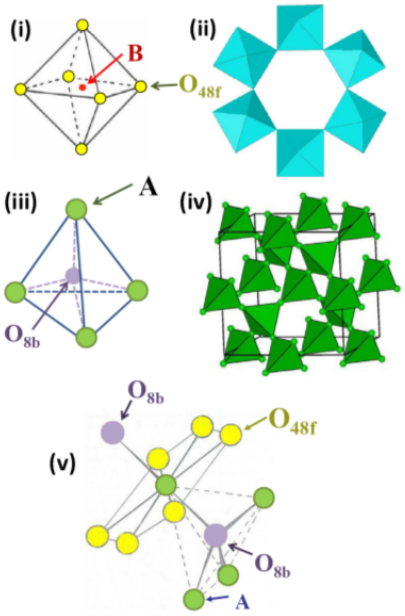

Figure 1.2: Octahedral and tetrahedral geometries of the pyrochlore lattice. An octahedron (i) is formed by B^{4+} and O_{48f} atoms such that six-octahedra make a puckered hexagonal ring (ii) sharing their corners. Four A^{3+} cations form a tetrahedron (iii) with an O_{8b} atom at its centre, which constitute the A-site tetrahedral network (iv). Finally (v), the puckered hexagonal ring bonds with the A_4O tetrahedron to provide the pyrochlore building block. Figure adapted from Ref.[5]

As mentioned above, the compositions of pyrochlore materials are of two types: $A_2^{2+}B_2^{5+}O_7$ and $A_2^{3+}B_2^{4+}O_7$, though our interest in this thesis is in the latter type only. Though any combination of $(3+, 4+)$ could satisfy the charge neutrality condition, only a few cations can form the pyrochlore structure. The A^{3+} cations can be rare-earth, Sc, Y, Bi, Tl or In, whereas B^{4+} can be a transition metal ion or any element of group IV(a) of the periodic table.

The relative cationic radii, i.e., cationic radius ratio ($RR = r_{A^{3+}}/r_{B^{4+}}$) and the oxygen x-parameter are responsible for the formation and stability of the pyrochlore lattices, and stable structures are typically formed only when the RR lies within the range 1.46-1.80 at atmospheric pressure (e.g., $r_{Gd^{3+}}/r_{Zr^{4+}} = 1.46$ in $Gd_2Zr_2O_7$ to $r_{Sm^{3+}}/r_{Ti^{4+}} = 1.78$ in $Sm_2Ti_2O_7$). There are a few exceptions though; e.g., $Pr_2Ru_2O_7$ exists in stable form with RR = 1.82, while, $Pr_2Mo_2O_7$ has never been realized

despite an RR = 1.73. For RR values below or close to 1.46, defect-fluorite structures are preferred over the pyrochlore structure, as in the case of the heavier rare-earth members of $RE_2Zr_2O_7$ (RE = Tb to Lu), but a monoclinic structure is formed if the RR is close to or above 1.80. It is also seen that in some of the cases a high pressure is required to get a stable structure, even if the RR lies within its stability range, i.e., 1.46-1.80. For more details related to structural stability, see Ref.[2]

1.1.2 Geometrical frustration

In magnetic systems, frustration implies the inability of a cluster of spins, with antiferromagnetic interactions, to attain a unique minimum energy configuration. The notion of magnetic frustration was first proposed by P. W. Anderson in a lecture at a summer school in Aspen in 1976[6], but it first appeared in a publication on spin glasses by Toulouse[7] in 1977 and later in one by Villain[8] in the same year.

In a crystalline geometrically frustrated magnet, the frustration results purely from the geometry of the lattice. A lattice of equilateral triangles or tetrahedra provides a simple example of geometrical frustration (GF) (Fig. 1.3). When the spins prefer an antiferromagnetic exchange interaction, the system can not find a unique minimum energy ground state that satisfies all the pair interactions simultaneously, which loosely implies that in any one configuration some of the spins do not know what to do and thus are frustrated.

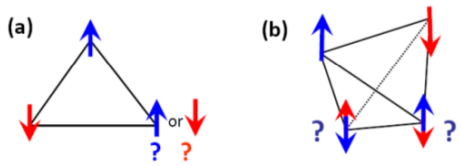

Figure 1.3: A schematic of magnetic frustration between antiferromagnetically coupled spins on a (a) triangular or (b) tetrahedral lattice.

The exchange Hamiltonian for an interacting cluster of spins can be written as,

$$H_{ex} = -\sum J_{ij} S_i S_j \tag{1.1}$$

where J_{ij} is the exchange interaction between two spins S_i and S_j, at sites i and j respectively. When J_{ij} is negative, it favours an antiparallel (antiferromagnetic) correlation, and if it is equal for all nearest neighbour pairs of a triangular or tetrahedral cluster (due to equilateral geometry), it is apparent that at a time any two of the spins (Fig. 1.3) can be satisfied and the third spin is unable to optimize both its bonds, i.e., the system is geometrically frustrated. Spin systems with geometrical frustration are very interesting because: (1) GF hinders long-range ordered states, i.e., the system has possibilities of having one of a variety of "spin-liquid" ground states with fascinating properties[9–11]; (2) as GF is local, it could lead to a macroscopically degenerate ground state with extensive zero temperature entropy (at

least in specific models if not in real systems) (3) these materials can be studied using various external tuning parameters and their results can often be mapped onto other materials with a high level of degeneracy, for example, ice phase of water, folding of proteins and so on.

A convenient, experimentally accessible, characterization of the geometrical frustration is in terms of a "frustration index", defined as[12]:

$$f = \frac{|\theta_{CW}|}{T_C} \tag{1.2}$$

where θ_{CW} is the Curie-Weiss temperature which can be measured from the high-temperature paramagnetic susceptibility of the system. T_C is the critical temperature at which the system realises a magnetically long-range ordered state. In case of a system that undergoes spin-glass transition, T_C is the freezing temperature T_f, whereas it is T_N in case of an antiferromagnetic transition. For a highly frustrated system, the value of T_C is much lower as compared to θ_{CW}. Systems with f values in the range from 1 to 5 are generally classified as non-frustrated[3]. $f \simeq 1$ typically for the magnetic systems that go into a ferromagnetically ordered state. However, in case of systems that have an antiferromagnetic order, f can be quite a bit higher depending on the exact magnetic structure that is involved. For example, in case of the non-frustrated $RCrO_3$ (R = rare-earth) cubic perovskite compounds, f ranges from 2 to 3. In the case of the frustrated $Y_2Mo_2O_7$ molybdenum pyrochlore, the value of $f \simeq 10$[13, 14].

1.1.3 Magnetic ground states

While the Hamiltonian of Eq. 1.1 is a good useful starting model for understanding the properties of a range of geometrically frustrated magnetic materials, several additional interactions may also need to be considered for building realistic models. These include single-ion anisotropy[15], further neighbour exchange[16], dipolar interactions[17, 18], Dzyaloshinskii-Moriya interactions[19], magnetoelastic coupling[20], site dilution[21, 22] and exchange randomness[23]. In many instances, the associated energy scales are small, below which they may influence magnetic order or spin freezing, but they can be ignored at higher temperatures.

Microscopic features of the perturbations specific to the system under investigation decide which interactions eventually take over leading the system to an ordered state that often displays a broad range of exciting and somewhat unconventional magnetic and thermodynamic properties at low temperatures. To name a few examples of the $A_2B_2O_7$ pyrochlores that show exotic phenomena: spin-glass freezing in $Y_2Mo_2O_7$[24] and $Tb_2Mo_2O_7$[25, 26]; complex antiferromagnetic order in $Er_2Ti_2O_7$, arising from the order by disorder mechanism[27]; spin-liquid phase or cooperative paramagnetism in $Tb_2Ti_2O_7$[11] which manifests signs of spin crystallization upon compression and phase transition at an elevated $T_N \sim 3K$[28], as well as spin-wave excitations under high magnetic fields[29]; a first-order phase transition in

the spin dynamics of $Yb_2Ti_2O_7$[9]; multiple magnetic transitions below 1 K in $Gd_2Ti_2O_7$[30]; crystal-field split nonmagnetic ground state in $Tm_2Ti_2O_7$[31]; spin-ice state in $Nd_2Mo_2O_7$[32], $Sm_2Mo_2O_7$[33], $Dy_2Sn_2O_7$[34], $Ho_2Sn_2O_7$[35], $Dy_2Ti_2O_7$[36], and $Ho_2Ti_2O_7$[15]; unconventional anomalous Hall effect in metallic $Nd_2Mo_2O_7$[32]; superconductivity in $Cd_2Re_2O_7$[37, 38]; Kondo-like effect in $Pr_2Ir_2O_7$[10]; magnetic Coulomb phase in $Ho_2Ti_2O_7$[39] and magnetic monopoles in $Dy_2Ti_2O_7$[40].

1.1.4 Vibrational properties

Pyrochlores belong to the face centred cubic family (space group: $Fd\bar{3}m$) with two formula units ($A_2B_2O_7$) per primitive unit cell. This leads to a total of 66 normal modes with irreducible representations as follows[41]:

16d : $A_{2u} + E_u + 2F_{1u} + F_{2u}$

16c : $A_{2u} + E_u + 2F_{1u} + F_{2u}$

48f : $A_{1g} + E_g + 2F_{1g} + 3F_{2g} + A_{2u} + E_u + 3F_{1u} + 2F_{2u}$

8b : $F_{1u} + F_{2g}$

Therefore, the entire representation for the Γ-point phonons is:

$$\begin{aligned} \Gamma_{Optical} &= A_{1g} + E_g + 2F_{1g} + 4F_{2g} + 3A_{2u} + 3E_u + 7F_{1u} + 4F_{2u} \\ \Gamma_{Acoustic} &= F_{1u} \end{aligned}$$

Out of these 26 irreducible representations, only six ($A_{1g}+E_g+4F_{2g}$) are Raman active and seven ($7F_{1u}$) are infrared active modes, while the remaining are inactive. There have been various theoretical and experimental studies to identify the different vibrational modes in this systems[42–46]. The irreducible representations of the different normal modes imply that the infrared active modes involve the vibrations of all the four non equivalent sites (A, B, O and O′) and are due to either bond stretching or angular bending. However, the Raman active modes involve the vibrations of the oxygen atoms only; the A and B atoms remain stationary because they occupy sites with inversion symmetry (site symmetry: D_{3d}). The Raman modes A_{1g}, E_g, and $3F_{2g}$ are due to the vibrations of oxygen atoms located at 48f Wyckoff sites, whereas the fourth F_{2g} Raman mode arises from the vibrations of O' atoms situated at 8b sites.

1.1.5 Phase stability and phase transitions

The stability of pyrochlore materials under extreme condition (i.e., irradiation, high temperature, and high pressure) is of vital concern in many fields, such as solid-state physics, material science, and nuclear engineering. For example, some zirconates, such as $Y_2Zr_2O_7$, $La_2Zr_2O_7$, and $Nd_2Zr_2O_7$ that are recognised for potential applications in magnetohydrodynamic power generation, must endure very

severe conditions.

Radiation-induced disordering or amorphization in pyrochlores has long been of concern, owing to the possible value of some pyrochlores as host matrices for the immobilization of actinides. The structural phase shift from ordered pyrochlore to disordered defect states or amorphous structures can be caused not only by self-radiation from actinide decay or external ion irradiation but also by subjecting the pyrochlore compounds to high pressure.

The pressure effect, at ambient temperatures, has been investigated for some of the titanate pyrochlore materials. $Sm_2Ti_2O_7$ and $Gd_2Ti_2O_7$ get anion disorder above 40 GPa and become amorphous above 51 GPa[47, 48]. $Gd_2Ti_2O_7$ display a structural deformation around 9 GPa[49].

Zhang et al.[50] explored high pressure Raman and X-ray diffraction studies to examine the structure evolution of pyrochlore titanates $Y_2Ti_2O_7$ and $Gd_2Ti_2O_7$. They observed pressure-induced order-disorder transitions in these systems. The cations and anions in $Y_2Ti_2O_7$ started to be disordered at pressures above 50 GPa and the structure switches from pyrochlore ($Fd\bar{3}m$) to defect fluorite structure ($Fm\bar{3}m$) A_4O_7. This change is not stable in $Gd_2Ti_2O_7$, and amorphization progresses at a pressure above 32 GPa.

1.1.6 Temperature dependent phonon studies

Recently, the vibrational properties of some of the pyrochlores have been investigated as a function of temperature by various groups[49, 51–56]. These studies not only show that phonons in the titanate pyrochlores are highly anomalous but also indicate the extreme sensitivity of vibrational spectroscopy toward probing detailed structural and electronic features. In the pyrochlore $Dy_2Ti_2O_7$, Raman spectroscopy exhibited a subtle structural deformation of the pyrochlore lattice upon cooling below $T = 100$ K[54]. In the pyrochlore $Tb_2Ti_2O_7$, new crystal-filed (CF) excitations were observed using Raman results at $T = 4$ K[53]. In the temperature-dependent studies, a signature of highly anomalous phonons (i.e., the decline in phonon frequency upon cooling; also referred to as phonon softening) has been detected in the pyrochlores $Er_2Ti_2O_7$[52], $Gd_2Ti_2O_7$[51, 52], and $Dy_2Ti_2O_7$[51, 52, 54].

Around a decade ago, Maczka et al.[57] conducted a temperature-dependent Raman study of $Ho_2Ti_2O_7$ and $Dy_2Ti_2O_7$ single crystals in the 5-873 K temperature range. Their temperature studies showed a large increase in the linewidths. These changes were interpreted in terms of strong third-order phonon-phonon anharmonic interactions. Their Raman spectra also showed anomalous softening of the majority of phonon modes upon cooling in the whole temperature range studied. In contrast to this behavior, the $F_{2g} \simeq 310$ cm^{-1} and $E_g \simeq 330$ cm^{-1} phonon modes showed hardening upon cooling down to about 100-120 K and then anomalous softening below this temperature. The suggestion was made by these authors that this anomalous behaviour of phonon wave numbers is related to an increase in octahedral distortion upon cooling.

In another work, Maczka et al.[52] carried out temperature-dependent studies of Raman mode frequencies and linewidths in $Gd_2Ti_2O_7$ and $Er_2Ti_2O_7$. These studies also detected phonon anomalies for a few phonon modes. These authors suggested that the anomalous phonon behaviour could result from the phonon-phonon anharmonic interactions.

This anomalous response has been qualitatively assigned by Bi et al.[58] to strong spin-phonon coupling in $Dy_2Ti_2O_7$ for a few modes. Since the strength of exchange interaction is comparatively much lower for titanate pyrochlores (ranging between $\sim$ 19 K in $Tb_2Ti_2O_7$[14, 59] and $\sim$ 25 K in $Sm_2Ti_2O_7$[55]), and there is no long-range spin order in $Dy_2Ti_2O_7$ as well as in $Gd_2Ti_2O_7$ and $Er_2Ti_2O_7$ down to very low temperatures, the validity of this qualitative account of the anomalous temperature dependence in terms of spin-phonon coupling is far from certain. Another description of this anomalous behavior in terms of a coupling between phonons and crystal field excitations can also be ruled out because $Gd_2Ti_2O_7$ also presents similar phonon anomalies even though for Gd^{3+} ions no crystal field effect is anticipated due to the spherical symmetry of the $4f$ charge cloud.

Saha et al.[54] recently performed temperature-dependent Raman studies on single crystals of $Dy_2Ti_2O_7$ (Fig. 1.4) and its nonmagnetic analogue $Lu_2Ti_2O_7$ (Fig. 1.5) over a temperature range of 12 to 300 K. These authors also observed the phonon anomalies in these titanate pyrochlores confirming that this anomalous behaviour is most likely due to the phonon-phonon anharmonic interactions.

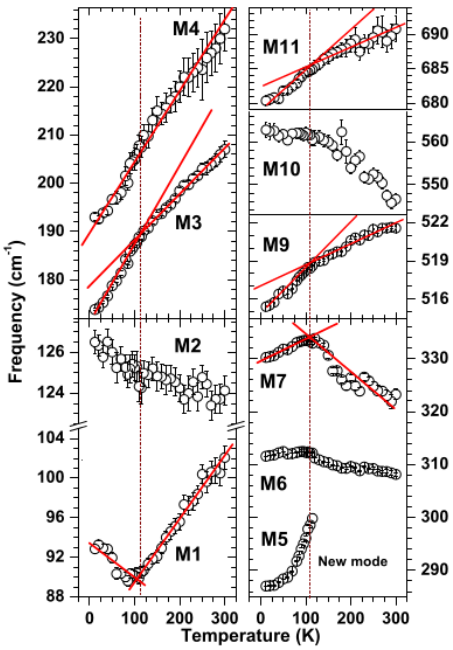

Figure 1.4: Experimental result of temperature dependence of the different modes of $Dy_2Ti_2O_7$. The figure is taken from Ref.[54]. For more details see the reference.

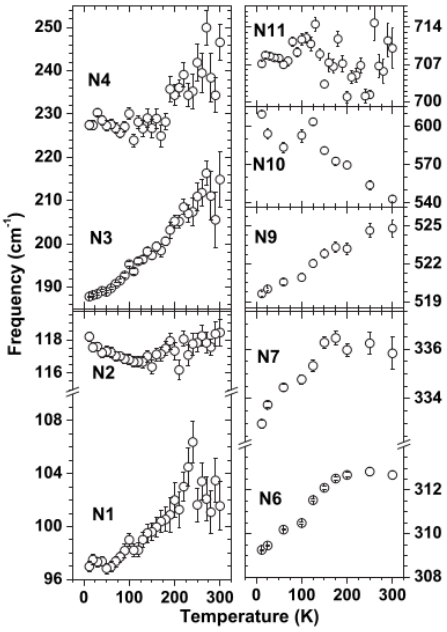

Figure 1.5: Experimental result of temperature dependence of the different modes of $Lu_2Ti_2O_7$. The figure is taken from Ref.[54]. For more details see the reference.

1.1.7 Our interest

Though the structural, electronic, and elastic properties of pyrochlore materials have been studied by several groups as mentioned above, still there are many fascinating properties related to the phonons, which are relatively unexplored. In the first-principles study of the zone centre phonons of few rare-earth titanates by Kumar et al.[41], a point was made that the local density approximation (LDA) works better than the generalized gradient approximation (GGA) for the pyrochlore oxides. By exploring the phonons throughout the first Brillouin zone, we show that this seems to be widely true.

In chapter 3, we present our DFT results of the structural, electronic, and vibrational properties in the rare-earth $RE_2B_2O_7$ (RE = Sm, Gd, Tb, Dy, Ho, Er, Yb, Lu and B = Ti, Zr, Hf) pyrochlores. Both the LDA and GGA results are presented for most of the calculations. The anomalous dynamical charges are reported for the transition metal elements and for the oxygen O_{48f}. Phonon properties are studied across the Brillouin zone, wherein the structural instabilities are found with respect to some of the optical modes, in the sense that the frequency of some of the optical modes is imaginary. A small distortion to the atomic positions in the unit-cell stabilizes the structure.

The mechanical and thermal properties of pyrochlores are also quite interesting. Pyrochlores are used as a thermal barrier coating (TBC) because they exhibit very small thermal conductivities at very high temperatures. In chapter 4, we present the comparative study of the elastic, mechanical, and thermal properties in the rare-earth $RE_2B_2O_7$ (RE = Sm, Gd, Tb, Dy, Ho, Er, Yb, Lu and B = Ti, Zr, Hf) pyrochlores. In this chapter also both LDA and GGA results are compared.

High-pressure X-ray diffraction, Brillouin scattering, and the Raman scattering spectroscopes showed that $Dy_2Ti_2O_7$ pyrochlore displays an isostructural phase transition around 9 GPa of pressure. Our interest is to see if we can also derive such an isostructural phase transition in $Dy_2Ti_2O_7$ using our high-pressure first-principles calculations of the structural, elastic, and vibrational properties. These studies are presented in the chapter 5.

Chapter 6 presents DFT results of the electronic, elastic, thermal, and vibrational properties of $Y_2B_2O_7$ (B = Ti, Zr, Hf) pyrochlores. Both LDA and GGA results are compared. Anomalous dynamical charges and the structural instabilities are briefly discussed.

As discussed in sec. 1.1.6, pyrochlore titanates display anomalous phonon behaviour with temperature. These phonon anomalies have been attributed to the phonon-phonon anharmonic interactions. In chapter 7, we present our temperature-dependent phonon studies in $Y_2Ti_2O_7$ pyrochlore. We have calculated the mode Grüneisen parameters for several phonon modes. We have calculated the temperature-dependent linear thermal expansion coefficient and the quasiharmonic frequency shifts for some of the optically active phonon modes. The two phonon density of states, phonon linewidths, and lineshifts are extensively explored. The most challenging part in the temperature-dependent phonon studies is to calculate the anharmonic interatomic force constants. In this chapter, we have calculated them using a well established approach in terms of a single fitting parameter to get the qualitative understanding of the phonons as a function of temperature.

In chapter 8, we present our temperature-dependent phonon studies in $Y_2Ti_2O_7$ pyrochlore, similar to the chapter 7, but here we have calculated the third-order interatomic force constant matrix elements exactly using the "$2n + 1$" theorem as implemented within the DFT linear response theory. All the calculations in the previous chapter were based on the ultrasoft pseudopotentials, whereas in this chapter, all the calculations are based on the norm-conserving pseudopotentials. Therefore, here again we have reexamined all the results of the previous chapter. In this chapter, we also present the temperature-dependent phonon properties of $Y_2Zr_2O_7$ pyrochlore to see how the anomalous nature of phonons changes by replacing the lighter Ti^{4+} ions by the heavier Zr^{4+} ions.

In chapter 9, we present temperature dependent phonon properties in $Dy_2Ti_2O_7$ and $Lu_2Ti_2O_7$ pyrochlores. In this chapter, we present all our anharmonic calculations by approximating the third order phonon coupling constants as was used in the chapter 7 to get the qualitative understanding of the behaviour of phonons as a function of temperature.

1.2 $SrTiO_3$ perovskite

Perovskite oxides are a wide class of materials with many technological applications. The ideal perovskite structure is cubic and is usually represented by the formula ABO_3, where the cations A and B are,

respectively coordinated with 12 and 6 oxygen anions.

The ideal perovskite structure can undergo a broad range of structural distortions, and several types of cations can occupy the A and B sites. The stability of the (ideal) cubic perovskite structure with respect to other structures is determined by the ionic radii of the constituent ions through the Goldschmidt tolerance factor t:

$$t = \frac{r_A + r_O}{\sqrt{2}(r_B + r_O)} \tag{1.3}$$

where r_A, r_B, and r_O are the ionic radii of the A-site cation, B-site cation, and the oxygen anion, respectively. The ideal cubic structure is obtained when $t = 1$; the deviation of t from unity leads to a distortion from the cubic structure with the lattice becoming first rhombohedral and then orthorhombic. Stable perovskite structures are predicted in the range of $0.77 \leq t \leq 1.0$; while for $t > 1$ only the hexagonal structure is stable. The perovskite structure stays extremely stable with respect to the injection of vacancies and cation substitutions, and numerous families of materials with unique compositions stem from this simple structure. For example, the family of tungsten bronzes, based on the $NaWO_3$ compound, can be seen as strongly A-deficient ABO_3 perovskites; while the family of $SrFrO_x$ compounds is an example of oxygen deficient perovskites. Furthermore, dopant cations can substitute some of the ions situating the A- and B-sites, leading a variety of structures with distinct compositions and properties. An example is the structures of the high temperature superconductors, $YBa_2Cu_3O_{7-x}$; in this case cations of distinct valence randomly occupy part of the A- and B-sites of the perovskite structure. Such a diversity of structures and chemical compositions enrich perovskite oxides and perovskite-like oxides with a vast diversity of electronic, dielectric, ferroic, and magnetic properties.

Strontium titanate $SrTiO_3$ (hereafter, it is referred to as STO) has many useful electronic properties. It is a wide band-gap semiconductor with an energy gap of 3.22 eV[60], which is usually of n-type[61]. However, electronic conductivity is prominently dependent on the oxygen defect concentration and under certain situations of oxygen partial pressure, can be converted to display p-type conductivity[62]. STO is generally assumed to be ionic with titanium in the 4+ state, strontium in the 2+ state and oxygen in the 2− state.

STO has been explored experimentally and is observed to exist in two phases, cubic and tetragonal[63]. Other perovskites are known to have orthorhombic and rhombohedral phases at lower temperatures. Below we describe the structural properties of the cubic and tetragonal phases of STO.

1.2.1 The cubic STO perovskite

The simplest and the highest symmetry phase of the STO is cubic, with a space group of $Pm\bar{3}m$ and a lattice parameter of 3.905 Å at room temperature[63] (see Fig. 1.6). The cubic phase in STO is observed above the transition temperature of 105 K[63–65]. In the cubic structure, the strontium and titanium

cation's average positions are at the centre of the oxygen cuboctahedra and octahedra, respectively. Each oxygen anion exactly bisects a pair of neighbouring titanium cations, and each oxygen anion bonds to two titanium cations (~ 2 Å) and four strontium cations (~ 2.8 Å). The Wyckoff positions for the cubic STO structure are given in Table. 1.2.

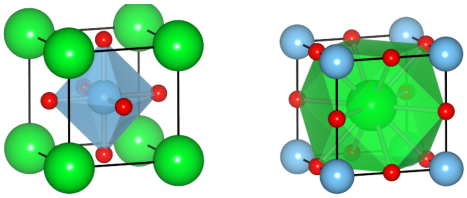

Figure 1.6: Representation of ideal cubic $Pm\bar{3}m$ perovskite, B centred (left) and A centred (right). Polyhedra show the coordination of each cation, the colours of which relate to the cation inside. To represent STO, green, blue and red characterize Sr, Ti and O ions, respectively. Adapted from Ref.[66]

Table 1.2: Wyckoff positions for strontium titanate in the high temperature cubic phase (space group $Pm\bar{3}m$ O_h^1 (SG 221)).

Atom	Position	Coordinates
A (Sr)	1b	$(\frac{1}{2}, \frac{1}{2}, \frac{1}{2})$
B (Ti)	1a	$(0, 0, 0)$
O	3d	$(\frac{1}{2}, 0, 0)(0, \frac{1}{2}, 0)(0, 0, \frac{1}{2})$

1.2.2 The tetragonal STO perovskite

Though all the perovskite materials exist in the cubic phase at high temperatures, when the temperature is lowered, they undergo different types of polar or non-polar structural phase transitions. For example, $BaTiO_3$ exhibits a sequence of three ferroelectric (FE) phase transitions from the cubic to the following phases successively: (i) a tetragonal phase ($T_C \simeq 130$°c) in which the polarization is oriented along the [001] axis (P4mm, SG: 99), (ii) an orthorhombic phase ($T_C \simeq 0$°c) with the polarization oriented along [011] (Pmm2, SG: 25) and (iii) a rhombohedral phase ($T_C \simeq -80$°c) with polarization oriented along [111] (P3m1, SG:156). If the centre of mass is taken as the reference, the cubic to tetragonal phase transition is characterized by an opposite move of cations and oxygen anions, causing a spontaneous polarization. Furthermore, these polar distortions are associated with a small change of the cell size and shape.

In contrast, STO shows only one phase transition from a high temperature paraelectric cubic phase to a non-polar antiferrodistortive (AFD) tetragonal phase (I4/mcm, SG: 140) at a temperature $T_C \sim 105$°C. This AFD phase transition arises from rotations of TiO_6 octahedra around the tetragonal axis, such that the whole set of ionic movements keep the crystal non-polar. Nevertheless, STO is regarded as

almost ferroelectric in the sense that a ferroelectric phase transition is expected at very low temperatures, but has not been found experimentally. The absence of the ferroelectric phase transition is due to quantum fluctuations. Materials displaying such behaviour ($SrTiO_3$[67], $CaTiO_3$[68, 69], $KTaO_3$[70, 71], ...) are known as incipient-ferroelectrics (or quantum paraelectrics).

The AFD phase transition is mediated by the condensation of a phonon mode[72]. Both first- and second-order phase transitions can be caused by a soft mode, i.e. a mode whose frequency decreases with the lowering of the temperature and vanishes (or nearly so) as the temperature reaches T_C. Near the critical temperature, ionic displacements connected with the soft mode begin freezing, forcing a structural distortion that characterizes the phase transition[73, 74]. The AFD phase transition in STO arises due to the condensation of a soft mode at the R-point of the first Brillouin zone causing the rotation of the TiO_6 octahedra and lowering of the crystal symmetry to tetragonal[72, 75]. Lattice dynamical calculations for the cubic structure often display unphysical imaginary phonon frequencies, which indicate that the ground state structure of that specific material is actually not cubic at 0 K. This kind of behaviour has been shown using the first-principles calculations in STO by various groups[76–78].

As is apparent from the above paragraphs, the true driving part from the cubic to tetragonal structure is the rotation of octahedra, and this is impossible with the unit cell shown in Fig. 1.6 as oxygen ions either side of a titanium ions are mirror images of one another and can only translate in the same direction. A larger unit cell is needed to mark the rotation and generally two different kinds of unit cell are used. The first kind of tetragonal structure is a supercell built using two of the cubic cell face diagonals as cell vectors. The third cell vector is just one of the cubic cell vectors times two (the vector that is orthogonal to the two face diagonals). Consequently, the tetragonal cell lengths are $a = b = a_0\sqrt{2}, c = 2a_0$, where a_0 is the lattice constant of the cubic phase. As it is evident, the c vector has been chosen to denote the long side of the cell. This first type of tetragonal structure has 20 atoms. The primitive unit cell of the body-centred tetragonal lattice contains only 10 atoms (two formula units of STO)[76]. The second type of tetragonal structure is obtained from the cubic unit cell by building a $2 \times 2 \times 2$ supercell. The second type of structure contains 40 atoms; it is easier to construct, but consists of twice as many atoms as the first cell, which in turn makes it computationally very costly. Both these types of structures are shown in Fig. 1.7.

The I4/mcm space group has three degrees of freedom, one of which is the rotation of the oxygen octahedra, the other two are the two distinct lattice parameters. The Wyckoff positions for the tetragonal STO phase are shown in Table. 1.3.

1.2.3 Vibrational properties

The primitive unit cell of the tetragonal STO phase (space group (SG) I4/mcm–D_{4h}^{18}) has two formula units (ABO_3), which implies that the system has total 30 vibrational modes. The factor group analysis

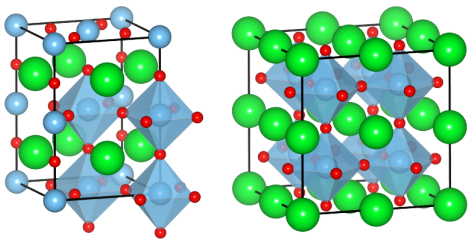

Figure 1.7: Representation of I4/mcm perovskite with two different types of cell: B centred with a $\sqrt{2} \times \sqrt{2} \times 2$ unit cell and selected octahedra drawn (left) and an A centred $2 \times 2 \times 2$ cell, with all octahedra drawn (right). Polyhedra show the coordination of each cation, the colours of which relate to the cation inside. To represent STO, green, blue and red represent Sr, Ti and O atoms, respectively. Adapted from Ref.[66]

Table 1.3: Wyckoff positions for strontium titanate in the low temperature tetragonal phase (space group I4/mcm D_{4h}^{18} (SG 140)).

Atom	Position	Coordinates
A (Sr)	4b	$(0, \frac{1}{2}, \frac{1}{4})$ $(\frac{1}{2}, 0, \frac{1}{4})$
B (Ti)	4c	$(0,0,0)$ $(0,0,\frac{1}{2})$
O	4a	$(0,0,\frac{1}{4})(0,0,\frac{3}{4})$
O	8h	$(u, u+\frac{1}{2}, 0)$ $(-u, -u+\frac{1}{2}, 0)$ $(-u+\frac{1}{2}, u, 0)$ $(u+\frac{1}{2}, -u, 0)$

shows that this space group contains 10 infrared active modes ($4A_{2u}$ and $6E_u$) and 7 Raman active modes (A_{1g}, B_{1g}, $2B_{2g}$, and $3E_g$). The cubic phase of STO has no Raman or IR active modes[76].

The vibrational properties in the cubic STO phase have been studied extensively by several groups. The self-consistent phonon calculations in the cubic STO by Terumasa et al.[79] show strong structural instabilities via the large magnitude of the imaginary frequencies (see Fig. 1.8).

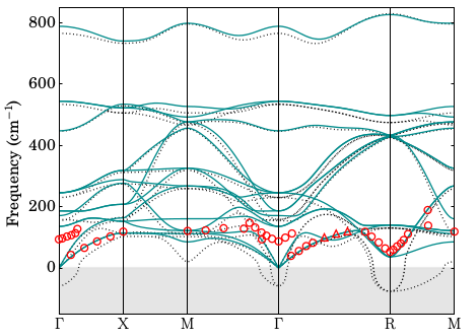

Figure 1.8: Anharmonic phonon dispersion of cubic STO at 300 K. The dotted lines show the harmonic phonon dispersion and the open symbols are experimental values at room temperature. Figure adapted from Ref.[79] (for more details, see this reference and references therein)

1.2.4 Temperature dependent phonon properties

Temperature dependent properties of perovskites are also quite fascinating. Using the self-consistent phonon calculations (SCPH), Terumasa et al. [79] showed that a few optical modes in cubic STO display anomalous behaviour with temperature (see Fig. 1.9).

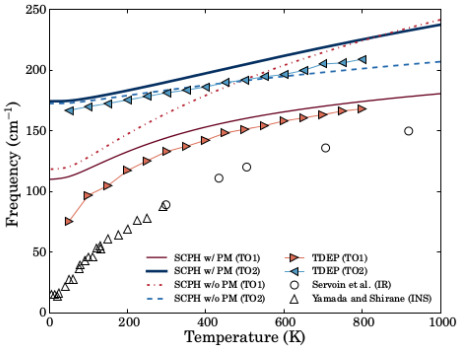

Figure 1.9: Temperature dependence of the anharmonic phonon frequencies of two optical modes in cubic STO. Figure adapted from Ref.[79] (for more details, visit this reference and references therein)

1.2.5 Our interest

Our interest is to study the phonon anharmonic effects in the tetragonal STO perovskite compound using the DFT and Green's function formalism. We present these results in chapter 10. We present the temperature dependence of the phonon linewidths, lineshifts, and the phonon frequency for several phonon modes. We are also interested in exploring the mode Grüneisen parameter, temperature variation of the linear thermal expansion coefficient, and frequency shift within the quasiharmonic approximation. To the best of our knowledge, no such calculations have been carried out in the low-temperature tetragonal phase of STO. We have also studied the vibrational properties in the high-temperature cubic phase of STO. Our calculations for the cubic structure show strong structural instabilities through large imaginary frequencies for some of the optical phonon modes. Our calculated values of the structural parameters and the vibrational frequencies for both the cubic and the tetragonal structures are in quite good agreement with the available experimental and theoretical results.

Chapter 2

Theoretical background

2.1 The Many body picture

The starting many body Hamiltonian for the system of electrons and nuclei is,

$$\hat{H} = -\frac{\hbar^2}{2m_e}\sum_i \boldsymbol{\nabla}_i^2 + \sum_{i,I}\frac{Z_I e^2}{|\boldsymbol{r}_i - \boldsymbol{R}_I|} + \frac{1}{2}\sum_{i\neq j}\frac{e^2}{|\boldsymbol{r}_i - \boldsymbol{r}_j|} - \sum_I \frac{\hbar^2}{2M_I}\boldsymbol{\nabla}_I^2 + \frac{1}{2}\sum_{I\neq J}\frac{Z_I Z_J e^2}{|\boldsymbol{R}_I - \boldsymbol{R}_J|} \tag{2.1}$$

where the lower case variables and subscripts correspond to the electrons and upper case variables and subscripts for the nuclei with mass M_I and charge Z_I. The electron-electron interaction makes the system complicated to solve, and needs to be handled appropriately to predict the diverse phenomena that such systems exhibit.

Since the masses of the nuclei, M_I are much larger than the electronic mass m_e ($M_I/m_e \approx 10^3 - 10^4$), the nuclear kinetic energy is small compared to electronic energies. As a first approximation, if we set the mass of the nuclei to infinity, then the kinetic energy of the nuclei can be ignored. This approximation, known as Born-Oppenheimer or adiabatic approximation, is an excellent approximation for many purposes, e.g., the calculation of nuclear vibrational modes in most solids[80, 81]. This simplification provides the foundation for the perturbation theory in electron-phonon interaction which is the basis for understanding the electrical transport in metals, polaron formation in insulators, certain metal-insulator transitions, and the BCS theory of the superconductivity.

Thus, ignoring the nuclear kinetic energy, the Hamiltonian for the theory of electronic structure is written as

$$\hat{H} = \hat{T} + \hat{V}_{ext} + \hat{V}_{ee} + E_{II} \tag{2.2}$$

where the kinetic energy term for the electrons is

$$\hat{T} = -\frac{\hbar^2}{2m_e}\sum_i \boldsymbol{\nabla}_i^2 \tag{2.3}$$

$\hat{V}_{ext}$ is the external potential acting on the electrons due to the nuclei,

$$\hat{V}_{ext} = \sum_{i,I}\frac{Z_I e^2}{|\boldsymbol{r}_i - \boldsymbol{R}_I|} \tag{2.4}$$

$\hat{V}_{ee}$ is the electron-electron Coulomb repulsion

$$\hat{V}_{ee} = \frac{1}{2}\sum_{i\neq j}\frac{e^2}{|\boldsymbol{r}_i - \boldsymbol{r}_j|} \tag{2.5}$$

and the final term E_{II} is the nuclear-nuclear classical interaction term and any other terms that contribute to the total energy of the system.

The time independent Schrödinger equation is written as

$$\hat{H}\Psi = E\Psi \tag{2.6}$$

where the many body wavefunction for the electrons is $\Psi = \Psi(\boldsymbol{r}_1, \boldsymbol{r}_2, ..., \boldsymbol{r}_N)$. (For simplicity, for the initial part of our discussion we ignore electron spin, but bring it in later) The fundamental requirement for the electronic wavefunction is the antisymmetry in the coordinates $\boldsymbol{r}_1, \boldsymbol{r}_2, ...\boldsymbol{r}_N$.

The particle density $n(\boldsymbol{r})$, a fundamental quantity in electronic structure theory, is obtained by the expectation value of the density operator $\hat{n}(\boldsymbol{r}) = \sum_{i=1}^{N}\delta(\boldsymbol{r} - \boldsymbol{r}_i)$,

$$n(\boldsymbol{r}) = \frac{\langle\Psi|\hat{n}(\boldsymbol{r})|\Psi\rangle}{\langle\Psi|\Psi\rangle} \tag{2.7}$$

The total energy is the expectation value of the Hamiltonian,

$$E = \frac{\langle\Psi|\hat{H}(\boldsymbol{r})|\Psi\rangle}{\langle\Psi|\Psi\rangle} = \langle\hat{H}\rangle = \langle\hat{T}\rangle + \langle\hat{V}_{ee}\rangle + \int d^3r V_{ext}(\boldsymbol{r})n(\boldsymbol{r}) + E_{II} \tag{2.8}$$

where the expectation value of the external potential has been explicitly written as a simple integral over the density function. The last term, E_{II}, is the electrostatic ion-ion interaction, which is important in the total energy calculation, but is only a classical additive term in the theory of electronic structure.

The eigenstates of the many-body Hamiltonian are stationary points (saddle points or minima) of Eq. (2.8). Since the eigenstates of the Hamiltonian form a complete orthogonal set and are normalized, i.e. $\langle\Psi|\Psi\rangle = 1$, the stationary states are obtained by extremizing the total energy using the variational

principle,

$$\delta \left[\langle \Psi | \hat{H} | \Psi \rangle - E(\langle \Psi | \Psi \rangle - 1) \right] = 0 \tag{2.9}$$

where E is the Lagrange multiplier. The ground state of the Hamiltonian corresponds to the state with the lowest energy, and the excited states are the saddle points of the energy with respect to the variations in Ψ.

2.2 Independent-electron approximation

Within the independent-electron approximation, individual particles move in the effective potential produced by the other electrons. Both Hartree and Hartree-Fock methods are based on this approximation.

2.2.1 Hartree approximation

Within the Hartree approximation, the many-body wavefunction is written as the product of single-particle wavefunctions $\phi_i(\boldsymbol{r})$,

$$\Psi(\boldsymbol{r}) = \phi_1(\boldsymbol{r}_1)\phi_2(\boldsymbol{r}_2)...\phi_N(\boldsymbol{r}_N) \tag{2.10}$$

The one-particle Schrödinger equation is written as

$$\hat{H}_{eff}\phi_i(\boldsymbol{r}) = \left[-\frac{\hbar^2}{2m_e} + V_{eff}(\boldsymbol{r}) \right] \phi_i(\boldsymbol{r}) = \epsilon_i \phi_i(\boldsymbol{r}) \tag{2.11}$$

where $V_{eff}(\boldsymbol{r})$ is an effective potential that acts on each electron at point $\boldsymbol{r}$.

$$V_{eff}(\boldsymbol{r}) = e^2 \int d^3r d^3r' \frac{n(\boldsymbol{r})n(\boldsymbol{r'})}{|\boldsymbol{r} - \boldsymbol{r'}|} \tag{2.12}$$

The single particle density is obtained as $n_i(\boldsymbol{r}) = |\phi_i(\boldsymbol{r})|^2$. The total energy and particle number are obtained as $E = \sum_i \epsilon_i$, and $N = \sum_i n_i$.

The Hartree approximation ignores the exchange and correlation terms of the electron-electron interaction, and hence can not capture the correct picture of the electronic properties of the systems. Fock extended the Hartree method by including the exchange interaction of the electrons.

2.2.2 Hartree-Fock Approximation

The many-body wavefunction within the Hartree-Fock method is written in the form of the Slater determinant,

$$\Psi = \frac{1}{\sqrt{N!}} \begin{vmatrix} \phi_1(\boldsymbol{r}_1)\chi_1(\sigma_1) & \phi_1(\boldsymbol{r}_2)\chi_1(\sigma_2) & \dots \phi_1(\boldsymbol{r}_N)\chi_1(\sigma_N) \\ \phi_2(\boldsymbol{r}_1)\chi_2(\sigma_1) & \phi_2(\boldsymbol{r}_2)\chi_2(\sigma_2) & \dots \phi_2(\boldsymbol{r}_N)\chi_2(\sigma_N) \\ \vdots & \vdots & \vdots \\ \phi_N(\boldsymbol{r}_1)\chi_N(\sigma_1) & \phi_N(\boldsymbol{r}_2)\chi_N(\sigma_2) & \dots \phi_N(\boldsymbol{r}_N)\chi_N(\sigma_N) \end{vmatrix} \tag{2.13}$$

where, $\chi_i(\sigma_i)$ correspond to the spin part of the wave function, and σ_i are the spin coordinates of the electrons. The expectation value of the many-body Hamiltonian is obtained as [82]

$$\begin{aligned} \langle\Psi|\hat{H}|\Psi\rangle &= \sum_i \int d\boldsymbol{r}\phi_i^*(\boldsymbol{r})[-\frac{1}{2}\boldsymbol{\nabla}^2 + V_{ext}(\boldsymbol{r})]\phi_i(\boldsymbol{r}) + \frac{1}{2}\sum_{i,j}\int d\boldsymbol{r}d\boldsymbol{r'}\phi_i^*(\boldsymbol{r})\phi_j^*(\boldsymbol{r'})\frac{1}{|\boldsymbol{r}-\boldsymbol{r'}|}\phi_i(\boldsymbol{r})\phi_j(\boldsymbol{r'}) \\ &- \frac{1}{2}\sum_{i,j}\int d\boldsymbol{r}d\boldsymbol{r'}\phi_i^*(\boldsymbol{r})\phi_j^*(\boldsymbol{r'})\frac{1}{|\boldsymbol{r}-\boldsymbol{r'}|}\phi_j(\boldsymbol{r})\phi_i(\boldsymbol{r'})\delta_{\chi_i,\chi_j} \end{aligned} \tag{2.14}$$

The first and second terms involve all the single-body terms, whereas the third and fourth terms are the direct and exchange terms, involving the two-body interactions. The terms for $i = j$ correspond to the "self-interaction" and get cancelled in the sum of the direct and exchange terms. The Hartree term is non zero for any two electrons, whereas the exchange term is non-zero only for two electrons of parallel spins. The exchange term is a consequence of form of the many body wave function in Eq. 2.13, which in turn is required by its antisymmetry. This can be seen easily by letting $\mathbf{r_i} = \mathbf{r_j}$ when $\sigma_i = \sigma_j$, in Eq. 2.13 such that the determinant contains two identical columns. In this case, the many-body wavefunction vanishes, i.e. $\Psi_{HF} = 0$, implying that the electrons of parallel spins can not approach close to each other, in contrast to those of opposite spin electrons - the vicinity of each electrons is surrounded by an "exchange hole".

The Hartree-Fock equations are obtained by minimizing the total energy with respect to the wave-function for the i^{th} orbital, leading to

$$\left[-\frac{1}{2}\boldsymbol{\nabla}^2 + V_{ext}(\boldsymbol{r}) + \sum_j \int d\boldsymbol{r'}\phi_j^*(\boldsymbol{r'})\phi_j(\boldsymbol{r'})\frac{1}{|\boldsymbol{r}-\boldsymbol{r'}|}\right]\phi_i(\boldsymbol{r}) - \sum_j \int d\boldsymbol{r'}\phi_j^*(\boldsymbol{r'})\phi_i(\boldsymbol{r'})\frac{1}{|\boldsymbol{r}-\boldsymbol{r'}|}\phi_j(\boldsymbol{r}) = \epsilon_i\phi_i(\boldsymbol{r}) \tag{2.15}$$

The Hartree-Fock method takes into account the exchange interaction of electrons but ignores the correlation effects (i.e., all interaction effects beyond the HF), which could be significant in materials.

Hohenberg and Kohn achieved a breakthrough in the field of many-body physics by suggesting that the total energy can be written as a functional of the density $n(\boldsymbol{r})$. In the next section, we provide a brief introduction to the theory of electronic structure based on this, namely density functional theory.

2.3 Density Functional theory

Density functional theory includes the effects of the exchange as well as correlations among the electrons despite being based on an independent particle approach and has been a great tool for the electronic structure calculations in condensed matter systems. Its formalism is based upon the remarkable paper by P. Hohenberg and W. Kohn in 1964[83]. These authors assigned special importance to the ground state density of particles of a many-body quantum system: all the properties of the system can be considered as unique functionals of the ground state density $n_0(\boldsymbol{r})$.

2.3.1 The Hohenberg-Kohn Theorems

The Hohenberg and Kohn approach applies to any interacting system in an external potential $V_{ext}(\boldsymbol{r})$. The density functional theory is based upon two theorems first proved by Hohenberg and Kohn.

According to the first theorem of Hohenberg and Kohn, the external potential (and hence the total energy) is a unique functional of the ground state electron density.

The second theorem of Hohenberg and Kohn says that the ground state energy of the system is the minimum of total energy functional, and the density which minimizes this energy functional, is the ground state density.

The Hohenberg-Kohn energy functional is given as,

$$E[n] = F[n] + \int V_{ext}(\boldsymbol{r})n(\boldsymbol{r})d\boldsymbol{r} \tag{2.16}$$

Where the universal functional $F[n]$ includes all internal energies, kinetic and potential, of the interacting electron system.

Though the Hohenberg-Kohn theorem provides a remarkable simplification in the field of many-body condensed matter theory by reducing the many-body wavefunction approach to the density functional approach, the problem remains complicated to solve due to the most difficult component of the exchange-correlation energy functional. Kohn and Sham came up with an excellent approximation where the many-body problem is reduced to the single body, where an electron moves in the effective field produced by other electrons and nuclei.

2.3.2 The Kohn-Sham Formalism

The Kohn-Sham approach is based upon replacing a difficult many-body interacting problem by a different auxiliary system that can be solved readily. As such there is no unique way to choose the simpler auxiliary systems, this is an ansatz that rephrases the problem. The ansatz of Kohn and Sham assumes that the ground state density can be obtained as the density of a non-interacting system.

This leads to equations for the single particle wave-functions of the non-interacting system that can be solved exactly, with all the difficult many-particle terms included in the exchange-correlation energy functional of the density[84]. The solutions of these equations give the ground state density and the energy of the original interacting systems with the accuracy limited by the approximations used in the exchange-correlation energy functional.

The Kohn-Sham total energy functional for a set of occupied one electron states ϕ_i can be written as

$$E[n] = \sum_i \int \phi_i[-\hbar^2/2m]\boldsymbol{\nabla}^2\phi_i d^3r + \int V_{ion}(\boldsymbol{r})n(\boldsymbol{r})d^3r + \frac{e^2}{2}\int \frac{n(\boldsymbol{r})n(\boldsymbol{r'})}{|\boldsymbol{r}-\boldsymbol{r'}|}d^3r d^3r' + E_{xc}[n(\boldsymbol{r})] + E_{ion}(\{\boldsymbol{R}_I\}) \tag{2.17}$$

Where V_{ion} is the static total electron-ion potential, E_{ion} is the ionic Coulomb interaction energy, the first term corresponds to the kinetic energy of the electrons, the third is the Hartree term, and E_{xc} is the exchange-correlation functional.

At the minimum energy, the Kohn-Sham energy functional is the ground state energy of the system of electrons with the ions in their equilibrium positions $\{\boldsymbol{R}_I\}$. Henceforth, the problem reduces to finding the set of wave functions ϕ_i that minimizes the Kohn-sham energy functional, and are obtained by the self-consistent solutions of the Kohn-sham equations:

$$\left[-\frac{\hbar^2}{2m}\boldsymbol{\nabla}^2 + V_{ion}(\boldsymbol{r}) + V_H(\boldsymbol{r}) + V_{xc}(\boldsymbol{r})\right]\phi_i(\boldsymbol{r}) = \epsilon_i\phi_i(\boldsymbol{r}) \tag{2.18}$$

where ϕ_i corresponds to the wave function of electronic state i with energy ϵ_i. V_H is the Hartree potential of the electrons,

$$V_H(\boldsymbol{r}) = e^2\int \frac{n(\boldsymbol{r'})}{|\boldsymbol{r}-\boldsymbol{r'}|}d^3r' \tag{2.19}$$

V_{xc} is the exchange-correlation potential, and is obtained as the functional derivative of the exchange-correlation energy functional E_{xc},

$$V_{xc}(\boldsymbol{r}) = \frac{\partial E_{xc}[n(\boldsymbol{r})]}{\partial n(\boldsymbol{r})} \tag{2.20}$$

The electronic charge density is obtained as,

$$n(\boldsymbol{r}) = \sum_i |\phi_i(\boldsymbol{r})|^2 \tag{2.21}$$

If one knows the exchange-correlation energy functional exactly, then the problem is easily solvable, by the self-consistent method.

The sum of single-particle Kohn-sham energies does not give the total energy of the electrons because this overcounts the effects of electron-electron interaction in the Hartree energy and the exchange-correlation energy. Kohn-sham eigenvalues are not exactly the energies of single-particle electron states,

but rather the derivatives of total energy to the occupation numbers of these states[85]. The actual total energy within the Kohn-Sham formalism is obtained as,

$$E = \sum_i \epsilon_i - \frac{e^2}{2} \int \frac{n(\boldsymbol{r})n(\boldsymbol{r'})}{|\boldsymbol{r} - \boldsymbol{r'}|} d\boldsymbol{r} d\boldsymbol{r'} - \int n(\boldsymbol{r}) V_{xc}(\boldsymbol{r}) d\boldsymbol{r} + E_{xc}[n] \tag{2.22}$$

2.3.3 Approximations for the exchange-correlation functional

The most difficult part in the density functional theory is the exchange-correlation energy, for which no known form exists, except for the free electron gas. However, there are some approximations, that allow us to calculate certain physical quantities reasonably well. Among them, the well known and widely used is the local density approximation(LDA;[84]). In LDA, the E_{xc} of an electronic system is evaluated by assuming that the exchange-correlation energy per particle at a point $\boldsymbol{r}$ in the electron gas, $\epsilon_{xc}(\boldsymbol{r})$ is equal to the exchange-correlation energy per electron in a homogeneous gas that has the same density as the electron gas at point $\boldsymbol{r}$. Thus, the total exchange-correlation energy functional is written as,

$$E_{xc}^{LDA}[n(\boldsymbol{r})] = \int \epsilon_{xc}^{hom}(n(\boldsymbol{r}))n(\boldsymbol{r}) d^3r \tag{2.23}$$

and the exchange-correlation potential is obtained as,

$$V_{xc}[n(\boldsymbol{r})] = \frac{\partial E_{xc}[n(\boldsymbol{r})]}{\partial n(\boldsymbol{r})} = \frac{\partial [n(\boldsymbol{r})\epsilon_{xc}^{hom}(n(\boldsymbol{r}))]}{\partial n(\boldsymbol{r})} \tag{2.24}$$

where $\epsilon_{xc}^{hom}(n(\boldsymbol{r}))$ is the exchange-correlation energy per particle for the homogeneous electron gas that can be computed by Quantum Monte Carlo[86] .

The LDA assumes that the exchange-correlation energy functional is purely local. There exist many parametrizations for the exchange-correlation energy of a homogeneous electron gas[87–90], all of them lead to similar results for the total energy. These parametrizations utilize interpolation methods to connect exact results for the exchange-correlation energy of high-density electron gases to the intermediate and low-density electron gases. The LDA, in principle, ignores corrections to the exchange-correlation energy at a point $\boldsymbol{r}$ due to nearby inhomogeneities in the electron density. A very popular method to account for the inhomogeneity in the electronic density is the generalized gradient approximation (GGA), where the gradient in the density is also included in the exchange-correlation energy functional. The GGA allows for corrections based on the changes in density away from the point $\boldsymbol{r}$.

$$E_{xc}^{GGA}[n] = \int \epsilon_{xc}(n(\boldsymbol{r}), \boldsymbol{\nabla} n(\boldsymbol{r}))n(\boldsymbol{r}) d^3r \tag{2.25}$$

Though both the LDA and GGA methods underestimate the cohesive energy of the system, they work very well for most of the ground state physical quantities. It is a well-known feature of the density

functional theory that the LDA underestimates the lattice constant, whereas the GGA overestimates it.

2.3.4 Lattice periodicity

As described in the previous section, the Kohn-Sham formalism maps a many-body interacting problem to a single-body non-interacting one. However, it remains a formidable task to handle a macroscopically large number of electrons moving in the static potential of a macroscopically large number of ions. There is also the additional difficulty that each wavefunction requires, for its description, an infinite basis set, though in practice it has to be truncated. For electrons in a crystal, the severity of these problems can be reduced by exploiting the periodicity of the crystal lattice and applying the Bloch's theorem to the electronic wavefunctions.

Bloch's theorem

Bloch's theorem states that in a periodic system each electronic wavefunction can be written as the product of a wave-like part and the cell-periodic part[91],

$$\phi_{n\boldsymbol{k}}(\boldsymbol{r}) = e^{i\boldsymbol{k}.\boldsymbol{r}} u_{n\boldsymbol{k}}(\boldsymbol{r}) \tag{2.26}$$

where n is the band index and $\boldsymbol{k}$ is the wave-vector of electrons in the reciprocal lattice, and u is the cell-periodic part. The cell periodic part can be expanded using a basis set consisting of a discrete set of plane waves whose wave vectors are reciprocal lattice vectors of the crystal,

$$u_{n\boldsymbol{k}}(\boldsymbol{r}) = \sum_{\boldsymbol{G}} C_{n\boldsymbol{k},\boldsymbol{G}} e^{i\boldsymbol{G}.\boldsymbol{r}} \tag{2.27}$$

where the reciprocal lattice vectors $\boldsymbol{G}$ are defined by $\boldsymbol{G}.\boldsymbol{T} = 2\pi m$ for all $\boldsymbol{T}$ where $\boldsymbol{T}$ is a lattice translation vector and m is an integer.

Therefore, each electronic wave function can be written as a sum of plane waves,

$$\phi_{n\boldsymbol{k}}(\boldsymbol{r}) = \sum_{\boldsymbol{G}} C_{n\boldsymbol{k},\boldsymbol{G}} e^{i(\boldsymbol{k}+\boldsymbol{G}).\boldsymbol{r}} \tag{2.28}$$

k-point sampling

Thus, crystal-periodicity allows us to work only within the Brillouin zone of the crystal, but the difficulty remains with how to handle a macroscopic number of k-points (equal to the number of unit cells in the crystal, as is easy to see using periodic boundary conditions) within the Brillouin zone. Since the electronic states at $\boldsymbol{k}$ points that are very close together will be nearly identical, it is sufficient to compute the Bloch states only over a thoughtfully chosen grid of $\boldsymbol{k}$ points, much less in number than

the number of unit cells in the whole lattice. This approach simplifies the problem considerably. Many special methods are in use for obtaining very accurate approximations to the electronic potential and the total energy from filled electronic bands, as in semiconductors or insulators, by calculating the electronic states at special sets of $\boldsymbol{k}$ points, fairly small in number, in the Brillouin zone[92–95]. However, for a metallic system, a denser $\boldsymbol{k}$ grid is required to define the Fermi surface precisely. The denser grid additionally helps to reduce the magnitude of error in the total energy of the system. In general, one has to converge the total energy with increasing k-point grid sizes to get the correct physical quantities.

Plane-wave basis sets

Bloch's theorem states that the electronic wave functions at each $\boldsymbol{k}$ point can be expanded in terms of a discrete plane-wave basis set. In principle, the expansion of the electronic wave functions will require an infinite number of plane wave basis states. However, the coefficients $C_{n\boldsymbol{k},\boldsymbol{G}}$ for the plane waves with the smaller values of the kinetic energy $(\hbar^2/2m)|\boldsymbol{k}+\boldsymbol{G}|^2$ are usually more important than those with large kinetic energy. Hence, in actual calculations, the plane-wave basis set is generally trimmed to include only plane waves that have kinetic energies smaller than some chosen energy cutoff. Additionally, one checks for convergence with increasing values for the energy cutoff.

2.3.5 Electron-ion interactions:Pseudopotential approximation

Although Bloch's theorem states that the electronic wave functions can be expanded using a discrete set of plane waves, due to the tightly bound core electrons and the rapid oscillations of the valence electrons in the core region, the plane wave basis is rather poorly suited. An extremely large plane-wave basis set would be required to calculate the electronic wave functions. The pseudopotential approximation[96, 97] leads to the construction of much smaller basis sets that are nevertheless adequate for generating the electronic wave functions. It is well-known that most (low energy) properties of a system are determined by the valence electrons rather than by the tightly bound core electrons. Due to this reason the pseudopotential approximations is introduced. This approximation exploits this fact to remove the core electrons and the strong nuclear potential and replace them with a weaker pseudopotential which acts on a set of pseudo wavefunctions rather than the actual valence wavefunctions. The valence wave functions oscillate rapidly in the region occupied by the core electrons due to the strong ionic potential in this region. The Pauli exclusion principle demands the orthogonality between the core and valence electron wave functions, and the rapid oscillations maintain this orthogonality.

2.3.6 Geometry optimization

The primary goal of any ab initio calculation is to determine the equilibrium structure of system such that forces and stresses on the atoms are essentially zero. Among the various geometry optimization

techniques, the gradient-based algorithms have been used extensively for most of the cases. The forces on atoms are obtained by exploiting the Hellmann-Feynman theorem[98],

$$\boldsymbol{F}_I = -\frac{\partial E}{\partial \boldsymbol{R}_I} = -\langle\Psi|\frac{\partial \hat{H}}{\partial \boldsymbol{R}_I}|\Psi\rangle \tag{2.29}$$

where $|\Psi\rangle$ are the electronic eigenstates of the Born Oppenheimer Hamiltonian $\hat{H}$ for a given nuclear configuration $\boldsymbol{R}$. $\boldsymbol{F}_I$ is the force on the I^{th} atom, and E is the Born Oppenheimer energy surface. The atoms within the unit cell or supercell are moved along the directions of the Hellmann-Feynman forces until the residual forces on all the atoms are smaller than a given tolerance value. The Broyden-Fletcher-Goldfarb-Shanno (BFGS) minimization method is widely used for atomic relaxation[99].

The stress tensor $\sigma_{\alpha\beta}$ is calculated using the formula by Nielsen and Martin[100].

2.4 Phonon calculations

Phonons are collective excitations of atoms or molecules in a solid, obtained by the quantization of the classical normal modes of vibrations of the interacting particles forming the solid about their equilibrium positions within a Harmonic approximation. At the harmonic level, the normal modes are decoupled from each other, which means that the excitation of one mode will never cause any motion of another mode, i.e. there is no transfer of energy between these harmonic normal modes. Solids with a monatomic basis in the unit cell have only one kind of phonons, i.e. the acoustic phonons; whereas solids with more than one atom in the unit-cell have two types of phonons: acoustic and optical phonons. Acoustic phonons are so named because in the limit of long-wavelength they exhibit a nearly in-phase movement of all the atoms in the crystal, leading to a linear dispersion (i.e., a linear relationship between their frequency and wave-vector), and correspondence with the (quantized versions of) sound waves in the crystal. They can be both longitudinal (LA, in the direction of propagation) or transverse (TA, perpendicular to the propagation direction). They mostly have a linear dispersion relationship between their frequency and phonon wavevector, wherein the frequency vanishes in the long-wavelength limit. On the other hand, optical phonons are short-wavelength, out-of-phase movements of the basis atoms in the unit cell of crystal, akin to molecular vibrations if one were to think of the basis atoms as constituting a molecule. They are called optical because, in some ionic crystals, they can be excited by electromagnetic radiation only through infrared absorption or Raman scattering.

Any crystal lattice is a repetition of the unit cell (building block), and a unit cell is described by the non-coplanar primitive lattice vectors, $\boldsymbol{a}_1, \boldsymbol{a}_2, \boldsymbol{a}_3$. The position of any lattice point can be described using $\boldsymbol{R}$, which is the linear combination of the basis vectors. The origin in any unit cell is defined as

$$\boldsymbol{R}^l = l_1\boldsymbol{a}_1 + l_2\boldsymbol{a}_2 + l_3\boldsymbol{a}_3 \tag{2.30}$$

where l_1, l_2, and l_3 are integers, and l is a cell index. The equilibrium positions of N atoms in the unit cell can be described by a set of vectors $\{\boldsymbol{\tau}_s\}$ for the sth atom in the unit cell. The position of an atom is written as

$$\boldsymbol{R}_s^l = \boldsymbol{R}^l + \boldsymbol{\tau}_s \tag{2.31}$$

In real systems, atoms are not stationary, they vibrate about their equilibrium positions. If we denote $\boldsymbol{u}_s^l$ as the displacement of an atom ls from its equilibrium position, then the actual position of an atom (Fig. 2.1) is written as

$$\boldsymbol{r}_s^l = \boldsymbol{R}_s^l + \boldsymbol{u}_s^l \tag{2.32}$$

Within the small displacement approximation, the total potential energy of the crystal can be written

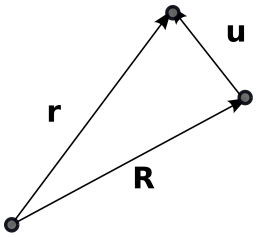

Figure 2.1: An instantaneous position of an atom

in terms of the atom displacements using the Taylor series expansion:

$$U = U_0 + \sum_{l,s,\alpha} \Phi_\alpha(ls) u_{s,\alpha}^l + \frac{1}{2} \sum_{ll',ss',\alpha\beta} \Phi_{\alpha\beta}(ls, l's') u_{s,\alpha}^l u_{s',\beta}^{l'} + \frac{1}{6} \sum_{ll'l'',ss's'',\alpha\beta\gamma} \Phi_{\alpha\beta\gamma}(ls, l's', l''s'') u_{s,\alpha}^l u_{s',\beta}^{l'} u_{s'',\gamma}^{l''} + ... \tag{2.33}$$

Here, the indices α, β, and γ represent the Cartesian coordinates. U_0 is the potential energy of the static lattice. The coefficient of the second term (Φ_α(ls)) corresponds to the force acting on an atom ls and vanishes at the equilibrium positions of the atoms. The second and third-order coefficients of the above expansion for the potential energy are called the Born-Von Karman force constants and are given by

$$\Phi_{\alpha\beta}(ls; l's') = \left. \frac{\partial^2 U}{\partial u_{s,\alpha}^l \partial u_{s',\beta}^{l'}} \right|_{\boldsymbol{u}=\boldsymbol{0}} \tag{2.34}$$

$$\Phi_{\alpha\beta\gamma}(ls; l's'; l''s'') = \left. \frac{\partial^3 U}{\partial u_{s,\alpha}^l \partial u_{s',\beta}^{l'} \partial u_{s'',\gamma}^{l''}} \right|_{\boldsymbol{u}=\boldsymbol{0}} \tag{2.35}$$

The physical meaning of the force constants can readily be understood as follows. The second-order force constant determines the force acting on the atom ls along the α direction when atom $l's'$ is displaced along the β direction as shown in Fig. 2.2 a). Similarly, the third-order force constant is linked with the force acting on atom ls along the α direction when atoms $l's'$ and $l''s''$ are displaced

along β and γ directions, respectively.

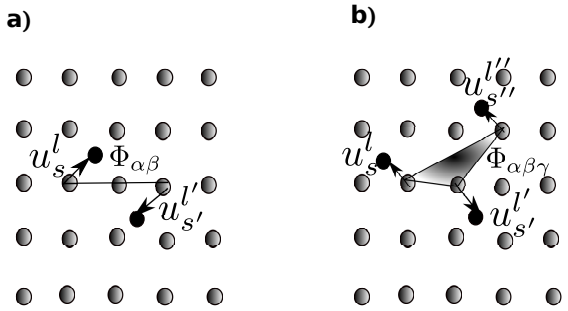

Figure 2.2: Illustration of a) second and b) third order force constants on a lattice. The second order force constant $\Phi_{\alpha\beta}$ determines the coupling between atoms ls and $l's'$, with the strength of interaction determined by the length of displacements $\boldsymbol{u}$. The third order force constant involves the coupling between three atoms.

In principle, there is an infinite number of force constants, which must be reduced to a manageable number for practical calculations. Crystal symmetry, and the fact that normally the Force constants have a short spatial range, play a vital role in reducing the number of essential force constants to be finite, making the calculations numerically viable.

2.4.1 Harmonic Approximation

In this section, we discuss one of the widely used approximations, known as the harmonic approximation. Within this approximation, the total lattice potential energy is expressed only up to the second-order in the atomic displacements, throwing away all the higher-order terms. If we ignore the static part of the potential energy, then the total Hamiltonian within the harmonic approximation is written as

$$H = \sum_{l,s,\alpha} \frac{(P^l_{s,\alpha})^2}{2M_s} + \frac{1}{2} \sum_{ll',ss',\alpha\beta} \Phi_{\alpha\beta}(ls, l's') u^l_{s,\alpha} u^{l''}_{s',\beta} \tag{2.36}$$

where $P^l_{s,\alpha}$ represents the α-th Cartesian component of the momentum of the s-th atom with mass M_s in the l-th unit cell. The classical equations of motion are obtained from Hamilton's equations:

$$\dot{u}^l_{s,\alpha} = \frac{\partial H}{\partial P^l_{s,\alpha}} = \frac{P^l_{s,\alpha}}{M_s} \tag{2.37}$$

$$\dot{P}^l_{s,\alpha} = -\frac{\partial H}{\partial u^l_{s,\alpha}} = -\sum_{l',s',\beta} \Phi_{\alpha\beta}(ls; l's') u^{l'}_{s',\beta} \tag{2.38}$$

The equation of motion for each atom is then obtained as,

$$M_s \ddot{u}^l_{s,\alpha} = -\sum_{l',s',\beta} \Phi_{\alpha\beta}(ls;l's')u^{l'}_{s',\beta} \tag{2.39}$$

For a system containing N atoms in the unit-cell, and $\mathcal{N}_u$ unitcells in the crystal, there are $3N \times \mathcal{N}_u$ equations of motion to solve. Because of the translational symmetry of the crystal, the force constants $\Phi_{\alpha\beta}(ls;l's')$ are only functions of $\boldsymbol{R}^l - \boldsymbol{R}^{l'}$. Hence the natural basis to solve these equations of motion is to use exponential plane waves, which are also compatible with periodic boundary conditions. The Cartesian component of the displacement of an atom is written as,

$$u^l_{s,\alpha} = \frac{1}{\sqrt{M_s}} \sum_{\boldsymbol{q},j} A(\boldsymbol{q}j)\epsilon_{s,\alpha}(\boldsymbol{q}j)e^{i[\boldsymbol{q}.\boldsymbol{R}^l_s - \omega_j(\boldsymbol{q})t]} \tag{2.40}$$

where $\boldsymbol{q}$ corresponds to the wave vector in the first Brillouin zone, j represents the normal mode branch index, $\omega_j(\boldsymbol{q})$ stands for the frequency of mode $\boldsymbol{q}j$. $\epsilon_{s,\alpha}(\boldsymbol{q}j)$ is a polarization vector of an atom s in α direction for a $\boldsymbol{q}j$ mode and $A(\boldsymbol{q}j)$ is the normal mode amplitude. Inserting Eq. 2.40 into Eq. 2.39 and exploiting the orthogonality of plane waves, we get,

$$\omega^2_j(\boldsymbol{q})\boldsymbol{\epsilon}_{s,\alpha}(\boldsymbol{q}j) = \sum_{s',\beta} D_{s,\alpha,s',\beta}(\boldsymbol{q})\boldsymbol{\epsilon}_{s',\beta}(\boldsymbol{q}j) \tag{2.41}$$

where $D_{s,\alpha,s',\beta}(\boldsymbol{q})$ is a $3N \times 3N$ matrix, called the dynamical matrix, essentially the lattice Fourier transform of a scaled force constant matrix given by,

$$D_{s,\alpha,s',\beta}(\boldsymbol{q}) = \frac{1}{\sqrt{M_s M_{s'}}} \sum_{l,l'} \Phi_{\alpha\beta}(ls;l's')e^{i\boldsymbol{q}.[\boldsymbol{R}^{l'}_{s'} - \boldsymbol{R}^l_s]} \tag{2.42}$$

The Eq. 2.41 gives $3N$ eigenvalues $\omega_j(\boldsymbol{q})$ for each $\boldsymbol{q}$ vector of the Brillouin zone. Three of the modes are described as acoustic, with $\omega(\boldsymbol{q}) \to 0$ as $\boldsymbol{q} \to 0$, and $3N-3$ are optical, with $\omega(\boldsymbol{q}) \to$ constant as $\boldsymbol{q} \to 0$. Since the dynamical matrix is Hermitian, the eigenvalues are guaranteed to be real; since they equal squares of vibrational frequencies, ω^2, for a stable crystal with normal modes that vibrate at real frequencies, they must also be positive. If not, the corresponding normal modes will have imaginary frequencies, leading to a dynamical instability of the crystal.

The Quantum mechanical picture

In the previous section, our approach was based on the classical framework, by solving Newton's equations of motion. Quantum-mechanically, each vibrational normal mode can be quantized straightforwardly as an independent harmonic oscillator. The corresponding quanta of excitations can be thought

of as quasi-particles called phonons, carrying quanta of energy equal to $\hbar\omega_j(\mathbf{q})$. Within this representation, the Helmholtz free energy, obtainable as the sum of harmonic oscillator free energies from each mode, can be reinterpreted in terms of phonons as (quasi)particles following Bose statistics. The position and momentum operators in terms of the phonon creation and annihilation operators are given by:

$$\hat{u}^l_{s,\alpha} = \sqrt{\frac{\hbar}{2NM_s}} \sum_{\boldsymbol{q},j} \frac{\epsilon_{s,\alpha}(\boldsymbol{q}j)}{\sqrt{\omega_j(\boldsymbol{q})}} e^{i\boldsymbol{q}.\boldsymbol{R}^l_s} (\hat{a}_{\boldsymbol{q}j} + \hat{a}^\dagger_{-\boldsymbol{q}j}) \tag{2.43}$$

$$\hat{P}^l_{s,\alpha} = -i\sqrt{\frac{\hbar M_s}{2N}} \sum_{\boldsymbol{q},j} \sqrt{\omega_j(\boldsymbol{q})} \epsilon_{s,\alpha}(\boldsymbol{q}j) e^{i\boldsymbol{q}.\boldsymbol{R}^l_s} (\hat{a}_{\boldsymbol{q}j} - \hat{a}^\dagger_{-\boldsymbol{q}j}) \tag{2.44}$$

In terms of the phonon creation and annihilation operators, the Hamiltonian within harmonic approximation is written as

$$H = \sum_{\boldsymbol{q},j} \hbar\omega_j(\boldsymbol{q}) (\hat{a}^\dagger_{\boldsymbol{q}j} \hat{a}_{\boldsymbol{q}j} + \frac{1}{2}) \tag{2.45}$$

The phonon density of states is the number of states with frequency ω,

$$g(\omega) = \frac{1}{(2\pi^3)} \sum_j \int_{BZ} \delta(\omega - \omega_j(\boldsymbol{q})) d\boldsymbol{q} \tag{2.46}$$

The density of states is a very important quantity which is used to determine the thermodynamic quantities like free energy.

2.4.2 Thermodynamic potentials

The free energy is expressed as,

$$F = -k_B T ln \mathcal{Z} \tag{2.47}$$

where the partition function is defined as

$$\mathcal{Z} = \mathrm{Tr}\, e^{-\beta H} \tag{2.48}$$

where β is the inverse temperature $1/k_B T$, and symbol Tr represents the sum over any complete set of quantum vibrational states of the system. It is convenient to choose them to be the eigenstates of the Harmonic Hamiltonian, which are also simultaneous eigenstates of all the the phonon number operators, $\{\hat{a}^\dagger_{\boldsymbol{q}j} \hat{a}_{\boldsymbol{q}j}\}$. Using the Hamiltonian from Eq. 2.45 within the harmonic approximation, the partition function is evaluated as,

$$\mathcal{Z} = \prod_{\boldsymbol{q}j} \frac{e^{-\beta\hbar\omega_j(\boldsymbol{q})/2}}{1 - e^{-\beta\hbar\omega_j(\boldsymbol{q})}} \tag{2.49}$$

The free energy is then obtained as,

$$\begin{aligned} F &= \sum_{\boldsymbol{q}j} \left[\frac{\hbar\omega_j(\boldsymbol{q})}{2} + k_B T ln[1 - e^{-\beta\hbar\omega_j(\boldsymbol{q})}] \right] \\ &= \int_0^\infty \left[g(\omega)\frac{\hbar\omega}{2} + g(\omega)k_B T ln[1 - e^{-\beta\hbar\omega}] \right] d\omega \end{aligned} \tag{2.50}$$

The free energy includes the zero-point energy as a result of the quantization the harmonic Hamiltonian.

2.4.3 Limitations of the harmonic approximation

The harmonic approximation is an excellent first approximation for various physical properties like the phonon dispersion relations, specific heat, and free energies, etc., but does not capture several other properties such as the heat transport, phonon lifetime and thermal expansion of the lattice. Furthermore, the properties such as the vibrational entropy and the phonon dispersion calculated within the harmonic approximation can be different from the measured one. To tackle these issues, it becomes important to include the phonon-phonon interactions, known as the anharmonic effects. In the next section, we describe these anharmonic effects.

2.5 Phonon dynamics in the presence of anharmonicity

To overcome the limitations of the harmonic approximation, it is imperative to include the anharmonic corrections to the total potential energy of the crystal. The first type of anharmonicity we consider is the thermal expansion of the lattice and is included in calculations via the quasiharmonic approximation. Furthermore, we discuss the higher-order anharmonic contributions, i.e. cubic and quartic anharmonic effects.

2.5.1 Quasiharmonic Approximation

In real crystals, the vibrational frequencies that show up in various phenomena such as Raman scattering, neutron inelastic scattering, etc., change with temperature, but this is not captured in the harmonic approximation. To incorporate the anharmonic effects, the higher-order terms in the expansion of the potential energy need to be taken into account. The first correction is due to the change in the harmonic potential energy as a result of lattice thermal expansion, which is the basis of quasi-harmonic approximation (QHA). This approach treats the potential still to be harmonic but takes into account the change in structure and potential energy due to changes in the cell volume as a function of temperature. This results in a shift in frequency. The temperature dependence of the phonon frequencies is described by their volume dependence, i.e. $\omega(V,T) \sim \omega(V(T))$.

The Helmholtz free energy as a function of volume and temperature is given by,

$$F = E_0(V) + \sum_{\boldsymbol{q}j} \frac{\hbar\omega_j(\boldsymbol{q})}{2} + k_B T \ln[1 - e^{-\beta\hbar\omega_j(\boldsymbol{q})}] \tag{2.51}$$

Where the static energy E_0 is the energy of the cell when all the atoms are at their equilibrium positions. For a given pressure P and temperature T, which correspond to the conditions under which experiments are usually done, i.e., in the Gibbs Ensemble, the Gibbs free energy $F + PV$ is optimized to obtain both ω_j and V at different temperatures.

The equation of state within the QHA is therefore given by,

$$P = -\frac{\partial F(V)}{\partial V}\bigg|_T \tag{2.52}$$

Carrying out the differentiation directly on the expression for F in Eq. 2.51, or a more elaborate argument starting from the expression for the energy (see Appendix A for details), we get

$$P = -\frac{\partial}{\partial V}\left[U^{(0)} + \sum_{\boldsymbol{q}j}\frac{1}{2}\hbar\omega_j(\boldsymbol{q})\right] + \sum_{\boldsymbol{q}j}\left(-\frac{\partial}{\partial V}(\hbar\omega_j(\boldsymbol{q}))\right) n_j(\boldsymbol{q}) \tag{2.53}$$

This equation can in principle be solved to obtain V as a function of P and T. The temperature (and pressure) dependence of the phonon frequencies is then obtained as $\omega_j(\boldsymbol{q}, V(P,T))$. Using thermodynamic relations, the linear thermal expansion coefficient is calculable as,

$$\alpha(T) = \frac{1}{3B}\left(\partial P/\partial T\right)_V \tag{2.54}$$

where B is the Bulk modulus defined as $B = -V(dP/dV)$. Within the QHA this leads to (see Appendix A for details),

$$\alpha = \frac{1}{3BV}\sum_{\boldsymbol{q}j}\left[\gamma_j(\boldsymbol{q})\frac{(\hbar\omega_j(\boldsymbol{q}))^2}{k_B T^2}\frac{e^{\hbar\omega_j(\boldsymbol{q})/k_B T}}{(e^{\hbar\omega_j(\boldsymbol{q})/k_B T}-1)^2}\right] \tag{2.55}$$

where $\gamma_j(\boldsymbol{q})$ is the mode Grüneisen parameter for a phonon mode j at the wavevector $\boldsymbol{q}$:

$$\gamma_j(\boldsymbol{q}) = -\frac{\partial \ln \omega_j(\boldsymbol{q})}{\partial \ln V} \tag{2.56}$$

Neglecting the temperature dependence of the Gruneisen parameter, and using Eq.s 2.55 and 2.56, the temperature dependent shift in the frequency of a phonon mode at the Γ point ($\mathbf{q} = \mathbf{0}$) within the

QHA is obtained as (see Appendix B for details),

$$\Delta_j^{(0)}(T) = \omega_j(0)\left[e^{-3\gamma_j \int_0^T \alpha(T')dT'} - 1\right] \tag{2.57}$$

where γ_j is the mode Grüneisen parameter at $\boldsymbol{q} = 0$.

2.5.2 Anharmonic Lattice Dynamics

As mentioned earlier, the harmonic approximation which treats the normal modes as independent describes most of the properties excellently but fails to describe the deviation of the specific heat from the Dulong and Petit law at high temperatures, and also the thermal expansion. These properties are well described within the anharmonic lattice treatment. The anharmonicity is treated as the perturbation to the harmonic approximation. It gives rise to (what can be loosely termed as) collisions between phonons, which change their lifetime and also their energy. Since the collision probability depends on the number of phonons, the lifetime and frequency will change with temperature. Many of the anharmonic aspects of phonons in crystals have been measured by the use of infrared absorption spectroscopy, but unfortunately, this technique is limited to long-wavelength optical modes. Raman spectroscopy (scattering technique) too captures these aspects but only for long-wavelength Raman active modes. In principle, Neutron scattering techniques provide the anharmonic aspects for all the vibrational modes, but in practice, they have a low resolution compared to the optical techniques. In this thesis, we study theoretically the anharmonic aspects of the *Gamma*-point phonons in the pyrochlores. For this purpose, we consider the anharmonic terms only up to the third order of phonon displacement. The Hamiltonian of the system within this approximation is written as,

$$H = H_0 + V_3 \tag{2.58}$$

Here, H_0 is the Hamiltonian within harmonic approximation, whose eigenvalues and eigenvectors are known and have been described earlier. The cubic part of the Hamiltonian can be written as,

$$V_3 = \sum_{\substack{\boldsymbol{q}_1,\boldsymbol{q}_2,\boldsymbol{q}_3 \\ j_1,j_2,j_3}} V^{(3)}(\boldsymbol{q}_1, j_1; \boldsymbol{q}_2, j_2; \boldsymbol{q}_3, j_3) A_{\boldsymbol{q}_1 j_1} A_{\boldsymbol{q}_2 j_2} A_{\boldsymbol{q}_3 j_3} \tag{2.59}$$

Here, $A_{\boldsymbol{q}j} = a^{\dagger}_{-\boldsymbol{q}j} + a_{\boldsymbol{q}j}$, and $V^{(3)}(\boldsymbol{q}_1, j_1; \boldsymbol{q}_2, j_2; \boldsymbol{q}_3, j_3)$ is the third order coupling constant between three phonon modes, given by

$$\begin{aligned} V^{(3)} &= \frac{1}{6}\left(\frac{\hbar^3}{8\omega_{j1}(\boldsymbol{q}_1)\omega_{j2}(\boldsymbol{q}_2)\omega_{j3}(\boldsymbol{q}_3)}\right)^{1/2} \sum_{ss's'',\alpha\beta\gamma}\left(\frac{1}{M_s M_{s'} M_{s''}}\right)^{1/2} e_{s,\alpha}(\boldsymbol{q}_1 j_1) e_{s',\beta}(\boldsymbol{q}_2 j_2) e_{s'',\gamma}(\boldsymbol{q}_3 j_3) \\ &\times \sum_{ll'} \frac{1}{N\sqrt{N}} \frac{\partial^3 E}{\partial u^0_{s,\alpha} \partial u^l_{s',\beta} \partial u^{l'}_{s'',\gamma}} e^{i\{\boldsymbol{q}_1 . \boldsymbol{R}^0_s + \boldsymbol{q}_2 . \boldsymbol{R}^l_{s'} + \boldsymbol{q}_3 . \boldsymbol{R}^{l'}_{s''}\}} \Delta(\boldsymbol{q}_1 + \boldsymbol{q}_2 + \boldsymbol{q}_3) \end{aligned} \tag{2.60}$$

where Δ ensures momentum conservation during the scattering process.

$$\Delta(\boldsymbol{q}_1 + \boldsymbol{q}_2 + \boldsymbol{q}_3) = \begin{cases} 1, & \text{if } \boldsymbol{q}_1 + \boldsymbol{q}_2 + \boldsymbol{q}_3 = \boldsymbol{0}, \boldsymbol{G} \\ 0, & \text{otherwise} \end{cases} \tag{2.61}$$

clearly, if the first two displacements have wavevectors $\boldsymbol{q}_1$ and $\boldsymbol{q}_2$, the third has the wavevector $-\boldsymbol{q}_1 - \boldsymbol{q}_2$. So we can write anharmonic term as

$$V_3 = \sum_{\boldsymbol{q}_1 \boldsymbol{q}_2, j_1 j_2 j_3} V^{(3)}(\boldsymbol{q}_1, j_1; \boldsymbol{q}_2, j_2; -\boldsymbol{q}_1 - \boldsymbol{q}_2, j_3) A_{\boldsymbol{q}_1 j_1} A_{\boldsymbol{q}_2 j_2} A_{-\boldsymbol{q}_1 - \boldsymbol{q}_2, j_3} \tag{2.62}$$

2.5.3 Green's function method

The calculation of the anharmonic phonon lifetime and frequency shift starting from anharmonic Hamiltonians such as in Eq. 2.58 are carried out most easily and systematically using the Green's function method.

We define the temperature-dependent phonon Green's function as,

$$G_{\boldsymbol{q}jj'} = -\langle T_\tau A_{\boldsymbol{q}j}(\tau) A^{\dagger}_{\boldsymbol{q}j'}(\tau') \rangle \tag{2.63}$$

where τ corresponds to the imaginary time, restricted between 0 and β, in the Matsubara formalism (see Appendix C for more details), T_τ is the time ordering operator which orders operators in a string according to their imaginary time arguments from right to left.

The free phonon propagator is diagonal in the index j, and is given by,

$$G^0(\boldsymbol{q}j, \omega_n) = \frac{2\omega_j(\boldsymbol{q})}{\omega_n^2 + \omega_j^2(\boldsymbol{q})} \tag{2.64}$$

where ω_n corresponds to the even Matsubara frequency, given by $2n\pi k_B T$. The interacting Green's function, in the simplest approximation where its off diagonal components are neglected can be written as,

$$G(\boldsymbol{q}j, \omega_n) = \frac{2\omega_j(\boldsymbol{q})}{\omega_j^2(\boldsymbol{q}) + \omega_n^2 - 2\omega_j(\boldsymbol{q})\Sigma_{\boldsymbol{q}j}(\omega_n)} \tag{2.65}$$

All the effects of the anharmonic interactions are included in the phonon self-energy Σ.

The self-energy of phonons within the cubic anharmonic approximation has been derived in the Appendix C using the Green's function approach. The other low order cubic and quartic phonon self-energy corrections are derived in Ref.[101]. The diagrams of the lowest order terms of the phonon self-energy are shown in Fig. 2.3.

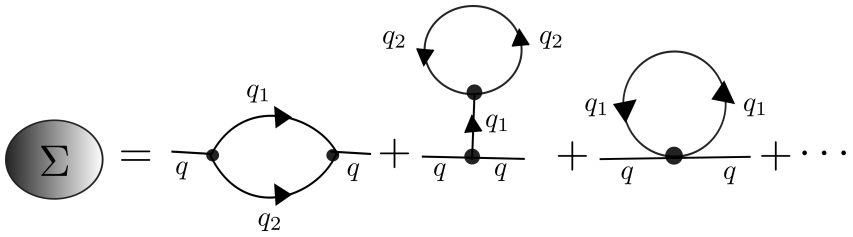

Figure 2.3: The lowest order terms of the phonon self energy

The diagrams with loops at the four phonon vertex as shown in Fig. 2.3 describe situations in which a phonon is created and destroyed at the same vertex. Such phonons are called instantaneous phonons. It should be noted that in a crystal instantaneous phonons can occur only at four phonon vertices as long as we retain only cubic and quartic anharmonic terms in the crystal Hamiltonian. The reason is that the matrix element associated with an instantaneous three phonon vertex has the form $V^{(3)}(\boldsymbol{q}_1 j_1; -\boldsymbol{q}_2 j_2; \boldsymbol{q}_2 j_2)$, and it can be shown ([101]) that this matrix element vanishes for centrosymmetric crystals in which every atom is at a centre of inversion symmetry.

If we write the self-energy in terms of real and imaginary parts, then the frequency shift and lifetime of phonons are explicitly obtained.

$$\Sigma_{\boldsymbol{q}j}(\omega_n) = -\Delta_{\boldsymbol{q}j}(\omega_n) + i\Gamma_{\boldsymbol{q}j}(\omega_n) \tag{2.66}$$

If we write the self energy for three lowest order terms as,

$$\Sigma_j = \Sigma_j^{(3)} + \Sigma_j^{(3')} + \Sigma_j^{(4)} \tag{2.67}$$

Then the lowest order contributions to the shifts, Δ, and the broadening, Γ, of the phonon mode j, are

derived from the real and imaginary parts of the cubic and quartic self-energies $\Sigma_j^{(3)}, \Sigma_j^{(3')}$ and $\Sigma_j^{(4)}$,

$$\begin{aligned}
\Delta^{(3)}(\boldsymbol{q}j;\omega) &= -\frac{18}{\hbar^2}\sum_{\boldsymbol{q}_1 j_1,\boldsymbol{q}_2 j_2}|V^{(3)}(\boldsymbol{q}j;\boldsymbol{q}_1 j_1;\boldsymbol{q}_2 j_2)|^2 \\
&\times \mathcal{P}\left[\frac{n_1+n_2+1}{\omega+\omega_1+\omega_2}-\frac{n_1+n_2+1}{\omega-\omega_1-\omega_2}+\frac{n_1-n_2}{\omega-\omega_1+\omega_2}-\frac{n_1-n_2}{\omega+\omega_1-\omega_2}\right] \qquad (2.68)\\
\Delta^{(3')}(\boldsymbol{q}j) &= -\frac{72}{\hbar^2}\sum_{j_1}\sum_{\boldsymbol{q}_2 j_2}V^{(3)}(\boldsymbol{q}j;\boldsymbol{q}j;\boldsymbol{0}j_1)V^{(3)}(\boldsymbol{0}j_1;-\boldsymbol{q}_2 j_2;\boldsymbol{q}_2 j_2)\mathcal{P}\left(\frac{1}{\omega_1}\right)\left(n_2+\frac{1}{2}\right) \qquad (2.69)\\
\Delta^{(4)}(\boldsymbol{q}j) &= \frac{24}{\hbar}\sum_{\boldsymbol{q}_1 j_1}V^{(4)}(\boldsymbol{q}j;\boldsymbol{q}j;\boldsymbol{q}_1 j_1;-\boldsymbol{q}_1 j_1)\left(n_1+\frac{1}{2}\right) \qquad (2.70)\\
\Gamma(\boldsymbol{q}j;\omega) &= \frac{18\pi}{\hbar^2}\sum_{\boldsymbol{q}_1 j_1,\boldsymbol{q}_2 j_2}|V^{(3)}(\boldsymbol{q}j;\boldsymbol{q}_1 j_1;\boldsymbol{q}_2 j_2)|^2 \\
&\times [(n_1+n_2+1)\delta(\omega-\omega_1-\omega_2)+2(n_1-n_2)\delta(\omega+\omega_1-\omega_2)] \qquad (2.71)
\end{aligned}$$

where ω is the phonon frequency and $\mathcal{P}$ denotes the Cauchy principal part. $V^{(3)}$ and $V^{(4)}$ are components of the anharmonic force constants expressed in the basis of the normal modes, as in Eq. 2.60, denoting the coupling between the phonon mode j to other modes $\boldsymbol{q}_i j_i$ having frequencies $\{\omega_i\}$ and occupancies $\{n_i\}$. Here, for convenience, we have simplified the notations, i.e. $n_i = n(\omega_{j_i}(\boldsymbol{q})), \omega_i = \omega_{j_i}(\boldsymbol{q}), i = 1, 2$

2.6 Density functional perturbation theory

A convenient way to calculate the desired properties of a system is by applying appropriate perturbations to it. Derivatives of the total ground state energy (for zero temperature) or the free energy (at finite temperatures) with respect to the perturbations applied to correspond to macroscopic properties of materials which can often be experimentally measured; for example, dielectric susceptibility, elastic constants and phonon frequencies. The density functional linear response perturbation theory[102] is a powerful technique that allows the calculations of such properties within the density functional framework.

The Born-Oppenheimer Hamiltonian depends on the nuclear configuration $\boldsymbol{R} \equiv \boldsymbol{R}_I$ via the electron-nucleus interaction (V_{ext}) and the classical nucleus-nucleus interaction (V_{II}), whose energy for the nuclear configuration $\boldsymbol{R}$ is the Ewald contribution, $E_{\boldsymbol{R}}^{Ewald}$[103]. The force on an atom is obtained as

$$\boldsymbol{F}_I = -\int n_{\boldsymbol{R}}(\boldsymbol{r})\frac{\partial V_{\boldsymbol{R}}(\boldsymbol{r})}{\partial \boldsymbol{R}_I}d\boldsymbol{r} - \frac{\partial E_{\boldsymbol{R}}^{Ewald}}{\partial \boldsymbol{R}_I} \qquad (2.72)$$

where $n_{\boldsymbol{R}}(\boldsymbol{r})$ is the electron density for the nuclear configuration $\boldsymbol{R}$:

$$n_{\boldsymbol{R}}(\boldsymbol{r}) = N_e\int d\boldsymbol{r}_2...d\boldsymbol{r}_{N_e}|\Psi(\boldsymbol{r},\boldsymbol{r}_2,...,\boldsymbol{r}_{N_e})|^2 \qquad (2.73)$$

The Hessian of the Born-Oppenheimer energy surface is obtained by differentiating the Hellmann-Feynman forces with respect to nucleus coordinates:

$$\frac{\partial^2 E(\boldsymbol{R})}{\partial \boldsymbol{R}_I \partial \boldsymbol{R}_J} = -\frac{\partial F_I}{\partial \boldsymbol{R}_J} = \int d\boldsymbol{r} \frac{\partial n_{\boldsymbol{R}}(\boldsymbol{r})}{\partial \boldsymbol{R}_J} \frac{\partial V_{\boldsymbol{R}}(\boldsymbol{r})}{\partial \boldsymbol{R}_I} + \int d\boldsymbol{r} n_{\boldsymbol{R}}(\boldsymbol{r}) \frac{\partial^2 V_{\boldsymbol{R}}(\boldsymbol{r})}{\partial \boldsymbol{R}_I \partial \boldsymbol{R}_J} + \frac{\partial^2 E^{Ewald}}{\partial \boldsymbol{R}_I \partial \boldsymbol{R}_J} \tag{2.74}$$

The calculation of the Hessian thus requires the calculation of the ground-state electron charge density, $n_{\boldsymbol{R}}(\boldsymbol{r})$, as well as of its linear response to a distortion of the nuclear geometry, $\partial n_{\boldsymbol{R}}(\boldsymbol{r})/\partial \boldsymbol{R}_I$. See Ref.[104] for the complete theoretical details about the density functional perturbation theory.

2.7 Elastic Constants

Whenever a material is subjected to an external stresses, it generally gets deformed. For linear elasticity, a generalized Hooke's law holds so that the applied stress is given as[91, 105]

$$\sigma_{ij} = C_{ijkl} \epsilon_{kl} \tag{2.75}$$

where ϵ is the resulting strain in the material and Cs are the elastic constants. Stresses and strains are both second rank tensors, so the elastic constants are fourth rank tensors, with the subscripts i, j, k, l representing the Cartesian coordinates.

For three dimensional materials, with 9 possible values for pairs of Cartesian indices, C_{ijkl} can be represented as a 9×9 matrix with 81 elastic constants. Voigt-notation can simplify the 9×9 matrix to a 6×6 matrix with 21 independent elastic constants (for more details see Appendix. D). Only the triclinic crystal (lowest-symmetry) has 21 independent elastic constants. This number is significantly reduced for the high symmetry crystals with mirror and n-fold rotation axes. For instance, a single crystal with cubic symmetry has only 3 independent elastic constants and isotropic materials have only 2.

The elastic constants, which are calculable as second derivatives of the free energy of strained crystals with respect to the strain components, are directly related to the atomic bonding of the material and are of fundamental importance. They are closely connected to the thermodynamic properties of the materials such as the specific heat, the Debye temperature and the Grüneisen parameter (which relates the thermal expansion coefficient to the specific heat at a constant volume), and also play a crucial role in structural phase transitions.

Chapter 3

Structural, electronic, and phonon properties of some $RE_2B_2O_7$ pyrochlores

In this chapter, we present our DFT results of the structural, electronic, and vibrational properties in several rare-earth $RE_2B_2O_7$(RE = Sm, Gd, Tb, Dy, Ho, Er, Yb and Lu; B = Ti, Zr and Hf) pyrochlores. We briefly discuss the anomalous dynamical charges and the structural instabilities obtained in titanates. We also discuss the dependence of these properties on the rare-earth and transition ions.

3.1 Motivation

Recently, phonons in pyrochlores, especially the rare-earth titanates $RE_2Ti_2O_7$, have been of great interest. The phonons in these materials show several interesting properties, e.g., structural instability under high pressure[47–49, 51], temperature-dependent phonon anomalies[51–54, 56], etc. The origin of the phonon anomalies in these compounds has been attributed to the strong anharmonic interactions[51–54]. Structural and electronic properties of pyrochlores have also been of great interest.

The structural, electronic, and vibrational properties of the pyrochlores have been studied extensively by various groups; Kumar et al.[41] performed the zone centre phonon calculations in rare-earth pyrochlore titanates, $RE_2Ti_2O_7$ using the local density approximation (LDA), Pruneda et al.[106] carried out the LDA calculations to study the structural and electronic properties of $A_2B_2O_7$ (A = La, Y and B = Ti, Sn, Hf, Zr), Srivastava et al.[107] studied the electronic and structural properties of pyrochlores, $Y_2B_2O_7$ (B = Ti, Sn) using the generalized gradient approximation (GGA). Farmer et al.[108] carried out the structural and crystal-chemical properties of rare-earth titanate pyrochlores $RE_2Ti_2O_7$ (RE =

Sm to Lu) as well as $Y_2Ti_2O_7$ using GGA calculations, Yang et al.[109] investigated the mechanical and thermal properties of rare-earth pyrochlore oxides using the first-principles calculations within the GGA formalism.

In this chapter, our interest is to comparatively study the structural, electronic, and vibrational properties of rare-earth titanate, zirconate, and hafnate pyrochlores using both LDA and GGA methods. We also carry out a comprehensive study of the phonon instabilities in these materials.

In our discussions of the electronic properties of the different compounds, we try to quantify the ionicity or covalency of the different bonds. Static and dynamical charges are frequently used to characterize the nature of bonds in molecules and solids. Static charges associated with an isolated atom are intuitive but ill-defined quantities. Dynamical charges, on the other side, are less intuitive, but appear as a more fundamental quantity. These dynamical charges are very sensitive not only to the structural aspects, but also to the partial hybridization between occupied and unoccupied states, and hence they can provide valuable information on the nature of the atomic bonds.

To the best of our knowledge, there is no earlier comparative study on the dynamical charges, phonon frequencies and the structural instabilities in the rare-earth titanate, zirconate, and hafnate pyrochlores studied in this thesis.

3.2 Computational details

Our studies were carried out using DFT calculations as implemented in the Quantum Espresso code[110]. Ultrasoft pseudopotentials were used to represent the ion-electron interactions while freezing out the 4f electronic states as well as the 1s, 2s, 2p, 3s, 3p, 4s, 3d, 4p and 4d electronic states corresponding to a core, as these states are highly localized and do not have any significant effect on the properties we are interested in. RE 5s, 6s, 5p, 6p and 5d states, Ti 3s, 4s, 3p and 3d states, Zr 4s, 5s, 4p and 4d states, Hf 5s, 6s, 5p and 5d states and oxygen 2s and 2p states were considered as valence states. For most of the calculations discussed in this chapter, we used both LDA and GGA methods to calculate the exchange-correlation energy functional. A plane-wave basis set with a cut-off of 60 Ry was used for all our calculations for all the titanate compounds, whereas a cut-off of 40 Ry was used for all the zirconate and hafnate materials to reduce computational costs, as it was found to be adequate for these materials. 480 Ry was used as the kinetic energy cut off for the calculation of the charge densities in the case of titanates, whereas 320 Ry was used for the zirconates and hafnates. The special points sampling integration over the Brillouin zone was performed using the Monkhorst-Pack method with a $4 \times 4 \times 4$ special k-points mesh[111]. The lattice parameters, including the lattice constants and the internal atomic coordinates, were modified independently to minimize the free energy, interatomic forces and unit-cell stresses. The Broyden-Fletcher-Goldfarb-Shanno (BFGS) minimization scheme[112] was

used for geometry optimization. The DFPT was carried out to investigate the phonon properties. For the phonon dispersions, Dynamical matrices were calculated for a grid of $2 \times 2 \times 2$ $\boldsymbol{q}$-points.

3.3 Results and discussion

3.3.1 Lattice parameters

Our calculated values of the lattice constant for titanates are shown in Table. 3.1. The LDA lattice constants are smaller by maximum around 2 % than the experimental values, whereas the GGA ones are surprisingly close to the experimental ones. This is consistent with the well-known aspects of the density functional theory calculations, namely that LDA generally underestimates the lattice constant, whereas the GGA slightly overestimates it.

Table 3.1: Calculated values of the lattice constants (Å), and displacement parameter x of $RE_2Ti_2O_7$ titanate pyrochlores. The results are compared with the available experimental data.

RE	a(Å)			x		
	This work		Exp.[113]		This work	Exp.[113]
	LDA	GGA		LDA	GGA	
Sm	10.0575	10.2590	10.2270	0.3290	0.3279	-
Gd	9.9840	10.1893	10.1860	0.3308	0.3296	0.3263
Tb	9.9523	10.1581	10.1590	0.3317	0.3303	0.3280
Dy	9.9214	10.1279	10.1240	0.3325	0.3311	0.3275
Ho	9.8929	10.1012	10.1041	0.3333	0.3318	0.3285
Er	9.8696	10.0789	10.0787	0.3340	0.3323	0.3278
Yb	9.8129	10.0243	10.0330	0.3356	0.3338	0.3310
Lu	9.7861	9.9981	10.0172	0.3364	0.3345	0.3297

Our calculated values of the lattice constant for zirconates and hafnates are shown in Tables. 3.2 and 3.3, respectively. The results are compared with the experimental data wherever possible.

Table 3.2: Calculated values of the lattice constants (Å), and displacement parameter x of $RE_2Zr_2O_7$ pyrochlores. The results are compared with the available experimental and theoretical data.

RE	a(Å)			x		
		This work	Exp.		This work	Exp.
	LDA	GGA		LDA	GGA	
Sm	10.4280	10.6361	10.58[114]	0.3398	0.3377	0.339[114]
Gd	10.3571	10.5696	10.53[115]	0.3419	0.3395	0.340[115]
Tb	10.3248	10.5393	-	0.3428	0.3404	-
Dy	10.2949	10.5112	-	0.3437	0.3412	-
Ho	10.2669	10.4846	-	0.3446	0.3419	-
Er	10.2431	10.4622	-	0.3453	0.3426	-
Yb	10.1870	10.4073	-	0.3471	0.3442	-
Lu	10.1627	10.3834	-	0.3479	0.3449	-

Table 3.3: Calculated values of the lattice constants (Å), and displacement parameter x of $RE_2Hf_2O_7$ pyrochlores. The results are compared with the available experimental and theoretical data.

RE	a(Å)			x		
		This work	Exp.		This work	Exp.
	LDA	GGA		LDA	GGA	
Sm	10.3241	10.5385	-	0.3361	0.3344	-
Gd	10.2538	10.4703	-	0.3381	0.3362	-
Tb	10.2227	10.4406	-	0.3389	0.3370	-
Dy	10.1931	10.4124	10.402[116]	0.3398	0.3378	0.348[116]
Ho	10.1655	10.3864	-	0.3406	0.3385	-
Er	10.1423	10.3643	10.358[116]	0.3413	0.3391	-
Yb	10.0872	10.3111	-	0.3430	0.3407	-
Lu	10.0620	10.2874	-	0.3438	0.3413	-

The radii of A and B cations are important intrinsic parameters that are closely related to the structural stability and also physical properties. Therefore, the ionic radii of all elements used in the later discussions are tabulated in Table. 3.4[117–119]. Generally, the ionic radii are derived from the interatomic distances[120, 121].

Table 3.4: Ionic radii of rare earth ions. Ionic radii of O^{2-}, Ti^{4+}, Zr^{4+} and Hf^{4+} ions are 1.38, 0.605, 0.72 and 0.71 Å, respectively.

RE^{3+}	r_{RE} (Å)
Sm	1.079
Gd	1.053
Tb	1.040
Dy	1.027
Ho	1.015
Er	1.004
Yb	0.985
Lu	0.977

The variation of the LDA and GGA lattice constants as a function of rare-earth ionic radius for titanates, zirconates, and hafnates is shown in Fig. 3.1. It can be seen from the figure that the LDA values are smaller than GGA ones for each of the titanates, zirconates, and hafnates. The lattice constant decreases systematically with decreasing rare-earth ionic radius from Sm to Lu. The calculated values of the lattice constant both within LDA and GGA lie in the order: $a^{Ti^{4+}} < a^{Hf^{4+}} < a^{Zr^{4+}}$ for all the rare-earth pyrochlores, consistent with the fact that the ionic radius of Ti^{4+}, Hf^{4+}, and Zr^{4+} also lie in the same order, i.e. $r^{Ti^{4+}} < r^{Hf^{4+}} < r^{Zr^{4+}}$.

3.3.2 Oxygen parameter

A pyrochlore is generally described by the cubic lattice parameter, a, and the O_{48f} positional parameter, x[122–124]. The oxygen O_{48f} site is located at $(x, 1/8, 1/8)$. The parameter x of O_{48f} defines the degree of distortion of the B-O (B = Ti, Zr, Hf) octahedron, and the limiting values of x are 5/16 and 3/8

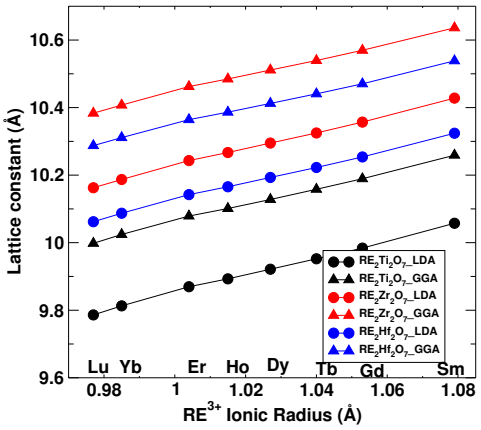

Figure 3.1: Variation of the lattice parameter of $RE_2B_2O_7$ (RE = Sm, Gd, Tb, Dy, Ho, Er, YB, Lu and B = Ti, Zr, Hf) as a function of RE^{3+} ionic radius. LDA and GGA results are compared.

for the pyrochlores. For $x = 5/16$, the B ions in the $A_2B_2O_7$ structure are in regular octahedral coordination, BO_6. When $x = 3/8$, the coordination around the A ion is a perfect cube, AO_8, and the BO_6 octahedron is unrealistically flat; the atomic positions correspond to the fluorite-type with ordered oxygen vacancies. The oxygen vacancy at the 8a site, located at (1/8, 1/8, 1/8), is surrounded by four B^{4+} cations in the pyrochlore structure.

Our calculated values of the x parameter, also listed in Tables 3.1, 3.2, and 3.3 vary from 0.3290 to 0.3364 for titanates, from 0.3361 to 0.3438 for hafnates, and from 0.3398 to 0.3479 for the zirconates.

The variation of x, the positional parameter of oxygen O_{48f}, as a function of the rare-earth ionic radius is shown in Fig. 3.2. The variation in x with respect to the transition metal ions follows the same trend as that of the lattice constant for all the rare-earth ions, i.e. $x^{Ti^{4+}} < x^{Hf^{4+}} < x^{Zr^{4+}}$.

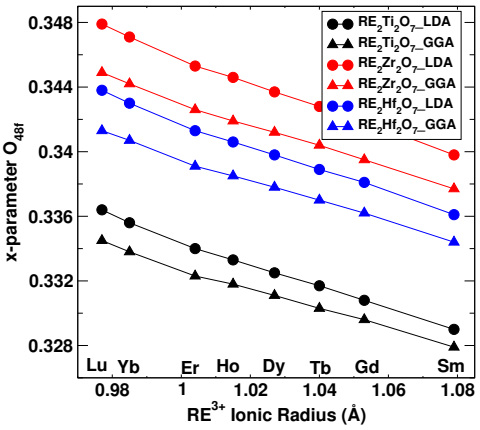

Figure 3.2: Variation of the positional parameter of oxygen O_{48f} of $RE_2B_2O_7$ (RE = Sm, Gd, Tb, Dy, Ho, Er, YB, Lu and B = Ti,Zr, Hf) as a function of RE^{3+} ionic radius. LDA and GGA results are compared.

3.3.3 Bond distances

The rare-earth cations are bonded with oxygen ions O_{48f} and O_{8b}, whereas the transition metal cations are bonded with only oxygen O_{48f}. We have calculated the various bond distances. The calculated values of the bond distances for titanates, zirconates, and hafnates are shown in Tables. 3.5, 3.6, and 3.7, respectively.

Table 3.5: Our calculated values of the bond distances (Å) in $RE_2Ti_2O_7$ titanate pyrochlores. The results are compared with the available experimental data.

RE	$d_{RE-O'}$			d_{RE-O}			d_{Ti-O}		
	This work		Exp.[108]	This work		Exp.[108]	This work		Exp.[108]
	LDA	GGA		LDA	GGA		LDA	GGA	
Sm	2.18	2.22	2.209	2.47	2.53	2.524	1.95	1.98	1.968
Gd	2.16	2.21	2.205	2.44	2.50	2.524	1.94	1.97	1.961
Tb	2.15	2.20	2.199	2.43	2.49	2.505	1.94	1.97	1.963
Dy	2.15	2.19	2.192	2.42	2.48	2.503	1.94	1.97	1.953
Ho	2.14	2.19	2.187	2.40	2.46	2.489	1.93	1.97	1.954
Er	2.14	2.18	2.182	2.39	2.45	2.488	1.93	1.96	1.946
Yb	2.12	2.17	2.172	2.37	2.43	2.454	1.93	1.96	1.950
Lu	2.12	2.16	2.169	2.36	2.42	2.459	1.93	1.96	1.943

Table 3.6: Our calculated values of the bond distances (Å) in $RE_2Zr_2O_7$ zirconate pyrochlores .

RE	$d_{RE-O'}$		d_{RE-O}			d_{Zr-O}		
	This work		This work		Exp.	This work		Exp.
	LDA	GGA	LDA	GGA		LDA	GGA	
Sm	2.26	2.30	2.49	2.55	-	2.07	2.10	-
Gd	2.24	2.29	2.46	2.52	2.483[125]	2.06	2.09	2.11[125]
Tb	2.24	2.28	2.44	2.51	-	2.06	2.09	-
Dy	2.23	2.28	2.43	2.50	-	2.06	2.09	-
Ho	2.22	2.27	2.42	2.49	-	2.06	2.09	-
Er	2.22	2.27	2.41	2.48	-	2.06	2.09	-
Yb	2.21	2.25	2.38	2.45	-	2.06	2.09	-
Lu	2.20	2.25	2.37	2.44	-	2.05	2.08	-

Table 3.7: Our calculated values of the bond distances (Å) in $RE_2Hf_2O_7$ hafnate pyrochlores .

RE	$d_{RE-O'}$		d_{RE-O}		d_{Hf-O}	
	LDA	GGA	LDA	GGA	LDA	GGA
Sm	2.24	2.28	2.49	2.55	2.03	2.06
Gd	2.22	2.27	2.46	2.52	2.03	2.06
Tb	2.21	2.26	2.45	2.51	2.02	2.06
Dy	2.21	2.26	2.43	2.50	2.02	2.06
Ho	2.20	2.25	2.42	2.49	2.02	2.05
Er	2.20	2.24	2.41	2.48	2.02	2.05
Yb	2.19	2.23	2.39	2.46	2.02	2.05
Lu	2.18	2.23	2.38	2.45	2.02	2.05

The RE-O_{48f} bond distances of the $RE_2B_2O_7$ materials for the RE's from Lu to Sm show an approximately linear dependence on the cation radius (Fig. 3.3). The bond distances indicate a significant

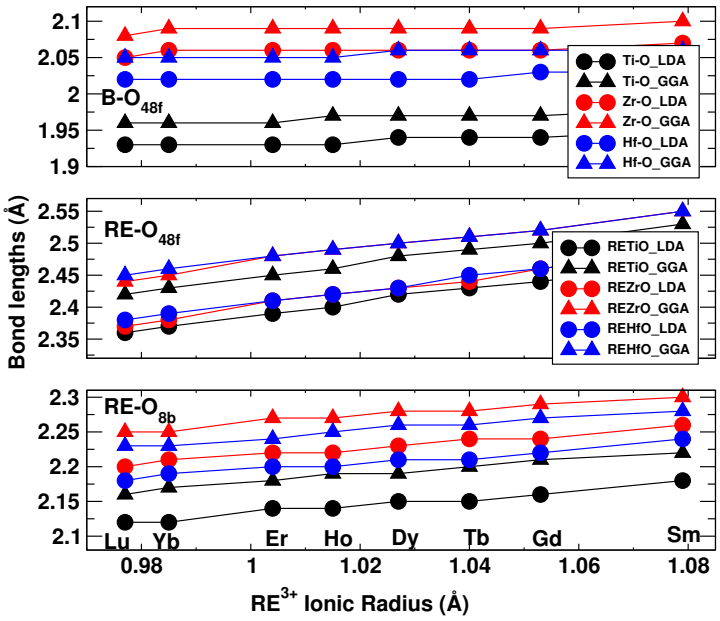

Figure 3.3: Variation of the bond distances of $RE_2B_2O_7$ (RE = Sm, Gd, Tb, Dy, Ho, Er, YB, Lu, and B = Ti, Zr, Hf) as a function of RE^{3+} ionic radius. LDA and GGA results are compared.

hybridization between RE 5p-O_{8b} and RE 5p-O_{48f} for the pyrochlores[117]. The short bond distance for RE-O_{8b} compared to RE-O_{48f} indicates a stronger hybridization of RE 5p-O_{8b}. As the rare-earth ionic radius increases, the hybridization becomes weaker. This effect is consistent with a predominant ionicity with decreasing the ionic radius, and it explains the relationship of the cubic lattice parameter and the bond distances of the RE-O_{48f} and RE-O_{8b} with changing the rare-earth ionic radius. Our results are also in reasonably good agreement with the experimental results.

3.4 Electronic properties

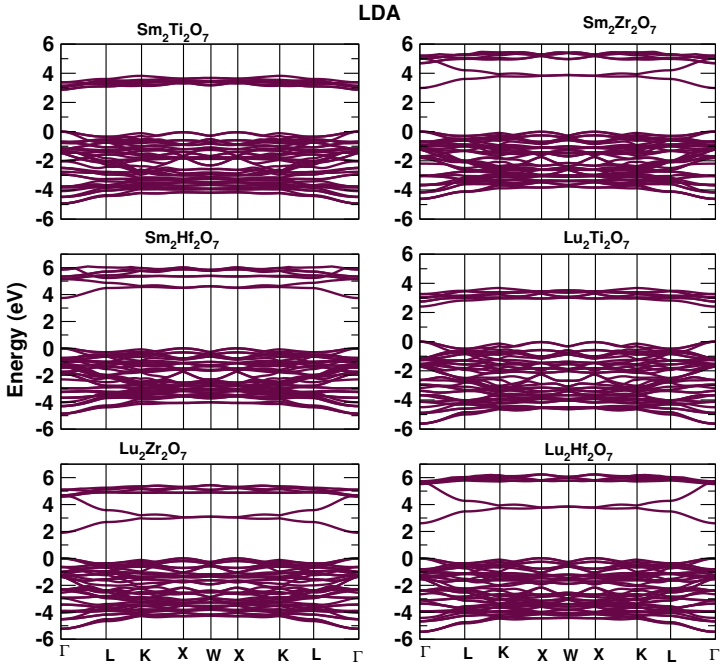

Figure 3.4: Electronic band structures of $RE_2B_2O_7$ (RE = Sm and Lu; B = Ti, Zr and Hf) within the LDA method. The valence band maximum is shifted to zero for our convenience.

Table 3.8: Energy band gaps (eV) in $RE_2B_2O_7$ (RE = Sm and Lu, B = Ti, Zr and Hf) pyrochlores using both the LDA and GGA methods, along with the available experimental and theoretical data.

System	LDA	GGA	Earlier theory	Expt.
$Sm_2Ti_2O_7$	2.88	2.82		
$Sm_2Zr_2O_7$	2.99	3.21	2.83 (Ref.[126]), 2.92 (Ref.[127])	3.81 (Ref.[127])
$Sm_2Hf_2O_7$	3.74	3.92		
$Lu_2Ti_2O_7$	2.40	2.53		
$Lu_2Zr_2O_7$	1.90	2.24		
$Lu_2Hf_2O_7$	2.61	2.90		

Since all our studied pyrochlore materials are similar, i.e. all are insulating, therefore, here in this section, we highlight the electronic properties only for six of the twenty-four $RE_2B_2O_7$ pyrochlores we have been discussing, namely for RE = Lu and Sm, representing the two ends of the ionic radii span, and for B= Ti, Zr and Hf. The six band-structures computed using LDA are shown in Fig. 3.4, and the same ones computed using GGA in Fig. 3.5. Table 3.8 shows a comparison of the band-gaps computed using both methods for each of the six materials with experiments as well as earlier calculations where available. Overall the agreement is reasonable.

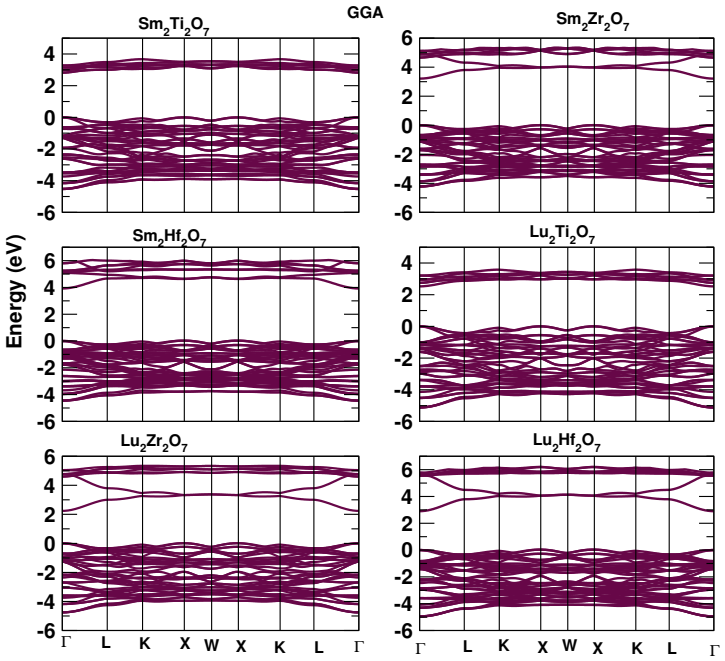

Figure 3.5: Electronic band structures of $RE_2B_2O_7$ (RE = Sm and Lu; B = Ti, Zr and Hf) within the GGA method. The valence band maximum is shifted to zero for our convenience.

3.4.1 Dynamical charges

The dynamical charges (or Born effective charges) are defined in terms of the polarization created when an atom is displaced from its equilibrium position. They have been used to characterize the ionicity or covalency in ferroelectric perovskites[106, 128]. The tensorial definition is

$$Z^*_{i,\alpha\beta} = \Omega_0 \frac{\partial P_\beta}{\partial u_{i\alpha}} \tag{3.1}$$

where P_β is the β component of the macroscopic polarization induced per unit cell when the atom i is displaced by an amount u_α in the α^{th} direction, and Ω_0 is the unit cell volume.

The Born effective charges for the four inequivalent lattice points of the rare-earth titanates, zirconates, and hafnates are shown in Tables 3.9, 3.10, and 3.11, respectively.

Table 3.9: Dynamical charge tensors of rare-earth, Ti, and oxygen elements in $RE_2Ti_2O_7$ calculated within LDA approach. The dynamical charges for any other atoms can be achieved by utilising the symmetry operations of the crystal. Eigenvalues of the symmetric part of the tensor are also given in the brackets.

	Z^*_{RE}	Z^*_{Ti}	$Z^*_{O_{48f}}$	$Z^*_{O_{8b}}$
$Sm_2Ti_2O_7$	$\begin{pmatrix} 4.05 & 0.09 & 0.09 \\ 0.09 & 4.05 & 0.09 \\ 0.09 & 0.09 & 4.05 \end{pmatrix}$ [3.96, 3.96, 4.23]	$\begin{pmatrix} 6.63 & -0.12 & -0.12 \\ -0.12 & 6.63 & -0.12 \\ -0.12 & -0.12 & 6.63 \end{pmatrix}$ [6.75, 6.75, 6.39]	$\begin{pmatrix} -2.50 & 0.00 & 0.00 \\ 0.00 & -3.40 & 1.50 \\ 0.00 & 1.50 & -3.40 \end{pmatrix}$ [-1.90, -2.50, -4.90]	-2.80
$Gd_2Ti_2O_7$	$\begin{pmatrix} 4.01 & 0.05 & 0.05 \\ 0.05 & 4.01 & 0.05 \\ 0.05 & 0.05 & 4.01 \end{pmatrix}$ [3.96, 3.96, 4.11]	$\begin{pmatrix} 6.64 & -0.15 & -0.15 \\ -0.15 & 6.64 & -0.15 \\ -0.15 & -0.15 & 6.64 \end{pmatrix}$ [6.79, 6.79, 6.34]	$\begin{pmatrix} -2.50 & 0.00 & 0.00 \\ 0.00 & -3.39 & 1.48 \\ 0.00 & 1.48 & -3.39 \end{pmatrix}$ [-1.91, -2.50, -4.87]	-2.76
$Tb_2Ti_2O_7$	$\begin{pmatrix} 3.99 & 0.04 & 0.04 \\ 0.04 & 3.99 & 0.04 \\ 0.04 & 0.04 & 3.99 \end{pmatrix}$ [3.95, 3.95, 4.07]	$\begin{pmatrix} 6.65 & -0.16 & -0.16 \\ -0.16 & 6.65 & -0.16 \\ -0.16 & -0.16 & 6.65 \end{pmatrix}$ [6.81, 6.81, 6.33]	$\begin{pmatrix} -2.50 & 0.00 & 0.00 \\ 0.00 & -3.39 & 1.47 \\ 0.00 & 1.47 & -3.39 \end{pmatrix}$ [-1.92, -2.50, -4.86]	-2.74
$Dy_2Ti_2O_7$	$\begin{pmatrix} 3.97 & 0.02 & 0.02 \\ 0.02 & 3.97 & 0.02 \\ 0.02 & 0.02 & 3.97 \end{pmatrix}$ [3.95, 3.95, 4.01]	$\begin{pmatrix} 6.65 & -0.17 & -0.17 \\ -0.17 & 6.65 & -0.17 \\ -0.17 & -0.17 & 6.65 \end{pmatrix}$ [6.82, 6.82, 6.31]	$\begin{pmatrix} -2.50 & 0.00 & 0.00 \\ 0.00 & -3.38 & 1.47 \\ 0.00 & 1.47 & -3.38 \end{pmatrix}$ [-1.91, -2.50, -4.85]	-2.72
$Ho_2Ti_2O_7$	$\begin{pmatrix} 3.95 & 0.01 & 0.01 \\ 0.01 & 3.95 & 0.01 \\ 0.01 & 0.01 & 3.95 \end{pmatrix}$ [3.94, 3.94, 3.97]	$\begin{pmatrix} 6.65 & -0.18 & -0.18 \\ -0.18 & 6.65 & -0.18 \\ -0.18 & -0.18 & 6.65 \end{pmatrix}$ [6.83, 6.83, 6.29]	$\begin{pmatrix} -2.50 & 0.00 & 0.00 \\ 0.00 & -3.38 & 1.47 \\ 0.00 & 1.47 & -3.38 \end{pmatrix}$ [-1.91, -2.50, -4.85]	-2.70
$Er_2Ti_2O_7$	$\begin{pmatrix} 3.94 & -0.01 & -0.01 \\ -0.01 & 3.94 & -0.01 \\ -0.01 & -0.01 & 3.94 \end{pmatrix}$ [3.92, 3.95, 3.95]	$\begin{pmatrix} 6.66 & -0.19 & -0.19 \\ -0.19 & 6.66 & -0.19 \\ -0.19 & -0.19 & 6.66 \end{pmatrix}$ [6.85, 6.785, 6.28]	$\begin{pmatrix} -2.50 & 0.00 & 0.00 \\ 0.00 & -3.38 & 1.47 \\ 0.00 & 1.47 & -3.38 \end{pmatrix}$ [-1.91, -2.50, -4.85]	-2.68
$Yb_2Ti_2O_7$	$\begin{pmatrix} 3.90 & -0.03 & -0.03 \\ -0.03 & 3.90 & -0.03 \\ -0.03 & -0.03 & 3.90 \end{pmatrix}$ [3.84, 3.93, 3.93]	$\begin{pmatrix} 6.68 & -0.20 & -0.20 \\ -0.20 & 6.68 & -0.20 \\ -0.20 & -0.20 & 6.68 \end{pmatrix}$ [6.88, 6.88, 6.28]	$\begin{pmatrix} -2.50 & 0.00 & 0.00 \\ 0.00 & -3.38 & 1.46 \\ 0.00 & 1.46 & -3.38 \end{pmatrix}$ [-1.92, -2.50, -4.84]	-2.64
$Lu_2Ti_2O_7$	$\begin{pmatrix} 3.88 & -0.05 & -0.05 \\ -0.05 & 3.88 & -0.05 \\ -0.05 & -0.05 & 3.88 \end{pmatrix}$ [3.78, 3.93, 3.93]	$\begin{pmatrix} 6.68 & -0.21 & -0.21 \\ -0.21 & 6.68 & -0.21 \\ -0.21 & -0.21 & 6.68 \end{pmatrix}$ [6.89, 6.89, 6.26]	$\begin{pmatrix} -2.50 & 0.00 & 0.00 \\ 0.00 & -3.38 & 1.46 \\ 0.00 & 1.46 & -3.38 \end{pmatrix}$ [-1.92, -2.50, -4.84]	-2.63

Table 3.10: Dynamical charge tensors of rare-earth, Zr, and oxygen elements in $RE_2Zr_2O_7$ calculated within LDA approach. The dynamical charges for any other atoms can be obtained by applying the symmetry operations of the crystal. Eigenvalues of the symmetric part of the tensor are also given in the brackets.

	Z^*_{RE}	Z^*_{Zr}	$Z^*_{O_{48f}}$	$Z^*_{O_{8b}}$
$Sm_2Zr_2O_7$	$\begin{pmatrix} 4.06 & 0.05 & 0.05 \\ 0.05 & 4.06 & 0.05 \\ 0.05 & 0.05 & 4.06 \end{pmatrix}$ [4.01, 4.01, 4.16]	$\begin{pmatrix} 5.67 & -0.41 & -0.41 \\ -0.41 & 5.67 & -0.41 \\ -0.41 & -0.41 & 5.67 \end{pmatrix}$ [6.08, 6.08, 4.85]	$\begin{pmatrix} -2.49 & 0.00 & 0.00 \\ 0.00 & -2.92 & 0.98 \\ 0.00 & 0.98 & -2.92 \end{pmatrix}$ [-1.94, -2.49, -3.90]	-2.74
$Gd_2Zr_2O_7$	$\begin{pmatrix} 4.03 & 0.01 & 0.01 \\ 0.01 & 4.03 & 0.01 \\ 0.01 & 0.01 & 4.03 \end{pmatrix}$ [4.02, 4.02, 4.05]	$\begin{pmatrix} 5.67 & -0.42 & -0.42 \\ -0.42 & 5.67 & -0.42 \\ -0.42 & -0.42 & 5.67 \end{pmatrix}$ [6.09, 6.09, 4.83]	$\begin{pmatrix} -2.50 & 0.00 & 0.00 \\ 0.00 & -2.91 & 0.97 \\ 0.00 & 0.97 & -2.91 \end{pmatrix}$ [-1.94, -2.50, -3.88]	-2.71
$Tb_2Zr_2O_7$	$\begin{pmatrix} 4.02 & 0.00 & 0.00 \\ 0.00 & 4.02 & 0.00 \\ 0.00 & 0.00 & 4.02 \end{pmatrix}$ [4.02, 4.02, 4.02]	$\begin{pmatrix} 5.67 & -0.42 & -0.42 \\ -0.42 & 5.67 & -0.42 \\ -0.42 & -0.42 & 5.67 \end{pmatrix}$ [6.09, 6.09, 4.83]	$\begin{pmatrix} -2.50 & 0.00 & 0.00 \\ 0.00 & -2.90 & 0.96 \\ 0.00 & 0.96 & -2.90 \end{pmatrix}$ [-1.94, -2.50, -3.86]	-2.69
$Dy_2Zr_2O_7$	$\begin{pmatrix} 4.00 & -0.02 & -0.02 \\ -0.02 & 4.00 & -0.02 \\ -0.02 & -0.02 & 4.00 \end{pmatrix}$ [3.96, 4.02, 4.02]	$\begin{pmatrix} 5.67 & -0.42 & -0.42 \\ -0.42 & 5.67 & -0.42 \\ -0.42 & -0.42 & 5.67 \end{pmatrix}$ [6.09, 6.09, 4.83]	$\begin{pmatrix} -2.50 & 0.00 & 0.00 \\ 0.00 & -2.90 & 0.96 \\ 0.00 & 0.96 & -2.90 \end{pmatrix}$ [-1.94, -2.50, -3.86]	-2.68
$Ho_2Zr_2O_7$	$\begin{pmatrix} 3.99 & -0.04 & -0.04 \\ -0.04 & 3.99 & -0.04 \\ -0.04 & -0.04 & 3.99 \end{pmatrix}$ [3.91, 4.03, 4.03]	$\begin{pmatrix} 5.67 & -0.43 & -0.43 \\ -0.43 & 5.67 & -0.43 \\ -0.43 & -0.43 & 5.67 \end{pmatrix}$ [6.10, 6.10, 4.81]	$\begin{pmatrix} -2.50 & 0.00 & 0.00 \\ 0.00 & -2.89 & 0.96 \\ 0.00 & 0.96 & -2.89 \end{pmatrix}$ [-1.93, -2.50, -3.85]	-2.66
$Er_2Zr_2O_7$	$\begin{pmatrix} 3.97 & -0.05 & -0.05 \\ -0.05 & 3.97 & -0.05 \\ -0.05 & -0.05 & 3.97 \end{pmatrix}$ [3.87, 4.02, 4.02]	$\begin{pmatrix} 5.67 & -0.43 & -0.43 \\ -0.43 & 5.67 & -0.43 \\ -0.43 & -0.43 & 5.67 \end{pmatrix}$ [6.10, 6.10, 4.81]	$\begin{pmatrix} -2.50 & 0.00 & 0.00 \\ 0.00 & -2.89 & 0.96 \\ 0.00 & 0.96 & -2.89 \end{pmatrix}$ [-1.93, -2.50, -3.85]	-2.65
$Yb_2Zr_2O_7$	$\begin{pmatrix} 3.93 & -0.07 & -0.07 \\ -0.07 & 3.93 & -0.07 \\ -0.07 & -0.07 & 3.93 \end{pmatrix}$ [3.79, 4.00, 4.00]	$\begin{pmatrix} 5.68 & -0.42 & -0.42 \\ -0.42 & 5.68 & -0.42 \\ -0.42 & -0.42 & 5.68 \end{pmatrix}$ [6.10, 6.10, 4.84]	$\begin{pmatrix} -2.49 & 0.00 & 0.00 \\ 0.00 & -2.89 & 0.96 \\ 0.00 & 0.96 & -2.89 \end{pmatrix}$ [-1.93, -2.49, -3.85]	-2.64
$Lu_2Zr_2O_7$	$\begin{pmatrix} 3.92 & -0.09 & -0.09 \\ -0.09 & 3.92 & -0.09 \\ -0.09 & -0.09 & 3.92 \end{pmatrix}$ [3.74, 4.01, 4.01]	$\begin{pmatrix} 5.68 & -0.42 & -0.42 \\ -0.42 & 5.68 & -0.42 \\ -0.42 & -0.42 & 5.68 \end{pmatrix}$ [6.10, 6.10, 4.84]	$\begin{pmatrix} -2.48 & 0.00 & 0.00 \\ 0.00 & -2.89 & 0.96 \\ 0.00 & 0.96 & -2.89 \end{pmatrix}$ [-1.93, -2.48, -3.85]	-2.63

Table 3.11: Dynamical charge tensors of rare-earth, Hf, and oxygen elements in $RE_2Hf_2O_7$ calculated within LDA approach. The dynamical charges for any other atoms can be obtained by applying the symmetry operations of the crystal. Eigenvalues of the symmetric part of the tensor are also given in the brackets.

	Z^*_{RE}	Z^*_{Hf}	$Z^*_{O_{48f}}$	$Z^*_{O_{8b}}$
$Sm_2Hf_2O_7$	$\begin{pmatrix} 4.03 & 0.09 & 0.09 \\ 0.09 & 4.03 & 0.09 \\ 0.09 & 0.09 & 4.03 \end{pmatrix}$	$\begin{pmatrix} 5.37 & -0.41 & -0.41 \\ -0.41 & 5.37 & -0.41 \\ -0.41 & -0.41 & 5.37 \end{pmatrix}$	$\begin{pmatrix} -2.43 & 0.00 & 0.00 \\ 0.00 & -2.78 & 0.86 \\ 0.00 & 0.86 & -2.78 \end{pmatrix}$	-2.73
	[3.94, 3.94, 4.21]	[5.78, 5.78, 4.55]	[-1.92, -2.43, -3.64]	
$Gd_2Hf_2O_7$	$\begin{pmatrix} 4.00 & 0.06 & 0.06 \\ 0.06 & 4.00 & 0.06 \\ 0.06 & 0.06 & 4.00 \end{pmatrix}$	$\begin{pmatrix} 5.36 & -0.42 & -0.42 \\ -0.42 & 5.36 & -0.42 \\ -0.42 & -0.42 & 5.36 \end{pmatrix}$	$\begin{pmatrix} -2.44 & 0.00 & 0.00 \\ 0.00 & -2.77 & 0.85 \\ 0.00 & 0.85 & -2.77 \end{pmatrix}$	-2.69
	[3.94, 3.94, 4.12]	[5.78, 5.78, 4.52]	[-1.92, -2.44, -3.62]	
$Tb_2Hf_2O_7$	$\begin{pmatrix} 3.99 & 0.04 & 0.04 \\ 0.04 & 3.99 & 0.04 \\ 0.04 & 0.04 & 3.99 \end{pmatrix}$	$\begin{pmatrix} 5.35 & -0.43 & -0.43 \\ -0.43 & 5.35 & -0.43 \\ -0.43 & -0.43 & 5.35 \end{pmatrix}$	$\begin{pmatrix} -2.44 & 0.00 & 0.00 \\ 0.00 & -2.76 & 0.84 \\ 0.00 & 0.84 & -2.76 \end{pmatrix}$	-2.68
	[3.95, 3.95, 4.07]	[5.78, 5.78, 4.49]	[-1.92, -2.44, -3.60]	
$Dy_2Hf_2O_7$	$\begin{pmatrix} 3.97 & 0.02 & 0.02 \\ 0.02 & 3.97 & 0.02 \\ 0.02 & 0.02 & 3.97 \end{pmatrix}$	$\begin{pmatrix} 5.35 & -0.43 & -0.43 \\ -0.43 & 5.35 & -0.43 \\ -0.43 & -0.43 & 5.35 \end{pmatrix}$	$\begin{pmatrix} -2.44 & 0.00 & 0.00 \\ 0.00 & -2.76 & 0.84 \\ 0.00 & 0.84 & -2.76 \end{pmatrix}$	-2.66
	[3.95, 3.95, 4.01]	[5.78, 5.78, 4.49]	[-1.92, -2.44, -3.60]	
$Ho_2Hf_2O_7$	$\begin{pmatrix} 3.95 & 0.01 & 0.01 \\ 0.01 & 3.95 & 0.01 \\ 0.01 & 0.01 & 3.95 \end{pmatrix}$	$\begin{pmatrix} 5.34 & -0.44 & -0.44 \\ -0.44 & 5.34 & -0.44 \\ -0.44 & -0.44 & 5.34 \end{pmatrix}$	$\begin{pmatrix} -2.44 & 0.00 & 0.00 \\ 0.00 & -2.75 & 0.84 \\ 0.00 & 0.84 & -2.75 \end{pmatrix}$	-2.64
	[3.94, 3.94, 3.97]	[5.78, 5.78, 4.46]	[-1.91, -2.44, -3.59]	
$Er_2Hf_2O_7$	$\begin{pmatrix} 3.94 & -0.01 & -0.01 \\ -0.01 & 3.94 & -0.01 \\ -0.01 & -0.01 & 3.94 \end{pmatrix}$	$\begin{pmatrix} 5.34 & -0.44 & -0.44 \\ -0.44 & 5.34 & -0.44 \\ -0.44 & -0.44 & 5.34 \end{pmatrix}$	$\begin{pmatrix} -2.44 & 0.00 & 0.00 \\ 0.00 & -2.75 & 0.83 \\ 0.00 & 0.83 & -2.75 \end{pmatrix}$	-2.62
	[3.92, 3.95, 3.95]	[5.78, 5.78, 4.46]	[-1.92, -2.44, -3.58]	
$Yb_2Hf_2O_7$	$\begin{pmatrix} 3.90 & -0.03 & -0.03 \\ -0.03 & 3.90 & -0.03 \\ -0.03 & -0.03 & 3.90 \end{pmatrix}$	$\begin{pmatrix} 5.34 & -0.43 & -0.43 \\ -0.43 & 5.34 & -0.43 \\ -0.43 & -0.43 & 5.34 \end{pmatrix}$	$\begin{pmatrix} -2.44 & 0.00 & 0.00 \\ 0.00 & -2.74 & 0.83 \\ 0.00 & 0.83 & -2.74 \end{pmatrix}$	-2.60
	[3.84, 3.93, 3.93]	[5.77, 5.77, 4.48]	[-1.91, -2.44, -3.57]	
$Lu_2Hf_2O_7$	$\begin{pmatrix} 3.89 & -0.04 & -0.04 \\ -0.04 & 3.89 & -0.04 \\ -0.04 & -0.04 & 3.89 \end{pmatrix}$	$\begin{pmatrix} 5.34 & -0.43 & -0.43 \\ -0.43 & 5.34 & -0.43 \\ -0.43 & -0.43 & 5.34 \end{pmatrix}$	$\begin{pmatrix} -2.44 & 0.00 & 0.00 \\ 0.00 & -2.74 & 0.83 \\ 0.00 & 0.83 & -2.74 \end{pmatrix}$	-2.59
	[3.81, 3.93, 3.93]	[5.77, 5.77, 4.48]	[-1.91, -2.44, -3.57]	

The charge neutrality sum rule ($\sum Z^* = 0$) is frequently used to benchmark the accuracy of the calculation, and in our case is satisfied to within 0.06e. The symmetry of the RE and B sites allows for a decomposition of the Born charge tensors into two independent eigenvalues, one for displacements pointing in the direction [111] and the others (degenerate) for displacements in the orthogonal plane. For the RE site, the highest eigencharge corresponds to the [111] direction, due to the presence of O_{8b} along this axis. On the other side, the [111] gives the smallest eigencharge for the B site because the O_{8a} site is unoccupied in pyrochlores. For the O_{48f} position, the diagonalization of the symmetric part of the Born tensor gives three nondegenerate eigenvectors, along the [011], [100], and [$0\bar{1}1$] directions (with increasing eigenvalues in the same order). If we consider the plane defined by the B-O-B elements, the first direction corresponds to the C_2 axis, the second is perpendicular to the plane, and the third goes from B to B. Finally, the O_{8b} tensor is isotropic, and only the diagonal component is given in the table.

The charge at the A site (generally higher than the nominal +3e for all the pyrochlores studied here) is almost independent of the B-site composition, with variations smaller than 1%. Similar variations ($\sim$ 6%) are obtained for O_{8b}. Large chemical dependence is observed for the dynamical charges associated with the octahedron formed by the B cation and the O_{48f}. In this case, there are differences in the Born charges for the B cation of up to 30%, and up to 26% for O_{48f}, when the B site is occupied by Hf instead of Ti.

The dynamical charges Z^*_B increase in the order B = Hf, Zr, Ti. The large anomalous charge contributions (additional charges to the given ionic values of A^{3+}, B^{4+}, and O^{2-}) originate from the electronic charge rearrangement induced when an atom is displaced from its actual position. They are associated with charge transfers between atoms and the dynamical changes in the hybridization between their orbitals. Large values of Born charges have been seen in titanium-based perovskites and attributed to the hybridization between the occupied O 2p orbitals and the unoccupied Ti 3d orbitals[129]. Hence, it would be natural to conclude that the degree of ionicity in pyrochlores increases in the same order (Hf, Zr, and Ti) as Z^*_B.

3.5 Vibrational properties; Structural instability analysis

We have performed density functional perturbation theory (DFPT)[102, 130] to study the phonon properties of the rare-earth pyrochlores. As described in chapter 1 (sec. 1.1.4), the pyrochlores (space group: $Fd\bar{3}m$) have a total of 66 normal modes in the primitive unit-cell classifiable into 26 irreducible representations at the zone centre of the Brillouin zone. Out of these, 6 modes (A_{1g}, E_g, and $4F_{2g}$) are Raman active, 7 modes ($7F_{1u}$) are infrared active, and the rest are optically inactive. Interestingly, when we perform our phonon calculations using LDA, we find that the frequencies of a few modes in some of

the rare-earth titanate pyrochlores turn out to be imaginary, indicating instability of the LDA derived equilibrium structure. When the same calculations are done using GGA, all the titanate pyrochlores are found to be unstable. In stark contrast, all the zirconates and hafnates are found to be stable whether we use LDA or GGA. We discuss these aspects in detail next.

3.5.1 A detailed description of the structural instability in pyrochlores

At equilibrium (corresponding to vanishing forces) a crystal is dynamically stable if its potential energy always increases for any combination of atomic displacements. In the harmonic approximation, this is equivalent to the condition that all the phonons have only real (by convention, positive) frequencies[131]. However, in certain cases, imaginary frequencies, corresponding to negative eigenvalues can appear in the solution of $\sum_{s',\beta} D_{s,\alpha,s',\beta}(\boldsymbol{q})\epsilon_{s',\beta}(\boldsymbol{q}j) = \omega_j^2(\boldsymbol{q})\epsilon_{s,\alpha}(\boldsymbol{q}j)$, where $D_{s,\alpha,s',\beta}(\boldsymbol{q})$ represents the dynamical matrices, $\epsilon_{s,\alpha}(\boldsymbol{q}j)$, the phonon eigenvectors and $\omega_j(\boldsymbol{q})$ is the phonon frequency (these quantities have been described in detail in sec. 2.4.1). This indicates an instability of the system.

As in the case of electronic spectra, we show in Fig.s 3.6 and 3.7 the DFPT calculated phonon spectra of the Lu and Sm pyrochlores calculated using LDA as well as GGA. Imaginary phonon frequencies, if any, are shown, for convenience of depiction, as negative frequencies. The figures clearly show the features mentioned above, namely that $Sm_2Ti_2O_7$ is unstable in both LDA and GGA, while $Lu_2Ti_2O_7$ is stable in LDA but unstable in GGA. In contrast, both the zirconates and hafnates shown are stable in LDA. Both, $Sm_2Zr_2O_7$ and $Sm_2Hf_2O_7$ are stable in GGA, whereas, $Lu_2Zr_2O_7$ and $Lu_2Hf_2O_7$ are unstable. The stability status for all of the Rare earth titanates is shown in Table 3.12, where both LDA and GGA results are compared. It is quite obvious from these results that the titanate pyrochlores show better structural stability in LDA calculations compared to the GGA ones.

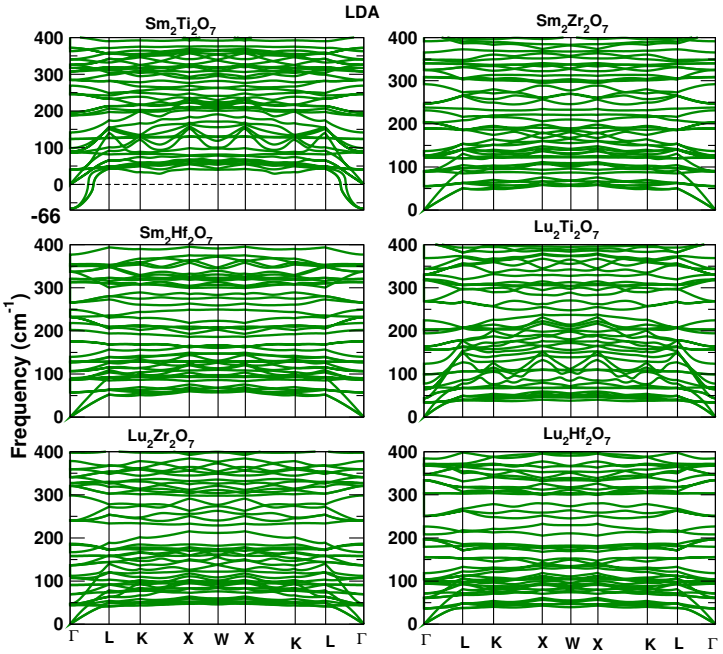

Figure 3.6: Phonon band spectra of $RE_2B_2O_7$ (RE = Sm and Lu, B = Ti, Zr and Hf) calculated using LDA method. For more details see the text.

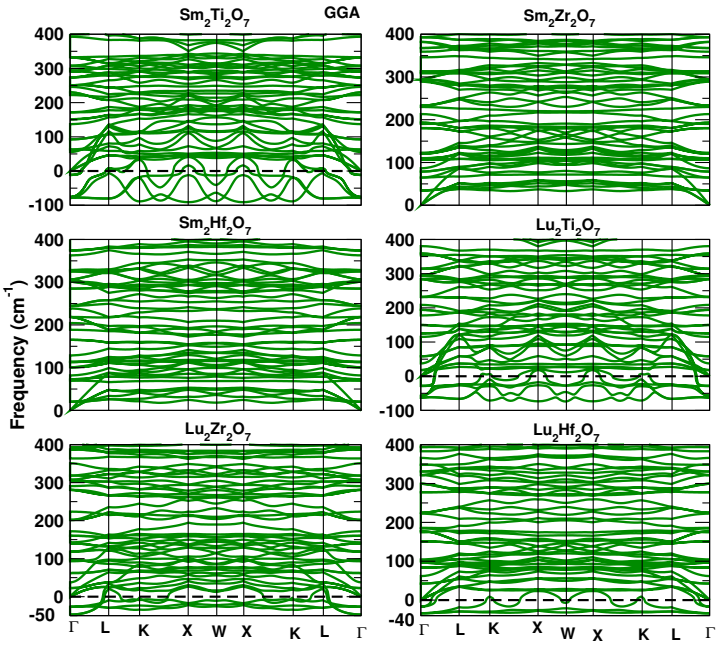

Figure 3.7: Phonon band spectra of $RE_2B_2O_7$ (RE = Sm and Lu, B = Ti, Zr and Hf) calculated using GGA method. For more details see the text.

Table 3.12: Structural stability analysis of LDA and GGA calculations. N_i stands for the number of imaginary phonon modes, ω_i represents the highest imaginary frequency.

$RE_2Ti_2O_7$	LDA			GGA		
	Stability	N_i	ω_i	Stability	N_i	ω_i
Sm	Unstable	3	66	Unstable	9	79
Gd	Unstable	3	59	Unstable	9	68
Tb	Unstable	3	57	Unstable	9	66
Dy	Stable	0	-	Unstable	9	67
Ho	Stable	0	-	Unstable	9	62
Er	Stable	0	-	Unstable	9	60
Yb	Stable	0	-	Unstable	9	60
Lu	Stable	0	-	Unstable	9	63

A small distortion to the atomic positions in the unit-cell stabilizes the crystal structure, i.e. the system with the distortion no longer has any modes with imaginary frequencies. In Table 3.13 we have shown the amount of distortion required to stabilize the structure of $Sm_2Ti_2O_7$ titanate pyrochlore, both in LDA and GGA calculations. As it can be seen that larger distortions are required to stabilize the structure in case of GGA, compared to the LDA ones. Since the distortions lower the symmetries, they increase the number of irreducible q-points in the BZ required for the phonon calculations and the number of irreducible representations for the phonon calculations at the Gamma-point. Nevertheless, we have done phonon calculations using the stable distorted structures both in LDA and GGA. As shown in the next section, the frequencies in the LDA are closer to the experimental values than the GGA.

Table 3.13: Amount of distortion(in Å) required to stabilize the structure of $Sm_2Ti_2O_7$ titanate pyrochlore. The results clearly show that the structure is highly unstable in GGA compared to LDA calculations.

Atom	LDA			GGA		
	dx	dy	dz	dx	dy	dz
Sm	0	0	0	0	0	0
Sm	0	0	0	0	0	0
Sm	0	0	0	0	0	0
Sm	0	0	0	0	0	0
Ti	0.01	0.03	-0.04	-0.07	0.02	0.02
Ti	0.04	0	0.04	0.01	-0.02	-0.07
Ti	-0.04	-0.03	0.01	0	-0.02	-0.07
Ti	-0.01	0	-0.01	0.09	0.03	0.02
O	0	0	0	0	0	0
O	0	0	0	0	0	0
O	0	0	0	0	0	0
O	0	0	0	0	0	0
O	0	0	0	0	0	0
O	0	0	0	0	0	0
O	0	0	0	0	0	0
O	0	0	0	0	0	0
O	0	0	0	0	0	0
O	0	0	0	0	0	0
O	0	0	0	0	0	0
O	0	0	0	0	0	0
O	0	0	0	0	0	0
O	0	0	0	0	0	0

3.5.2 Description of Raman and Infra-red active modes

In the pyrochlore titanates[41, 132], low frequency modes in the range 50-240 cm^{-1} have been observed, with the lowest frequency Raman modes around 220 cm^{-1}. All Raman active modes involve vibrations of oxygen atoms only, and our DFT calculations do not show any Raman active mode such as F_{2g} around 220 cm^{-1} in any of the pyrochlore titanates, agreeing with the Kumar et al.[41] results of $RE_2Ti_2O_7$ (RE = Gd, Dy, Ho, Er, Lu) studied using the LDA calculations. But we observe an IR-active mode (F_{1u}) around 225 cm^{-1} in titanates, which is normally Raman-inactive but appears in Raman spectra[45–47, 49, 51, 52, 54, 57, 133–135] due to displacive disorder of RE and O′ sites in these systems. This displacive disorder leads to relaxation of selection rules[41], as a result of which IR modes can appear in Raman spectra and vice-versa, and silent modes may become active and appear in Raman and IR spectra. Our ab initio results are consistent with the predictions of the ab initio calculations by Kumar et al.[41], and also with ab initio calculations of Fischer et al.[136] (lowest F_{2g} mode at 265 cm^{-1} and F_{1u} mode at 190 cm^{-1}). Similarly, other Raman-active modes (assigned as F_{2g}) observed at 269 cm^{-1},297 cm^{-1} in $Dy_2Ti_2O_7$, $H_2Ti_2O_7$[51] and at 244 cm^{-1} (at 295 K), 176 cm^{-1} (at 4.2 K) in $Dy_2Ti_2O_7$, and 219 cm^{-1} (at 295K), 187 cm^{-1} (at 4.2 K) in $Er_2Ti_2O_7$[52] can be attributed to the relaxation of selection

rules.

In the frequency range 24-400 cm^{-1}, our DFT calculations predict an F_{2g} mode at around 320 cm^{-1} (see Table. 3.14) in $RE_2Ti_2O_7$ titanate pyrochlores, in reasonably good agreement with experimental values observed at around 310 cm^{-1}[47, 49, 135]. This mode involves vibrations of oxygen atoms (O) at site 48f, whereas oxygens (O′) at the 8b site, at the centre of tetrahedra, RE_4O' formed by four RE atoms, is at rest. In the ideal pyrochlore structure, TiO_6 octahedra are distorted in such a way that O-Ti-O bond angles are different (83.7° and 96.3°), but the Ti-O bond lengths are equal. The above-discussed phonon mode has a dominant component of O-Ti-O bending in the distorted octahedra. Furthermore, frequency of this mode remains almost constant, with only a slight decrease from Yb to Lu titanate as we move from Sm → Gd → Tb → Dy → Ho → Er → Yb → Lu titanates, indicating comparable strengths of the O-Ti-O bending force constant. It also implies that the RE^{3+} ion has a negligible effect on the frequency of this mode. In this vibrational mode, the force constant contributions arising from the RE-O′ bonds in the RE_4O' tetrahedra, and those from O-RE-O′ bending are absent, as the O′ atoms are at rest.

In the pyrochlore titanates[52, 53, 137], the E_g mode is generally observed around 330 cm^{-1}. Our DFT values for the E_g mode calculated for $RE_2Ti_2O_7$ are in good agreement with the experimental results (see Table. 3.14). In the E_g mode, TiO_6 octahedra distortion takes place mainly due to the bending of the O-Ti-O bonds, resulting in the modulation of the O-Ti-O angles. Our results indicate that similar O-Ti-O bending force constants are present in all the considered pyrochlores. However, comparing the frequency in Sm and Lu titanates suggest that the RE^{3+} ions play a negligible role in the O-RE-O bending in this mode. Also, this phonon mode does not involve vibrations of the O′ atoms, implying no contributions from RE-O′ stretching and O-RE-O′ bending force constants.

One of the F_{2g} modes and A_{1g} modes of the pyrochlore titanates[132], happening mainly due to vibrations of TiO_6 octahedra, are usually observed around 450 cm^{-1} and around 510 cm^{-1}, respectively. Our calculated values are in quite good agreement with the experimental results. This F_{2g} mode involves the vibration of both oxygens, at 48f as well as 8b sites, leading to contributions from RE-O′ stretching, and O-RE-O′ bending force constants in addition to the dominant contribution from O-Ti-O bending involving the TiO_6 octahedra. The frequency of this mode remains almost constant as we go through the sequence of Sm → Gd → Tb → Dy → Ho → Er → Yb → Lu titanates, suggesting rather a minimal variation in the strength of the O-Ti-O, O-RE-O′, and RE-O′ force constants as the systems change. The main contribution to the A_{1g} mode is from the O-Ti-O bending force constant in titanates. The frequency of this mode is found to be around 510 cm^{-1} for all the titanates we have studied, showing the almost equal contribution of O-Ti-O bending force constant. RE-O′ stretch and O-RE-O′ bending force constants do not contribute to this mode as O_{8b} are at rest.

We are left with the two high-frequency Raman modes with symmetry F_{2g}. The calculated values

of the frequency for these two modes are found to be around 590 cm^{-1} and 800 cm^{-1}, respectively. The frequency of the F_{2g} mode around 590 cm^{-1} is in quite good agreement with the experimental values as reported in Table. 3.14. This mode, like the F_{2g} mode around 450 cm^{-1}, includes the vibrations of both O_{48f} and O_{8b}. This signifies that the RE-O′ stretching and O-RE-O′ bending do make contributions through vibrations of the RE_4O' tetrahedra. However, the main contribution to this mode comes again from the O-Ti-O bending and Ti-O stretching force constants. We find nearly identical frequencies of this mode in all our rare-earth titanate pyrochlores, indicating nearly identical force constants.

The most interesting mode in our DFT calculations is the one around 800 cm^{-1}, assigned as overtones or combination of vibrational modes in the experimental measurements of Saha et al.[54], and in the lattice dynamical calculations by Gupta et al.[46] in titanates. Recent measurements on single crystal $Dy_2Ti_2O_7$ and $Ho_2Ti_2O_7$ pyrochlore titanates by Maczka et al.[57] have not encountered any mode as high as 800 cm^{-1}, and hence they assigned all modes above 580 cm^{-1} as overtones. But in contrast, ab initio calculations by Kumar et al.[41] have found an F_{2g} mode at a high frequency around 800 cm^{-1} for rare-earth pyrochlore titanates, $RE_2Ti_2O_7$ (RE = Gd, Dy, Ho, Er, Lu). We also note here that ab initio calculations by Fischer et al.[136] have found an F_{2g} mode at a high frequency of 880 cm^{-1} in $Cd_2Nb_2O_7$, and ab initio calculations by Patterson[138] predict the highest F_{2g} mode at 711 cm^{-1} for $Bi_2Ti_2O_7$ pyrochlore. From our calculations, we find the high-frequency F_{2g} mode around 780-830 cm^{-1} in all the rare-earth titanate pyrochlores. This mode involves the vibrations of only O_{48f}, indicating the absence of RE_4O' tetrahedra vibrations. It is essentially attributed to the dominant contribution of Ti-O stretch as proposed by Vandenborre et al.[45] in titanates and stanates, and to the O-Ti-O bending force constant in manganates as suggested by Brown et al.[132], in addition to the O-RE-O bending force constant. A clear increase of frequency from 777 to 826 cm^{-1} is observed in going from Sm to Lu, indicating an increase in the strength of the force constants. This increase in frequency suggests more tightly packed octahedra in $Lu_2Ti_2O_7$ compared to $Sm_2Ti_2O_7$. However, no such significant increase in force constants for other low-frequency modes is found while moving from the Sm to the Lu titanates. It is perhaps reasonable to suggest that non-appearance of the high-frequency F_{2g} mode in experiments may be due to its low intensity of F_{2g} mode in these pyrochlores as well as non-ambient conditions.

Table 3.14: Raman mode frequencies (cm^{-1}) of rare-earth pyrochlore titanates $RE_2Ti_2O_7$ with assignments along with the literature data. Modes with $\star$ indicate that they are experimentally observed, but not found from DFT. Frequencies with † implies that they are not assigned experimentally to any Raman-active mode, and with ‡ means they are assigned as overtones in experiments. Theory A shows results for other first-principles simulations.

Mode	F^*_{2g}	F^*_{2g}	F_{2g}	E_g	F_{2g}	A_{1g}	F_{2g}	F_{2g}
$Sm_2Ti_2O_7$								
LDA	-	-	322	334	450	502	593	777
GGA	-	-	295	305	425	471	561	738
Expt.[135]	225	-	317	-	-	515	515	580
Expt.[108]	-	-	309	-	-	516	-	-
$Gd_2Ti_2O_7$								
LDA	-	-	325	338	453	507	590	789
GGA	-	-	296	310	427	476	559	751
Theory A[41]	-	-	321	335	452	505	596	782
Expt.[135]	227	-	317	-	-	515	515	580
Expt.[51]	205	260	310	325	450†	517	554	-
$Tb_2Ti_2O_7$								
LDA	-	-	325	339	455	507	589	794
GGA	-	-	297	310	428	478	563	757
$Dy_2Ti_2O_7$								
LDA	-	-	324	343	458	510	587	801
GGA	-	-	296	316	428	472	576	771
Theory A[41]	-	-	321	338	454	508	593	793
Expt.[51]	212	269	308	328	451†	519	550	-
Expt.[54]	174	-	312	330	453	515	563	800‡
$Ho_2Ti_2O_7$								
LDA	-	-	325	346	461	513	588	808
GGA	-	-	298	320	431	480	568	770
Theory A[41]	-	-	320	339	455	509	592	799
Expt.[51]	214	297	311	329	452†	522	562	-
$Er_2Ti_2O_7$								
LDA	-	-	324	339	461	511	589	811
GGA	-	-	294	318	434	476	577	776
Theory A[41]	-	-	320	339	456	511	590	804
Expt.[52]	-	219	311	331	450†	525	565	-
$Yb_2Ti_2O_7$								
LDA	-	-	328	343	463	515	587	821
GGA	-	-	288	317	438	483	578	783
Expt.[135]	220	-	320	-	-	525	525	590
$Lu_2Ti_2O_7$								
LDA	-	-	319	344	463	516	586	826
GGA	-	-	290	318	438	483	584	787
Theory A[41]	-	-	316	341	458	513	590	813
Expt.[54]	188	-	313	336	458	520	609	800‡

Table 3.15: Calculated Infra-red mode frequencies (cm^{-1}) of rare-earth pyrochlore titanates, $RE_2Ti_2O_7$ with assignments along with the literature data. Theory A shows results for other first-principles simulations.

Mode	F_{1u}	F_{1u}	F_{1u}	F_{1u}	F_{1u}	F_{1u}	F_{1u}
$Sm_2Ti_2O_7$							
LDA	89	129	186	240	374	444	522
GGA	69	107	163	231	340	407	538
Expt.[135]	78	140	240	285	400	440	550
$Gd_2Ti_2O_7$							
LDA	85	123	182	231	382	443	532
GGA	66	107	162	223	348	407	511
Theory A[41]	69	120	177	239	372	452	533
Expt.[135]	80	140	240	285	400	444	550
Expt.[139]	-	136	242	293	408	456	552
Expt.[2]	-	140	250	300	410	442	524
$Tb_2Ti_2O_7$							
LDA	84	120	178	227	384	442	534
GGA	71	113	163	219	350	408	514
$Dy_2Ti_2O_7$							
LDA	82	111	188	226	390	442	548
GGA	86	118	165	215	349	408	522
Theory A[41]	66	114	173	230	380	450	541
Expt.[139]	-	136	242	291	421	456	557
Expt.[58]	-	137	226	261	374	440	545
Expt.[2]	-	139	245	297	420	450	550
$Ho_2Ti_2O_7$							
LDA	80	109	186	222	394	445	553
GGA	78	105	161	212	359	408	524
Theory A[41]	63	112	171	227	383	450	545
Expt.[2]	-	136	245	292	424	445	558
$Er_2Ti_2O_7$							
LDA	83	115	178	212	388	447	558
GGA	78	106	160	208	365	411	525
Theory A[41]	60	109	168	222	386	450	548
Expt.[2]	-	136	247	292	427	452	560
$Yb_2Ti_2O_7$							
LDA	70	103	170	207	401	446	562
GGA	77	105	156	200	367	410	541
Expt.[135]	75	136	235	270	400	450	570
$Lu_2Ti_2O_7$							
LDA	65	99	164	203	402	447	565
GGA	87	113	157	199	370	415	546
Theory A[41]	53	99	155	-	392	454	556

Next, we discuss our results for the IR active modes. Our calculated frequencies of these modes are tabulated in Table. 3.15 along with their symmetry assignments and available experimental results. For the first four low frequency F_{1u} modes (50-300 cm^{-1}), we observe a decrease in frequency while going from Sm to Lu (except in a few cases, which could be due to the limitations of the DFT calculations), whereas the high-frequency F_{1u} modes (350-600 cm^{-1}) show an increase in their frequencies. In case of the low-frequency modes, the effect of the increase of mass compared to increase in force constants is probably prevailing in going from Sm to Lu titanates, so we observe a decrease in frequencies; whereas the increase in the frequency in case of the high frequency modes when going in the same order of the rare-earth titanates suggests dominant contributions from the stretching force constants. The first four low-frequency IR modes have a dominant contribution from O′-RE-O′ bending, O-RE-O bending, RE-TiO_6 stretching, and O-Ti-O bending force constants. The high-frequency IR modes have a dominant contribution from the stretching force constants of RE-O and RE-O′ bonds. Our results are again in quite good agreement with the experimental results.

The Raman and IR mode frequencies in the $RE_2Zr_2O_7$ zirconates are given in Table. 3.16 and 3.17, respectively; for $RE_2Hf_2O_7$ hafnates, the Raman and IR modes frequencies are tabulated in Table. 3.18 and 3.19, respectively. The trends in the frequencies of these modes with changes in the RE are quite similar to the trends in the titanate.

Table 3.16: Calculated Raman mode frequencies (cm^{-1}) of rare-earth pyrochlore zirconates, $RE_2Zr_2O_7$ with assignments along with experimental data.

Mode	F_{2g}	E_g	F_{2g}	A_{1g}	F_{2g}	F_{2g}
$Sm_2Zr_2O_7$						
LDA	327	344	421	501	539	778
$Gd_2Zr_2O_7$						
LDA	325	345	422	503	540	785
Expt.[134]		318	407	543	597	
$Tb_2Zr_2O_7$						
LDA	325	347	422	504	541	788
$Dy_2Zr_2O_7$						
LDA	327	349	419	505	541	791
$Ho_2Zr_2O_7$						
LDA	324	350	416	505	542	793
$Er_2Zr_2O_7$						
LDA	323	352	417	506	542	795
$Ho_2Zr_2O_7$						
LDA	322	354	411	507	541	800
$Lu_2Zr_2O_7$						
LDA	324	360	410	510	541	801

Table 3.17: Calculated infra-red mode frequencies (cm^{-1}) of rare-earth pyrochlore zirconates, $RE_2Zr_2O_7$ with assignments along with experimental data.

Mode	F_{1u}	F_{1u}	F_{1u}	F_{1u}	F_{1u}	F_{1u}	F_{1u}
$Sm_2Zr_2O_7$							
LDA	94	120	190	213	342	406	527
$Gd_2Zr_2O_7$							
LDA	85	122	175	209	337	414	536
Expt.[134]		142	250	296	390	485	599
$Tb_2Zr_2O_7$							
LDA	82	119	172	206	336	417	538
$Dy_2Zr_2O_7$							
LDA	78	115	168	204	335	422	541
$Ho_2Zr_2O_7$							
LDA	73	112	165	201	334	425	543
$Er_2Zr_2O_7$							
LDA	68	109	162	198	333	428	545
$Yb_2Zr_2O_7$							
LDA	56	102	154	191	330	432	548
$Lu_2Zr_2O_7$							
LDA	50	91	157	188	327	434	549

Table 3.18: Calculated Raman mode frequencies (cm^{-1}) of rare-earth pyrochlore hafnates, $RE_2Hf_2O_7$ with assignments along with experimental data.

Mode	F_{2g}	E_g	F_{2g}	A_{1g}	F_{2g}	F_{2g}
$Sm_2Hf_2O_7$						
LDA	334	352	437	513	555	806
Expt.[2]	312	-	395	-	532	765
Expt.[116]	342	-	428	520	548	-
$Gd_2Hf_2O_7$						
LDA	337	356	435	516	552	815
Expt.[2]	323	-	395	492	-	-
$Tb_2Hf_2O_7$						
LDA	337	357	435	517	553	819
$Dy_2Hf_2O_7$						
LDA	337	360	435	519	553	823
$Ho_2Hf_2O_7$						
LDA	337	360	435	520	553	826
$Er_2Hf_2O_7$						
LDA	337	362	436	521	554	829
$Ho_2Hf_2O_7$						
LDA	335	364	434	522	555	835
$Lu_2Hf_2O_7$						
LDA	334	364	427	522	554	836

Table 3.19: Calculated infra-red mode frequencies (cm^{-1}) of rare-earth pyrochlore hafnates, $RE_2Hf_2O_7$ with assignments along with experimental data.

Mode	F_{1u}	F_{1u}	F_{1u}	F_{1u}	F_{1u}	F_{1u}	F_{1u}
$Sm_2Hf_2O_7$							
LDA	86	134	174	228	310	416	550
Expt.[2]	72	130	184	237	344	412	555
$Gd_2Hf_2O_7$							
LDA	81	128	170	221	310	419	559
Expt.[2]	-	-	-	-	-	429	561
$Tb_2Hf_2O_7$							
LDA	79	125	168	217	309	421	563
Expt.[2]	-	-	-	-	-	410	550
$Dy_2Hf_2O_7$							
LDA	77	122	165	214	308	422	566
$Ho_2Hf_2O_7$							
LDA	74	119	163	210	307	424	569
$Er_2Hf_2O_7$							
LDA	71	116	161	207	307	427	572
$Yb_2Hf_2O_7$							
LDA	64	110	156	199	303	429	577
$Lu_2Hf_2O_7$							
LDA	59	106	153	194	301	430	579

3.6 Conclusions

In summary, in this chapter, we explored the structural, electronic, and vibrational properties in pyrochlore materials using first-principles DFT calculations. Both the LDA and GGA methods were used for all our calculations.

Our calculated lattice constants and the internal structure parameter for the titanate, zirconate, and hafnates are in reasonable agreement with the experimental values. As expected, the LDA values are smaller than the GGA ones and the GGA results are slightly larger compared to the measured data. The lattice constant increases smoothly with increasing values of the ionic radii, i.e. from Lu to Sm and they lie in the order: $a^{Ti^{4+}} < a^{Hf^{4+}} < a^{Zr^{4+}}$. This is because the ionic radius of Ti^{4+}, Hf^{4+}, and Zr^{4+} also lie in the same order.

Our calculated values of the bond distances are also in reasonable agreement with the data available in the literature. The RE-O bond distance displays a linear dependence on the ionic radii of the rare-earth from Lu to Sm. The bond distances indicate a significant hybridization between the 5p states of RE and the 2p states of O_{8b} and O_{48f}. The hybridization weakens with increasing the rare-earth ionic radius.

All the studied pyrochlores are insulating in nature and the calculated LDA energy band gaps of around 3 eV, are in good agreement with the values quoted in the literature.

We also calculated the dynamical charge, a quantity that describes a change in the polarization when an atom is displaced from its equilibrium position. The dynamical charge for the RE site atoms in $RE_2B_2O_7$ is calculated to be higher than its nominal $+3e$ value and is nearly independent of the B-site composition. Large chemical dependence is found for the dynamical charges of B cations and the O_{48f}. The dynamical charges $Z_B^\star$ increase in the order B = Hf, Zr, Ti. The large anomalous charge contributions (additional charges to the given ionic values of RE^{3+}, B^{4+}, and O^{2-}) stem from the electronic charge rearrangement when an atom is moved from its original position. They are correlated to charge transfers between atoms and the dynamical changes in the hybridization.

Using linear response theory as embedded in the DFPT, we investigated the lattice dynamical properties of pyrochlores. We performed both the LDA and GGA calculations to confirm which one works better for the pyrochlore oxides. A remarkable finding of the GGA calculations in *all* the titanate compounds is that there are a few phonon modes at the zone centre of the Brillouin zone which have imaginary frequencies. The LDA results also lead to modes with imaginary frequencies, but only for a few of the titanates and with a smaller magnitude of the imaginary frequencies. These phonon modes with imaginary frequencies correspond to the structural instabilities. We find that small distortion to the atomic positions in the unit cell is able to stabilize the crystal structure. From our calculations, it is quite clear that the GGA results show more structural instability compared to the LDA ones. Our calculations show that this structural instability is characterized by the large amplitude of Ti^{4+} vibrations. This is because the centre of tetrahedra formed by Ti cations remains vacant, which in turn provides Ti^{4+} ions a more room to oscillate. When the Ti^{4+} ions are replaced by the heavier ions, Zr^{4+} or Hf^{4+}, no structural instability is seen in either of the density functional approaches.

In the literature, there exists confusion in assigning the symmetries of the phonon modes. In the pyrochlore titanates[132], low frequency modes in the range 50-240 cm^{-1} have been observed, with the lowest frequency Raman modes around 220 cm^{-1}. All the Raman active modes involve only the vibrations of oxygen atoms and our calculations do not show any modes with frequencies as low as 220 cm^{-1} as Raman active. Our first calculated low-frequency Raman mode is found around 320 cm^{-1}. These results are consistent with the Ab initio results by Kumar et al.[41]. The authors in Ref.[41] attributed all experimentally observed modes below 300 cm^{-1} to the relaxation of selection rules due to displacive disorder in pyrochlores. The experimentally observed frequency around 450 cm^{-1} has been assigned to an F_{2g} mode, which was attributed to TiO_2 impurities in the $Gd_2Ti_2O_7$ and $Er_2Ti_2O_7$ titanates, and were not attributed to any mode in $Dy_2Ti_2O_7$, $Ho_2Ti_2O_7$, and $Y_2Ti_2O_7$ compounds. An interesting mode in our DFT calculations is seen around 800 cm^{-1}, attributed as overtones or combination of vibrational modes in experimental measurements of Saha et al.[54], and in lattice dynamical calculations by Gupta et al.[46] in titanates. The assignment of this mode is consistent with ab initio calculations by Fischer et al.[136] and Kumar et al.[41]. Comparison between

the calculated Raman active mode frequencies (except the high frequency mode) for the $RE_2Ti_2O_7$ (RE = Sm, Gd, Tb, Dy, Ho, Er, Yb, Lu) series shows that the nature of the RE^{3+} ion has a very little effect on the Raman active mode frequencies. This shows that the relevant force constants for these modes in the titanates are very similar, except for the high frequency F_{2g} mode. These results are similar for the zirconates and hafnates. The increase in the frequency of the high-frequency F_{2g} mode from Sm to Lu indicates that the BO_6 octahedra in $Lu_2B_2O_7$ is more tightly packed than the BO_6 octahedra in $Sm_2B_2O_7$. In case of the low frequency infrared active modes (50 - 250 cm^{-1}), the effect of an increase in mass is more predominant than the effect of an increase in force constants, when moving from Sm to Lu. Whereas an increase in the frequency in case of the high frequency infrared active modes (300 - 600 cm^{-1}) when going from Sm to Lu, indicates that contributions from the stretching force constants of the RE-O, RE-O′, and B-O bonds prevail over the effect of the increment in mass for these modes.

Chapter 4

Elastic, mechanical, and thermal properties of $RE_2B_2O_7$ pyrochlores

In this chapter, we present our first-principles DFT study of the elastic, mechanical, and thermal properties in the rare-earth $RE_2B_2O_7$ (RE = Sm, Gd, Tb, Dy, Ho, Er, Yb, and Lu; B = Ti, Zr, and Hf) pyrochlores. We have performed a systematic study of the elastic constants, bulk, shear, and Young's moduli, Poisson's and Pugh's ratios, transverse, longitudinal, and the mean sound velocities, Debye temperature, and the minimum thermal conductivity.

4.1 Motivation

As discussed in Chapter 1, $RE_2B_2O_7$ (RE = rare-earth, and B is a tetravalent metallic cation) pyrochlores are important materials due to their technological uses. These materials have a low thermal conductivity, a high melting point, a high thermal expansion coefficient, high stability and the ability to accommodate defects[140]. These unique properties make $RE_2B_2O_7$ compounds promising candidates for high-permittivity dielectrics[141], thermal barrier coatings (TBC)[140], as potential solid electrolytes in high temperature fuel cells, as immobilization hosts of actinides in nuclear waste[142] and as oxidation catalysts[143]. A significant effort has been put to optimize the specific properties (high radioactive resistance, low thermal conductivity, low migration energy), and at the same time to ensure the requirements, such as the physical stability, and the chemical or thermal compatibility with other materials involved in the design. However, experimental data is rather inadequate in building the connections between the crystal structure and various physical properties in these materials.

Recently, both atomistic-scale simulations and ab initio calculations have been carried out[106, 144–150] on pyrochlore oxides. Based on empirical potential methods, atomistic-scale simulations showed

that the structural, mechanical and thermal properties, together with defect-formation energy were connected to the cationic radius[144–146]: (1) $RE_2B_2O_7$ compounds with similar atomic radii for RE and B elements have better radiation resistance than those with dissimilar ones and (2) the B cation radii correlate with the structural, mechanical and thermal properties. Ab initio calculations have focused on examinations the crystal structure, electronic structure, and defect-formation energetics of bismuth, titanate, stanate, and hafnate pyrochlores[106, 147–150].

However, not all the pyrochlore oxides have been studied in terms of the relationship between the mechanical/thermal properties and the crystal structure or the kind of chemical bonding. It is interesting to study the systematics of this relationship. The elastic properties of solids are closely associated with many solid-state properties, such as the equation of state, specific heat, thermal expansion coefficient, and Debye temperature. For example, elastic constants provide knowledge about the bonding strengths between neighbouring planes, the anisotropy of chemical bonding, as well as structural stability. As candidates for high-performance TBC materials, the thermal conductivity of pyrochlores is also one of the properties of prime interest. Therefore, it is quite interesting to examine the intrinsic relationships between the crystal structure, chemical bonding, mechanical, and thermal properties of pyrochlores.

Recently, Liu et al.[151] performed plane-wave pseudopotential total energy calculations on $La_2T_2O_7$ (T = Ge, Ti, Sn, Zr, Hf) pyrochlores to study the elastic constants, the intrinsic mechanical properties and the thermal conductivity. More recently, Yang et al.[109] carried out an investigation of the mechanical and thermal properties of rare-earth pyrochlore oxides by first-principles calculations within the GGA framework.

In the present chapter, we have performed DFT calculations in the rare-earth $RE_2B_2O_7$ (RE = Sm, Gd, Tb, Dy, Ho, Er, Yb, and Lu; B = Ti, Zr, and Hf) pyrochlores to study the elastic, mechanical, and thermal properties. We have used both the LDA and GGA methods to compare these properties.

4.2 Computational details

The QUANTUM ESPRESSO code[110] was used in the present DFT calculations, and the Vanderbilt-type ultrasoft pseudopotentials[152] were used to represent the electron-ion interactions. The 4f states along with the 1s, 2s, 2p, 3s, 3p, 4s, 3d, 4p, and 4d states in the rare-earth elements were taken as core like states since these states are mostly localized. RE 5s, 6s, 5p, 6p, and 5d states, Ti 3s, 4s, 3p, and 3d states, Zr 4s, 5s, 4p, and 4d states, Hf 5s, 6s, 5p, and 5d states and oxygen 2s and 2p states were considered as valence states. For most of the calculations discussed in this chapter, we used both LDA and GGA methods to calculate the exchange-correlation energy functional. A plane-wave basis set with a cut-off of 60 Ry was used for all our calculations for all the titanate compounds, whereas a cut-off of 40 Ry was used for all the zirconate and hafnate materials. The special points sampling integration over

the Brillouin zone was performed using the Monkhorst-Pack method with a $4 \times 4 \times 4$ special k-points mesh[111].

4.3 Results and discussion

4.3.1 Elastic properties

Since pyrochlores belong to the cubic family, they have only three independent elastic constants, C_{11}, C_{12}, and C_{44}. The two elastic constants C_{11} and C_{12} determine the energy cost for an orthorhombic deformation of the structure and also the isotropic bulk modulus (calculated from the equation of state). In our calculations, the orthorhombic strain is imposed by modifying the cubic unit cell as:

$$\boldsymbol{D}_{ortho} = a_0 \begin{pmatrix} 1+\epsilon & 0 & 0 \\ 0 & 1-\epsilon & 0 \\ 0 & 0 & 1 \end{pmatrix} \tag{4.1}$$

The third elastic modulus C_{44} is calculated by applying a shear strain to the system, which in our case modifies the unit cell as

$$\boldsymbol{D}_{shear} = a_0 \begin{pmatrix} 1 & \epsilon & \epsilon \\ \epsilon & 1 & \epsilon \\ \epsilon & \epsilon & 1 \end{pmatrix} \tag{4.2}$$

Under shear deformation, the elastic energy is written as

$$E = E_0 + 6V_0C_{44}\epsilon^2 + O(\epsilon^4) \tag{4.3}$$

Whereas, under the orthorhombic deformation, the elastic energy of the system is calculated as

$$E = E_0 + 2V_0C'\epsilon^2 + O(\epsilon^4) \tag{4.4}$$

where E_0 is the total energy per unit cell of the system with no strain. The orthorhombic shear modulus is $C' = (C_{11} - C_{12})/2$. The bulk modulus is $B = (C_{11} + 2C_{12})/3$.

For both the deformations, a series of total energy calculations were performed for small but finite strain values ϵ up to a maximum of 0.02. The energy values as functions of the strain were then fitted to the 2^{nd} degree polynomials discussed above and the best fit values of the elastic constants C_{44} and C' were determined.

The elastic constants for cubic crystals must satisfy the mechanical stability criteria[153, 154] i.e.

$C_{11} > 0, C_{44} > 0, C_{11} - C_{12} > 0, C_{11} + 2C_{12} > 0$ and $C_{11} > B > C_{12}$. The degree of anisotropy in the elastic properties of solids can be quantified by the Zener anisotropy factor $A = 2C_{44}/(C_{11} - C_{12})$, which takes the value 1 for an isotropic material.

The bulk modulus and its pressure derivative are obtained by fitting our calculated pressure-volume data with the third-order Birch-Murnaghan equation of state[155], given as

$$P = \frac{3B_0}{2}\left[\left(\frac{V}{V_0}\right)^{-7/3} - \left(\frac{V}{V_0}\right)^{-5/3}\right]\left\{1 + \frac{3}{4}(B_0' - 4)\left[\left(\frac{V}{V_0}\right)^{-2/3} - 1\right]\right\} \tag{4.5}$$

where V is the cell volume, V_0 is the zero pressure cell volume, B_0 is the bulk modulus, and B_0' is the pressure derivative of the bulk modulus. The bulk modulus B is then calculated as $B = B_0 = (C_{11} + 2C_{12})/3$.

The calculated elastic constants of titanate, zirconate, and hafnate pyrochlores are listed in Tables. 4.1, 4.2, and 4.3, respectively. It is worth noting that our calculated elastic constants satisfy the mechanical stability criteria for cubic crystals mentioned above ($C_{11} > 0, C_{44} > 0, C_{11} > C_{12}$, and $C_{11} + 2C_{12} > 0$)[156].

Table 4.1: Calculated elastic constants, Zener anisotropy factor, bulk, shear, and Young's moduli, Poisson's and Pugh's ratio of the rare-earth $RE_2Ti_2O_7$ pyrochlores, along with the available experimental data.

	C_{11}	C_{12}	C_{44}	B	A	G	E	ν	B/G
$Sm_2Ti_2O_7$									
LDA	361	140	114	214	1.0298	113	287	0.2762	1.9008
GGA	324	116	97	185	0.9324	100	254	0.2714	1.8548
$Gd_2Ti_2O_7$									
LDA	374	138	114	217	0.9667	116	294	0.2738	1.8774
GGA	331	115	97	187	0.8963	101	257	0.2706	1.8467
$Tb_2Ti_2O_7$									
LDA	381	140	117	220	0.9664	118	301	0.2719	1.8583
GGA	337	115	97	189	0.8684	102	260	0.2706	1.8461
Expt.[157]	347	133	96	204					
$Dy_2Ti_2O_7$									
LDA	383	137	112	221	0.9144	116	297	0.2762	1.9006
GGA	348	117	96	194	0.8285	103	263	0.2738	1.8766
Expt.[157]	346	122	97	197					
$Ho_2Ti_2O_7$									
LDA	390	138	113	222	0.9144	118	301	0.2742	1.8808
GGA	346	113	97	191	0.8226	104	265	0.2689	1.8299
Expt.[157]	355	123	98	200					
$Er_2Ti_2O_7$									
LDA	395	137	112	223	0.8697	119	302	0.2743	1.8816
GGA	349	114	95	192	0.8076	104	263	0.2717	1.8562
$Yb_2Ti_2O_7$									
LDA	403	136	110	225	0.8252	119	303	0.2754	1.8929
GGA	357	111	93	193	0.7588	104	265	0.2715	1.8553
Expt.[157]	318	113	82	181					
$Lu_2Ti_2O_7$									
LDA	408	135	109	226	0.8012	119	304	0.2756	1.8948
GGA	361	111	92	194	0.7403	104	265	0.2725	1.8648

Table 4.2: Calculated elastic constants, Zener anisotropy factor, bulk, shear, and Young's moduli, Poisson's and Pugh's ratio in the rare-earth $RE_2Zr_2O_7$ pyrochlores, along with the available literature data. Theory A, B, and C show results for other first-principles simulations.

	C_{11}	C_{12}	C_{44}	B	A	G	E	ν	B/G
$Sm_2Zr_2O_7$									
LDA	330	127	99	195	0.9790	100	256	0.2810	1.9502
GGA	289	100	87	163	0.9166	90	228	0.2670	1.8126
Theory A[158]	328	132	101	197		100	252	0.287	1.98
Theory B[159]	286	107	88	167		89	226	0.274	1.88
$Gd_2Zr_2O_7$									
LDA	336	124	98	195	0.9231	101	259	0.2789	1.9283
GGA	296	97	86	163	0.8599	91	231	0.2643	1.7879
Theory A[158]	277	110	52	165		63	214	0.284	2.62
Theory B[159]	289	103	85	165		88	224	0.273	1.87
Theory C[160]	314	113	106	180					
$Tb_2Zr_2O_7$									
LDA	342	124	97	197	0.8851	102	260	0.2799	1.9383
GGA	297	96	85	163	0.8410	91	230	0.2649	1.7933
$Dy_2Zr_2O_7$									
LDA	347	123	96	198	0.8583	102	261	0.2800	1.9391
GGA	301	96	83	164	0.8125	90	229	0.2673	1.8158
$Ho_2Zr_2O_7$									
LDA	349	124	95	199	0.8406	102	261	0.2818	1.9577
GGA	304	94	83	164	0.7887	91	231	0.2654	1.7983
$Er_2Zr_2O_7$									
LDA	351	124	94	200	0.8252	101	260	0.2832	1.9730
GGA	305	95	82	165	0.7757	91	230	0.2681	1.8225
$Yb_2Zr_2O_7$									
LDA	359	121	91	200	0.7667	101	260	0.2833	1.9738
GGA	313	94	80	167	0.7280	91	230	0.2700	1.8406
$Lu_2Zr_2O_7$									
LDA	362	121	90	201	0.7458	101	260	0.2845	1.9868
GGA	314	92	78	166	0.7049	90	228	0.2707	1.8472

Table 4.3: Calculated elastic constants, Zener anisotropy factor, bulk, shear, and Young's moduli, Poisson's and Pugh's ratio in the rare-earth $RE_2Hf_2O_7$ pyrochlores, along with the available literature data. Theory A shows results for other first-principles simulations.

	C_{11}	C_{12}	C_{44}	B	A	G	E	ν	B/G
$Sm_2Hf_2O_7$									
LDA	352	133	111	206	1.0187	110	281	0.2726	1.8660
GGA	307	103	98	171	0.9579	100	250	0.2562	1.7172
$Gd_2Hf_2O_7$									
LDA	360	131	110	207	0.9621	112	284	0.2712	1.8519
GGA	317	102	97	174	0.9009	101	254	0.2567	1.7216
Theory A[159]	301	105	94	170		96	242	0.264	1.78
$Tb_2Hf_2O_7$									
LDA	364	130	110	208	0.9412	113	286	0.2704	1.8448
GGA	319	103	96	175	0.8869	101	253	0.2587	1.7390
$Dy_2Hf_2O_7$									
LDA	368	129	109	209	0.9148	113	287	0.2708	1.8482
GGA	323	101	95	175	0.8616	101	254	0.2578	1.7309
$Ho_2Hf_2O_7$									
LDA	371	128	108	209	0.8866	113	288	0.2706	1.8461
GGA	324	100	94	175	0.8422	101	254	0.2583	1.7356
$Er_2Hf_2O_7$									
LDA	375	127	107	210	0.8643	114	289	0.2710	1.8502
GGA	331	99	94	176	0.8074	102	257	0.2566	1.7211
$Yb_2Hf_2O_7$									
LDA	381	125	105	210	0.8188	114	289	0.2707	1.8475
GGA	336	98	91	177	0.7670	101	255	0.2596	1.7468
$Lu_2Hf_2O_7$									
LDA	386	126	104	213	0.7968	114	290	0.2734	1.8730
GGA	338	97	90	177	0.7446	101	255	0.2599	1.7495

The calculated elastic constants of $RE_2B_2O_7$ pyrochlores as a function of rare-earth ionic radii are shown in Fig. 4.1 (both the LDA and GGA values are shown for comparison). With fixed "RE" site elements, the elastic constants C_{11}, C_{12}, and C_{44} decrease with increasing B ionic radius, i.e. from Ti to Zr. This reflects the fact that these elastic moduli are directly related to the B-O bond strength, which decreases from Ti to Zr. However, with fixed "B" site element, C_{11} decreases from Lu to Sm with increasing rare-earth ionic radius, whereas the shear modulus C_{44} increases slightly with increasing rare-earth ionic radius. Hence, it is clear that C_{11} is also directly related to the RE-O bond strength, agreeing with the prediction by Liu et al.[151], whereas C_{44} does not show a close relationship with the RE-O bond strength. The shear modulus C_{44} is related to the distortion of the soft RE-O polyhedra and the rotation of the rigid B-O octahedra[151]. The rotation of the B-O octahedra may depend (perhaps slightly) on the size of the RE site element, and this could be the reason why C_{44} slightly increases by changing the RE site element. The LDA values of the elastic constants are larger than the GGA ones, as expected from the density functional calculations since the LDA overestimates the binding strengths in the system.

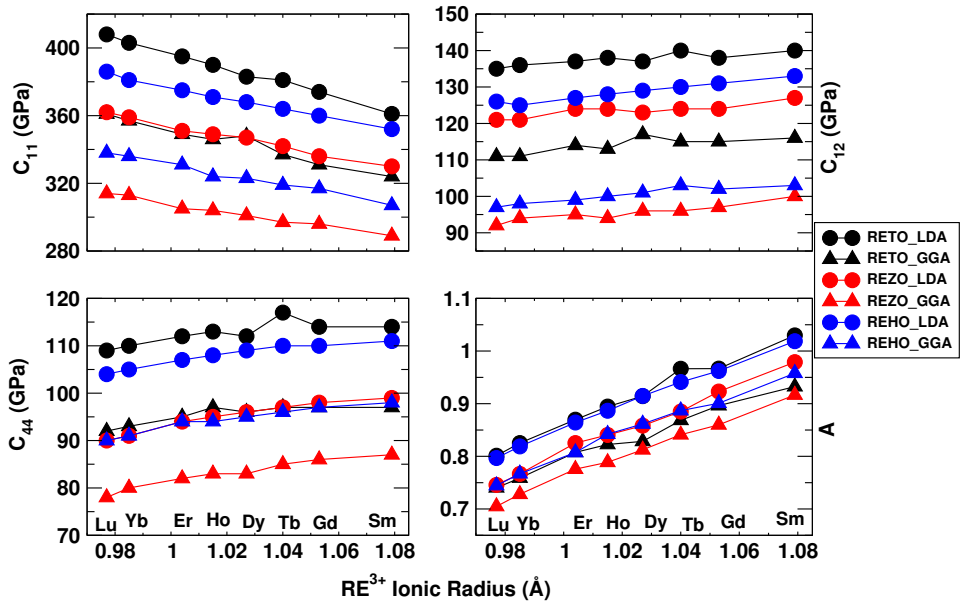

Figure 4.1: Variation of the elastic constants in the rare-earth $RE_2B_2O_7$ (RE = Sm, Gd, Tb, Dy, Ho, Er, Yb, Lu, and B = Ti, Zr, Hf) pyrochlores as a function of RE^{3+} ionic radius. Both LDA and GGA results are compared.

4.3.2 Mechanical properties

For polycrystalline samples, it is hard to estimate the individual elastic constants C_{ij}, but one can obtain the polycrystalline bulk and shear moduli. Mechanical properties of polycrystalline structures including the bulk modulus B, shear modulus G, and Young's modulus E are relevant quantities to characterize the mechanical properties of a material. The bulk modulus relates the resistance of a material to the volume change and provides an evaluation of its elastic response to hydrostatic pressure. Shear modulus denotes the shape change resistance of materials, while Young's modulus characterizes the resistance against the uniaxial tensions or compressions. We have used the Voigt-Reuss-Hill approximation[161–163] to calculate the polycrystalline elastic moduli. For the cubic systems, the Reuss and Voigt bounds on the shear modulus are given by:

$$\begin{aligned} G_R &= \frac{5C_{44}(C_{11}-C_{12})}{4C_{44}+3(C_{11}-C_{12})} \\ G_V &= \frac{C_{11}-C_{12}+3C_{44}}{5} \end{aligned} \tag{4.6}$$

Finally, the Voigt-Reuss-Hill (VRH) mean value is obtained by

$$G = \frac{1}{2}(G_V + G_R) \tag{4.7}$$

We also calculate Young's modulus E and the Poisson's ratio ν, which are evaluated for the polycrystals when studying the hardness of materials. These quantities are related to the shear and bulk modulus by the following equations[164]

$$\begin{aligned} E &= \frac{9BG}{3B+G} \\ \nu &= \frac{3B-E}{6B} \end{aligned} \tag{4.8}$$

Tables. 4.1, 4.2, and 4.3 also summarize the calculated bulk, Young's, and shear moduli for titanate, zirconate, and hafnate pyrochlores, respectively. All the moduli depend on the ionic sizes and the trend of modulus variation is inversely proportional to the ionic radii of both A and B cations. The moduli change vs B cations is in the order of $RE_2Ti_2O_7$ > $RE_2Hf_2O_7$ > $RE_2Zr_2O_7$. For $RE_2Ti_2O_7$, their moduli are in the range of 287-304 (254-265) GPa for E, 214-226 (185-194) GPa for B, and 113-119 (100-104) GPa for G in LDA (GGA) calculations. In the case of $RE_2Hf_2O_7$, the moduli are in the range of 281-290 (250-257) GPa for E, 206-213 (171-177) GPa for B, and 110-114 (100-102) GPa for G in LDA (GGA) calculations. Finally, in the case of $RE_2Zr_2O_7$, the moduli are in the range of 256-260 (228-231) GPa for E, 195-201 (163-167) GPa for B, and 100-102 (90-91) for G in LDA (GGA) calculations.

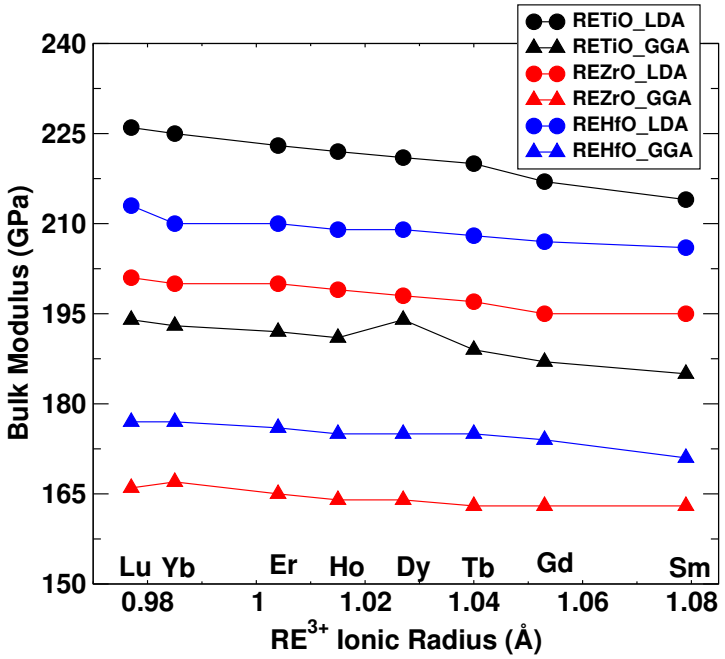

Figure 4.2: Variation of the bulk modulus in the rare-earth $RE_2B_2O_7$ (RE = Sm, Gd, Tb, Dy, Ho, Er, Yb, Lu, and B = Ti, Zr, Hf) pyrochlores as a function of RE^{3+} ionic radius. Both LDA and GGA results are compared.

The bulk modulus for titanates, zirconates, and hafnates as a function of both "RE^{3+}" and "B" ionic radii are shown in Fig. 4.2. Both the LDA and GGA results are compared. It can be seen from our

theoretical data that the bulk modulus decreases by changing the B site element from Ti to Zr, whereas it changes slightly by changing the rare-earth ionic size from Lu to Sm. This behaviour is similar to the trend obtained for the elastic constants of the corresponding compounds, which can be understood by considering the bonding nature and properties of B atoms as described earlier. The LDA values are larger than the GGA ones.

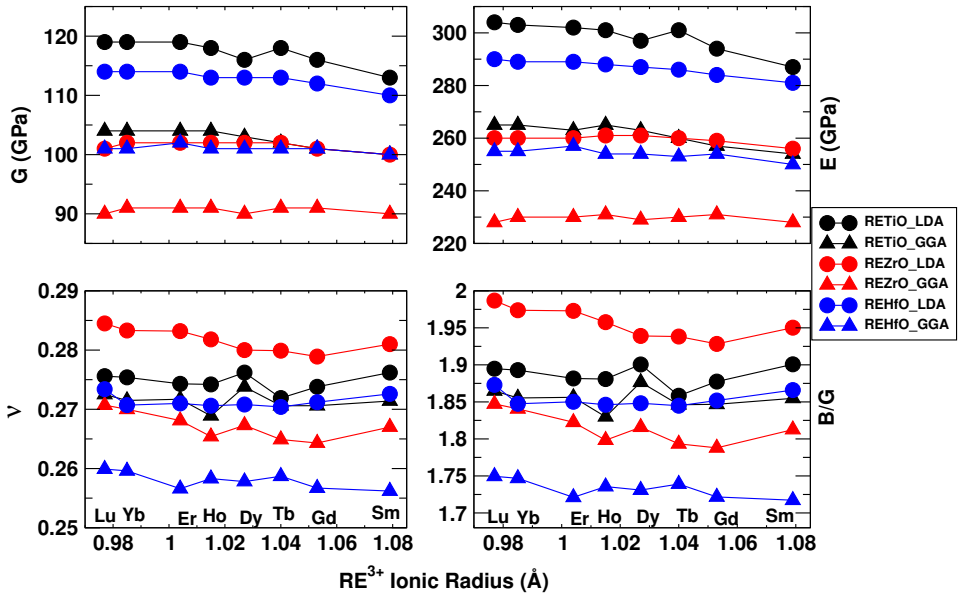

Figure 4.3: Variation of the shear and Young's moduli, Poisson's and B/G ratios in the rare-earth $RE_2B_2O_7$ (RE = Sm, Gd, Tb, Dy, Ho, Er, Yb, Lu, and B = Ti, Zr, Hf) pyrochlores as a function of RE^{3+} ionic radius. Both the LDA and GGA results are compared.

The variation of the shear and Young's moduli as a function of both "RE^{3+}" and "B" ionic radii are shown in Fig. 4.3. Both the LDA and GGA results are compared. The trends in these two moduli are similar to the trend discussed for the bulk modulus, i.e. both G and E decrease from Ti - Zr but change slightly with the change of the "RE^{3+}" ionic radii.

The RE and B site element dependence of the Poisson's and the Pugh's[165] ratios are shown in Tables. 4.1, 4.2, and 4.3 for titanates, zirconates, and hafnates, respectively. The results are compared with the available literature data whenever possible, and it can be seen that our theoretical results are in reasonably good agreement with the available data. Both the LDA and GGA results are displayed in the tables. The variation of the Poisson's and Pugh's ratios as a function of both the "RE^{3+}" and "B" ionic radii is also shown in Fig. 4.3. Generally speaking, a small Poisson's ratio indicates that the material is the covalent compound, whereas the large value of it (0.25 and above) means that the material is the ionic in nature[166]. Here, all the calculated values are > 0.25, indicating the ionic character of the pyrochlores under study.

The Pugh's ratio, defined as B/G, is a reference of damage tolerance of ceramics since it roughly

reflects the ability to resist shear deformation. It is widely accepted that a material with a low B/G value tends to brittle, while a material with a high value is ductile and has a better tolerance to shear deformation. The cut-off value is 1.75. Here, all the studied pyrochlores are ductile because of their high B/G values.

4.3.3 Thermal properties

The elastic properties of materials are directly associated with their thermodynamic properties. One of them is the Debye temperature of a material, which is related directly to the thermal vibrations of atoms. It corresponds in the Debye theory to the highest phonon frequency. At low temperatures, the Debye temperature calculated from the elastic moduli is the same as that obtained from the specific heat measurements. A relationship between the Debye temperature Θ_D and the mean sound velocity[107, 153, 167] is written as

$$\Theta_D = \frac{h}{k_B}\left[\frac{3n}{4\pi}\left(\frac{N_A\rho}{M}\right)\right]^{1/3} v_m \tag{4.9}$$

where h is the Plank's constants, k_B the Boltzman's constant, N_A the Avogadro's number, ρ crystal's density, M the molecular weight, and n corresponds to the number of atoms in the unit cell. The mean sound velocity v_m is obtained as[167]

$$\frac{1}{v_m^3} = \frac{1}{3}\left(\frac{1}{v_l^3} + \frac{2}{v_t^3}\right) \tag{4.10}$$

where v_l and v_t are the longitudinal and transverse sound velocities of an isotropic system and are obtained using the shear and bulk modulus from Navier's equations[164].

$$v_l = \sqrt{\frac{3B + 4G}{3\rho}} \tag{4.11}$$

$$v_t = \sqrt{\frac{G}{\rho}} \tag{4.12}$$

Table 4.4: Calculated crystal density, sound velocities, Debye temperature, and the minimum thermal conductivity in the rare-earth $RE_2Ti_2O_7$ pyrochlores, along with the available experimental data.

	ρ (g cm^{-3})	v_l (m s^{-1})	v_t (m s^{-1})	v_m (m s^{-1})	Θ_D (K)	$\kappa_{min}(Wm^{-1}K^{-1})$
$Sm_2Ti_2O_7$						
LDA	6.64	7406	4118	4586	604	1.55
GGA	6.26	7130	3993	4444	574	1.44
Expt.	6.36[108]					
$Gd_2Ti_2O_7$						
LDA	7.00	7296	4072	4534	601	1.55
GGA	6.56	7007	3929	4373	568	1.43
Expt.	6.57[108]					
$Tb_2Ti_2O_7$						
LDA	7.08	7304	4088	4551	606	1.56
GGA	6.66	6990	3920	4363	569	1.44
Expt.	6.66[108]					
$Dy_2Ti_2O_7$						
LDA	7.25	7204	4006	4461	595	1.55
GGA	6.81	6979	3896	4337	567	1.44
Expt.	6.82[108]					
$Ho_2Ti_2O_7$						
LDA	7.38	7172	4000	4454	596	1.55
GGA	6.93	6903	3881	4319	566	1.44
Expt.	6.93[108]					
$Er_2Ti_2O_7$						
LDA	7.49	7131	3977	4428	594	1.55
GGA	7.04	6848	3834	4268	561	1.43
Expt.	7.04[108]					
$Yb_2Ti_2O_7$						
LDA	7.79	7018	3907	4351	587	1.54
GGA	7.30	6739	3774	4201	555	1.42
Expt.	7.29[108]					
$Lu_2Ti_2O_7$						
LDA	7.90	6979	3885	4326	585	1.54
GGA	7.41	6700	3746	4170	552	1.42
Expt.	7.37[108]					

Table 4.5: Calculated crystal density, sound velocities, Debye temperature, and the minimum thermal conductivity in the rare-earth $RE_2Zr_2O_7$ pyrochlores, along with the available literature data. Theory A shows results for other first-principles simulations.

	ρ (g cm^{-3})	v_l (m s^{-1})	v_t (m s^{-1})	v_m (m s^{-1})	Θ_D (K)	$\kappa_{min}(Wm^{-1}K^{-1})$
$Sm_2Zr_2O_7$						
LDA	6.97	6862	3787	4220	536	1.32
GGA	6.57	6562	3699	4115	512	1.24
Theory A[158]		7050	3871	4316	538	
Exp.[168]						1.5
$Gd_2Zr_2O_7$						
LDA	7.28	6731	3727	4152	531	1.32
GGA	6.85	6445	3648	4057	508	1.23
Theory A[158]		5985	3009	3374	424	
Exp.[168]						1.6
$Tb_2Zr_2O_7$						
LDA	7.39	6708	3708	4132	530	1.32
GGA	6.95	6395	3617	4023	505	1.23
$Dy_2Zr_2O_7$						
LDA	7.54	6656	3680	4100	527	1.32
GGA	7.09	6336	3570	3972	500	1.22
$Ho_2Zr_2O_7$						
LDA	7.66	6607	3642	4059	524	1.31
GGA	7.20	6300	3560	3959	500	1.22
$Er_2Zr_2O_7$						
LDA	7.77	6566	3611	4025	520	1.31
GGA	7.30	6258	3523	3919	496	1.22
$Yb_2Zr_2O_7$						
LDA	8.05	6452	3548	3955	514	1.30
GGA	7.55	6177	3467	3858	491	1.21
$Lu_2Zr_2O_7$						
LDA	8.16	6418	3522	3926	512	1.30
GGA	7.65	6114	3428	3815	487	1.20

Table 4.6: Calculated crystal density, sound velocities, Debye temperature, and the minimum thermal conductivity in the rare-earth $RE_2Hf_2O_7$ pyrochlores.

	ρ (g cm^{-3})	v_l (m s^{-1})	v_t (m s^{-1})	v_m (m s^{-1})	Θ_D (K)	$\kappa_{min}(Wm^{-1}K^{-1})$
$Sm_2Hf_2O_7$						
LDA	9.29	6165	3447	3837	492	1.23
GGA	8.74	5897	3376	3751	471	1.15
$Gd_2Hf_2O_7$						
LDA	9.65	6073	3403	3787	489	1.23
GGA	9.07	5834	3339	3709	469	1.15
$Tb_2Hf_2O_7$						
LDA	9.78	6052	3395	3778	489	1.23
GGA	9.18	5802	3310	3679	467	1.14
$Dy_2Hf_2O_7$						
LDA	9.96	6010	3370	3750	487	1.23
GGA	9.34	5758	3290	3655	465	1.14
$Ho_2Hf_2O_7$						
LDA	10.10	5969	3348	3726	485	1.23
GGA	9.47	5716	3263	3626	462	1.14
$Er_2Hf_2O_7$						
LDA	10.23	5943	3331	3707	484	1.23
GGA	9.59	5708	3266	3629	464	1.15
$Yb_2Hf_2O_7$						
LDA	10.55	5854	3283	3653	480	1.22
GGA	9.88	5621	3203	3560	457	1.14
$Lu_2Hf_2O_7$						
LDA	10.68	5843	3263	3633	478	1.22
GGA	9.99	5587	3182	3537	455	1.13

4.3.4 Minimum thermal conductivity

As discussed earlier the thermal properties of pyrochlore oxides are quite interesting to study as these materials are used as TBCs. Thermal conductivity is the ability of a material to conduct heat. In crystalline materials, heat is carried in two ways: electronic conduction and phonon (lattice vibration) conduction. Since the pyrochlore titanates are insulating in nature, the electronic heat conduction is almost negligible compared to the phonon conduction. At sufficiently high temperatures, the crystal structure becomes fully populated with phonons, and phonon-phonon interactions cause the phonon mean free path to be as short as possible[169]. In this temperature range, the heat capacity and speed of sound are almost independent of temperature and thus the thermal conductivity shows a high-temperature minimum κ_{min}. The value of κ_{min} has been modelled in two different methods[169, 170], but here in this study, we have used the method as suggested by Clarke[169].

According to the Clarke model, the minimum thermal conductivity is given as

$$\kappa_{min} = k_B v_m \Lambda_{min} \rightarrow 0.87 k_B \Omega_a^{-2/3} \left(E/\rho\right)^{1/2} \tag{4.13}$$

where Λ_{min} is the minimum phonon mean free path, $\Omega_a = (M/n\rho N_A)$ is the average volume per atom, E is the elastic modulus, and ρ is the density. The different atoms in a molecule are replaced with an equivalent atom having a mean atomic mass given by M/n, where M is the molecular mass and n is the number of atoms per molecule.

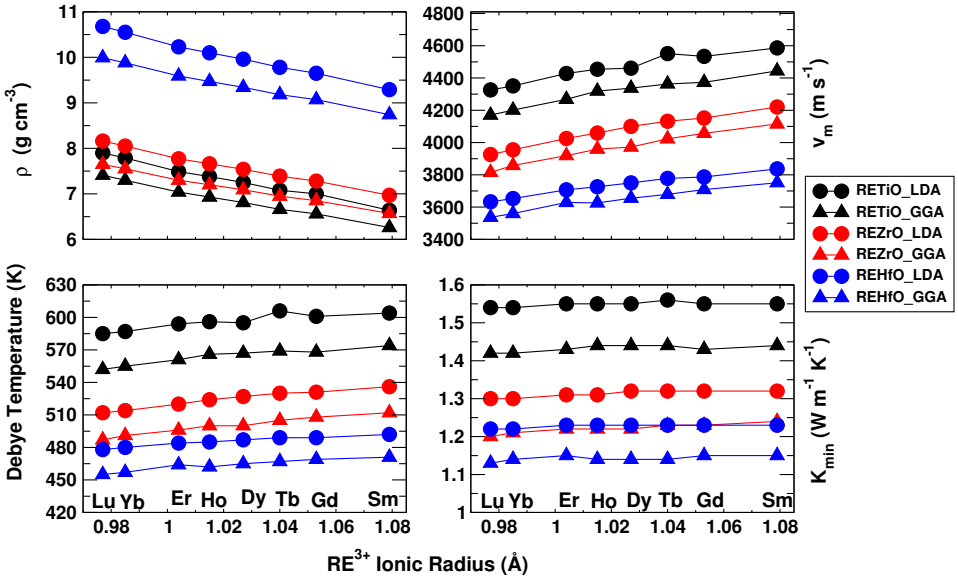

Figure 4.4: Variation of the crystal density, mean sound velocity, Debye temperature, and the minimum thermal conductivity in the rare-earth $RE_2B_2O_7$ (RE = Sm, Gd, Tb, Dy, Ho, Er, Yb, Lu, and B = Ti, Zr, Hf) pyrochlores as a function of RE^{3+} ionic radii. Both the LDA and GGA results are compared.

It is well known that Young's modulus has a close connection with the high-temperature thermal conductivity[171]. A lower Young's modulus can help to decrease the thermal conductivity and suggests promising TBC.

The LDA and GGA values of the crystal density, longitudinal, transverse, and mean sound velocities, Debye temperature, and the minimum thermal conductivity in titantes, zirconates, and hafnates are shown in Tables. 4.4, 4.5, and 4.6, respectively. Our calculated results are compared with the literature data whenever possible. There is not enough data available in the literature to compare with our theoretical data. In $RE_2Ti_2O_7$, the calculated physical quantities lie in the range of 6.64 - 7.90 (6.26 - 7.41) g cm^{-3} for ρ, 6979 - 7406 (6700 - 7130) m/s for v_l, 3885 - 4118 (3746 - 3993) m/s for v_t, 4326 - 4586 (4170 - 4444) m/s for v_m, 585 - 606 (552 - 574) K for Θ_D, and 1.54 - 1.56 (1.42 - 1.44) $Wm^{-1}K^{-1}$ for κ_{min} in LDA (GGA) methods. In the case of $RE_2Zr_2O_7$, the calculated physical quantities lie in the range of 6.97 - 8.16 (6.57 - 7.65) g cm^{-3} for ρ, 6418 - 6862 (6114 - 6562) m/s for v_l, 3522 - 3787 (3428 - 3699) m/s for v_t, 3929 - 4220 (3815 - 4115) m/s for v_m, 512 - 536 (487 - 512) K for Θ_D, and 1.30 - 1.32 (1.20 - 1.24) $Wm^{-1}K^{-1}$ for κ_{min} in LDA (GGA) methods. Finally, in the case of $RE_2Hf_2O_7$, the calculated physical quantities lie in the range of 9.29 - 10.68 (8.74 - 9.99) g cm^{-3} for ρ, 5843 - 6165

(5587 - 5897) m/s for v_l, 3263 - 3447 (3182 - 3376) m/s for v_t, 3633 - 3837 (3537 - 3751) m/s for v_m, 478 - 492 (455 - 471) K for Θ_D, and 1.22 - 1.23 (1.13 - 1.15) $Wm^{-1}K^{-1}$ for κ_{min} in LDA (GGA) methods.

The variation of the crystal density, the mean sound velocity, the Debye temperature, and the minimum thermal conductivity as a function of both the "RE^{3+}" and "B^{4+}" ionic radii is shown in Fig. 4.4. For a fixed RE site element, the crystal density increases in the order Ti, Zr, Hf, whereas for a fixed B site element, it increases from Sm to Lu. The trend is the same in both the LDA and GGA methods. These results are consistent with the fact that the crystal density is directly proportional to the total mass of the crystal. For a fixed RE site element, the mean sound velocity decreases in the order Ti, Zr, Hf, which is also the order in which their mass increases, whereas for a fixed B element, it decreases from Sm-Lu in increasing order of mass. For a fixed RE site element, the Debye temperature and the minimum thermal conductivity decrease from Ti, Zr, to Hf, while they remain almost invariant by changing the RE site element but by fixing the B site element. The trends in LDA and GGA are similar in all the calculations. It is clear from our theoretical calculations that the sound velocities, the Debye temperature, and the minimum thermal conductivity are dependent on the ionic mass in the crystal, especially the sound velocities. The values of the Debye temperature and the minimum thermal conductivity are largely dependent on the B site element rather than on the RE site element, i.e. their values decrease in the order Ti, Zr, Hf, while these quantities vary slightly from Lu-Sm.

4.4 Conclusions

In summary, in this chapter we presented results from DFT calculations of the elastic, mechanical, and thermal properties in the rare-earth $RE_2B_2O_7$ (RE = Sm, Gd, Tb, Dy, Ho, Er, Yb, and Lu; B = Ti, Zr, and Hf) pyrochlores using both the LDA and GGA methods.

From our calculations, it is clear that the elastic moduli satisfy the mechanical stability criteria for the cubic crystals. With the fixed RE site elements, the elastic moduli C_{11}, C_{12}, and C_{44} decrease with increasing the B ionic radii, i.e. B = Ti, Hf, Zr. However, with the fixed B site element, the elastic constant C_{11} decreases with increasing the rare-earth ionic radii, whereas, the elastic constant C_{44} varies slowly. The elastic constant C_{11} is directly related to the bond strengths. With increasing the RE and/or B ionic radii, the lengths of RE-O and B-O bonds increase, making the average bond strength weak. Therefore, the C_{11} decreases accordingly. In contrast, the shear modulus C_{44} is associated with the distortion of the soft RE-O polyhedra and the rotation of the rigid B-O octahedra, and thus C_{44} does not show a close relationship with the RE and/or B cation size.

The bulk, shear, and Young's moduli are highly dependent on the B site elements, while they are almost independent of the RE site elements, i.e. their values decrease in the order Ti, Hf, Zr but vary only slightly from Lu-Sm. Our calculated values of the Poisson's ratio is greater than 0.25 in all the

compounds studied, indicating that the materials are ionic crystals. The Pugh's ratio is calculated to be larger than 1.75 in almost all the cases (except for the $RE_2Hf_2O_7$ calculated using the GGA method, where its value is found to be around 1.75, which could be well within the limitations of the DFT calculations), suggesting that the materials under study are ductile, i.e. they have a high tolerance towards the shear deformations.

From our theoretical calculations, we find that the sound velocities, the Debye temperature, and the minimum thermal conductivity are dependent on the ionic mass in the crystal, especially the sound velocities. The Debye temperature and the minimum thermal conductivity are largely dependent on the B site element rather than on the RE site element, i.e. their values decrease in the order Ti, Zr, Hf, while these quantities vary only slightly from Lu-Sm.

Chapter 5

High pressure study of structural, mechanical, elastic, and vibrational properties in $Dy_2Ti_2O_7$ pyrochlore

In this chapter, we present our first-principles DFT studies of the structural, elastic, and vibrational properties in $Dy_2Ti_2O_7$ pyrochlore under the application of large hydrostatic pressures and compare our results with x-ray diffraction(XRD), Brillouin scattering, and Raman measurements.

5.1 Motivation

Several of the pyrochlores have been studied under pressure to understand their structural stability. Some of the previous works on pyrochlore materials have reported phase changes to a monoclinic[172–175], a defect fluorite[50, 113, 176, 177] or an amorphous structure[50, 113, 172, 174, 176, 177]. Kumar et al.[172] reported a pressure-induced phase change to a monoclinic phase and subsequently to an amorphous structure for $Tb_2Ti_2O_7$, $Tb_2Sn_2O_7$ and Tb_2TiSnO_7, and a similar transition sequence was observed in $Cd_2Nb_2O_7$ by Zhang et al.[174]. Zhang et al.[173] and Kumar et al.[175] both reported that upon the application of high pressures, the pyrochlore $Gd_2Zr_2O_7$ changes to a monoclinic structure. Pressure-induced disorder to a defect fluorite phase was found in $Y_2Ti_2O_7$ and $Gd_2Ti_2O_7$ by Zhang et al.[50], with $Gd_2Ti_2O_7$ becoming amorphous at higher pressures. Using ion radiation, Lian et al.[113, 177] observed a transition to a defect fluorite structure and amorphization in the entire $A_2Ti_2O_7$ (A = Sm to Lu, and Y) pyrochlore series. Ab initio calculations by Xiao et al.[176] claimed that under pressure the defect fluorite structure is energetically favourable followed by amorphization at higher pressures in $Y_2Ti_2O_7$.

Experimentally[178], using X-ray, Brillouin and Raman scattering measurements under high pressure in $Dy_2Ti_2O_7$ it is found that the cell-volume, internal structure parameter, elastic moduli, and frequencies of a few optical phonon modes show a slope change around 9 GPa of pressure. This change in the slopes of these physical quantities is related to an isostructural phase transition as the space group remains invariant across the pressure range. Our interest is to carry out first-principles DFT calculations to study the structural, elastic, and vibrational properties in $Dy_2Ti_2O_7$ under high pressure. It is worth mentioning that the pressures we study go only up to 30 GPa where no structural phase transition to defect fluorite or amorphous structures is expected. To the best of our knowledge, no such studies in $Dy_2Ti_2O_7$ have been carried out previously.

5.2 Theoretical details

Most of the computational details are same as used in the previous chapter. Here, all the calculations are done using only the LDA method. Kohn-Sham wave functions were represented using a plane-wave basis with an energy cutoff of 60 Ry. Dy 5s, 6s, 5p, 6p and 5d electrons, Ti 3s, 4s, 3p and 3d electrons and oxygen 2s and 2p electrons were considered as valence electrons. The 4f electrons of Dy atoms were taken into the core of the pseudopotential.

At each target pressure (hydrostatic), the structures were fully relaxed by allowing the relaxation of the cell parameters as well as of the atomic positions. In the optimized configurations, the forces on the atoms were smaller than 1 mRy/Bohr. The optimized cell volume at each hydrostatic pressure up to 30 GPa, was then fitted with the third-order Birch-Murnaghan equation of state (BM- EOS)[155] to obtain the bulk modulus and its pressure derivative. Density functional perturbation theory (DFPT) was used to investigate the vibrational properties at the zone centre of the BZ. The elastic constants C_{ij}, in the Voigt notation[91] were obtained by computing the energy for a small, volume conserving strains (2 % in our case), and fitting the results to quadratic forms, as in the previous chapter.

5.3 Results and discussion

The third order Birch-Murnaghan equation of state (BM-EOS), as mentioned in the previous chapter, is given by[155]:

$$P = \frac{3B_0}{2}\left[\left(\frac{V}{V_0}\right)^{-7/3} - \left(\frac{V}{V_0}\right)^{-5/3}\right]\left\{1 + \frac{3}{4}(B_0' - 4)\left[\left(\frac{V}{V_0}\right)^{-2/3} - 1\right]\right\} \tag{5.1}$$

where V is the cell volume, V_0 is the zero pressure cell volume, B_0 is the zero pressure bulk modulus, and B_0' is the pressure derivative of the bulk modulus. From the pressure dependence of the optical

phonon frequency (section 5.4), it is clear that a slope change of some of the phonon modes occurs at 8.5 GPa pressure, therefore, we fit BM-EOS with two different values for the parameter set (V_0, B_0, B_0') in the low and high pressure regions (Fig. 5.1). The best fits are obtained for $V_0 = 244.1425$ Å^3, $B_0 = 219$ GPa, $B_0' = 4.2584$ below 8.5 GPa and $V_0 = 244.1123$ Å^3, $B_0 = 221$ GPa, $B_0' = 4.1367$ above 8.5 GPa. The slope change in the cell volume is rather small and not visually obvious in Fig. 5.1 but the phase transition is more clearly reflected in a slope change of the fractional coordinate of oxygen 48f (see inset of Fig. 5.1) versus pressure, around the same transition pressure of 8.5 GPa. The calculated results are consistent with the experimental ones presented earlier, where also the slope changes in the cell volume and the fractional coordinate of oxygen O_{48f} were observed, around 9 GPa pressure. The slope change in the x_{O48f} is associated with an isostructural phase transition as experimentally it has been found that no change in the space group symmetry occurs in this pressure range.

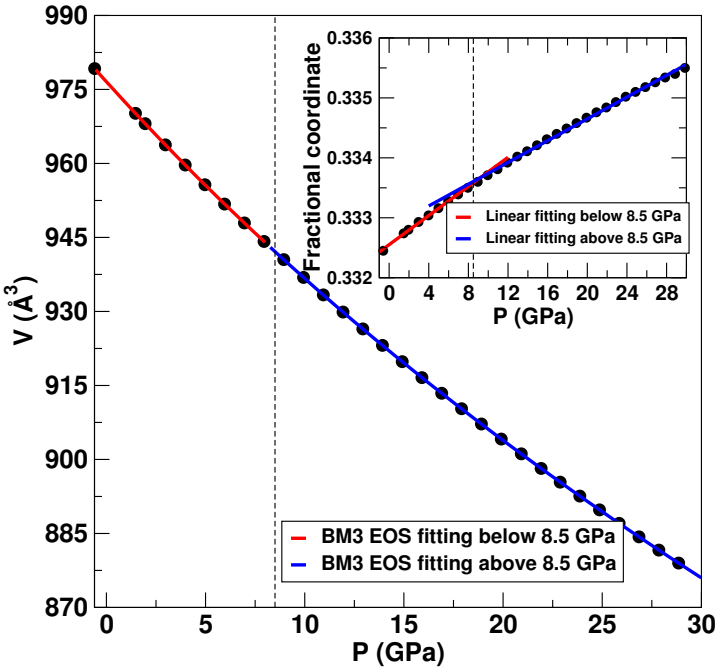

Figure 5.1: (Color online) The calculated volume of the unit cell as a function of pressure. The black solid circle symbols represent the calculated data while the blue and red solid lines are obtained from fitting the data to the BM EOS with two different parameter sets in the low and high-pressure regions respectively; Inset: The variation of the fractional coordinate of the oxygen O_{48f} ions with pressure. The vertical dashed line is placed at the position where the phase transition occurs.

5.3.1 Elastic properties

The elastic constants of $Dy_2Ti_2O_7$ pyrochlore are calculated from the DFT following exactly the same procedure as described in detail in Chapter 4, section 4.3.1. It is important to ensure that the ionic positions are allowed to fully relax in the presence of the strained unit cell to obtain the correct

elastic constants[106]. In Table 5.1 we show the calculated results for the elastic constants and the anisotropy factor for the structures obtained after geometry relaxations. The geometry relaxation has a significant effect on the C_{44} which is softened by more than 20% when the ionic positions are optimized. Furthermore, it has a very important effect on the anisotropy factor as well, which changes from a value greater than 1 without geometry relaxation to a value less than 1 with the geometry optimization, well in accordance with the Resonant ultrasonic measurements (RUS) where also A is found to be less than 1 in $Dy_2Ti_2O_7$[157]. The elastic constants and the anisotropy factor obtained with geometry relaxations are in reasonable agreement with the experimental results.

Table 5.1: Calculated elastic constants (in GPa), and the anisotropy factor for $Dy_2Ti_2O_7$ pyrochlore.

	C_{11}	C_{12}	C_{44}	A
This work(LDA)	383	137	112	0.91
This work (Exp)	344	120	101	0.90
RUS	347	122	97	0.87

The pressure dependence of the elastic constants for the relaxed structures are shown in Fig. 5.2. A clear slope change in the shear modulus C_{44} and the anisotropy factor A can be seen around 8.5 GPa, agreeing with the experimental results of C_{44} and A.

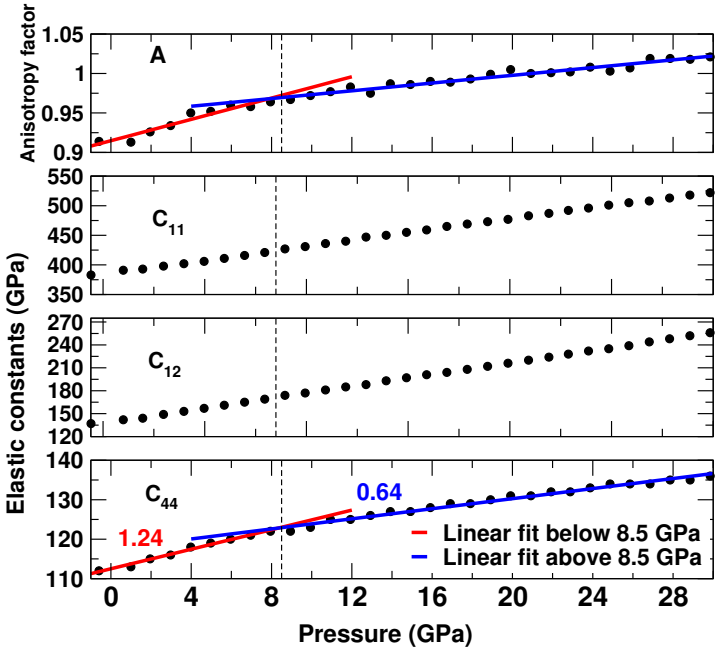

Figure 5.2: (Color online) Pressure dependence of the elastic constants for the structure resulting in internal atomic relaxation. A linear fit below and above 8.5 GPa shows a clear slope change in the shear modulus C_{44}. The dashed vertical line is placed at the location where the slope change occurs.

5.4 Pressure dependence of the Raman and IR active phonon modes

The pressure dependence of the calculated frequencies of three Raman and two infra-red active modes is shown in Fig. 5.3. All these modes, involving the oxygen O_{48f} vibrations, show slope changes (marked in the figure) around 8.5 GPa, in agreement with the high-pressure Raman measurements, where also the changes are observed around 9 GPa pressure. The frequencies of the zone centre Raman active modes for the optimized equilibrium structure are summarized in Table5.2 along with the available experimental results. The calculated frequencies are in fairly good agreement with the experimental ones.

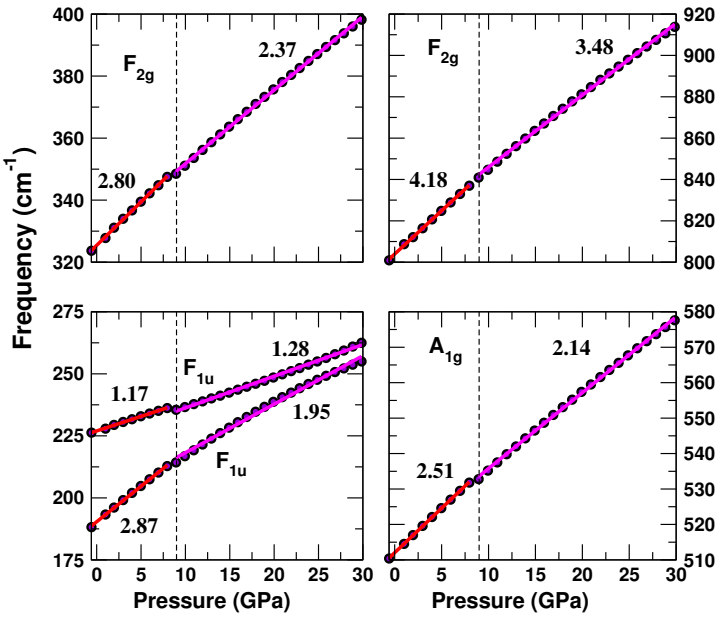

Figure 5.3: Pressure dependence of the phonon frequencies of $Dy_2Ti_2O_7$ calculated using DFPT. The change of slope (numbers shown, in cm^{-1}/GPa), at around 8.5 GPa, of some of the phonon modes is in accordance with the changes of slopes as measured by the Raman data as a function of pressure reported earlier in this paper. Vertical dashed lines are placed at the positions where the change in slope is observed.

Table 5.2: Comparison of our calculated Raman mode frequencies (cm^{-1}) (at zero pressure and temperature) with the experimental values at room temperature and pressure. A mode with Superscript a means that it is experimentally observed but not found in theory, while frequencies with superscript b are overtones in experiments.

Mode	This work LDA	Expt. Ref.[54]	Expt. Ref.[57]
F^a_{2g}	-	174	190
F_{2g}	324	312	311
E_g	343	330	329
F_{2g}	458	453	450
A_{1g}	510	515	513
F_{2g}	587	563	583
F_{2g}	801	800^b	-

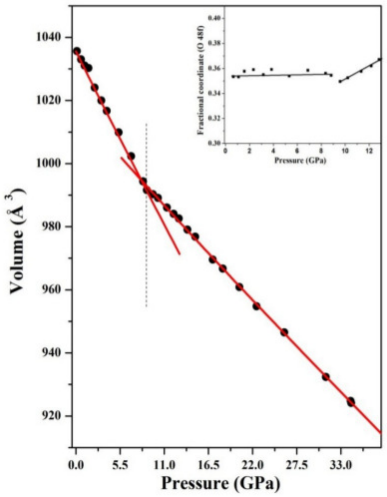

Figure 5.4: Experimental results for the cell volume as a function of pressure. Inset graph shows the pressure dependence of the fractional coordinate of oxygen 48f.

5.5 Conclusions

Our pressure-dependent calculations of the elastic moduli and the phonon frequencies in $Dy_2Ti_2O_7$ pyrochlore show a clear slope change as a function of pressure at around 8.5 GPa pressure. This change in slope is also seen in the internal coordinate and the cell volume at around the same pressure and corresponds to an isostructural phase transition as the space group remains invariant across the phase transition. Our theoretical results are consistent with the experimental results found in X-ray diffraction (XRD), Brillouin scattering and Raman scattering, where also clear slope changes in the cell volume, internal parameter, elastic constants and the Raman frequencies are observed at around 9 GPa pressure.

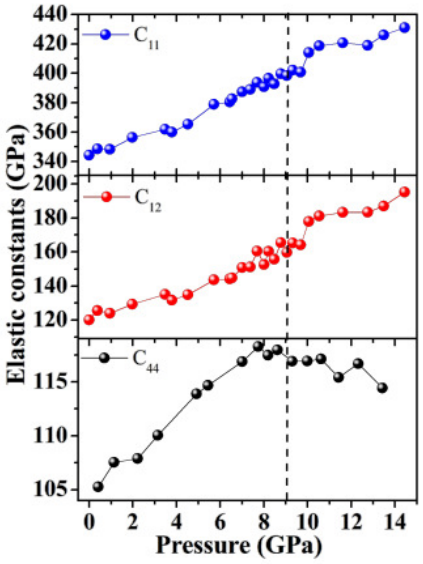

Figure 5.5: Experimental results for the elastic moduli as a function of pressure. A vertical line is marked at 9 GPa pressure where the slope change in the moduli occurs

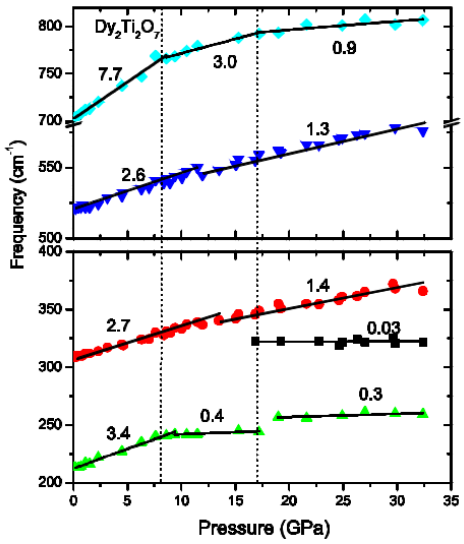

Figure 5.6: Experimental results for the phonon frequencies as a function of pressure. A vertical line is marked at 9 GPa pressure where the slope change in the moduli occurs.

Chapter 6

Electronic, elastic, thermal, and vibrational properties of $Y_2B_2O_7$ pyrochlores

In this chapter, we present results from our first-principles DFT calculations of the structural, electronic, elastic, mechanical, thermal, and vibrational properties in $Y_2B_2O_7$ (B = Ti, Zr, and Hf) pyrochlores. For most of the calculations, both the LDA and GGA methods are used for comparison.

6.1 Motivation

One of the extraordinary achievements of solid-state physics at current times is the first principles microscopic understanding of the vibrational properties of crystals. Density functional linear response theory has been quite successful in accounting for the harmonic-phonon properties in a vast variety of materials.

Though the yttrium based pyrochlore materials have been explored extensively by various groups[106–108, 176, 179, 180], their phonon properties have not been explored thoroughly using the first-principles DFT calculations. Srivastava et al.[107] performed ab initio studies of electronic, elastic, and thermal properties in $Y_2B_2O_7$ (B = Ti, Sn) within the GGA framework. Recently, structural and crystal-chemical properties in $Y_2Ti_2O_7$ were studied by Farmer et al.[108] using ab initio calculations within the GGA method. Kumar et al.[41] have carried out a first-principles study of the zone-centre phonons in $Y_2Ti_2O_7$ within the LDA scheme.

In this chapter, we present a comparative analysis of structural, electronic, elastic, mechanical, thermal, and vibrational properties in $Y_2B_2O_7$ (B = Ti, Zr, Hf) pyrochlores using DFT calculations

within both the LDA and GGA frameworks. To the best of our understanding, no such comparative study exists in the literature. We present extensive studies of the zone centre phonons as well as of the phonons across the Brillouin zone. We present the anomalous dynamical charges and the dynamical instabilities as found in our theoretical calculations. We present how these properties change by replacing the lighter Ti elements by the heavier elements like Zr or Hf.

6.2 Computational details

As in the previous chapters, our first-principles DFT calculations[83, 84] were implemented using the Quantum Espresso code[110], with ultrasoft pseudopotentials[152] to represent the interaction between ionic cores and valence electrons. Both the LDA and GGA methods were used for the exchange-correlation energy functional. A plane-wave basis set with an energy cut-off of 60 Ry was used for the titanate, whereas a cut-off of 40 Ry was used for the zirconate and hafnate to reduce computational costs, as it was found to be adequate for these materials. The k-points summation of the electronic energy calculations over the BZ was implemented by using the Monkhorst-Pack method with a $4 \times 4 \times 4$ special k-points mesh[111]. The DFPT was carried out to investigate the phonon properties. For the phonon dispersions, Dynamical matrices were calculated for a grid of $2 \times 2 \times 2$ $\boldsymbol{q}$-points. The lattice constants were optimized to minimize the total energy, interatomic forces, and unit-cell stresses. The Broyden-Fletcher-Goldfarb-Shanno (BFGS) minimization scheme[112] was used in geometry optimization.

6.3 Structural properties

Calculated values of the lattice constants and the the displacement parameter x in $Y_2B_2O_7$ (B = Ti, Zr, and Hf) pyrochlores are shown in Table. 6.1. Compared to the experimental values, the LDA lattice constants are smaller by a maximum of around 2%, whereas the GGA ones are slightly larger. This is in consistent with the well-known aspects of the density functional theory calculations, namely that LDA generally underestimates the lattice constant, whereas the GGA slightly overestimates it. The calculated values of the lattice constants using both the LDA and GGA lie in the order: $a^{Ti^{4+}} < a^{Hf^{4+}} < a^{Zr^{4+}}$, for all three pyrochlores, consistent with the fact that the ionic radius of Ti^{4+}, Hf^{4+}, and Zr^{4+} also lie in the same order, i.e. $r^{Ti^{4+}} < r^{Hf^{4+}} < r^{Zr^{4+}}$.

The Y^{3+} cations are bonded with oxygen ions O_{48f} and O_{8b}, whereas the transition metal cations are bonded with only oxygen O_{48f}. We have calculated the various bond distances (see Table. 6.1). As can be seen, our theoretical values of the bond distances and angles are quite close to the available literature data.

Table 6.1: Calculated lattice parameters for $Y_2B_2O_7$ (B = Ti, Zr, and Hf) pyrochlores, along with the available theoretical and experimental data. Theory A and B show results for other first-principles simulations.

	a	x	$d_{Y-O_{8b}}$	$d_{Y-O_{48f}}$	$d_{B-O_{48f}}$	$B\hat{O}B$
$Y_2Ti_2O_7$						
LDA (This work)	9.9672	0.3310	2.16	2.44	1.94	130.8
GGA (This work)	10.1567	0.3298	2.20	2.49	1.97	131.4
Expt.(Ref.[113])	10.100	0.3300	2.18	2.46	1.96	131.3
Theory A[106]	9.974	0.3321	2.16	2.43	1.94	130.2
Theory B[148]	10.049	0.329				
$Y_2Zr_2O_7$						
LDA (This work)	10.2831	0.3425	2.23	2.44	2.06	124.7
GGA (This work)	10.4724	0.3410	2.27	2.49	2.08	125.5
Theory A[106]	10.335	0.3417	2.24	2.45	2.06	125.1
Theory B[148]	10.463	0.342	2.26	2.48	2.08	125.0
$Y_2Hf_2O_7$						
LDA (This work)	10.2425	0.3382	2.22	2.45	2.02	127.0
GGA (This work)	10.4474	0.3367	2.26	2.51	2.06	127.7
Theory A[106]	10.300	0.3399	2.23	2.46	2.04	126.1

6.4 Elastic, mechanical, and thermal properties

Following the same approach as discussed in Chapter 4 we have calculated the elastic, mechanical, and thermal properties of $Y_2B_2O_7$ pyrochlores. Here also we have given two volume conserving, namely the orthorhombic and shear deformations to determine the elastic constants. For both the deformations, a series of total energy calculations were performed for small but finite strain values ϵ up to a maximum of 0.02. The energy values as functions of the strain were then fitted to the 2^{nd} degree polynomials and the best fit values of the elastic constants were determined. The bulk modulus and its pressure derivatives were obtained, as before, by fitting our calculated pressure-volume data with the third-order Birch-Murnaghan equation of state[155]. We have used the Voigt-Reuss-Hill approximation[161–163] to calculate the polycrystalline elastic moduli. We have also calculated Young's modulus E and the Poisson's ratio ν, which are evaluated for the polycrystals when studying the hardness of materials. Furthermore, we have calculated the Pugh[165] ratio B/G to study the brittle or ductile nature of materials under examination. A high value compares to the ductility, whereas a low value is associated with brittleness. The critical value dividing ductile and brittle materials is 1.75.

The thermal properties of pyrochlores are also quite interesting to study. So, we have calculated the Debye temperature, longitudinal, transverse, and mean sound velocities. Since pyrochlore compounds are very good candidates for the thermal barrier coatings because of their low thermal conductivities, we have also calculated the minimum thermal conductivity for the systems under study, using the same method as discussed in chapter 4.

The LDA and GGA values of the elastic constants, anisotropy factor, bulk, shear, and Young's

moduli, Poisson's and the Pugh's ratios are listed in Table. 6.2. As can be seen, our calculated elastic constant C_{11} decreases in the order Ti, Hf, and Zr, which is because their average bond strengths also decrease in the same order. The connection between the elastic constants to the strengths of bonds was discussed in great detail in chapter 4. The LDA gives a better connection between the elastic moduli and the strengths of the bonds, whereas there is a small discrepancy in the GGA results which could be well within the limitations of the DFT calculations. Generally speaking, a small Poisson's ratio indicates that the material is the covalent compound, whereas the large value of it (0.25 and above) means that the material is the ionic in nature[166]. Here, all the calculated values are > 0.25, indicating the ionic character of the pyrochlores under study. The Pugh's ratio, defined as B/G, is an indicator of the damage tolerance of ceramics since it roughly reflects the ability to resist the shear deformation. It is widely accepted that the material with a low B/G value tends to brittle, while the material with a high value is ductile and has a better tolerance to the shear deformation. The cut-off value is 1.75. Here, all the systems studied display a larger value of B/G ratio in both the methods used (except for the GGA values for the $Y_2Hf_2O_7$ compound, where the value is found to be slightly smaller than the cut-off value of 1.75, which could be well within the limitations of the DFT calculations), and hence they are ductile. Overall, our theoretical results are in reasonably good agreement with the available literature data.

Table 6.2: Calculated elastic moduli for $Y_2B_2O_7$ (B = Ti, Zr, and Hf) pyrochlores, along with the available literature data. Theory A, B, and C show results for other first-principles simulations.

	C_{11}	C_{12}	C_{44}	B	A	G	E	ν	B/G
$Y_2Ti_2O_7$									
LDA	374	137	109	216	0.9189	113	288	0.2778	1.9165
GGA	333	112	92	186	0.8384	99	252	0.2740	1.8788
Theory A[106]	381	153	241	229					
Theory B[180]	352	112	73	184		85	221	0.30	2.15
Theory C[181]	350	127	97	201		103	263	0.282	
$Y_2Zr_2O_7$									
LDA	348	126	96	200	0.8609	102	261	0.2825	1.9657
GGA	311	106	86	174	0.8440	92	235	0.2747	1.8860
Theory A[106]	351	163	198	225					
$Y_2Hf_2O_7$									
LDA	356	128	106	204	0.9336	109	278	0.2730	1.8693
GGA	315	101	100	172	0.9357	103	257	0.2509	1.6741
Theory A[106]	379	167	221	238					

The calculated values of the crystal density, sound velocities, Debye temperature, and the minimum thermal conductivity of $Y_2B_2O_7$ (B = Ti, Zr, and Hf) are shown in Table. 6.3. As can be seen, the various physical quantities in $Y_2B_2O_7$ lie in the range of 5.17 - 8.0 (4.89 - 7.53) g cm^{-3} for ρ, 6611 - 8415 (6404 - 8066) m/s for v_l, 3694 - 4668 (3693 - 4500) m/s for v_t, 4113 - 5200 (4100 - 5011) for v_m, 532 - 691 (520 - 653) K for θ_D, 1.34 -1.79 (1.27 - 1.65) $Wm^{-1}K^{-1}$ for κ_{min} in the case of LDA (GGA)

theoretical calculations. The LDA values of all the above quantities are larger than the GGA ones, consistent with the fact that LDA underestimates the lattice constants and the LDA elastic constants are larger than the GGA ones. Values of the sound velocities, Debye temperature, and the minimum thermal conductivity decrease with increasing atomic mass at the B site, in the sequence Ti, Zr, Hf.

Table 6.3: Calculated crystal density, longitudinal, transverse, and mean sound velocities, Debye temperature, and the minimum thermal conductivity in $Y_2B_2O_7$ (B = Ti, Zr, and Hf). Results are compared with the available literature data.

	ρ (g cm^{-3})	v_l (m s^{-1})	v_t (m s^{-1})	v_m (m s^{-1})	Θ_D (K)	$\kappa_{min}(Wm^{-1}K^{-1})$
$Y_2Ti_2O_7$						
LDA	5.17	8415	4668	5200	691	1.79
GGA	4.89	8066	4500	5011	653	1.65
Expt.	4.97[108]					
$Y_2Zr_2O_7$						
LDA	5.77	7665	4174	4656	600	1.51
GGA	5.46	7380	4118	4585	580	1.42
$Y_2Hf_2O_7$						
LDA	8.00	6611	3694	4113	532	1.34
GGA	7.53	6404	3693	4100	520	1.27

6.5 Electronic properties

According to the literature data, $Y_2Ti_2O_7$ has an experimental energy bandgap of 3.12 eV[182]. From our DFT calculations we find the energy band gap of 2.85 eV in LDA while 2.81 eV in GGA, which are in good agreement with the calculated value of 2.87 eV by Terki et al.[179], 2.84 eV reported by Jiang et al.[180], and also with the calculated value of 2.798 eV by Srivastava et al.[107].

In LDA, both the maximum of the valence band and minimum of the conduction band occur at the Γ-point. However, the energy difference between the maxima of the valence band at the Γ-point and at the X-point is rather small (0.014 eV). On the other hand, in GGA, the maximum of the valence band occurs at the X-point while the minimum of the conduction band is still at the Γ-point. Again, the energy difference between the maxima of the valence band at the X-point and the Γ-point is rather small (0.02 eV). The energy band structure is plotted in Fig. 6.1.

The composition analysis of the electronic band structure, corresponding to the contribution by different atomic orbitals, also known as the partial density of states (PDOS), is shown in Fig. 6.2. The occupied valence band is derived from the admixture of O-2p, Y-4d and Ti-3d states. The s and p states of the Y and Ti atoms also contribute to the valence band but their contribution is small compared to O-2p, Y-4d and Ti-3d states. The valence band between -6 eV and 0 eV consists mainly of oxygen 2p-states, whereas, the conduction band is mainly composed of Ti 3d-states and a small contribution of 2p-states of oxygen at the symmetry site 48f (due to the hybridization of neighbouring O_{48f} 2p-states and Ti 3d-states), and also of Y 4d- states.

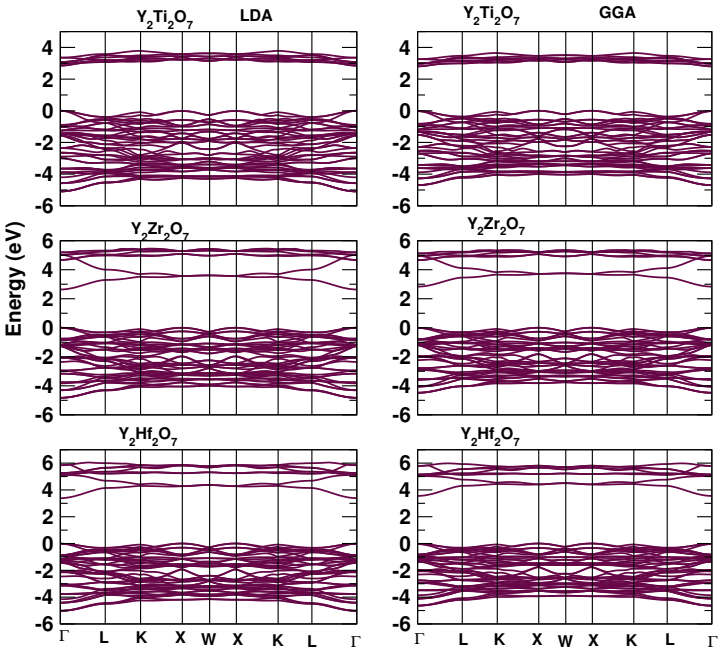

Figure 6.1: Electronic band structure of $Y_2B_2O_7$ (B = Ti, Zr, and Hf) calculated both within the LDA and GGA approaches. The valence band maximum is shifted to zero for our convenience.

From the DOS it can be seen that the two inequivalent oxygen 48f and 8b sites have different features. Moreover, we can see that the density of states for the first oxygen at symmetry site 48f has higher values than that of at 8b symmetry site. The different environment of O_{48f} and O_{8b} sites may be one of the reasons for the difference in their density of states. As we know that the first site of oxygen atoms O is coordinated by Ti and Y atoms while the second site O′ is coordinated only by Y atoms.

6.5.1 Dynamical charges

The dynamical charges (see sec. 3.4.1 for more details) of $Y_2B_2O_7$ (B = Ti, Zr, and Hf) are shown in Table. 6.4. The charge for the Y element (generally higher than the nominal +3e) is almost independent of the B-site composition, with variations smaller than 1%. Similar variations ($\sim 2\%$) are obtained for the oxygen O_{8b}. Large chemical dependence is observed for the dynamical charges associated with the octahedron formed by the B cation and the oxygen O_{48f}. In this case, there are differences in the Born charges for the B cation of up to 30%, and up to 26% for O_{48f}, when the B site is occupied by Hf instead of Ti. The dynamical charges Z^*_B increase in the order B = Hf, Zr, Ti, implying that the degree of ionicity also increases in the same order (Hf, Zr, and Ti) as Z^*_B.

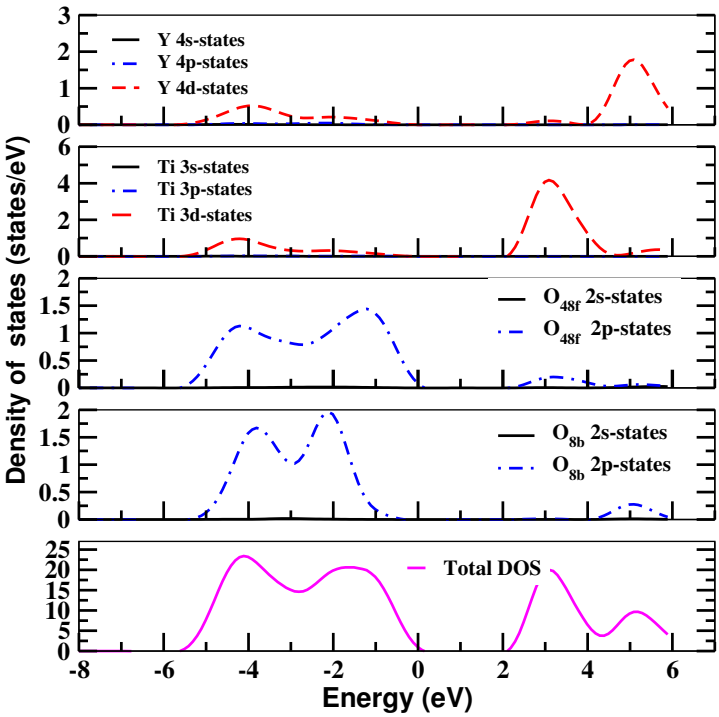

Figure 6.2: Calculated partial density of states for $Y_2Ti_2O_7$ within LDA.

6.6 Vibrational properties; Structural instability analysis

We have performed density functional perturbation theory (DFPT)[102, 130] calculations to study the phonon properties. As described in Chapter 1 (sec. 1.1.4), the pyrochlores (space group: $Fd\bar{3}m$) have a total 66 normal modes in the primitive unit-cell and only 26 irreducible modes at the zone centre of the BZ. Out of these, 6 modes (A_{1g}, E_g, and $4F_{2g}$) are Raman active, 7 modes ($7F_{1u}$) are infrared active, and the rest are optically inactive. Below, we briefly describe the structural instability found in YTO pyrochlore.

6.6.1 A detailed description of the structural instability

The phonon spectra of $Y_2Ti_2O_7$ calculated within the LDA and GGA methods are shown in Figs. 6.3 and 6.4, respectively. A remarkable feature in the LDA phonon spectra is that one unstable phonon mode $F_{2u}(3)$ has the imaginary frequency of 58 cm^{-1} at the Γ point, whereas the GGA results show that there are three optical phonon modes, i.e. $F_{1u}(3)$, $F_{2u}(3)$, and $F_{2u}(3)$ which lead to instability with imaginary frequencies of magnitudes 75, 57, and 24 cm^{-1} at the Γ point, respectively. In the GGA spectra, the imaginary frequencies can be seen for some of the optical phonon modes across the high symmetry $\boldsymbol{q}$ points of the BZ. In the LDA calculations, the unstable phonon modes are due to the displacements of Ti^{4+} ions, whereas in GGA calculations the unstable phonon modes involve the

Table 6.4: Dynamical charge tensors of Y, B (B = Ti, Zr, and Hf), and oxygen elements in $Y_2B_2O_7$ calculated within the LDA approach. The dynamical charges for any other atoms can be achieved by utilizing the symmetry operations of the crystal. Eigenvalues of the symmetric part of the tensor are also given in the brackets.

	Z^*_Y	Z^*_B	$Z^*_{O_{48f}}$	$Z^*_{O_{8b}}$
$Y_2Ti_2O_7$	$\begin{pmatrix} 3.93 & 0.02 & 0.02 \\ 0.02 & 3.93 & 0.02 \\ 0.02 & 0.02 & 3.93 \end{pmatrix}$	$\begin{pmatrix} 6.64 & -0.13 & -0.13 \\ -0.13 & 6.64 & -0.13 \\ -0.13 & -0.13 & 6.64 \end{pmatrix}$	$\begin{pmatrix} -2.48 & 0.00 & 0.00 \\ 0.00 & -3.38 & 1.50 \\ 0.00 & 1.50 & -3.38 \end{pmatrix}$	-2.69
	[3.91, 3.91, 3.97]	[6.77, 6.77, 6.38]	[-1.88, -2.48, -4.88]	
$Y_2Zr_2O_7$	$\begin{pmatrix} 3.97 & -0.02 & -0.02 \\ -0.02 & 3.97 & -0.02 \\ -0.02 & -0.02 & 3.97 \end{pmatrix}$	$\begin{pmatrix} 5.67 & -0.41 & -0.41 \\ -0.41 & 5.67 & -0.41 \\ -0.41 & -0.41 & 5.67 \end{pmatrix}$	$\begin{pmatrix} -2.52 & 0.00 & 0.00 \\ 0.00 & -2.94 & 0.98 \\ 0.00 & 0.98 & -2.94 \end{pmatrix}$	-2.69
	[3.93, 3.99, 3.99]	[6.08, 6.08, 4.85]	[-1.96, -2.52, -3.92]	
$Y_2Hf_2O_7$	$\begin{pmatrix} 3.93 & 0.02 & 0.02 \\ 0.02 & 3.93 & 0.02 \\ 0.02 & 0.02 & 3.93 \end{pmatrix}$	$\begin{pmatrix} 5.35 & -0.42 & -0.42 \\ -0.42 & 5.35 & -0.42 \\ -0.42 & -0.42 & 5.35 \end{pmatrix}$	$\begin{pmatrix} -2.42 & 0.00 & 0.00 \\ 0.00 & -2.76 & 0.86 \\ 0.00 & 0.86 & -2.76 \end{pmatrix}$	-2.63
	[3.91, 3.91, 3.97]	[5.77, 5.77, 4.51]	[-1.90, -2.42, -3.62]	

displacements of all the ions, but the displacements of Ti^{4+} ions are still the most significant.

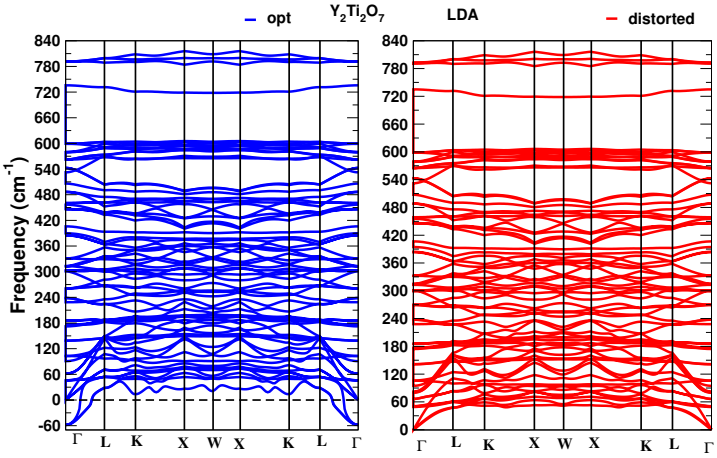

Figure 6.3: Phonon band spectra of $Y_2Ti_2O_7$ calculated using the LDA method. Left panel (in blue colour) is for the optimized structure, while the right panel (in red colour) is for the distorted structure. For more details see the text.

A small distortion to the atomic positions in the unit-cell stabilizes the crystal structure, i.e. the system with the distortion no longer has any modes with imaginary frequencies. In Table 6.5 we have shown the amount of distortion required to stabilize the structure of $Y_2Ti_2O_7$ titanate pyrochlore, both in LDA and GGA calculations. As can be seen, larger distortions are required to stabilize the structure in case of GGA, compared to the LDA ones. The distortion in LDA is so small that it could be within the accuracy limits of DFT, and may not be observable experimentally.

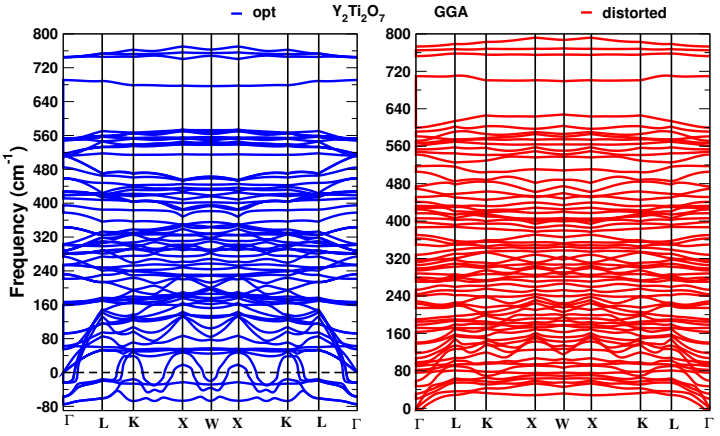

Figure 6.4: Phonon band spectra of $Y_2Ti_2O_7$ calculated using the GGA method. Left panel (in blue) is for the optimized structure, while the right panel (in red) is for the distorted structure. For more details see the text.

Table 6.5: Amount of distortion(in Å) required to stabilize the structure of $Y_2Ti_2O_7$ titanate pyrochlore. The results clearly show that the structure is highly unstable in GGA compared to LDA calculations.

Atom	LDA			GGA		
	dx	dy	dz	dx	dy	dz
Y	0	0	0	0.11	-0.02	-0.04
Y	0	0	0	0.04	-0.04	0.12
Y	0	0	0	-0.08	0	0.12
Y	0	0	0	-0.09	0	-0.05
Ti	-0.03	0.04	-0.01	-0.09	0	-0.02
Ti	0.01	0	0.01	-0.05	0.01	-0.10
Ti	-0.01	-0.04	-0.03	0.01	-0.01	-0.10
Ti	0.03	0	0.03	0.11	0	0.01
O	0	0	0	0	0.04	0
O	0	0	0	0	0.04	0
O	0	0	0	0	0.04	0.01
O	0	0	0	0	0.04	0.01
O	0	0	0	0	0.04	0.01
O	0	0	0	0	0.04	0.01
O	0	0	0	-0.01	0.04	0.01
O	0	0	0	-0.01	0.04	0.01
O	0	0	0	-0.01	0.04	0.02
O	0	0	0	-0.01	0.04	0.01
O	0	0	0	-0.01	0.04	0.01
O	0	0	0	-0.01	0.04	0.01
O	0	0	0	-0.01	0.04	0.01
O	0	0	0	0	0.04	0.01

When the Ti^{4+} ions are replaced by the heavier ions like Zr^{4+} or Hf^{4+}, no structural instability is found in either of the approaches used. The phonon spectra of $Y_2Zr_2O_7$ and $Y_2Hf_2O_7$ compounds, calculated both within the LDA and GGA methods, are shown in Fig. 6.5 and Fig. 6.6, respectively.

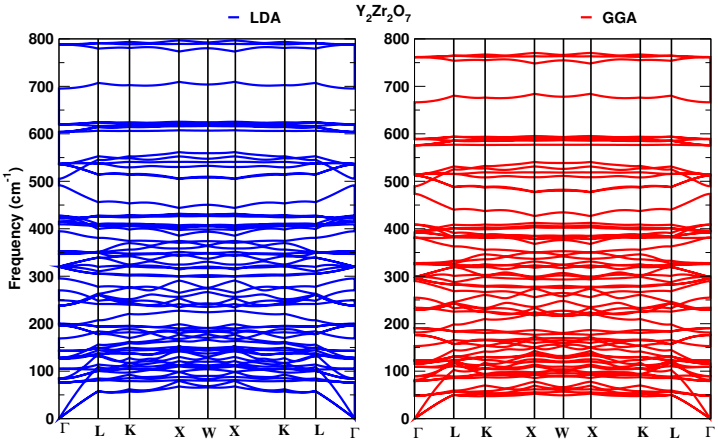

Figure 6.5: Phonon band spectra of $Y_2Zr_2O_7$ pyrochlore. Both the LDA (left panel) and GGA (right panel) spectra are shown.

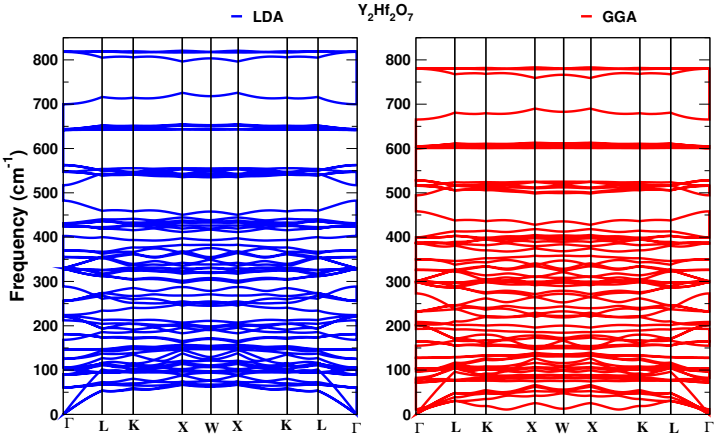

Figure 6.6: Phonon band spectra of $Y_2Hf_2O_7$ pyrochlore. Both the LDA (left panel) and GGA (right panel) spectra are shown.

To see the effect of distortion on the electronic properties of $Y_2Ti_2O_7$, we have plotted the LDA and GGA electronic density of states in Fig. 6.7, for both the undistorted (optimized) and distorted structures. From the DOS it is clear that the distortion in the case of LDA does not affect the electronic properties, while in the case of GGA, the effect is visible at few places in energy range, but it may be insignificant.

To get a better understanding of the effect of distortion on the electronic dos in the GGA calculations, we have calculated the partial density of states for $Y_2Ti_2O_7$ for each valance orbital of every individual atom (Fig. 6.8). As can be seen, there is a slight change in the density of states of the 4d orbitals of the

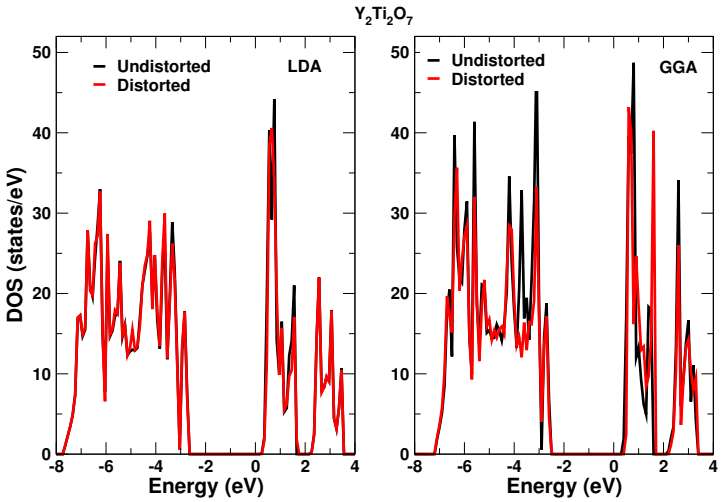

Figure 6.7: Electronic density of states (DOS) of $Y_2Ti_2O_7$ pyrochlore. Both the LDA (left panel) and GGA (right panel) results are shown. The DOS for the optimized (undistorted) and the distorted crystal structures are plotted together for the comparison.

Y atoms, 3d orbitals of the Ti atoms, and 2p orbitals of the O atoms.

6.6.2 Description of Raman and Infrared active modes

The calculated values of the frequencies of Raman active modes in $Y_2B_2O_7$ (B = Ti, Zr, and Hf) pyrochlores are shown in Table 6.6. The results are compared with the available literature data.

In the pyrochlore titanates[41, 132], low frequency Raman modes in the range 50-240 cm^{-1} have been observed, with the lowest frequency modes around 220 cm^{-1}. All Raman active modes involve vibrations of oxygen atoms only, and our DFT calculations do not show any Raman active mode such as F_{2g} around 220 cm^{-1} in $Y_2Ti_2O_7$ pyrochlore, agreeing with the Kumar et al.[41] results. But we observe two IR-active modes, one around 180 cm^{-1} and another around 240 cm^{-1}, which are normally Raman-inactive but can appear in Raman spectra[49, 51, 54, 133, 135] due to displacive disorder of RE and O′ sites in these systems. This displacive disorder leads to a relaxation of the selection rules[41], as a result of which IR modes can appear in Raman spectra and vice-versa, and silent modes may become active and appear in Raman and IR spectra.

In the frequency range 24-400 cm^{-1}, our DFT calculations predict an F_{2g} mode at around 320 cm^{-1} in $Y_2Ti_2O_7$ titanate pyrochlore, in reasonably good agreement with the literature values. In the pyrochlore titanates[52, 53, 137], the E_g mode is generally observed around 330 cm^{-1}. Our DFT value for the E_g mode calculated for $Y_2Ti_2O_7$ is in good agreement with the literature values. One each of the F_{2g} modes and A_{1g} modes of the pyrochlore titanates[132] are usually observed around 450 cm^{-1} and 510 cm^{-1}, respectively. Again, our calculated values are in reasonably good agreement with the available literature values. Among the two high frequency Raman active modes with F_{2g} symmetry, one

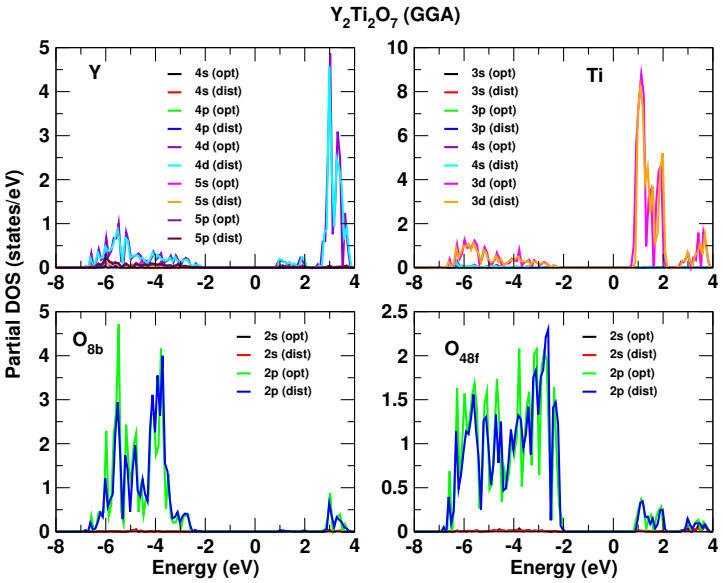

Figure 6.8: The partial density of states (PDOS) of $Y_2Ti_2O_7$ calculated using the GGA method. The DOS for the optimized (undistorted) and the distorted crystal structures are plotted together for the comparison.

is found to be around 580 cm^{-1}, again in reasonably good agreement with the experimental value. Our LDA value of the frequency of the high frequency Raman active mode is found to be around 790 cm^{-1}, whereas it is observed to be around 590 cm^{-1} in the experiment. Thus, the frequency of this mode is not in agreement with the experimental value reported in the table 6.6. The assignment for this high frequency Raman active mode has been quite of some interest in the titanate pyrochlores. It has been assigned as an overtone or combination of vibrational modes in the experimental measurements of Saha et al.[54], and in the lattice dynamical calculations by Gupta et al.[46] in titanates. Our calculated values are consistent with the calculations by Kumar et al.[41].

The assignment of the frequencies of the Raman active modes in the case of $Y_2Zr_2O_7$ and $Y_2Hf_2O_7$ (also shown in Table 6.6) pyrochlores are consistent with the assignment as discussed above for $Y_2Ti_2O_7$ pyrochlore.

The calculated values of the frequencies of the IR active modes in $Y_2B_2O_7$ (B = Ti, Zr, and Hf) pyrochlores are shown in Table 6.7. The results are compared with the available literature data. Again, the frequencies for most of the IR active modes are in reasonably good agreement with the available data.

Table 6.6: Calculated Raman mode frequencies (cm^{-1}) in $Y_2B_2O_7$ (B = Ti, Zr, and Hf) pyrochlores with assignments along with the literature data. Modes with $\star$ indicate that they are experimentally observed, but not found from the DFT. Frequencies with † implies that they are not assigned experimentally to any Raman-active mode, and with ‡ means they are assigned as overtones in experiments. Theory A shows results for other first-principles simulations.

Mode	F^*_{2g}	F^*_{2g}	F_{2g}	E_g	F_{2g}	A_{1g}	F_{2g}	F_{2g}
$Y_2Ti_2O_7$								
LDA	-	-	317	333	447	504	579	792
GGA	-	-	299	315	428	474	572	764
Theory A[41]	-	-	316	334	449	508	582	796
Expt.[45]	225	-	318	333	450†	527	531	586
$Y_2Zr_2O_7$								
LDA			328	349	419	507	542	793
$Y_2Hf_2O_7$								
LDA			330	355	428	517	545	818

Table 6.7: Calculated Infra-red mode frequencies (cm^{-1}) in $Y_2B_2O_7$ (B = Ti, Zr, and Hf) pyrochlores with assignments along with the literature data. Theory A shows results for other first-principles simulations.

Mode	F_{1u}	F_{1u}	F_{1u}	F_{1u}	F_{1u}	F_{1u}	F_{1u}
$Y_2Ti_2O_7$							
LDA	67	143	190	238	387	460	537
GGA	51	125	179	234	365	418	555
Theory A[41]	74	142	189	238	391	456	546
Expt.[135]	105	176	248	285	410	462	568
Expt.[139]	-	177	245	293	424	467	571
Expt.[2]	-	182	248	299	429	460	562
$Y_2Zr_2O_7$							
LDA	89	147	198	208	353	425	539
$Y_2Hf_2O_7$							
LDA	88	162	182	221	323	428	564

6.7 Conclusions

In summary, in this chapter we have studied the structural, electronic, elastic, thermal, and vibrational properties in $Y_2B_2O_7$ (B = Ti, Zr, and Hf) pyrochlores using DFT calculations.

From our calculations, it is clear that the elastic moduli satisfy the mechanical stability criteria for the cubic crystals. The elastic moduli C_{11}, C_{12}, and C_{44} decrease with increasing the B ionic radii, i.e. B = Ti, Hf, Zr. C_{11} is directly related to the bond strengths. With increasing B ionic radii, the lengths of B-O bonds increase, making the average bond strength weaker. Therefore, the C_{11} decreases accordingly. In contrast, the shear modulus C_{44} is associated with the distortion of the soft Y-O polyhedra and the rotation of the rigid B-O octahedra, and thus C_{44} does not show a close relationship with the B cation size.

The bulk, shear, and Young's moduli are highly dependent on the B site elements, i.e. their values decrease in the order Ti, Hf, and Zr. Our calculated values of the Poisson's ratio is greater than 0.25 in all the compounds studied, indicating that the $Y_2B_2O_7$ are ionic crystals. The Pugh's ratio is calculated to be larger than 1.75 in almost all the cases (except for the $Y_2Hf_2O_7$ calculated using the GGA method, where its value is found to be slightly smaller than 1.75, which could be well within the limitations of the DFT calculations) suggesting that the materials under study are ductile, i.e. they have a high tolerance towards the shear deformations.

From our theoretical calculations, we find that the sound velocities, the Debye temperature, and the minimum thermal conductivity are dependent on the ionic mass in the crystal, especially the sound velocities. Values of the Debye temperature and the minimum thermal conductivity decrease in the order Ti, Zr, and Hf.

We also calculated the dynamical charge, a quantity that describes a change in the polarization when an atom is displaced from its equilibrium position. The dynamical charge for the Y site atom in $Y_2B_2O_7$ is calculated to be higher than its nominal $+3e$ value and is nearly independent of the B-site composition. Large chemical dependence is found for the dynamical charges of B cations and the O_{48f}. The dynamical charges $Z^{\star}_{B}$ increase in the order B = Hf, Zr, Ti. The large anomalous charge contributions (additional charges to the given ionic values of Y^{3+}, B^{4+}, and O^{2-}) stem from the electronic charge rearrangement when an atom is moved from its original position. They are correlated to charge transfers between atoms and the dynamical changes in the hybridization.

Using linear response theory as embedded in the DFPT, we investigated the lattice dynamical properties of pyrochlores. We performed both LDA and GGA calculations. A remarkable finding of the GGA calculations in $Y_2Ti_2O_7$ is that there are a few phonon modes at the zone centre of the Brillouin zone which have imaginary frequencies. The LDA results also lead to modes with imaginary frequencies, but with a smaller magnitude of the imaginary frequencies. These phonon modes with imaginary frequencies correspond to the structural instabilities. We find that small distortion of the atomic positions in the unit cell is able to stabilize the crystal structure. This distortion is so small that it may not be easy to observe experimentally. From our calculations, it is quite clear that the GGA results show more structural instability compared to the LDA ones. Our calculations show that this structural instability is characterized by the large amplitude of Ti^{4+} vibrations. This is because the centre of tetrahedra formed by Ti cations remains vacant, which in turn provides Ti^{4+} ions a more room to oscillate. When the Ti^{4+} ions are replaced by the heavier ions, Zr^{4+} or Hf^{4+}, no structural instability is seen in either of the density functional approaches.

We also discussed in detail assignment of the phonon frequencies and their comparison with the literature data. Our calculated frequencies for most of the modes are found to be in reasonably good agreement with the available theoretical and experimental results.

Chapter 7

Temperature dependent phonon properties of $Y_2Ti_2O_7$ pyrochlore

As mentioned earlier (sec. 1.1.6), experimentally it has been found that several of the phonon modes in pyrochlore titanates show an unconventional behaviour with cooling, i.e. they display a redshift, or soften. It was suggested in these studies that phonon-phonon interactions are responsible for the anomalous nature of these phonon modes. Motivated by these studies, we have carried out temperature dependent phonon calculations in $Y_2Ti_2O_7$ using first principles density functional theory calculations and the many-body Green's function approach to see if we can theoretically capture these anomalies within a perturbative treatment of third-order anharmonic interactions. In this chapter we present our calculations and results for the Grüneisen parameter values for various phonon modes, the temperature variation of the linear thermal expansion coefficient, and the temperature dependence of the quasi-harmonic contribution to the various normal modes. We also present a comprehensive analysis of the two-phonon density of states, phonon linewidths, and frequency shifts for some of the phonon modes.

7.1 Introduction

At present, the harmonic properties of materials are quite well understood due to the availability of a large number of experimental data and several calculations. In this regard, DFPT has been a very useful and powerful ab-initio method for calculating the linear response lattice properties of materials such as phonon frequencies and eigenvectors[102, 130]. However, this approach neglects the effects of anharmonic lattice dynamics. Furthermore, one is also interested in studying the properties which arise from the lattice anharmonicity such as the temperature dependence of lifetimes and frequency shifts of phonon modes.

In a purely harmonic crystal, phonons are noninteracting, so a nonequilibrium phonon population will persist in time[91]. However, it is experimentally found that such phonon populations decay towards equilibrium on a time scale of a few picoseconds. The decay of high frequency phonons into phonons of lower frequency is responsible for energy relaxation in semiconductors as it controls the creation and time evolution of the nonequilibrium phonon populations that are emitted by high density excited carriers when they decay towards their ground state[183].

Experimentally, lifetimes of individual zone centre phonons can be extracted from their measured linewidths if inhomogeneous broadening effects are negligible. It is hard to study the temperature dependent nature in systems such as heterostructures, where composition and/or strain inhomogeneities provide an additional contribution to the general (e.g., isotopic) broadening factors. Experiments in the time domain by ultrafast spectroscopies have also become more and more sophisticated in recent years, and provide useful information, especially for the long-lived phonons.

Within the framework of lattice anharmonic effects, each of the harmonic normal mode frequencies $\omega_j(\boldsymbol{q})$, which determine the unperturbed "single-particle" energies of the phonons, undergoes a complex shift $\Delta_j(\boldsymbol{q}) + i\Gamma_j(\boldsymbol{q})$, the real part of which represents the change in frequency, and the imaginary part of which is the inverse of the lifetime of the single-particle amplitude for the phonon mode labelled by $(\boldsymbol{q}j)$. Both the real and imaginary parts are temperature dependent. In experiments, the imaginary part is connected to the broadening of the peaks in the Raman spectra or the energy distribution of the scattered neutrons, and Γ is the half-width at half-maximum (HWHM) of the peak. The real part corresponds to the shift in the centre of the peak.

Recently, experimentally it was found by Saha et al.[54, 56] that several phonons in titanate pyrochlores, namely $Tb_2Ti_2O_7$, $Dy_2Ti_2O_7$, and $Lu_2Ti_2O_7$ show anomalous temperature dependence (softening of the phonon modes, i.e. the decrease of the phonon frequency with the cooling) and a suggestion was made by these authors that phonon-phonon interactions may be the main cause of the phonon anomalies in these titanate pyrochlores.

In this chapter, we present our theoretical calculations using the DFT and Green's function formalism to study the temperature-dependent phonon properties in $Y_2Ti_2O_7$ titanate pyrochlore. Our interest is to see if we can theoretically capture the phonon anomaly for some of the phonon modes in this compound. To the best of our knowledge, no such theoretical calculations exist in the literature for this material. We have extensively explored the phonon properties, mode Grüneisen parameters, temperature-dependent linear thermal expansion coefficient and quasiharmonic contributions, two phonon density of states, temperature-dependence of phonon linewidths and the third-order anharmonic contributions to some of the optical phonon modes.

A calculation of the contribution to the temperature dependent shifts in the phonon frequencies (and the phonon line-widths) arising from the third-order anharmonic interactions requires a knowledge of

the third-order interatomic force constant matrix elements. The calculations presented in this chapter have been carried out by approximating these matrix elements in terms of an assumed form involving a single coupling constant, which is then used as a fitting parameter. This approach of calculating the anharmonic force constants has been provided by Ipatova et al.[184] and has been successfully used by Lan et al. to study the phonon anharmonicity of rutile TiO_2[185] and SnO_2[186].

7.2 Computational details

As mentioned before, our DFT calculations[83, 84] were carried out using the Quantum Espresso code[110], with ultrasoft pseudopotentials[152] to represent the interaction between ionic cores and valence electrons. The LDA method was used for the exchange-correlation energy functional. A plane-wave basis set with a cut-off of 60 Ry was used for all our calculations. The k-points summation of the electronic energy calculations over the BZ was implemented by using the Monkhorst-Pack method with a $4 \times 4 \times 4$ special k-points mesh[111]. The DFPT was used to investigate the phonon properties in the BZ. For the full phonon dispersion, dynamical matrices were calculated for a grid of $2 \times 2 \times 2$ $\boldsymbol{q}$-points. The lattice constant was optimized to minimize the total energy, interatomic forces, and unit-cell stresses. The Broyden-Fletcher-Goldfarb-Shanno (BFGS) minimization scheme[112] was used in geometry optimization.

7.3 Results and discussions

7.3.1 Quasiharmonic results

The quasiharmonic approximation has been described in great detail in section 2.5.1 of Chapter 2. The mode Grüneisen parameter for the j^{th} phonon mode at the centre of BZ were calculated as

$$\gamma_j = -\frac{\partial \ln \omega_j}{\partial \ln V} = -\frac{V}{\omega_j}\frac{\partial \omega_j}{\partial V} \tag{7.1}$$

where V is the cell volume and ω_j is the frequency of j^{th} phonon mode. Frequencies were calculated at four different cell volumes (247.9514, 245.3388, 243.1584, and 241.1145 $Å^3$) by applying hydrostatic pressure to the system in the range of 0 - 3.0 GPa in steps of 1.0 GPa. After obtaining a smooth function of frequency versus volume using the cubic splines fitting, we calculated the derivatives of the phonon eigenvalues with volume for different phonon modes at $V = 246.5840$ $Å^3$. The calculated values of the mode Grüneisen parameters for several phonon modes are provided in Table 7.1. To the best of our knowledge, there is no experimental or theoretical data available in the literature for the mode Grüneisen parameters for $Y_2Ti_2O_7$ compound to compare with our theoretical results.

Table 7.1: Calculated values of the phonon frequencies and the mode Grüneisen parameters in $Y_2Ti_2O_7$.

Mode	Frequency (cm^{-1})	γ
	LDA	
F_{1u}	67	3.28
F_{1u}	141	5.95
E_u	177	2.81
F_{1u}	186	3.61
F_{1u}	238	0.75
F_{2g}	314	2.44
E_g	333	2.28
F_{1u}	384	2.40
F_{2g}	446	1.46
F_{1u}	459	1.83
A_{1g}	507	0.68
F_{1u}	543	1.26
F_{1g}	565	1.60
F_{2g}	579	1.15
F_{2u}	598	1.71
F_{2g}	793	1.16

Within the quasiharmonic approximation, the temperature dependence of frequency shift is obtained via the temperature dependence of the linear thermal expansion coefficient:

$$\Delta_j^{(0)}(T) = \omega_j(0)\left[e^{-3\gamma_j\int_0^T \alpha(T')dT'} - 1\right] \tag{7.2}$$

where $\omega_j(0)$ and γ_j correspond to the frequency and the mode Grüneisen parameter for $(\mathbf{0}j)$ mode at temperature $T = 0$ K. The linear thermal expansion coefficient is calculated using the expression

$$\alpha = \frac{1}{3BV}\sum_{\boldsymbol{q}j}\left[\gamma_j(\boldsymbol{q})\frac{(\hbar\omega_j(\boldsymbol{q}))^2}{k_BT^2}\frac{e^{\hbar\omega_j(\boldsymbol{q})/k_BT}}{(e^{\hbar\omega_j(\boldsymbol{q})/k_BT}-1)^2}\right] \tag{7.3}$$

where B is the bulk modulus, V the cell-volume, and $\gamma_j(\boldsymbol{q})$ is the mode Grüneisen parameter for the j^{th} vibrational mode with wave-vector $\mathbf{q}$.

Calculation of the linear thermal expansion coefficient (Eq. 7.3) involves the dispersion of the mode Grüneisen parameter, $\gamma_j(\boldsymbol{q})$, which is a bit trickier to calculate as it is defined as the logarithmic derivative of frequencies with respect to the volume. The cubic spline polynomial fittings were used to calculate $\gamma_j(\boldsymbol{q})$ as well.

Our calculated values of the mode Grüneisen parameters for the Raman active modes are shown in Fig. 7.1 along the high symmetry directions of the BZ. The range of $\gamma_j(\boldsymbol{q})$ lies between 0.5 - 2.3 across the first BZ; their values vary significantly for two low frequency Raman active modes, whereas for the high frequency modes they vary much less. The temperature dependence of the linear thermal expansion coefficient and the quasiharmonic shifts in some of the phonon modes are also shown in Fig. 7.1. For all

the modes, $\Delta_j^{(0)}(T)$ decreases with increasing the temperature and hence can not explain the phonon anomaly. To the best of our knowledge, no experimental or theoretical results of the temperature variation of the quasiharmonic contribution to any of the modes in $Y_2Ti_2O_7$ pyrochlore exist in the literature to compare with our theoretical results.

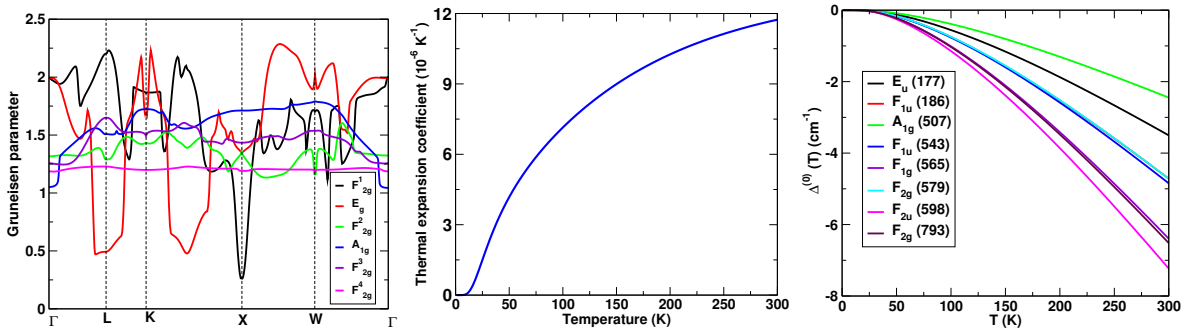

Figure 7.1: (Left panel) Variation of the mode Grüneisen parameters for the Raman active modes along the high symmetry directions in the first BZ; (Middle panel) Temperature dependence of the linear thermal expansion coefficient; (Right panel) Temperature dependence of the Quasiharmonic contribution to some of the optical modes.

7.3.2 Anharmonic calculations

The renormalized phonon frequency, $\omega_j(T)$ that includes the anharmonic contributions is the solution of the Dyson equation:

$$\omega_j^2(T) = \omega_j^2(0) + 2\omega_j(0)\Delta_j(\omega, T) \tag{7.4}$$

Where, the real part of the self energy includes all the anharmonic terms,

$$\Delta_j(\omega, T) = \Delta_j^{(0)}(\omega, T) + \Delta_j^{(3)}(\omega, T) + \Delta_j^{(4)}(\omega, T) + \ldots \tag{7.5}$$

where, the $\Delta_j^{(0)}(\omega, T)$ is the shift in frequency within the quasiharmonic approximation and has been studied in the previous section. The $\Delta_j^{(3)}(\omega, T)$ and $\Delta_j^{(4)}(\omega, T)$ correspond to the cubic and quartic anharmonic corrections. Generally, the quartic and higher order corrections are important only at higher temperatures, therefore, we have ignored all the terms beyond the cubic anharmonic corrections in this work.

The real and imaginary parts of the phonon self-energy to leading order in the cubic anharmonic interactions are calculated as

$$\begin{aligned} \Delta^{(3)}(\boldsymbol{q}j;\omega) &= -\frac{18}{\hbar^2}\sum_{\boldsymbol{q}_1 j_1, \boldsymbol{q}_2 j_2} |V^{(3)}(\boldsymbol{q}j;\boldsymbol{q}_1 j_1;\boldsymbol{q}_2 j_2)|^2 \\ &\times \mathcal{P}\left[\frac{n_1+n_2+1}{\omega+\omega_1+\omega_2} - \frac{n_1+n_2+1}{\omega-\omega_1-\omega_2} + \frac{n_1-n_2}{\omega-\omega_1+\omega_2} - \frac{n_1-n_2}{\omega+\omega_1-\omega_2}\right] \end{aligned} \tag{7.6}$$

$$\begin{aligned}\Gamma(\boldsymbol{q}j;\omega) &= \frac{18\pi}{\hbar^2}\sum_{\boldsymbol{q}_1 j_1,\boldsymbol{q}_2 j_2}|V^{(3)}(\boldsymbol{q}j;\boldsymbol{q}_1 j_1;\boldsymbol{q}_2 j_2)|^2 \\ &\times [(n_1+n_2+1)\delta(\omega-\omega_1-\omega_2)+2(n_1-n_2)\delta(\omega+\omega_1-\omega_2)] \end{aligned} \tag{7.7}$$

where, in the short hand notations, $\omega_i = \omega_{j_i}(\boldsymbol{q}), n_i = n(\omega_{j_i}(\boldsymbol{q})), i = 1,2$. The phonon occupation number for the $(\boldsymbol{q}j)$ mode is given as,

$$n(\omega_j(\boldsymbol{q})) = \frac{1}{e^{\hbar\omega_j(\boldsymbol{q})/k_BT}-1} \tag{7.8}$$

The cubic phonon coupling constant is written as

$$\begin{aligned}V^{(3)} &= \frac{1}{6}\left(\frac{\hbar^3}{8\omega_{j_1}(\boldsymbol{q}_1)\omega_{j_2}(\boldsymbol{q}_2)\omega_{j_3}(\boldsymbol{q}_3)}\right)^{1/2}\sum_{ss's'',\alpha\beta\gamma}\left(\frac{1}{M_sM_{s'}M_{s''}}\right)^{1/2}e_{s,\alpha}(\boldsymbol{q}_1 j_1)e_{s',\beta}(\boldsymbol{q}_2 j_2)e_{s'',\gamma}(\boldsymbol{q}_3 j_3) \\ &\times \sum_{ll'}\frac{1}{N\sqrt{N}}\frac{\partial^3 E}{\partial u^0_{s,\alpha}\partial u^l_{s',\beta}\partial u^{l'}_{s'',\gamma}}e^{i\{\boldsymbol{q}_1.\boldsymbol{R}^0_s+\boldsymbol{q}_2.\boldsymbol{R}^l_{s'}+\boldsymbol{q}_3.\boldsymbol{R}^{l'}_{s''}\}}\Delta(\boldsymbol{q}_1+\boldsymbol{q}_2+\boldsymbol{q}_3)\end{aligned} \tag{7.9}$$

The phonon coupling constant has been discussed in great detail in section 2.5.2. Various phonon vertices involved in the processes contributing to Eqs. 7.6 and 7.7 are shown pictorially in Fig. 7.2, where a phonon mode $\boldsymbol{q}j$ either gets created or destroyed during the scattering process.

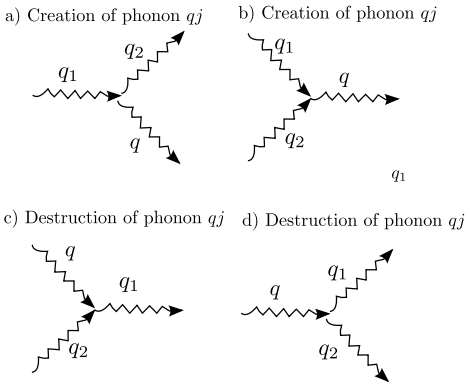

Figure 7.2: Three-phonon interaction processes that may create or destroy the phonon $\boldsymbol{q}j$.

Since the experiments probing the Raman and infrared active phonon modes correspond to very small wave-vectors ($q \sim \omega/c$, where c is the velocity of light), we set $\boldsymbol{q} = \boldsymbol{0}$ in all our calculations. Because of the momentum conservation, if $\boldsymbol{q}_1 = \boldsymbol{q}$, then $\boldsymbol{q}_2 = -\boldsymbol{q}$. Consequently, the equations for the frequency shifts and the phonon linewidths can be rewritten as

$$\begin{aligned}\Delta^{(3)}(\omega_j) &= -\frac{18}{\hbar^2}\sum_{\boldsymbol{q},j_1 j_2}|V^{(3)}(\boldsymbol{0}j;\boldsymbol{q}j_1;-\boldsymbol{q}j_2)|^2 \\ &\times \mathcal{P}\left[\frac{n_1+n_2+1}{\omega+\omega_1+\omega_2}-\frac{n_1+n_2+1}{\omega-\omega_1-\omega_2}+\frac{n_1-n_2}{\omega-\omega_1+\omega_2}-\frac{n_1-n_2}{\omega+\omega_1-\omega_2}\right]\end{aligned} \tag{7.10}$$

$$\begin{aligned}\Gamma(\omega_j) &= \frac{18\pi}{\hbar^2}\sum_{\boldsymbol{q},j_1j_2}|V^{(3)}(\mathbf{0}j;\boldsymbol{q}j_1;-\boldsymbol{q}j_2)|^2 \\ &\times \quad [(n_1+n_2+1)\delta(\omega-\omega_1-\omega_2)+2(n_1-n_2)\delta(\omega+\omega_1-\omega_2)] \end{aligned} \tag{7.11}$$

where, $\omega_1=\omega_{j_1}(\boldsymbol{q})$ and $\omega_2=\omega_{j_2}(-\boldsymbol{q})$. Finally, the phonon coupling constant is rewritten as

$$\begin{aligned}V^{(3)}(\mathbf{0},j;\boldsymbol{q},j_1;-\boldsymbol{q},j_2) &= \left(\frac{\hbar^3}{8\omega_j(\mathbf{0})\omega_{j_1}(\boldsymbol{q})\omega_{j_2}(-\boldsymbol{q})}\right)^{1/2}\sum_{ss's'',\alpha\beta\gamma}\left(\frac{1}{M_sM_{s'}M_{s''}}\right)^{1/2}e_{s,\alpha}(\mathbf{0}j)e_{s',\beta}(\boldsymbol{q}j_1)e_{s'',\gamma}(-\boldsymbol{q}j_2) \\ &\times \quad \sum_{ll'}\frac{1}{N\sqrt{N}}\frac{\partial^3E}{\partial u^0_{s,\alpha}\partial u^l_{s',\beta}\partial u^{l'}_{s'',\gamma}}e^{i\boldsymbol{q}.(\boldsymbol{R}(l)-\boldsymbol{R}(l'))} \end{aligned} \tag{7.12}$$

Numerical evaluations of Eqs. 7.10 and 7.11 using phonon frequencies calculated for a discrete grid of wave-vectors in the BZ require careful handling of the Cauchy-principal value and the Dirac-delta functions. A standard prescription is to use the replacements[101, 187, 188]

$$\mathcal{P}\left(\frac{1}{\omega}\right)=\lim_{\epsilon\to0^+}\frac{\omega}{\omega^2+\epsilon^2} \tag{7.13}$$

$$\delta(\omega)=\lim_{\epsilon\to0^+}\frac{\epsilon}{\omega^2+\epsilon^2} \tag{7.14}$$

and do the calculations using an appropriate, small but finite value of the broadening parameter, ϵ, corresponding to a smearing out of the harmonic phonon reference spectrum, which otherwise is a sequence of the delta functions at the phonon frequencies. If the value of ϵ is too large, then it washes out all the details of the phonon spectrum, whereas, if it is too small, the calculations can lead to spurious peaks. The optimum value of ϵ depends on the values of the $\boldsymbol{q}$ points and the frequencies of the phonon modes involved and can only be determined by trial and error which makes calculations computationally challenging.

The next essential step is to choose an appropriate $\boldsymbol{q}$-mesh to perform the summations over the frequency shifts and the phonon linewidths. We employ the Monkhorst and Pack scheme to generate the special $\boldsymbol{q}$-points in the first Brillouin zone given by[94]

$$\boldsymbol{q}(n_1,n_2,n_3)=\sum_{i=1}^{3}\frac{2n_i-N_i-1}{2N_i}\boldsymbol{b}_i\ ;\ n_i=1,2,\ldots N_i \tag{7.15}$$

where the $\boldsymbol{b}_i$ are the reciprocal lattice vectors.

Perhaps the most challenging part is the numerical evaluation of the third-order phonon coupling constants, $V^{(3)}(\mathbf{0}j;\boldsymbol{q}j_1;-\boldsymbol{q}j_2)$ (Eq. 7.12). In the next section, we describe the details of the calculations of this third-order coupling constant.

Evaluation of third-order anharmonic coupling constants

The evaluation of the third-order anharmonic force or coupling constants is typically based on simple models consistent with empirical anharmonic elastic constants or thermal expansion[189, 190]. The first-principles frozen phonon methods[191] have been used to study the phonon linewidths. Around two decades back, the DFPT was used to calculate the phonon lifetime[192]. This method is often used for optical phonons[183, 193, 194], but very few first-principles calculations for phonons away from the BZ centre[195, 196] exist. Recently, Tang and Dong[197, 198] extended the direct supercell finite-displacement (SCFD) approach to calculate the third-order anharmonic coupling constants. While DFPT and frozen phonon methods are efficient for studying the anharmonicity tensor of a particular phonon, the SCFD approach provides a direct calculation of force constants and is more efficient for obtaining all phonons in the BZ. The SCFD method has been used extensively, but primarily for systems having only a few atoms in the unit cell[199–202]. The method involves displacing atoms in the unit cell, which in turn breaks the symmetry and requires a larger supercell to achieve commensuration with the lattice periodicity. This makes the method computationally very expensive, especially for the larger and complicated systems like pyrochlore oxides. In this chapter, we follow a different approach used in Refs.[184, 186] to evaluate the anharmonic coupling constants.

In this approach, the anharmonic coupling constants for an s-phonon process written in the form

$$V(j;\boldsymbol{q}_1 j_1;\ldots;\boldsymbol{q}_{s-1}j_{s-1}) = \frac{1}{2s!}\left(\frac{\hbar}{2N}\right)^{s/2} N\Delta(\boldsymbol{q}_1+\cdots+\boldsymbol{q}_{s-1})[\omega_{j0}\omega_1\ldots\omega_{s-1}]^{\frac{1}{2}} C(j;\boldsymbol{q}_1 j_1;\ldots;\boldsymbol{q}_{s-1}j_{s-1}) \tag{7.16}$$

where $\Delta(\boldsymbol{q}_1+\cdots+\boldsymbol{q}_{s-1})$ ensures the momentum conservation and the $C(.)$'s, referred to as elements of the s-phonon anharmonic coupling constants, are assumed to be slowly varying functions of their arguments.

Since our interest is in the zone centre optical phonons (as discussed earlier) and the cubic anharmonic tenors, the coupling constant for the three-phonon process is obtained as

$$V^{(3)}(j;\boldsymbol{q}j_1;-\boldsymbol{q}j_2) = \frac{1}{12}\left(\frac{\hbar}{2N}\right)^{3/2} N[\omega_{j0}\omega_1\omega_2]^{\frac{1}{2}} C(j;\boldsymbol{q}j_1;-\boldsymbol{q}j_2) \tag{7.17}$$

If the anharmonicity tensor C does not vary significantly for different phonon processes, we can replace the $C(j;\boldsymbol{q}j_1;-\boldsymbol{q}j_2)$ by its average over $\mathbf{q}$, j_1 and j_2 and use them as fitting parameters:

$$C_j^{(3)} = \langle C(j;\boldsymbol{q}j_1;-\boldsymbol{q}j_2)\rangle \equiv \sum_{\boldsymbol{q}j_1j_2} C(j;\boldsymbol{q}j_1;-\boldsymbol{q}j_2)/\sum_{\boldsymbol{q}j_1j_2} 1 \tag{7.18}$$

Within this approximation the phonon linewidth and the frequency shift are given by

$$\Gamma(\omega_j) = \frac{\pi\hbar}{64}\omega_{j0}|C_j^{(3)}|^2 \sum_{\boldsymbol{q}j_1j_2} \omega_1\omega_2 \left[(n_1+n_2+1)\delta(\omega-\omega_1-\omega_2) + 2(n_1-n_2)\delta(\omega+\omega_1-\omega_2)\right] \tag{7.19}$$

$$\Delta^{(3)}(\omega_j) = -\frac{\hbar}{64}\omega_{j0}|C_j^{(3)}|^2 \sum_{\boldsymbol{q}j_1j_2} \omega_1\omega_2\mathcal{P}\left[\frac{n_1+n_2+1}{\omega+\omega_1+\omega_2} - \frac{n_1+n_2+1}{\omega-\omega_1-\omega_2} + \frac{n_1-n_2}{\omega-\omega_1+\omega_2} - \frac{n_1-n_2}{\omega+\omega_1-\omega_2}\right] \tag{7.20}$$

To calculate the phonon linewidth (Eq. 7.19) and shift (Eq. 7.20) for a j^{th} phonon mode, we need the value of the single mode coupling parameter, $C_j^{(3)}$, which can be obtained by fitting the above equation of linewidth or shift to the experimentally obtained values of these quantities. Since we have very little experimental data available for this purpose, to get a qualitative understanding we assume $C_j^{(3)}$ to be a constant value ($|C_j^{(3)}|^2 \sim 1.0 \times 10^{10}$ erg^{-1}) for all the modes, a number approximately equal to the one used in Ref.[186] in the case of rutile SnO_2. The studies in Ref.[186] are based on first-principles and many body Green's function approach to study the temperature dependent phonon properties.

The phonon linewidth (Eq. 7.19) is closely related to the two phonon density of states (TDOS), which at $\boldsymbol{q} = 0$ is defined as

$$D(\omega) = \sum_{\boldsymbol{q}j_1j_2} \left[(n_1+n_2+1)\delta(\omega-\omega_1-\omega_2) + 2(n_1-n_2)\delta(\omega+\omega_1-\omega_2)\right] \tag{7.21}$$

Physically, the TDOS is related to various decay processes involved within the third order anharmonic theory. The first term in Eq. 7.21 corresponds to a process where a mode of frequency ω decays into two lower frequency modes, the second term represents the scattering process where a mode of frequency ω along with a mode of frequency ω_1 decays into a mode of high frequency ω_2. These are known as the down and up conversion decay processes, respectively. The Dirac delta functions in Eq. 7.21 again need to be evaluated using the expression as given in Eq. 7.14. In general, results have to be converged with respect to the broadening parameter ϵ. The TDOS calculated at different values of ϵ is shown in Fig. 7.3. Generally, for a very small value of ϵ, vibrational modes do not interact with each other, while for a very large value of ϵ, we lose the actual details of the interactions. An optimum value of ϵ has to be chosen where the results are insensitive with respect to its value. Based on our calculations, we find that $\epsilon = 3.0$ cm^{-1} works quite well. Therefore, we have taken this value of ϵ in all our further calculations. The up and down conversion processes of TDOS calculated at temperatures $T = 0$ K and $T = 300$ K are also shown in Fig. 7.3. As can be seen, at $T = 0$ K the contribution from up conversion process is quite small compared to the down conversion process, while at higher temperatures, both the terms contribute, but the contribution from the later term is still higher than the former one. This is because there are several channels available for high frequency modes to decay into the low frequency modes.

A difference between the TDOS and the phonon linewidth is in terms of the three phonon coupling

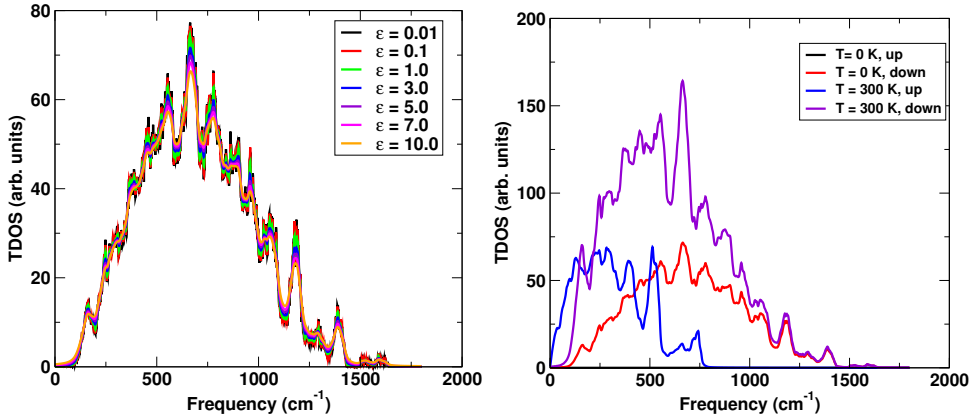

Figure 7.3: (Right panel) Two phonon density of states (TDOS) of $Y_2Ti_2O_7$. The broadening parameters (ϵ) are in cm^{-1}. (Left panel) The up and down conversion decay processes of TDOS are shown for two different temperature values and for $\epsilon = 3$ cm^{-1}.

constant (Eq. 7.12). The frequency dependence of the phonon linewidth as calculated using Eq. 7.19 is shown in Fig. 7.4.

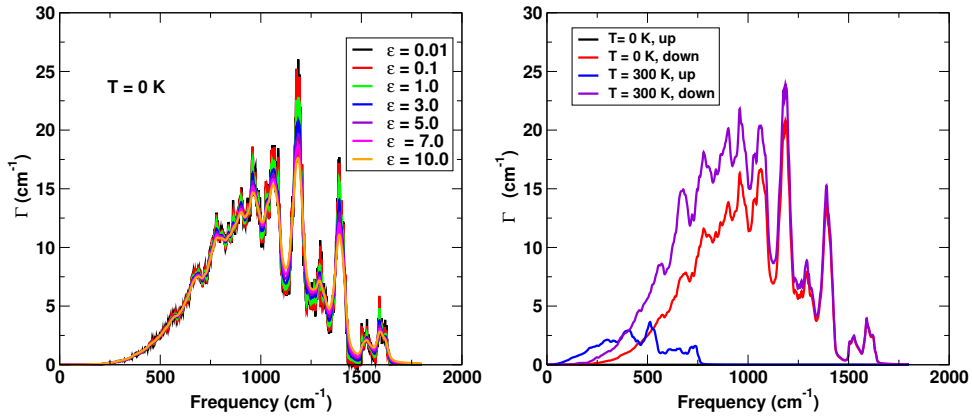

Figure 7.4: Phonon linewidth as a function of frequency of $Y_2Ti_2O_7$. The broadening parameters (ϵ) are in cm^{-1}. The up and down conversion decay processes are shown for two different temperature values and for $\epsilon = 3$ cm^{-1}.

The temperature dependence of the third-order contribution to Δ for 8 vibrational modes including 2 low frequency and 6 high frequency modes is shown in Fig. 7.5. As is evident from the results, $\Delta^{(3)}(T)$ increases with cooling for both the low frequency modes and hence the frequencies of these modes will behave normally, i.e. they will display blue shift or hardening with cooling, unlike in the experiments, where a phonon mode around 200 cm^{-1} shows a huge softening anomaly (see Fig. 7.6). In contrast, out of 6 high frequency modes, 4 modes show interesting behaviour, i.e. their shifts decrease with cooling, which are likely signatures of phonon anomalies. The actual quantitative values of the shifts in the phonon frequencies will depend on the three phonon coupling constant, $V^{(3)}(\mathbf{0}j, \boldsymbol{q}j_1, -\boldsymbol{q}j_2)$, which

we calculate exactly in the next chapter to capture both qualitative and quantitative understanding of temperature dependence of the phonon frequencies. Experimentally also it has been found that the frequency of some of the high frequency modes behaves anomalously.

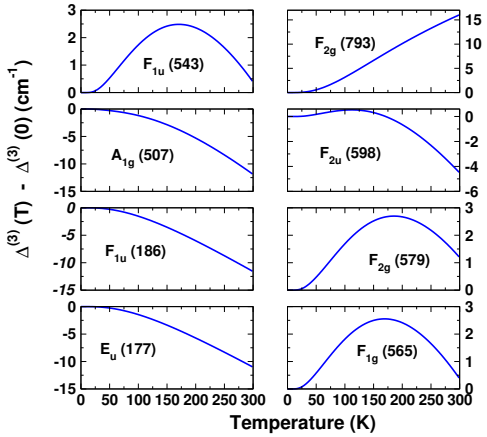

Figure 7.5: Temperature dependence of the cubic contribution to some of the modes in $Y_2Ti_2O_7$. $|C_j^{(3)}|^2 = 1.0 \times 10^{10}$ erg^{-1} was used for all the modes.

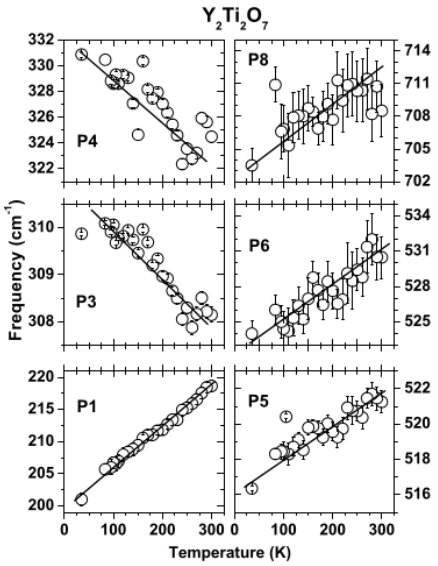

Figure 7.6: Experimental result of temperature dependence of the modes P_1, P_3, P_4, P_5, P_6, and P_8 of non-magnetic pyrochlore $Y_2Ti_2O_7$. Solid lines are quide to eye. The figure is taken from Ref.[5]. See the reference for more details about the assignment of different modes.

7.4 Conclusions

In summary, in this chapter we discussed the temperature dependence of the phonon modes in $Y_2Ti_2O_7$ arising from 3rd order anharmonic interactions.

Within the quasiharmonic approximation, we calculated the mode Grüneisen parameters, temperature dependence of the linear thermal expansion coefficient and frequency shifts for several modes. The temperature variation of the quasiharmonic shifts shows a normal behaviour, i.e. they increase with cooling.

We extensively analysed the two-phonon density of states in $Y_2Ti_2O_7$ to get an understanding of the possible decay channels involved in the phonon linewidths.

The most challenging part in the anharmonic calculations is the ab-initio evaluation of the third-order anharmonic force constant matrix elements. In this chapter, we calculated them using a well-established approach in terms of a single fitting parameter for each mode. Using these, we calculated the third-order frequency shifts as functions of temperature for several modes. An unusual finding in $Y_2Ti_2O_7$ titanate compound is that the third-order shift in frequency for a few of the phonon modes decreases with cooling, a behaviour not generally observed in normal materials, and hence it could lead to anomalous behaviour of these normal modes. Our theoretical calculations fail to capture the phonon anomaly for low frequency modes as observed in experiments, while we do seem able to capture theoretically a qualitative understanding of the phonon anomaly for a few high frequency modes, also observed in experiments. In the next chapter we calculate the properties similar to those studied in this chapter but by calculating the third-order interatomic force constants exactly using the "$2n + 1$" theorem as implemented within the DFT linear response theory.

Chapter 8

Temperature dependent phonon properties of $Y_2Ti_2O_7$ and $Y_2Zr_2O_7$ pyrochlores

In this chapter, we study the temperature-dependent phonon properties in $Y_2Ti_2O_7$ and $Y_2Zr_2O_7$ pyrochlores using DFT and Green's function formalism. These studies are similar to the ones described in the previous chapter but here we actually calculate the third-order interatomic force constant matrix elements exactly using the "$2n + 1$" theorem as implemented within the DFT linear response theory in the Quantum Espresso code. In the previous chapter, all the calculations were carried out using ultrasoft pseudopotentials, while in this chapter the calculations are based on the optimized norm-conserving Vanderbilt pseudopotentials. We have also calculated the mode Grüneisen parameters, the temperature dependence of the linear thermal expansion coefficient and the quasiharmonic contributions to several phonon modes. The full width at half maximum (FWHM) at the zone centre of the BZ and the phonon lifetimes for several modes are studied extensively. Temperature dependence of the FWHM and the cubic shifts are examined and compared for many modes in both the compounds studied in this chapter.

8.1 Introduction

As discussed in earlier chapters, phonons in pyrochlore oxides, particularly titanates reveal a wide variety of interesting properties, e.g., structural instability under pressure, temperature-dependent phonon anomalies, etc. The phonon anomalies in these materials have been attributed to strong phonon-phonon anharmonic interactions, ruling out any contributions from electron-phonon, crystal field-phonon, and

spin-phonon couplings.

Within the harmonic approximation of the lattice potential energy as a function of the nuclear coordinates, the total energy of the system is a sum of energies of the individual harmonic oscillators. Phonons, in this case, are infinitely lived and lead to an infinite thermal conductivity. However, no crystals are strictly harmonic, and it is desirable to incorporate the anharmonic terms of the lattice potential energy. The physical quantity that characterizes the anharmonic effects is the phonon self energy, $\Sigma(\omega, T) = \Delta(\omega, T) - i\Gamma(\omega, T)$, which is a complex function. For a phonon frequency ω, the real part of self-energy, $\Delta(\omega, T)$, is connected with the change in frequency due to the scattering by other phonons. The imaginary part of self energy, $\Gamma(\omega, T)$, represents the probability of phonon decay, and the phonon lifetime is obtained as $\tau(\omega, T) = 1/2\Gamma(\omega, T)$. The later quantity can be evaluated directly in time-resolved experiments[203], while phonon linewidths can be measured by Raman spectroscopy[204, 205].

Initially, ab initio studies of the effects of anharmonic interactions in any materials were based on the frozen-phonon method[195]; but only the Γ-point features can be obtained with this method without the use of supercells, and the supercell calculations required for other points in the BZ are quite challenging numerically.

The extension of DFT to non-linear response functions with the help of the "$2n + 1$" theorem[206] provides an opportunity to calculate the anharmonic coefficients of the total energy. This theorem allows us to obtain the third derivative of the total energy by using only the first derivative of ground-state density and wave functions; contrary to the finite differences method, it is not required to carry out expensive supercell calculations. This method has been used successfully to calculate the anharmonic phonon coupling constant[207] and to examine the phonon linewidths of elemental semiconductors[192] producing very good results compared to experimental results[192, 208].

Here we present the temperature-dependent phonon properties of $Y_2Ti_2O_7$ and $Y_2Zr_2O_7$ pyrochlores using DFT and the Green's function approach. To the best of our knowledge, no such study exists in the literature.

8.2 Computational details

As mentioned earlier, our DFT calculations [83, 84] were carried out using the Quantum Espresso code[110], with optimized norm-conserving Vanderbilt (ONCV) pseudopotentials [152] to represent the interaction between ionic cores and valence electrons. The exchange-correlation energy of electrons was described within the LDA scheme[86]. The Kohn-Sham wave functions were represented using a plane-wave basis with an energy cutoff of 80 Ry. The k-points summation of the electronic energy calculations over the BZ was implemented using the Monkhorst-Pack method with a $3 \times 3 \times 3$ special

k-points mesh[111]. The DFPT calculations were carried out to investigate the phonon properties in the BZ. For the phonon dispersion, dynamical matrices were calculated for a grid of $2 \times 2 \times 2$ $\boldsymbol{q}$-points. The lattice constant was optimized to minimize the total energy, interatomic forces and unit-cell stresses. The Broyden-Fletcher-Goldfarb-Shanno (BFGS) minimization scheme[112] was used in geometry optimization. The "$2n + 1$" theorem as implemented within the Quantum Espresso code was used to calculate the third-order interatomic force constants (IFC3s)[192, 196, 206, 207]. In this context, a grid of $2 \times 2 \times 2$ $\boldsymbol{q}$-points was used for the required dynamical matrix calculations in the BZ.

8.3 Results and discussion

8.3.1 Quasiharmonic results

The quasiharmonic approximation has been described in great detail in section 2.5.1 of Chapter 2. The mode Grüneisen parameter for the j^{th} phonon mode at the centre of BZ were calculated as

$$\gamma_j = -\frac{\partial \ln \omega_j}{\partial \ln V} = -\frac{V}{\omega_j}\frac{\partial \omega_j}{\partial V} \tag{8.1}$$

where V is the cell volume and ω_j is the frequency of j^{th} phonon mode. Frequencies were calculated at different cell volumes and the derivative of the frequency with respect to the volume was calculated by fitting ω_j-V data with the cubic spline polynomials. Calculated values of the mode Grüneisen parameters for several modes of $Y_2Ti_2O_7$ are provided in Table 8.1. To the best of our knowledge, there is no experimental or theoretical data available for the mode Grüneisen parameters for $Y_2Ti_2O_7$ compound to compare with our theoretical results. These results are slightly different from those found in the previous chapter because here the calculations are based on the norm-conserving pseudopotentials, whereas, in the previous chapter, all the calculations were based on the ultrasoft pseudopotentials. Calculated values of the mode Grüneisen parameters for several modes in the case of $Y_2Zr_2O_7$ material are also listed in Table 8.1.

Table 8.1: Calculated values of phonon frequencies and mode Grüneisen parameters in $Y_2Ti_2O_7$ and $Y_2Zr_2O_7$, at $T = 0$ K.

Mode	ω (cm^{-1})	γ	ω (cm^{-1})	γ
	$Y_2Ti_2O_7$		$Y_2Zr_2O_7$	
F_{1u}	74	4.37	85	1.11
E_u	107	4.32		
F_{1u}	143	4.73	134	4.97
E_u	178	1.84		
F_{1u}	189	2.53	189	2.48
F_{1u}	240	1.12	197	0.95
F_{1g}	270	2.28	246	1.82
F_{2g}	301	1.98	310	2.18
A_{2u}	305	2.31	294	0.44
F_{2u}	317	1.88	316	1.35
E_g	334	2.11	350	1.93
F_{1u}	385	2.27	345	2.39
A_{2u}	395	1.10	394	1.28
A_{2u}	409	1.44		
F_{2g}	447	1.96	406	1.35
F_{1u}	462	1.73	414	1.64
E_u	487	2.40	425	1.47
A_{1g}	506	1.45	506	1.18
F_{1u}	540	3.23	533	1.31
F_{1g}	570	1.10	604	1.78
F_{2g}	580	1.73	527	1.04
F_{2u}	602	1.70	619	1.71
F_{2g}	797	1.37	784	1.21

Within the quasiharmonic approximation, the temperature dependence of the frequency shift is obtained via the temperature dependence of the linear thermal expansion coefficient:

$$\Delta_j^{(0)}(T) = \omega_j(0)\left[e^{-3\gamma_j \int_0^T \alpha(T')dT'} - 1\right] \tag{8.2}$$

where $\omega_j(0)$ and γ_j correspond to the frequency and the mode Grüneisen parameter for $(\mathbf{0}j)$ mode at

temperature $T = 0$ K. The linear thermal expansion coefficient is calculated using the expression

$$\alpha = \frac{1}{3BV} \sum_{\boldsymbol{q}j} \left[\gamma_j(\boldsymbol{q}) \frac{(\hbar\omega_j(\boldsymbol{q}))^2}{k_B T^2} \frac{e^{\hbar\omega_j(\boldsymbol{q})/k_B T}}{(e^{\hbar\omega_j(\boldsymbol{q})/k_B T} - 1)^2} \right] \tag{8.3}$$

where B is the bulk modulus, V the cell-volume, and $\gamma_j(\boldsymbol{q})$ is the mode Grüneisen parameter for the j^{th} vibrational mode with wave-vector $\mathbf{q}$.

The calculation of the linear thermal expansion coefficient (Eq. 8.3) involves the dispersion of the mode Grüneisen parameter, $\gamma_j(\boldsymbol{q})$, which is a bit trickier to calculate as it is defined as the logarithmic derivative of frequencies with respect to the volume. Cubic spline polynomials were used to calculate $\gamma_j(\boldsymbol{q})$.

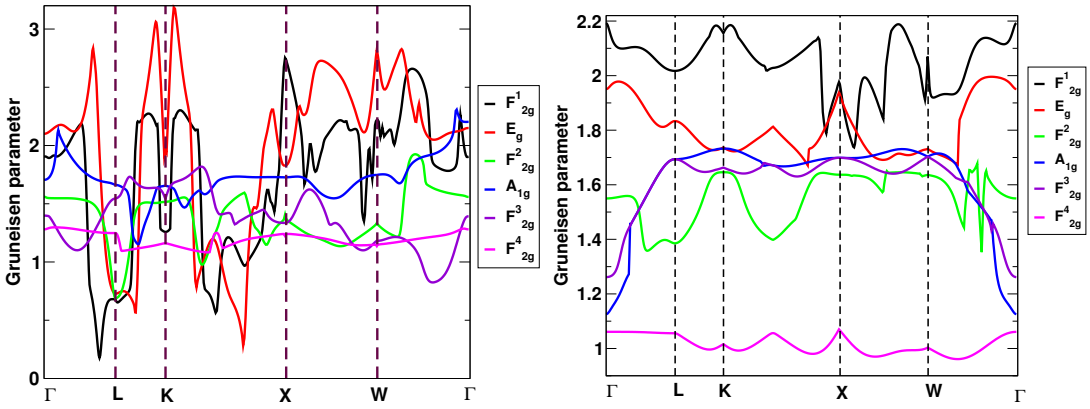

Figure 8.1: Variation of the mode Grüneisen parameters for Raman active modes in $Y_2Ti_2O_7$ (left panel) and $Y_2Zr_2O_7$ (right panel), along the high symmetry directions in the BZ.

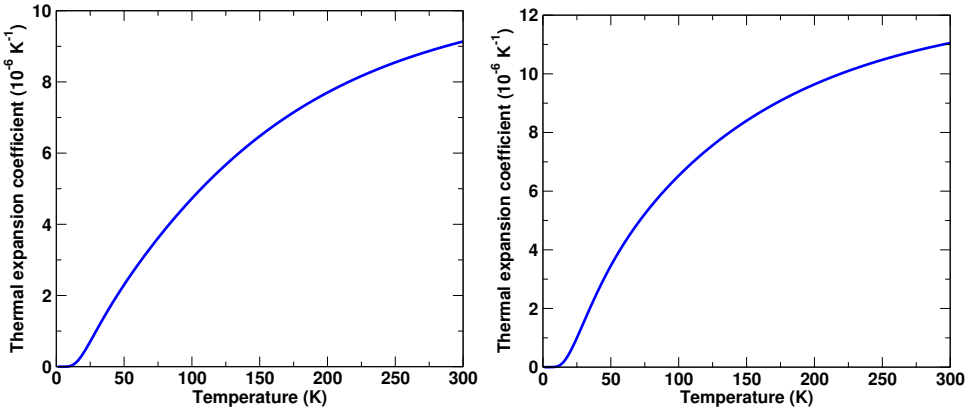

Figure 8.2: Temperature dependence of the linear thermal expansion coefficient in $Y_2Ti_2O_7$ (left panel) and $Y_2Zr_2O_7$ (right panel).

The calculated $\gamma_j(\boldsymbol{q})$ values for the Raman active modes of $Y_2Ti_2O_7$ and $Y_2Zr_2O_7$ pyrochlore compounds are shown in Fig. 8.1 along the high symmetry directions of the BZ. These results were obtained

by calculating the wavevector dependence of frequencies at a few high pressure values and fitting the $\omega_j(\boldsymbol{q}) - V$ data using cubic spline polynomials. The range of $\gamma_j(\boldsymbol{q})$ obtained lies between 0.3-3.1 and 0.8-2.2 for $Y_2Ti_2O_7$ and $Y_2Zr_2O_7$, respectively. The temperature variation of the linear thermal expansion coefficient of $Y_2Ti_2O_7$ and $Y_2Zr_2O_7$ pyrochlores is shown in Fig. 8.2.

The temperature dependent contributions from the quasiharmonic shifts for Raman active, IR active, and silent modes of $Y_2Ti_2O_7$ and $Y_2Zr_2O_7$ pyrochlores are shown in Figs. 8.3 and 8.4, respectively. As expected, these shifts in frequency for all the studied modes decrease with cooling in both the compounds. To the best of our knowledge, there are no experimental data or previous theoretical calculations available for these systems with which to compare our theoretical results.

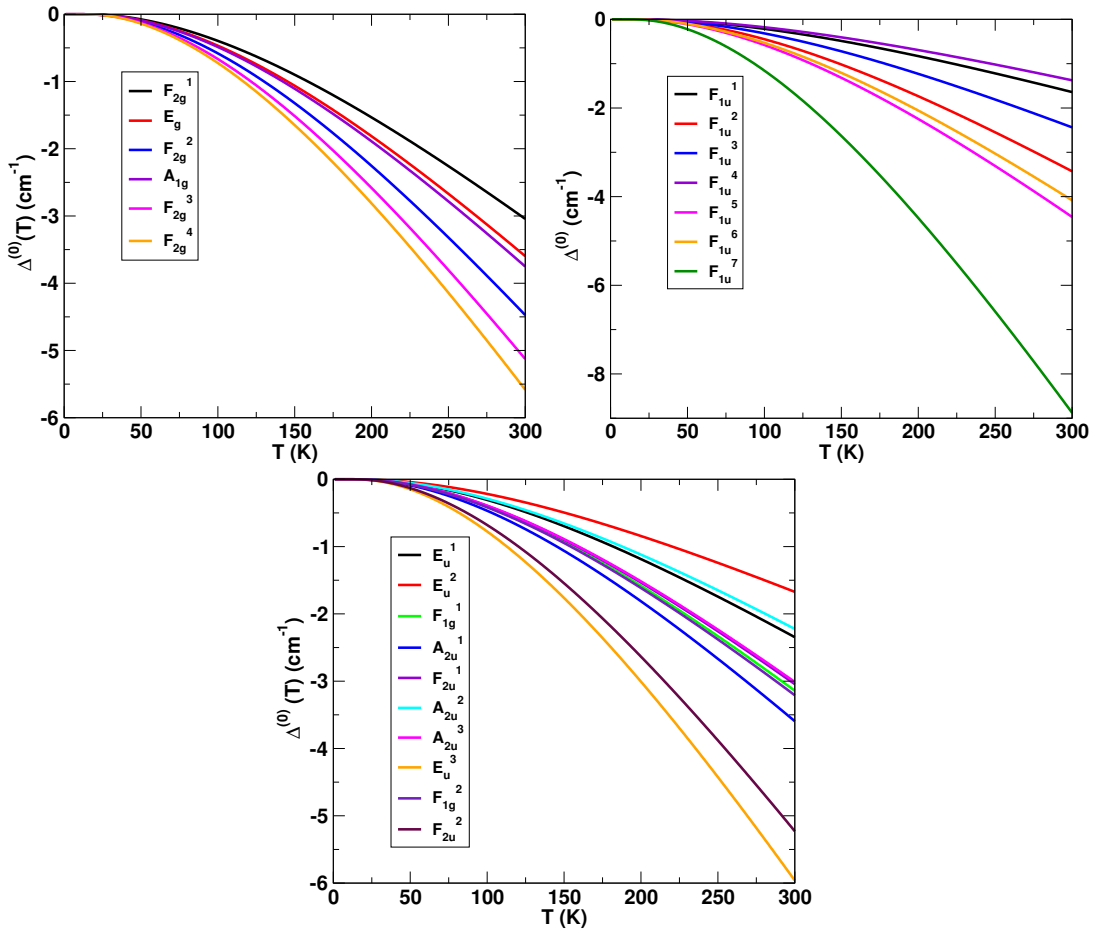

Figure 8.3: Temperature dependence of the Quasiharmonic contribution to Raman active(top left), IR active (top right), and silent modes(bottom) in $Y_2Ti_2O_7$ compound.

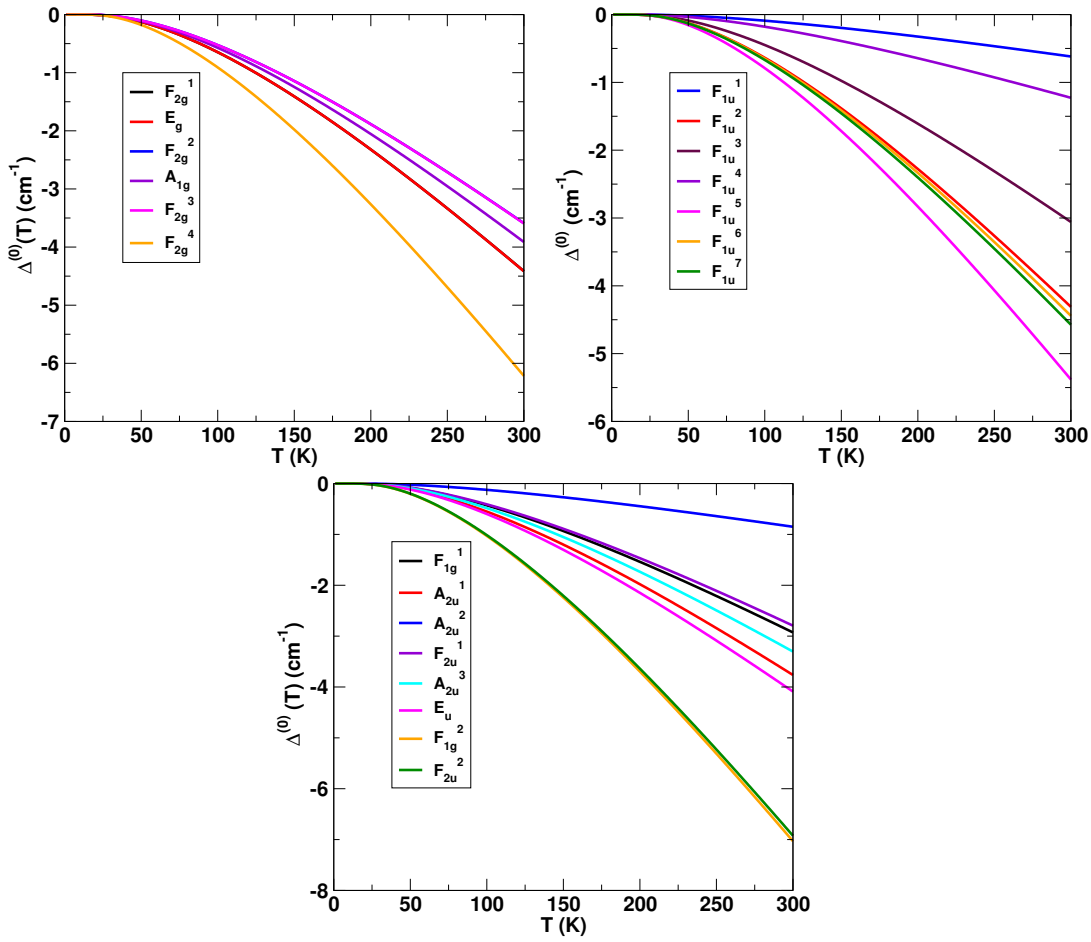

Figure 8.4: Temperature dependence of the Quasiharmonic contribution to Raman active(top left), IR active (top right), and silent modes(bottom) in $Y_2Zr_2O_7$ compound.

8.3.2 Anharmonic calculations

After neglecting the electron-phonon, crystal field-phonon, and spin-phonon, and all the terms beyond the third-order anharmonic corrections, the temperature dependence of the frequency of the j^{th} phonon mode at the centre of the BZ is obtained as

$$\omega_j(T) = \omega_j(0) + \Delta_j^{(0)}(\omega, T) + \Delta_j^{(3)}(\omega, T) \tag{8.4}$$

where $\Delta_j^{(0)}(\omega, T)$ and $\Delta_j^{(3)}(\omega, T)$ are the quasiharmonic and the (leading) third-order anharmonic contributions to the shifts, respectively.

As discussed earlier, the phonon lineshifts and the linewidths are calculated as

$$\begin{aligned}\Delta^{(3)}(\omega_j) &= -\frac{18}{\hbar^2}\sum_{\boldsymbol{q},j_1j_2}|V^{(3)}(\mathbf{0}j;\boldsymbol{q}j_1;-\boldsymbol{q}j_2)|^2 \\ &\times \mathcal{P}\left[\frac{n_1+n_2+1}{\omega+\omega_1+\omega_2}-\frac{n_1+n_2+1}{\omega-\omega_1-\omega_2}+\frac{n_1-n_2}{\omega-\omega_1+\omega_2}-\frac{n_1-n_2}{\omega+\omega_1-\omega_2}\right] \qquad (8.5)\end{aligned}$$

$$\begin{aligned}\Gamma(\omega_j) &= \frac{18\pi}{\hbar^2}\sum_{\boldsymbol{q},j_1j_2}|V^{(3)}(\mathbf{0}j;\boldsymbol{q}j_1;-\boldsymbol{q}j_2)|^2 \\ &\times [(n_1+n_2+1)\delta(\omega-\omega_1-\omega_2)+2(n_1-n_2)\delta(\omega+\omega_1-\omega_2)] \qquad (8.6)\end{aligned}$$

where $\omega_1 = \omega_{j_1}(\boldsymbol{q})$ and $\omega_2 = \omega_{j_2}(-\boldsymbol{q})$. The three phonon coupling constant matrix elements are evaluated as

$$\begin{aligned}V^{(3)}(\mathbf{0},j;\boldsymbol{q},j_1;-\boldsymbol{q},j_2) &= \left(\frac{\hbar^3}{8\omega_j(\mathbf{0})\omega_{j_1}(\boldsymbol{q})\omega_{j_2}(-\boldsymbol{q})}\right)^{1/2}\sum_{ss's'',\alpha\beta\gamma}\left(\frac{1}{M_sM_{s'}M_{s''}}\right)^{1/2}e_{s,\alpha}(\mathbf{0}j)e_{s',\beta}(\boldsymbol{q}j_1)e_{s'',\gamma}(-\boldsymbol{q}j_2) \\ &\times \sum_{ll'}\frac{1}{N\sqrt{N}}\frac{\partial^3E}{\partial u^0_{s,\alpha}\partial u^l_{s',\beta}\partial u^{l'}_{s'',\gamma}}e^{i\boldsymbol{q}.(\boldsymbol{R}(l)-\boldsymbol{R}(l'))} \qquad (8.7)\end{aligned}$$

The most challenging part, as we have mentioned before, is the numerical evaluation of the third order phonon coupling constant, $V^{(3)}(\mathbf{0}j;\boldsymbol{q}j_1;-\boldsymbol{q}j_2)$. In the next section, we describe the details of the calculations of this third-order coupling constant.

Third order derivative by density-functional perturbation theory

The harmonic frequencies and atomic displacements corresponding to a phonon mode can readily be obtained utilizing the DFPT by carrying out the linear response to a perturbation that, in our case, is a displacement of the atom from the equilibrium position. The linear response to a small perturbation is also adequate for evaluating the third-order derivative of the total energy with respect to the small perturbation. This is the special case of "$2n+1$" theorem. The formulation of this theorem in a density-functional framework is due to Gonze and Vigneron[206], which provides a specific formula for the third-order derivative. This expression was subsequently reformulated by Debernardi and Baroni for facilitating numerical calculations[207]. This technique has been successfully used to compute the anharmonic phonon coupling constants[207] and to study the phonon linewidths of elemental semiconductors[192], providing very good results compared to experimental data[208].

It is useful to turn to reciprocal space and to introduce the reciprocal-space anharmonic force constants defined as

$$C_{ss's'',\alpha\beta\gamma}(\boldsymbol{q}_1,\boldsymbol{q}_2,\boldsymbol{q}_3)=\frac{1}{\sqrt{N^3}}\sum_{l,l',l''}\frac{\partial^3 E_{tot}}{\partial u^l_{s,\alpha}\partial u^{l'}_{s',\beta}\partial u^{l''}_{s'',\gamma}}e^{i\boldsymbol{q}_1.\boldsymbol{R}^l}e^{i\boldsymbol{q}_2.\boldsymbol{R}^{l'}}e^{i\boldsymbol{q}_3.\boldsymbol{R}^{l''}} \tag{8.8}$$

where the $\boldsymbol{q}$'s are in the first BZ. The translational invariance of the system leads to the constraint:

$$\boldsymbol{q}_1+\boldsymbol{q}_2+\boldsymbol{q}_3=\boldsymbol{G} \tag{8.9}$$

where $\boldsymbol{G}$ is a reciprocal-lattice vector. It can easily be recognized that $C_{ss's'',\alpha\beta\gamma}(\boldsymbol{0},\boldsymbol{q},-\boldsymbol{q})$ is the anharmonic term that appears in the last line of Eq. 8.7. The atomic displacement in reciprocal space is defined as

$$\boldsymbol{u}_s(\boldsymbol{q})=\frac{1}{\sqrt{N}}\sum_l \boldsymbol{u}^l_s e^{-\boldsymbol{q}.\boldsymbol{R}^l} \tag{8.10}$$

In the following we replace, for simplicity, the double index (s,α) by p ($p=1,\ldots,3n$). Using the formula for the derivative of many variable functions, we rewrite the anharmonic tensor C in term of derivatives with respect to $\boldsymbol{u}(\boldsymbol{q})$:

$$C_{pp'p''}(\boldsymbol{q}_1,\boldsymbol{q}_2,\boldsymbol{q}_3)=\frac{\partial^3 E_{tot}}{\partial u_p(\boldsymbol{q}_1)\partial u_{p'}(\boldsymbol{q}_2)\partial u_{p''}(\boldsymbol{q}_3)} \tag{8.11}$$

By solving the linear response equations, one can obtain the first derivate of the density and wavefunction corresponding to the three phonons. The third derivative of the total energy can then be obtained from[209]:

$$\begin{aligned}\frac{\partial^3 E_{tot}}{\partial u_p(\boldsymbol{q}_1)\partial u_{p'}(\boldsymbol{q}_2)\partial u_{p''}(\boldsymbol{q}_3)} &= \frac{1}{6}[\tilde{E}_{pp'p''}(\boldsymbol{q}_1,\boldsymbol{q}_2,\boldsymbol{q}_3)+\tilde{E}_{p'pp''}(\boldsymbol{q}_2,\boldsymbol{q}_1,\boldsymbol{q}_3)+\tilde{E}_{pp''p'}(\boldsymbol{q}_1,\boldsymbol{q}_3,\boldsymbol{q}_2)\\ &+ \tilde{E}_{p''pp'}(\boldsymbol{q}_3,\boldsymbol{q}_1,\boldsymbol{q}_2)+\tilde{E}_{p'p''p}(\boldsymbol{q}_2,\boldsymbol{q}_3,\boldsymbol{q}_1)+\tilde{E}_{p''p'p}(\boldsymbol{q}_3,\boldsymbol{q}_2,\boldsymbol{q}_1)]\end{aligned} \tag{8.12}$$

where

$$\begin{aligned}\tilde{E}_{pp'p''}(\boldsymbol{q}_1,\boldsymbol{q}_2,\boldsymbol{q}_3) &= Z_{pp'p''}(\boldsymbol{q}_1,\boldsymbol{q}_2,\boldsymbol{q}_3)+\frac{\partial^3 E_{ion}}{\partial u_p(\boldsymbol{q}_1)\partial u_{p'}(\boldsymbol{q}_2)\partial u_{p''}(\boldsymbol{q}_3)}+\int n(\boldsymbol{r})\frac{\partial^3 V_{ion}}{\partial u_p(\boldsymbol{q}_1)\partial u_{p'}(\boldsymbol{q}_2)\partial u_{p''}(\boldsymbol{q}_3)}d\boldsymbol{r}\\ &+ 3\int\frac{\partial n(\boldsymbol{r})}{\partial u_p(\boldsymbol{q}_1)}\frac{\partial^2 V_{ion}}{\partial u_{p'}(\boldsymbol{q}_2)\partial u_{p''}(\boldsymbol{q}_3)}d\boldsymbol{r}+\int\int\int\frac{\delta^3 E_I[n]}{\delta n(\boldsymbol{r})\delta n(\boldsymbol{r}')\delta n(\boldsymbol{r}'')}\\ &\times \frac{\partial n(\boldsymbol{r})}{\partial u_p(\boldsymbol{q}_1)}\frac{\partial n(\boldsymbol{r}')}{\partial u_{p'}(\boldsymbol{q}_2)}\frac{\partial n(\boldsymbol{r}'')}{\partial u_{p''}(\boldsymbol{q}_3)}d\boldsymbol{r}d\boldsymbol{r}'d\boldsymbol{r}''\end{aligned} \tag{8.13}$$

Here the first term on the right hand side of the above equation is given by[183, 207, 209]

$$\begin{aligned} Z_{pp'p''}(\boldsymbol{q}_1, \boldsymbol{q}_2, \boldsymbol{q}_3) &= \sum_{v} \left\langle \frac{\partial \psi_v}{\partial u_p(\boldsymbol{q}_1)} \left| P_c \frac{\partial H}{\partial u_{p'}(\boldsymbol{q}_2)} P_c \right| \frac{\partial \psi_v}{\partial u_{p''}(\boldsymbol{q}_3)} \right\rangle \\ &- \sum_{vv'} \left\langle \frac{\partial \psi_v}{\partial u_p(\boldsymbol{q}_1)} |P_c| \frac{\partial \psi_{v'}}{\partial u_{p'}(\boldsymbol{q}_2)} \right\rangle \left\langle \psi_{v'} \left| \frac{\partial H}{\partial u_{p''}(\boldsymbol{q}_3)} \right| \psi_v \right\rangle \end{aligned} \tag{8.14}$$

where the index v represents the occupied or valance states and P_c is the projector defined on the manifold spanned by the empty states (conduction band states). The second term on the right side of Eq. 8.13 is the ionic contribution to the third derivative of the total energy.

The details regarding the first-order change in the density and eigenvectors with respect to the phonon displacement vector $\boldsymbol{u}(\boldsymbol{q})$ within linear response theory, Ionic contribution, and the derivatives of the external potential are given in Ref.[209].

The FWHM calculated at $\boldsymbol{q} = \boldsymbol{0}$ and the lifetimes of several phonon modes of $Y_2Ti_2O_7$ are shown in Table 8.2. To the best of our knowledge, no experimental data or prior theoretical calculations are available for these quantities in $Y_2Ti_2O_7$ to compare with our theoretical results. As is evident from our calculations, the low frequency modes have higher lifetimes than the high frequency modes. The lifetime of F_{1g} silent mode of frequency 570 cm^{-1} is the smallest among all the modes, and the next smallest lifetime is for the F_{2g} Raman active mode of frequency 797 cm^{-1}. The lowest lifetimes found for these two modes are most likely related to the anomalous nature of these two modes as also found in the previous chapter.

Table 8.2: Calculated values of phonon frequencies, FWHM, and lifetimes in $Y_2Ti_2O_7$, at $T = 0$ K.

Mode	ω (cm^{-1})	$2\Gamma(0)$ (cm^{-1})	τ (ps)
F_{1u}	74	0.05	106.1
E_u	107	0.06	84.2
F_{1u}	143	0.41	13.0
E_u	178	0.30	18.0
F_{1u}	189	0.80	6.6
F_{1u}	240	0.84	6.3
F_{1g}	270	4.52	1.2
F_{2g}	301	2.08	2.6
A_{2u}	305	1.93	2.8
F_{2u}	317	3.88	1.4
E_g	334	4.15	1.3
F_{1u}	385	3.51	1.5
A_{2u}	395	4.45	1.2
A_{2u}	409	1.10	4.8
F_{2g}	447	3.56	1.5
F_{1u}	462	1.03	5.1
E_u	487	5.80	0.9
A_{1g}	506	6.04	0.9
F_{1u}	540	7.93	0.7
F_{1g}	570	23.81	0.2
F_{2g}	580	3.99	1.3
F_{2u}	602	5.64	0.9
F_{2g}	797	17.33	0.3

The FWHM and lifetimes of several modes in $Y_2Zr_2O_7$ compound are shown in Table 8.3. Again, to the best of our knowledge, no literature data is available for this system too to compare with our theoretical results. In the case of $Y_2Zr_2O_7$ material also, the low frequency modes are found to be longer lived compared to the high frequency modes.

Table 8.3: Calculated values of phonon frequencies, FWHM, and lifetimes in $Y_2Zr_2O_7$, at $T = 0$ K.

Mode	ω (cm^{-1})	$2\Gamma(0)$ (cm^{-1})	τ (ps)
F_{1u}	85	0.02	265.3
F_{1u}	134	0.06	93.1
F_{1u}	189	1.11	4.8
F_{1u}	197	0.66	8.1
F_{1g}	246	8.72	0.6
A_{2u}	268	0.65	8.2
A_{2u}	294	0.64	8.3
F_{2g}	310	3.31	1.6
F_{2u}	316	2.11	2.5
F_{1u}	345	2.23	2.4
E_g	350	0.98	5.4
A_{2u}	394	0.56	9.5
F_{2g}	406	1.78	3.0
F_{1u}	414	3.58	1.5
E_u	425	2.60	2.0
A_{1g}	506	4.26	1.2
F_{2g}	527	5.87	0.9
F_{1u}	533	3.88	1.4
F_{1g}	604	7.81	0.7
F_{2u}	619	5.75	0.9
F_{2g}	784	15.43	0.3

The temperature variation of the third-order contributions to the Raman, IR, and silent modes of $Y_2Ti_2O_7$ and $Y_2Zr_2O_7$ pyrochlore oxides is shown in Figs. 8.5 and 8.6, respectively. The shifts for total 5 modes in each of the systems decrease with cooling, but when we add all the contributions, i.e. quasiharmonic and the third-order anharmonic contributions to the zeroth order term, only two modes - the F_{1g} mode of frequency 570 cm^{-1} and the F_{2g} mode of frequency 797 cm^{-1} - turn out to be anomalous (i.e. they show a redshift with cooling) in the case of $Y_2Ti_2O_7$ (Fig. 8.7), whereas all the modes behave normally (i.e. they show a blueshift with cooling) in the case of $Y_2Zr_2O_7$ (Fig. 8.8). Among the two anomalous modes in $Y_2Ti_2O_7$, the F_{1g} mode shows a huge anomaly (i.e. $\omega(300K) - \omega(0K) = 15$ cm^{-1}) compared to the other anomalous mode (i.e. $\omega(300K) - \omega(0K) = 0.4$ cm^{-1}). The anomalous F_{2g} mode - a Raman active mode - behaves interestingly with temperature, i.e. its frequency first increases with increasing temperature up to 200 K, then it starts decreasing, but the change is quite small in both the regimes.

These results for the temperature dependent phonon frequencies in $Y_2Ti_2O_7$ and $Y_2Zr_2O_7$ are similar to the experimental results in $Sm_2Ti_{2-x}Zr_xO_7$, where some of the phonon modes in $Sm_2Ti_2O_7$ display anomalous behaviour with cooling, whereas no anomaly is observed for any of the phonon modes in the case of $Sm_2Zr_2O_7$.

Our theoretical calculations fail to explain the phonon anomaly for the low frequency modes as observed in experiments in the case of $Y_2Ti_2O_7$ titanate pyrochlore, but are able to capture the anomalous

nature of two high frequency modes. Our theoretical findings of the anomalous behaviour of the high frequency modes is consistent with the experimental observations where also it has been found that a few high frequency modes in $Y_2Ti_2O_7$ show anomalous behaviour with cooling. Thus, it is still an open theoretical problem to explain the phonon anomaly for the low frequency modes. It would be quite interesting to see what happens when one also includes the higher order terms of the lattice anharmonic potential, other than the leading quasiharmonic and third order anharmonic corrections. At present there is no access to lattice anharmonic interactions beyond the third-order in the DFT linear response theory.

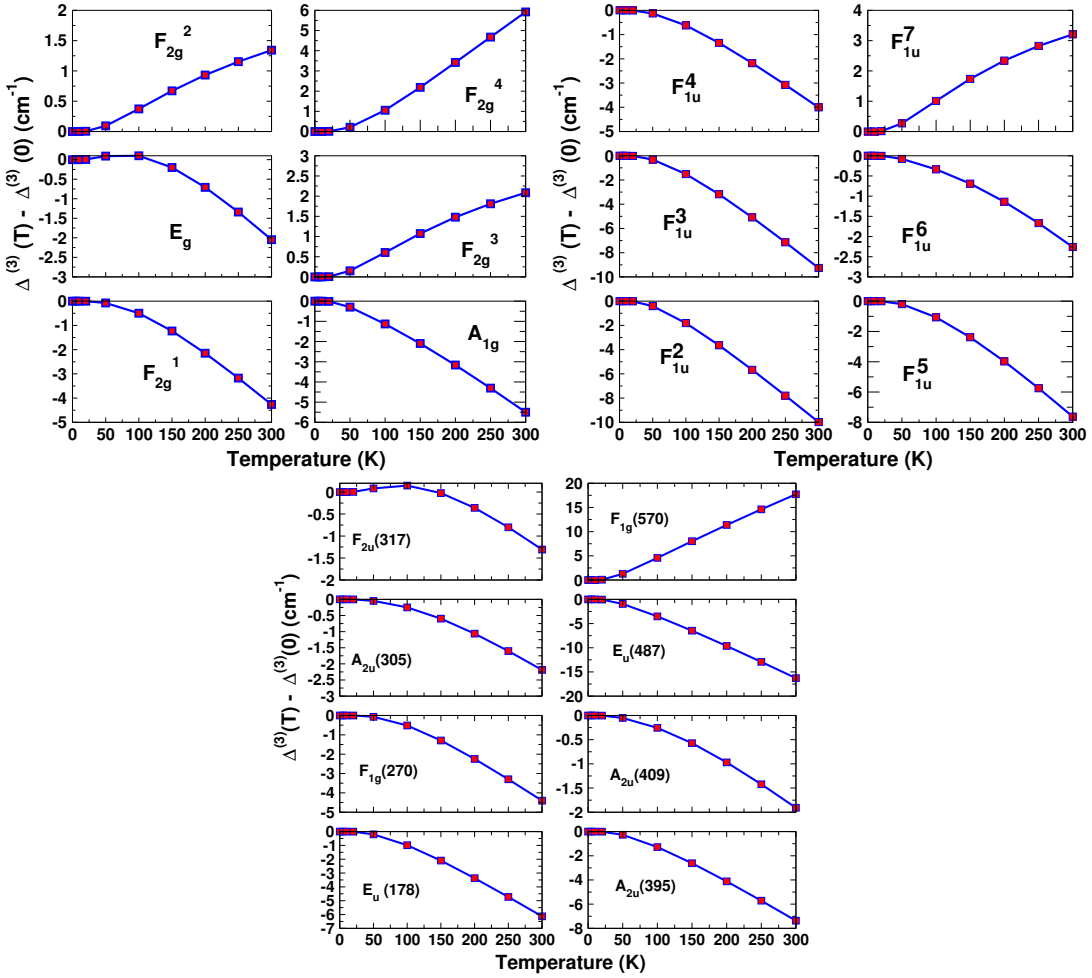

Figure 8.5: Temperature dependence of cubic contribution to Raman active(top left), IR active (top right), and silent modes(bottom) in $Y_2Ti_2O_7$.

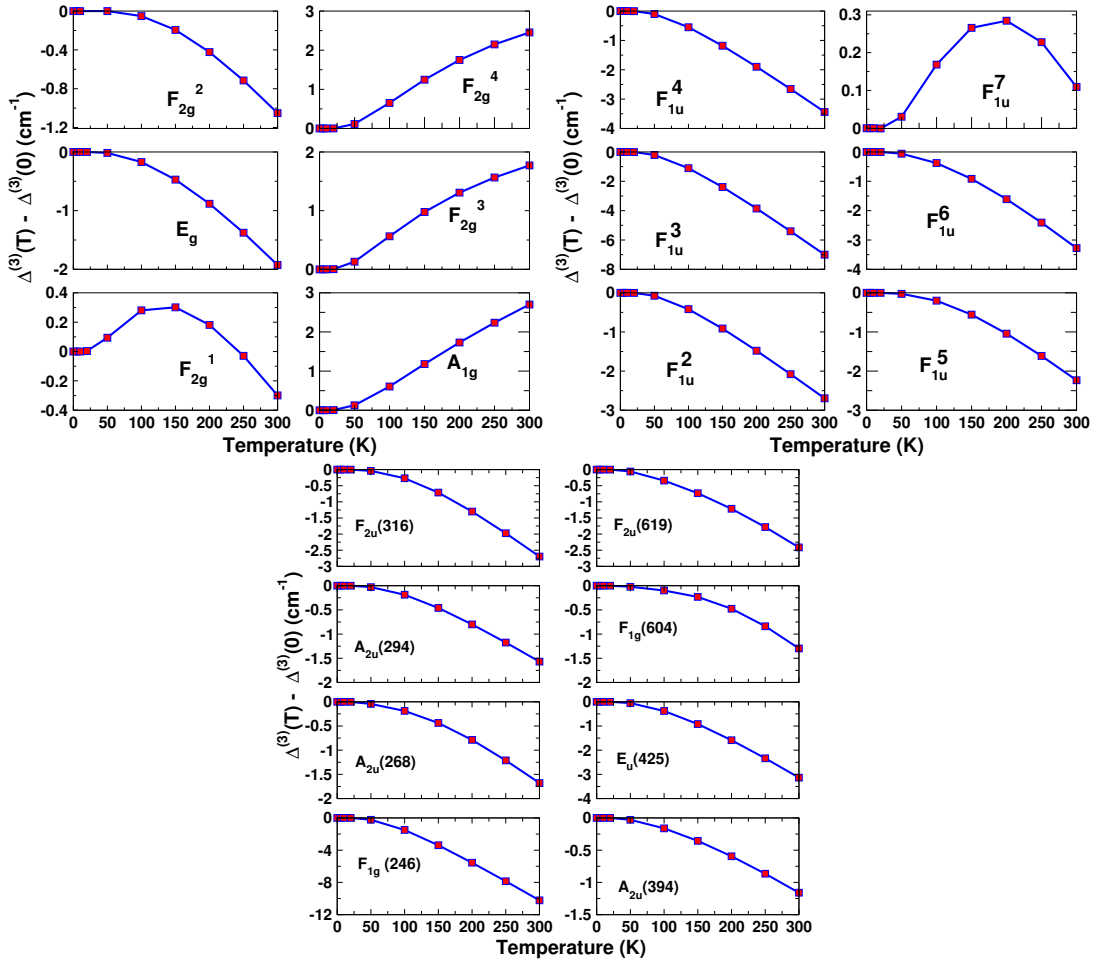

Figure 8.6: Temperature dependence of cubic contribution to Raman active(top left), IR active (top right), and silent modes(bottom) in $Y_2Zr_2O_7$.

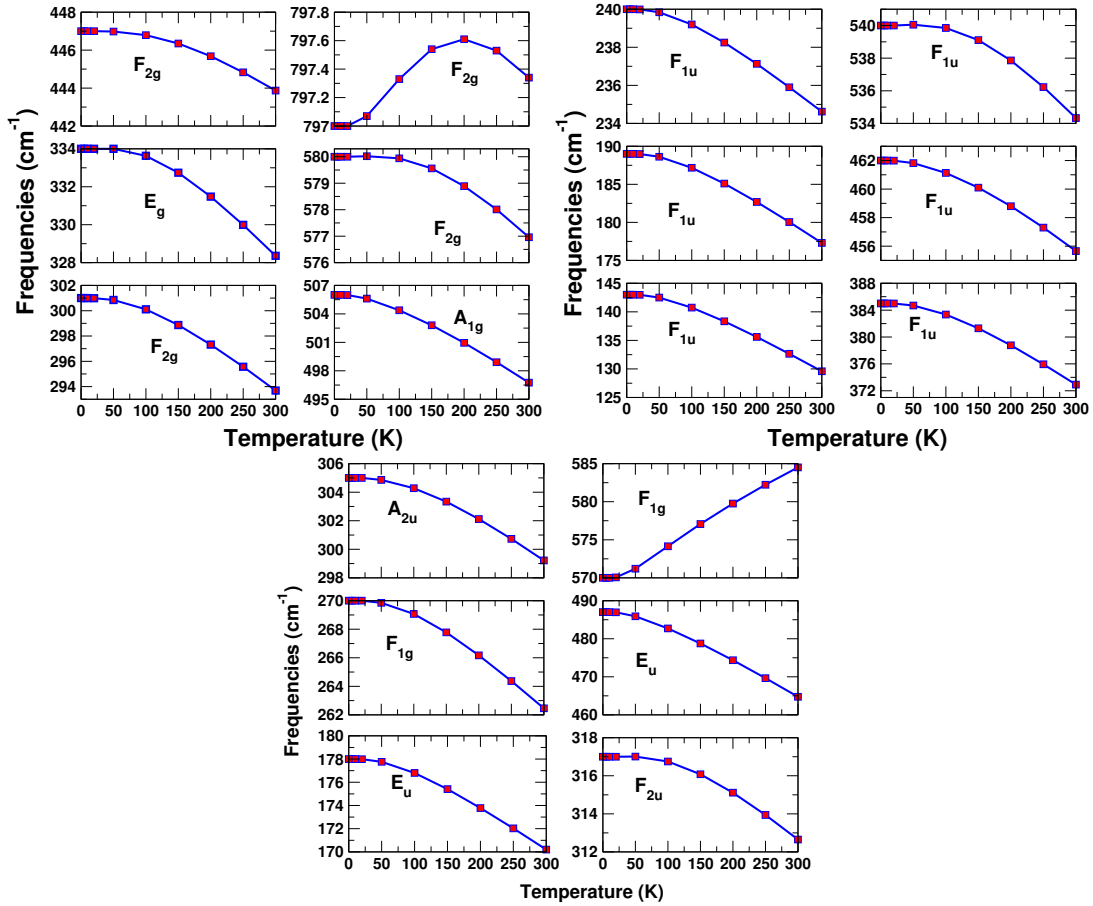

Figure 8.7: Temperature variation of phonon frequencies of Raman active(top left), IR active (top right), and silent modes(bottom) in $Y_2Ti_2O_7$.

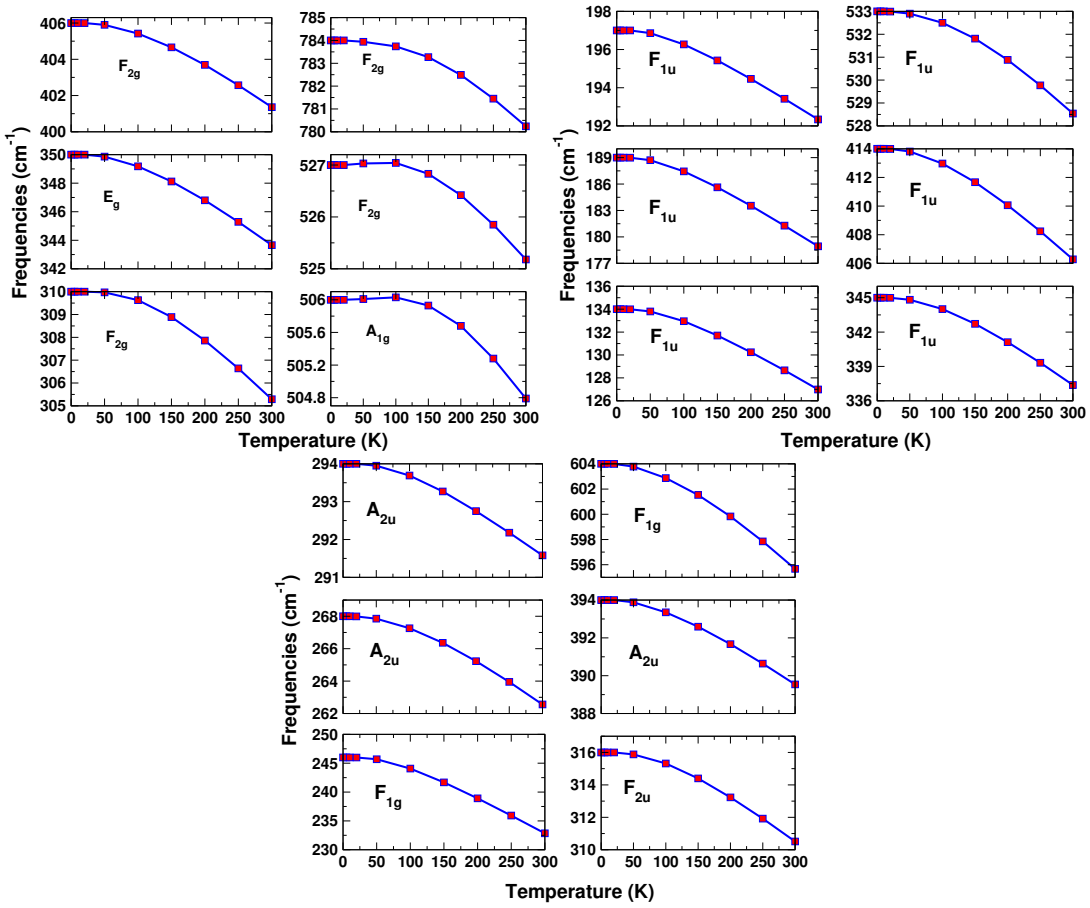

Figure 8.8: Temperature variation of phonon frequencies of Raman active(top left), IR active (top right), and silent modes(bottom) in $Y_2Zr_2O_7$.

The temperature variation of the FWHM or 2Γ for the Raman active, IR active, and silent modes calculated at the centre of the BZ is shown in Figs. 8.9 and 8.9 for $Y_2Ti_2O_7$ and $Y_2Zr_2O_7$, respectively. Since the FWHM is directly proportional to the phonon population, its value should increase with increasing the temperature; as the temperature increases, the phonon population in any $\boldsymbol{q}j$ mode also increases. Our theoretical results clearly show a similar trend, wherein the FWHM increases for all the modes with increasing the temperature. At very low temperatures, they are almost constant for all the modes, while at very high temperatures, they vary linearly with temperature. These behaviours of FWHM can easily be understood in the limiting regimes of temperatures.

At very low temperatures, contributions from the down conversion processes are significantly larger than the up conversion processes (as discussed in great detail in the previous chapter). Thus, after neglecting the up conversion term, the phonon linewidth is obtained as

$$\Gamma(\omega_j) \simeq \frac{18\pi}{\hbar^2} \sum_{\boldsymbol{q},j_1 j_2} |V^{(3)}(\boldsymbol{0}j;\boldsymbol{q}j_1;-\boldsymbol{q}j_2)|^2 (n_1+n_2+1)\delta(\omega-\omega_1-\omega_2) \tag{8.15}$$

where the phonon occupation number is given as

$$n(\omega_j(\boldsymbol{q})) = \frac{1}{e^{\hbar\omega_j(\boldsymbol{q})/k_BT} - 1} \tag{8.16}$$

Since the sum over the $\boldsymbol{q}$-grid in Eq. 8.15 excludes the $\boldsymbol{q} = 0$ point in the calculations, at very low temperatures $\hbar\omega_j(\boldsymbol{q})/k_BT \gg 1$, and hence the phonon occupation number goes as $n(\omega_j(\boldsymbol{q})) \sim e^{-\hbar\omega_j(\boldsymbol{q})/k_BT}$. Thus, the term $(n_1 + n_2 + 1)$ is almost independent of temperature at very low temperatures; in our case the FWHM remains almost constant for temperatures up-to 30 K for both the compounds under study.

On the other hand, as the temperature increases, the up conversion process also starts contributing. In this case the linewidth or the FWHM is calculated from Eq. 8.6. At very high temperatures ($T \sim$ 1000 K or more), $\hbar\omega_j(\boldsymbol{q})/k_BT \ll 1$, and the phonon occupation number is directly proportional to temperature, i.e. $n(\omega_j(\boldsymbol{q})) \sim k_BT/\hbar\omega_j(\boldsymbol{q})$. Thus, the linewidths at very high temperatures are given by

$$\begin{aligned}\Gamma(\omega) &\simeq k_BT\frac{18\pi}{\hbar^2}\sum_{\boldsymbol{q},j_1j_2}|V^{(3)}(\mathbf{0}j;\boldsymbol{q}j_1;-\boldsymbol{q}j_2)|^2 \\ &\times \left[\left(\frac{1}{\hbar\omega_1}+\frac{1}{\hbar\omega_2}+1\right)\delta(\omega-\omega_1-\omega_2)+2\left(\frac{1}{\hbar\omega_1}-\frac{1}{\hbar\omega_2}\right)\delta(\omega+\omega_1-\omega_2)\right]\end{aligned} \tag{8.17}$$

Thus, at high temperatures, the FWHM varies linearly with temperature. But, at very high temperatures, other anharmonic terms of the lattice potential, other than the quasiharmonic and the third-order anharmonic corrections, may also be important to include in the calculations. Hence, all our calculations in this work are up to the temperature of 300 K only.

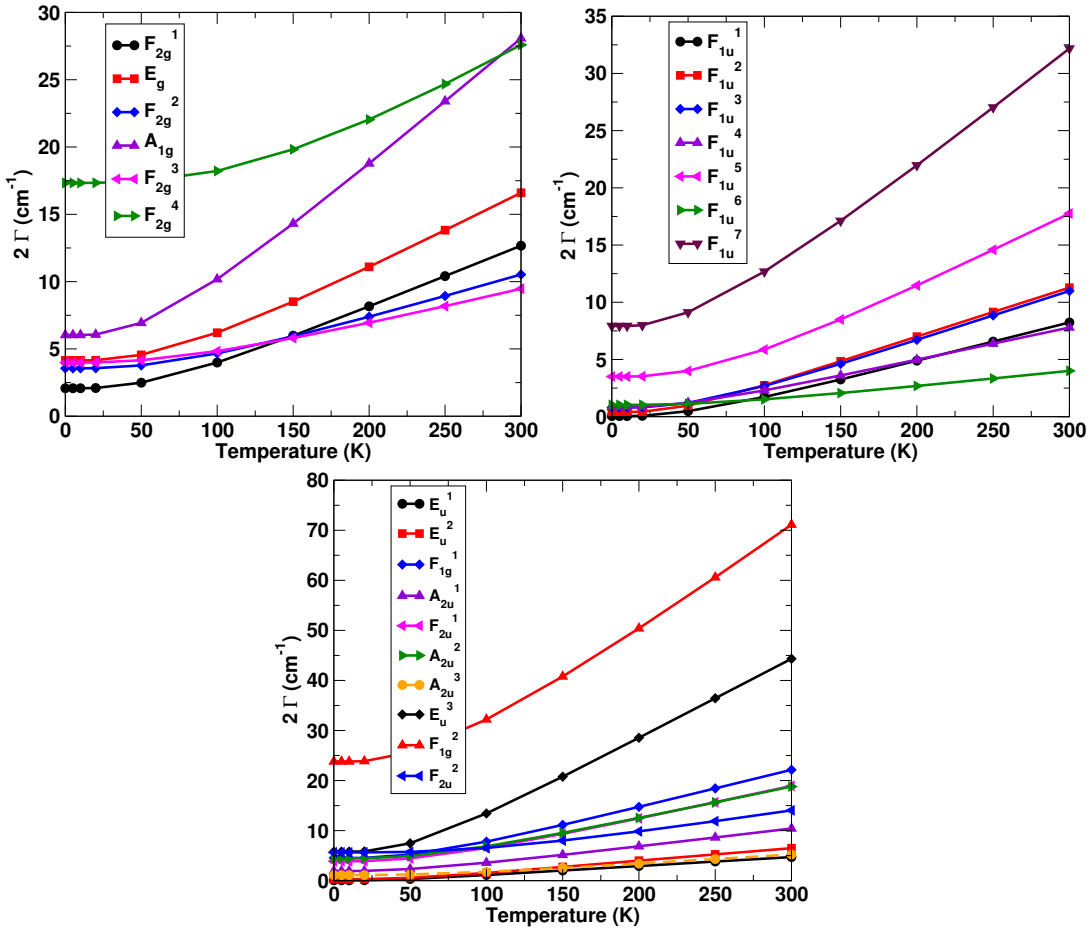

Figure 8.9: Temperature variation of the FWHM of Raman active(top left), IR active (top right), and silent modes(bottom) in $Y_2Ti_2O_7$.

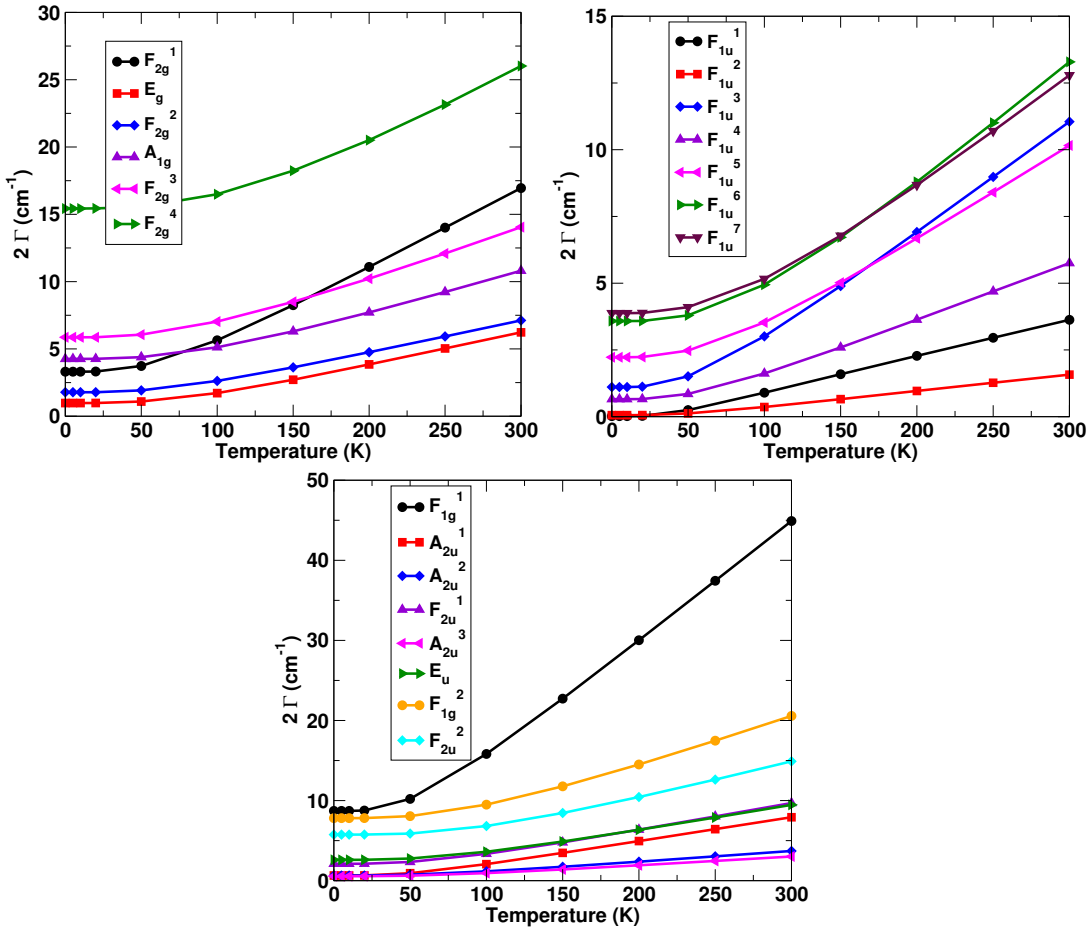

Figure 8.10: Temperature variation of the FWHM of Raman active(top left), IR active (top right), and silent modes(bottom) in $Y_2Zr_2O_7$.

8.4 Conclusions

In summary, in this chapter we discussed the temperature dependence of the phonon modes in $Y_2Ti_2O_7$ and $Y_2Zr_2O_7$ arising from 3rd order anharmonic interactions.

Within the quasiharmonic approximation, we calculated the mode Grüneisen parameters, the temperature dependence of the linear thermal expansion coefficient and of the phonon frequency shifts for several optical modes. The temperature dependence of the quasiharmonic frequency shifts show normal behaviour, i.e. they increase with cooling.

The most challenging part in the anharmonic calculations is the ab-initio evaluation of the third-order anharmonic force constant matrix elements. In this chapter, we calculated them using the "$2n+1$" theorem implemented within the density functional linear response theory. Using these, we calculated the resulting third-order frequency shifts as functions of temperature for several modes. A rather unusual finding in $Y_2Ti_2O_7$ is that two high frequency phonon modes behave anomalously with cooling, i.e. their frequencies decrease with decreasing temperature. Among these two anomalous modes, the silent mode F_{1g} with frequency of 570 cm^{-1} shows a huge anomaly (i.e. $\omega(300K) - \omega(0K) = 15$ cm^{-1}) compared to the other anomalous mode that is a Raman active one with F_{2g} symmetry and a frequency of 797 cm^{-1} (i.e. $\omega(300K) - \omega(0K) = 0.4$ cm^{-1}). Our theoretical calculations, therefore, fail to explain the anomaly for the low frequency modes as observed in experiments. However, the anomaly for the high frequency modes as found from our theoretical calculations is in reasonably good agreement with experiments where also some high frequency modes are anomalous. On the other hand, our theoretical calculations show no anomaly for any of the modes in the case of $Y_2Zr_2O_7$ zirconate pyrochlore. These results for the temperature dependent phonon frequencies in $Y_2Ti_2O_7$ and $Y_2Zr_2O_7$ are similar to the experimental results in $Sm_2Ti_{2-x}Zr_xO_7$, where some of the phonon modes in $Sm_2Ti_2O_7$ display anomalous behaviour with cooling, whereas no anomaly is observed for any of the phonon modes in the case of $Sm_2Zr_2O_7$.

Chapter 9

Temperature dependent phonon properties of $Dy_2Ti_2O_7$ and $Lu_2Ti_2O_7$ pyrochlores

In this chapter we have studied the temperature-dependent phonon properties in the rare-earth $Dy_2Ti_2O_7$ and $Lu_2Ti_2O_7$ pyrochlores. In experiments, some of the phonon modes in both the compounds display an anomalous behaviour with cooling. Here we have used the same approach as used in chapter 7 to see whether the leading order effects arising from the third-order anharmonic interactions can explain the phonon anomalies in these systems. We have extensively examined the mode Grüneisen parameters, linear thermal expansion coefficient, two phonon density of states, quasiharmonic and anharmonic contributions to frequency shifts for several phonon modes.

9.1 Introduction

As mentioned earlier, a major part of this thesis is devoted to the study of phonons in pyrochlores, especially those in the rare-earth titanates ($RE_2Ti_2O_7$), which show a wide variety of interesting properties, such as temperature-dependent phonon anomalies, structural transitions, etc. As discussed in the previous chapters, the phonon anomalies in these systems are generally thought to be due to strong phonon-phonon anharmonic interactions.

Recently, Saha et al.[54] has carried out temperature-dependent Raman study in $Dy_2Ti_2O_7$ and $Lu_2Ti_2O_7$ pyrochlores. These authors have found that some of the optical modes in these materials behave anomalously with temperature, i.e. their frequencies show a red-shift with cooling, a behaviour, generally not observed in normal materials. In their study, the authors also have attributed this anomaly

to phonon-phonon anharmonic interactions.

Here, we present temperature-dependent phonon properties in $Dy_2Ti_2O_7$ and $Lu_2Ti_2O_7$ pyrochlores using DFT plus Green's function formalism. Our interest is to see if we can also capture the phonon anomaly for some of the phonon modes in these systems at least qualitatively. To the best of our knowledge, no such theoretical calculations exist in the literature for these compounds. We have extensively explored the mode Grüneisen parameters, temperature-dependent linear thermal expansion coefficient and quasiharmonic contributions, two phonon density of states, temperature-dependence of phonon linewidths and third-order anharmonic contributions.

In this chapter, we have gone back to modelling the anharmonic force constants in terms of fitting parameters using the same approach as used in chapter 7. This way of calculating the anharmonic force constants has been provided by Ipatova et al.[184] and has been successfully used by Lan et al. to study the phonon anharmonicity of rutile TiO_2[185] and SnO_2[186]. Furthermore, we have seen from the calculations presented in Chapters 7 and 8 that the results from this approach are qualitatively the same as what we get when the anharmonic constants are calculated from first principles, and the latter is very expensive computationally.

9.2 Computational details

As earlier, we have performed DFT calculations[83, 84] as implemented in the Quantum Espresso code[110], with ultrasoft pseudopotentials[152] to represent the interaction between ionic cores and valence electrons. The LDA method was used for the exchange-correlation energy functional. A plane-wave basis set with a cut-off of 60 Ry was used for all our calculations. The k-points summation of the electronic energy calculations over the BZ was performed by using the Monkhorst-Pack method with a $4 \times 4 \times 4$ special k-points mesh[111]. The DFPT was employed to investigate the phonon properties in the BZ. For the phonon dispersion, dynamical matrices were calculated for a $2 \times 2 \times 2$ grid of $\boldsymbol{q}$-points. The lattice constant was optimized to minimize the total energy, interatomic forces and unit-cell stresses. The Broyden-Fletcher-Goldfarb-Shanno (BFGS) minimization scheme[112] was used in geometry optimization.

9.3 Results and discussion

9.3.1 Quasi-harmonic results

The formalism for the quasi-harmonic approximation we employ is the same as in earlier chapters. For the convenience of reading, we reproduce the salient aspects here, instead of referring to the earlier

accounts. The mode Grüneisen parameter was calculated as

$$\gamma_j = -\frac{\partial \ln \omega_j}{\partial \ln V} = -\frac{V}{\omega_j}\frac{\partial \omega_j}{\partial V} \tag{9.1}$$

where V is the cell volume and ω_j is the frequency of j^{th} phonon mode. Frequencies were calculated at different cell volumes and the derivative of the frequency with respect to the volume was calculated by fitting ω_j-V data with cubic spline polynomials. Calculated values of the mode Grüneisen parameters for several modes, along with the available experimental results, are given in Table 9.1. As is clear from the table, the experimental values of the mode Grüneisen parameters for $Dy_2Ti_2O_7$ are available only for four modes, and the differences between theory and experiment range from $\sim 6\%$ to $\sim 100\%$. To the best of our knowledge, no experimental data of the mode Grüneisen parameters are available in the case of $Lu_2Ti_2O_7$.

Table 9.1: Calculated phonon frequencies and mode Grüneisen parameters in $Dy_2Ti_2O_7$ and $Lu_2Ti_2O_7$ pyrochlores, along with the available experimental results.

Mode	Frequency (cm^{-1})		γ		Frequency (cm^{-1})		γ
	LDA	Expt.[5]	LDA	Expt.[5]	LDA	Expt.[5]	LDA
$Dy_2Ti_2O_7$					$Lu_2Ti_2O_7$		
F_{1u}	82		3.23		65		4.30
F_{1u}	111		5.66		99		8.10
E_u	174	174	1.41	2.2	157	188	1.13
F_{1u}	188	193	3.68		164	228	3.94
F_{1u}	226		1.06		203		1.64
F_{2g}	324	312	1.81	1.7	319	309	2.04
E_g	343	330	2.03		344	333	1.91
F_{1u}	390		1.87		402		1.97
F_{1u}	442		1.93		447		1.97
F_{2g}	458	453	1.28		463	458	1.42
A_{1g}	510	515	1.21	0.9	516	520	1.06
F_{1u}	548		1.08		565		1.18
F_{1g}	574		1.82		586		1.36
F_{2g}	587	560	1.32		599	582	1.65
F_{2u}	614		1.66		649		1.72
F_{2g}	801	680	1.17	2.2	826	707	1.22

Within the quasiharmonic approximation, the temperature dependence of frequency shift is obtained via the temperature dependence of the linear thermal expansion:

$$\Delta_j^{(0)}(T) = \omega_j(0)\left[e^{-3\gamma_j \int_0^T \alpha(T')dT'} - 1\right] \tag{9.2}$$

where $\omega_j(0)$ and γ_j correspond to the frequency and the mode Grüneisen parameter for the $(\mathbf{0}j)$ mode

at temperature $T = 0$ K. The linear thermal coefficient is written as

$$\alpha = \frac{1}{3BV} \sum_{\boldsymbol{q}j} \left[\gamma_j(\boldsymbol{q}) \frac{(\hbar\omega_j(\boldsymbol{q}))^2}{k_B T^2} \frac{e^{\hbar\omega_j(\boldsymbol{q})/k_B T}}{(e^{\hbar\omega_j(\boldsymbol{q})/k_B T} - 1)^2} \right] \tag{9.3}$$

where B is the bulk modulus, V the cell-volume, and $\gamma_j(\boldsymbol{q})$ is the mode Grüneisen parameter for $\boldsymbol{q}j$ vibrational mode.

Calculation of the linear thermal expansion coefficient (Eq. 9.3) involves the dispersion of the mode Grüneisen parameter, $\gamma_j(\boldsymbol{q})$, which is a bit trickier to calculate as it is defined as the logarithmic derivative of frequencies with respect to the volume. The cubic spline polynomials were again used to calculate $\gamma_j(\boldsymbol{q})$.

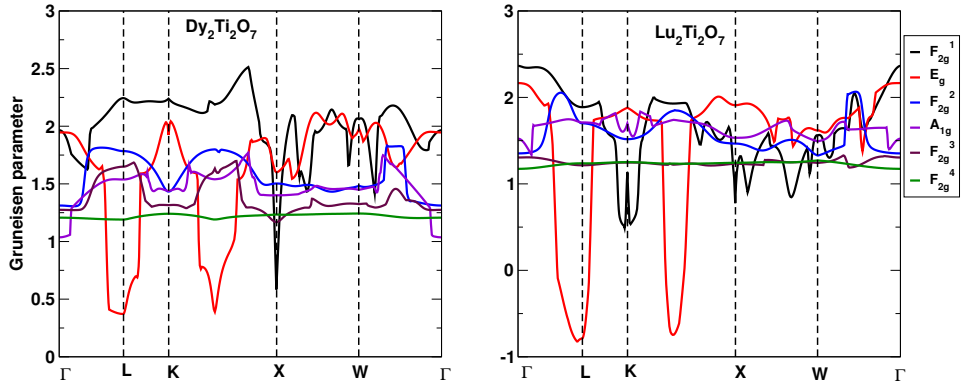

Figure 9.1: Variation of the mode Grüneisen parameters for Raman active modes in $Dy_2Ti_2O_7$ and $Lu_2Ti_2O_7$ pyrochlores, along the high symmetry directions in the BZ.

The $\gamma_j(\boldsymbol{q})$ values for the Raman active modes along the high symmetry directions of the BZ are shown in Fig. 9.1. As can be seen from the figure, values of the mode Grüneisen parameters vary significantly for two low frequency Raman active modes, whereas for high frequency modes the values change slightly. The temperature dependence of the linear thermal expansion coefficient for both the systems is shown in Fig. 9.2. The quasiharmonic shifts to some of the phonon modes are shown in Fig. 9.3. The shifts again decrease with increasing the temperature for all the modes in both the systems and hence can not explain the phonon anomalies in any of the modes. To the best of our knowledge, no experimental or theoretical results of the temperature variation of the quasiharmonic contributions for any of the modes in $Dy_2Ti_2O_7$ or $Lu_2Ti_2O_7$ pyrochlores exist in the literature for the comparison.

9.3.2 Anharmonic calculations

As in the earlier chapters, after neglecting electron-phonon, crystal field-phonon, and spin-phonon effects, and all the terms beyond the third-order anharmonic corrections, the temperature dependence of the

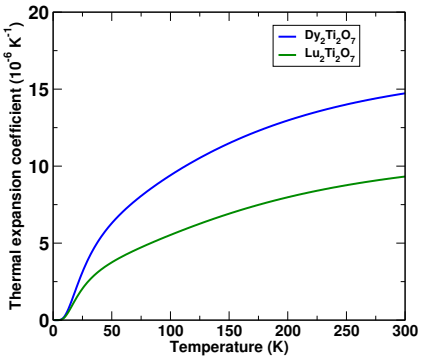

Figure 9.2: Temperature dependence of the linear thermal expansion coefficient of $Dy_2Ti_2O_7$ and $Lu_2Ti_2O_7$ pyrochlores.

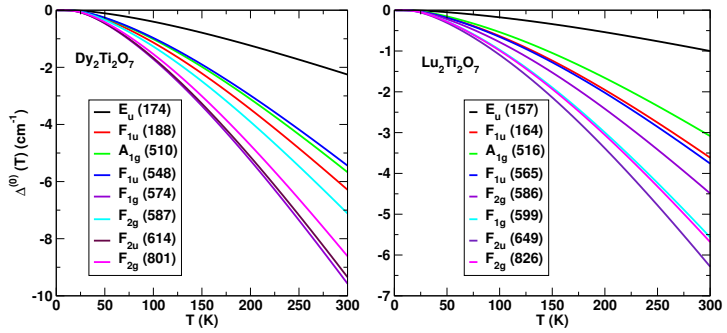

Figure 9.3: Temperature dependence of the Quasiharmonic contribution to some of the modes in $Dy_2Ti_2O_7$ and $Lu_2Ti_2O_7$ pyrochlores.

frequency of the j^{th} phonon mode at centre of the BZ is obtained as

$$\omega_j(T) = \omega_j(0) + \Delta_j^{(0)}(\omega, T) + \Delta_j^{(3)}(\omega, T) \tag{9.4}$$

where $\Delta_j^{(0)}(\omega, T)$ and $\Delta_j^{(3)}(\omega, T)$ are the quasiharmonic and third-order anharmonic shifts, respectively.

As discussed earlier, the phonon lineshifts and the linewidths are calculated as

$$\begin{aligned}\Delta^{(3)}(\omega_j) &= -\frac{18}{\hbar^2}\sum_{\boldsymbol{q},j_1j_2}|V^{(3)}(\mathbf{0}j;\boldsymbol{q}j_1;-\boldsymbol{q}j_2)|^2 \\ &\times \mathcal{P}\left[\frac{n_1+n_2+1}{\omega+\omega_1+\omega_2} - \frac{n_1+n_2+1}{\omega-\omega_1-\omega_2} + \frac{n_1-n_2}{\omega-\omega_1+\omega_2} - \frac{n_1-n_2}{\omega+\omega_1-\omega_2}\right]\end{aligned} \tag{9.5}$$

$$\begin{aligned}\Gamma(\omega_j) &= \frac{18\pi}{\hbar^2}\sum_{\boldsymbol{q},j_1j_2}|V^{(3)}(\mathbf{0}j;\boldsymbol{q}j_1;-\boldsymbol{q}j_2)|^2 \\ &\times [(n_1+n_2+1)\delta(\omega-\omega_1-\omega_2) + 2(n_1-n_2)\delta(\omega+\omega_1-\omega_2)]\end{aligned} \tag{9.6}$$

where $\omega_1 = \omega_{j_1}(\boldsymbol{q})$ and $\omega_2 = \omega_{j_2}(-\boldsymbol{q})$. The three phonon coupling constant matrix elements are given

by

$$V^{(3)}(\mathbf{0},j;\boldsymbol{q},j_1;-\boldsymbol{q},j_2) = \left(\frac{\hbar^3}{8\omega_j(\mathbf{0})\omega_{j_1}(\boldsymbol{q})\omega_{j_2}(-\boldsymbol{q})}\right)^{1/2} \sum_{ss's'',\alpha\beta\gamma} \left(\frac{1}{M_s M_{s'} M_{s''}}\right)^{1/2} e_{s,\alpha}(\mathbf{0}j) e_{s',\beta}(\boldsymbol{q}j_1) e_{s'',\gamma}(-\boldsymbol{q}j_2)$$
$$\times \sum_{ll'} \frac{1}{N\sqrt{N}} \frac{\partial^3 E}{\partial u^0_{s,\alpha} \partial u^l_{s',\beta} \partial u^{l'}_{s'',\gamma}} e^{i\boldsymbol{q}.(\boldsymbol{R}(l)-\boldsymbol{R}(l'))} \tag{9.7}$$

As discussed earlier, the numerical evaluation of the third order phonon coupling constants, $V^{(3)}(\mathbf{0}j;\boldsymbol{q}j_1;-\boldsymbol{q}j_2)$ is computationally expensive. In this chapter, we follow the same approach as was used in chapter 7 to model them in terms of a single fitting parameter for each mode j. Specifically, the coupling constant within the three-phonon process is represented as,

$$V^{(3)}(j;\boldsymbol{q}j_1;-\boldsymbol{q}j_2) = \frac{1}{12}\left(\frac{\hbar}{2N}\right)^{3/2} N[\omega_{j0}\omega_1\omega_2]^{\frac{1}{2}} C(j;\boldsymbol{q}j_1;-\boldsymbol{q}j_2) \tag{9.8}$$

where the cubic anharmonic tensor $C(j;\boldsymbol{q}j_1;-\boldsymbol{q}j_2)$ is approximated as a constant, $C_j^{(3)}$.

Within this approximation the phonon linewidths and the frequency shifts are given by

$$\Gamma(\omega_j) = \frac{\pi\hbar}{64}\omega_{j0}|C_j^{(3)}|^2 \sum_{\boldsymbol{q}j_1j_2} \omega_1\omega_2 \left[(n_1+n_2+1)\delta(\omega-\omega_1-\omega_2) + 2(n_1-n_2)\delta(\omega+\omega_1-\omega_2)\right] \tag{9.9}$$

$$\Delta^{(3)}(\omega_j) = -\frac{\hbar}{64}\omega_{j0}|C_j^{(3)}|^2 \sum_{\boldsymbol{q}j_1j_2} \omega_1\omega_2 \mathcal{P}\left[\frac{n_1+n_2+1}{\omega+\omega_1+\omega_2} - \frac{n_1+n_2+1}{\omega-\omega_1-\omega_2} + \frac{n_1-n_2}{\omega-\omega_1+\omega_2} - \frac{n_1-n_2}{\omega+\omega_1-\omega_2}\right] \tag{9.10}$$

To calculate the phonon linewidth (Eq. 9.9) and lineshift (Eq. 9.10) for a j^{th} phonon mode, we need the value of the single mode coupling parameter, $C_j^{(3)}$, which can in principle be obtained by fitting the above equation of linewidth or shift to the experimentally obtained values of these quantities. However, one can get the qualitative understanding of the phonon linewidths and lineshifts if one assumes this coupling constant as being the same for all the modes. For the calculations presented in this chapter, we have used the same value of $|C_j^{(3)}|^2$ around 1.0×10^{10} erg^{-1} as in Chapter 7. Just as in Chapter 7, we also compute the two phonon density (TDOS) of states, which at $\boldsymbol{q} = 0$ is given by

$$D(\omega) = \sum_{\boldsymbol{q}j_1j_2} \left[(n_1+n_2+1)\delta(\omega-\omega_1-\omega_2) + 2(n_1-n_2)\delta(\omega+\omega_1-\omega_2)\right] \tag{9.11}$$

The computational details are the same as were given in Chapter 7. We use a broadening parameter $\epsilon = 3.0$ cm^{-1} for the calculations reported below. The two phonon DOS, and the contributions from the up and down conversion processes to the two phonon DOS calculated at $T = 0$ K and $T = 300$ K for both the compounds under study are shown in Fig. 9.4. As can be seen, at $T = 0$ K the

contribution from the up conversion process is quite small compared to the down conversion process, while at higher temperatures, both the terms contribute, but the contribution from the latter term is still higher than that from the former one. This is because there are several channels available for high frequency modes to decay into the low frequency modes. The temperature dependence of the full width

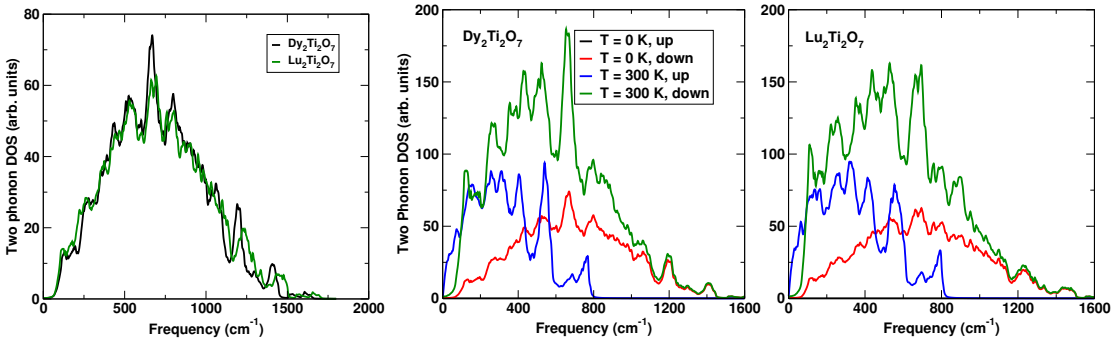

Figure 9.4: Two phonon density of states (TDOS) of $Dy_2Ti_2O_7$ and $Lu_2Ti_2O_7$ pyrochlores. The up and down conversion decay processes of TDOS are shown for two different temperature values.

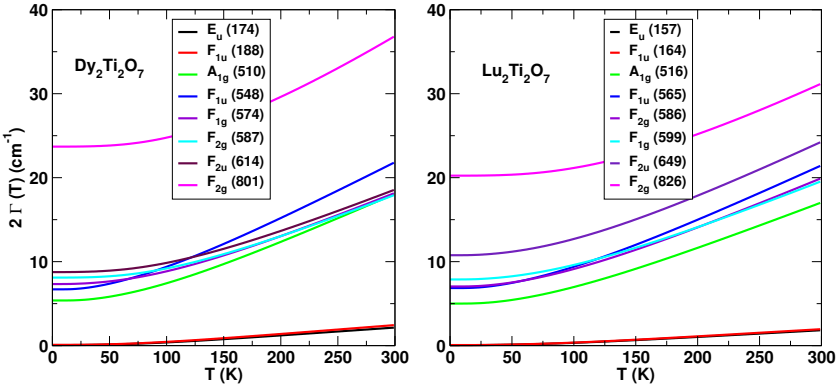

Figure 9.5: Temperature dependence of the full width at half maximum for some of the modes calculated at $\epsilon = 3.0$ cm^{-1}.

at half maximum for several modes calculated at the centre of the BZ is shown in Fig. 9.5. The FWHM increases with increasing temperature, as expected since any mode $\boldsymbol{q}j$ becomes highly populated at higher temperatures.

The temperature dependence of the third-order contribution to Δ for total 8 vibrational modes including 2 low frequency and 6 high frequency modes of $Dy_2Ti_2O_7$ and $Lu_2Ti_2O_7$ pyrochlores is shown in Figs. 9.6 and 9.7, respectively. It is evident from the results that in both the compounds $\Delta^{(3)}(T)$ increases with cooling for both the low frequency modes and hence the frequency of these modes will behave normally, i.e. will display the blue shift with cooling, unlike in the experiments, where a phonon mode around 200 cm^{-1} shows huge anomaly. On the other hand, out of 6 high frequency modes, 4 modes in both the materials show interesting behaviour, i.e. their shifts decrease with cooling, which

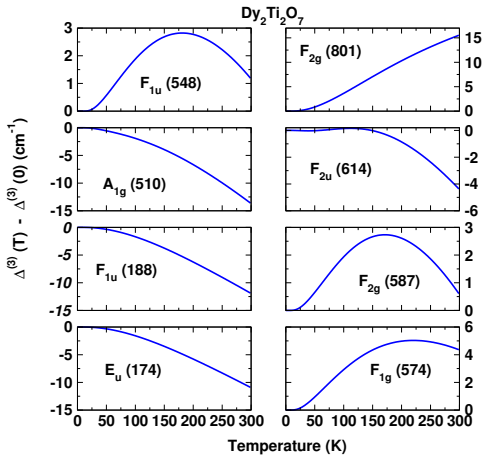

Figure 9.6: Temperature dependence of the cubic contribution to some of the modes in $Dy_2Ti_2O_7$. $|C_j^{(3)}|^2 = 1.0 \times 10^{10}$ erg^{-1} was used for all the modes.

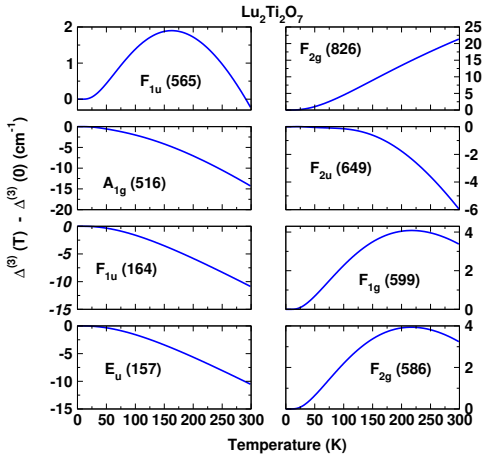

Figure 9.7: Temperature dependence of the cubic contribution to some of the modes in $Lu_2Ti_2O_7$. $|C_j^{(3)}|^2 = 1.0 \times 10^{10}$ erg^{-1} was used for all the modes.

are likely signatures of phonon anomaly. Therefore, our theoretical calculations fail to capture the phonon anomaly for the low frequency modes, whereas they do seem to suggest the phonon anomalies for the high frequency modes. The quantitative details of the anomaly and the actual number of anomalous phonon modes will depend on the three phonon coupling constants, $V^{(3)}(\mathbf{0}j, \boldsymbol{q}j_1, -\boldsymbol{q}j_2)$. It would be interesting to study the temperature dependent phonon properties in both the compounds by calculating the three phonon coupling constants exactly and also by taking into account the higher order terms of the lattice potential.

To get a better understanding of the temperature dependent third-order shifts, we have individually analysed all the four terms of Eq. 9.10 for one low frequency IR active F_{1u} mode (Frequency of 188 cm^{-1} for $Dy_2Ti_2O_7$ and of 164 cm^{-1} for $Lu_2Ti_2O_7$) and one high frequency Raman active F_{2g} mode

(Frequency of 801 cm^{-1} for $Dy_2Ti_2O_7$ and of 826 cm^{-1} for $Lu_2Ti_2O_7$). All the four terms in the case of F_{1u} mode in both the compounds decrease with increasing temperature, while in the case of F_{2g} mode, the first term decreases with increasing temperature, whereas the other three terms (one down conversion and two up conversion) increase with increasing temperature, making them responsible for the anomalous behaviour of this high frequency phonon mode.

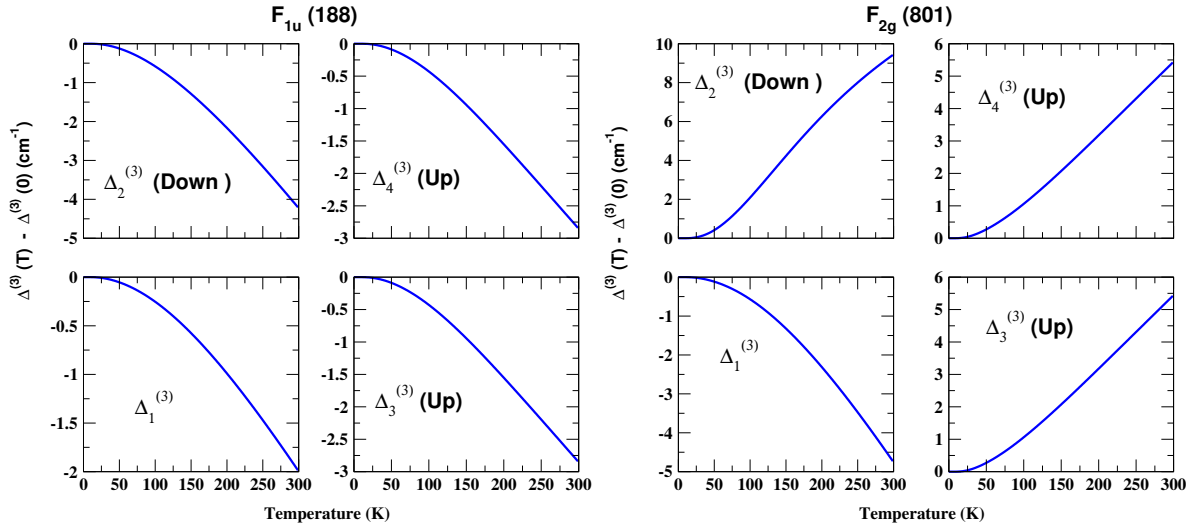

Figure 9.8: Temperature dependent contributions from different terms of third-order shift for an infrared active mode F_{1u} (188 cm^{-1}) and a high frequency Raman active mode F_{2g} (801 cm^{-1}) of $Dy_2Ti_2O_7$.

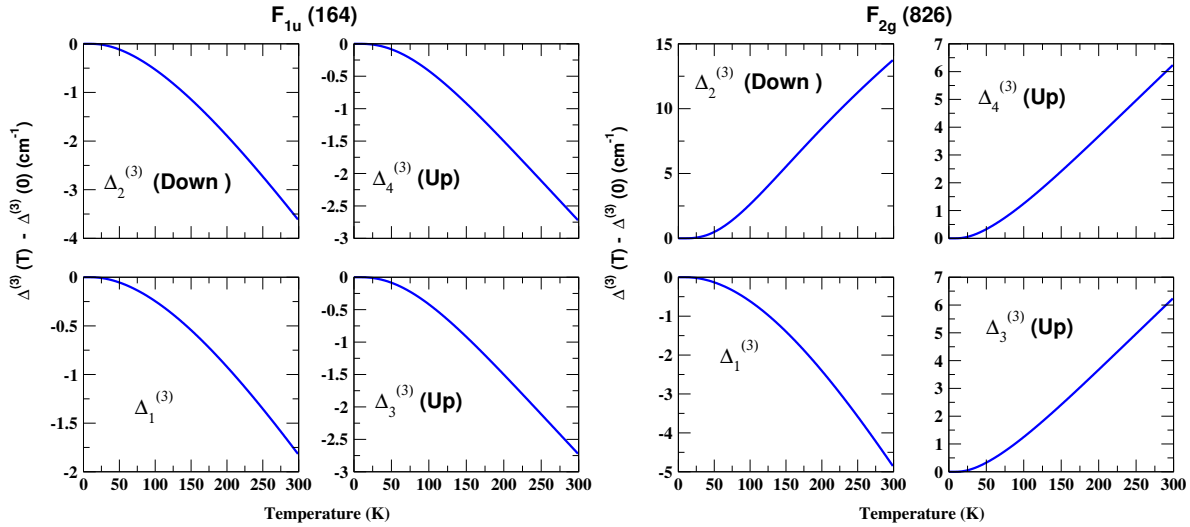

Figure 9.9: Temperature dependent contributions from different terms of third-order shift for an infrared active mode F_{1u} (164 cm^{-1}) and a high frequency Raman active mode F_{2g} (826 cm^{-1}) of $Lu_2Ti_2O_7$.

9.4 Conclusions

In this chapter, we studied the temperature-dependent phonon properties in $Dy_2Ti_2O_7$ and $Lu_2Ti_2O_7$ titanate pyrochlores using DFT plus Green's function formalism. We calculated the mode grüneisen parameters for several modes, the wave-vector dependence of the mode grüneisen parameters for the Raman active modes, the temperature dependence of the linear thermal expansion coefficient and the quasiharmonic contributions to the frequency shifts for several phonon modes. The two phonon density of states were discussed in detail for both the systems under investigation. Within the third-order anharmonic approximation, phonon linewidths and lineshifts for several phonon modes were extensively studied. The interesting finding from our theoretical calculations is that the third order anharmonic shifts for a few high frequency modes decreases with cooling, a behaviour generally not seen in normal materials, and hence it may lead to the anomalous nature of these high frequency modes if one can calculate the third-order anharmonic force constant matrix elements exactly. Our theoretical calculations fail to explain the phonon anomaly for the low frequency modes as observed experimentally in both the systems under examination but are able to explain the qualitative nature of the anomaly for a few high frequency modes as observed in experiments. Therefore, this is still an open question to explain the phonon anomaly for the low frequency modes. It would be interesting, though very challenging, to see what happens when one includes other higher order terms of the lattice anharmonic potential, i.e. the terms beyond the leading quasiharmonic and third order anharmonic corrections. At present, there is no access to lattice anharmonic terms beyond the third-order in the DFT linear response theory.

Chapter 10

Temperature-dependent phonons of tetragonal $SrTiO_3$ perovskite

In this chapter, we study temperature-dependent phonon properties in the tetragonal $SrTiO_3$ perovskite using DFT and Green's function formalism. We present results for the zone centre phonon properties, phonon dispersion, the mode Grnüneisen parameters, linear thermal expansion coefficient, quasiharmonic frequency shifts, the two-phonon density of states, phonon linewidth and lineshift within the third order anharmonic approximation, and the temperature variation of the frequency for several phonon modes.

10.1 Introduction

Phonon anharmonicity plays a vital role in describing many physical properties of solids and molecules, including temperature dependence of phonon frequencies, lattice thermal expansion, and phase stability of solids[210]. Due to the lattice anharmonicity, phonons have a finite lifetime and materials have a finite thermal conductivity κ_L. The magnitude of the anharmonicity depends on the material under study. For example, covalently bonded materials such as silicon, diamond, and graphene are very harmonic and exhibit high thermal conductivities[211, 212]. In contrast, thermoelectric and ferroelectric (FE) materials often display huge anharmonicity, revealed from their inelastic neutron scattering spectra and ultra-low κ_L values[213, 214].

Many-body perturbation theory is a standard technique to handle the lattice anharmonic corrections. This technique obtains the anharmonic effects by the calculation of self-energies[101] using Feynman diagrams, where the lowest-order approximation is generally used in the ab initio calculations based

on DFT. The calculation requires the cubic and quartic force constants, which are third and fourth-order derivatives of the total energy of the system, respectively. In general, the quartic corrections are significant at larger temperatures only. In this work, our temperature of interest is up-to only 300 K, therefore, we neglect all the anharmonic terms beyond the cubic. Third-order terms can be obtained efficiently and systematically using either DFT linear response theory[102] or the finite-displacement method[215]. The cubic terms are used to calculate the phonon linewidths and lineshifts. Several groups have performed this type of calculation to predict the lattice thermal conductivity of many solids[202, 216].

Temperature dependent phonon calculations have already been carried out in the high temperature cubic phase of $SrTiO_3$ perovskite[79], whereas to the best of our knowledge, no such calculations exist in the literature for the low-temperature tetragonal phase of $SrTiO_3$. For comparison, we also present the vibrational properties of cubic $SrTiO_3$ phase.

10.2 Computational details

We have performed DFT calculations [83, 84] as implemented in the Quantum Espresso code[110], with the optimized norm-conserving Vanderbilt (ONCV) pseudopotentials [152] to characterize the interaction between ionic cores and valence electrons. The exchange-correlation energy of electrons was represented within the LDA[86]. The Kohn-Sham wave functions were described using a plane-wave basis with an energy cutoff of 80 Ry. The k-points summation of the electronic energy calculations over the BZ was used by the Monkhorst-Pack method with a $4 \times 4 \times 4$ special k-points mesh[111]. The DFPT was carried out to examine the phonon properties. For phonon dispersion, the dynamical matrices were calculated for a $2 \times 2 \times 2$ grid of $\boldsymbol{q}$-points. The lattice constants were optimized to minimize the total energy, interatomic forces and unit-cell stresses. The Broyden-Fletcher-Goldfarb-Shanno (BFGS) minimization scheme[112] was employed in geometry optimization. We have used the "$2n+1$" theorem as implemented within the Quantum Espresso code to calculate the third-order interatomic force constants (IFC3)[192, 196, 206, 207].

10.3 Phonon symmetry in cubic and tetragonal phases

Table 10.1 shows the phonon symmetry in the STO crystal for $\Gamma(0,0,0)$ and $R(1/2,1/2,1/2)$ symmetry points of the BZ for a simple cubic lattice. Here, the assignments of the vibrational modes are similar to the ones used in Ref.[76]. The space group irreducible representations (hereafter referred to as irreps) are induced from those site symmetry group irreps which correspond to transformations of atomic displacements (x, y, z) : T_{1u} of the site symmetry group O_h (Ti and Sr atoms); A_{2u}, E_u of the site symmetry group D_{4h} (O atom).

One can obtain four T_{1u} modes and one T_{2u} mode at the Γ point of the BZ (one T_{1u} mode is acoustic). Three phonon modes of the T_{1u} symmetry are IR active, and one mode of the T_{2u} symmetry is neither IR nor Raman active (silent mode). The latter mode is only due to the vibrations of O atoms. Three modes $1^+, 3^+,$ and 4^+ at the R point of the BZ (with the degeneracy 1, 2, and 3, respectively) are due to the vibrations of O atom only. The threefold degenerate R_{4^-} and R_{5^+} modes are due to the displacements of Ti and Sr-O, respectively.

The symmetry of the phonons in the AFD STO phase at the Γ point of the BZ is also shown in Table 10.1 along with the splitting of the phonon frequencies due to lowering of the crystal symmetry. The symmetry of the acoustic phonons is $(A_{2u} + E_u)$; eight modes are IR active $(3A_{2u} + 5E_u)$; seven modes are Raman active $(A_{1g}, B_{1g}, 2B_{2g}, 3E_g)$. The silent modes have the symmetry A_{1u}, B_{1u}, and $2A_{2g}$.

As can be seen from the Table 10.1, the A_{1g} and B_{1g} Raman active modes involve the vibrations of the O atoms only. The Raman active modes with the symmetry B_{2g} and E_g are Sr-O vibrational modes. The vibrations associated with Ti atom displacements are active only in IR spectra ($A_{2u}, 5E_u$ modes).

10.4 Results and discussion

10.4.1 Structural and vibrational properties

As discussed in sec. 1.2, STO exists in the cubic phase at high temperatures, whereas it transforms into the tetragonal structure at a critical temperature $T_C \sim 105$ K. Generally, perovskites are the best examples of the ferroelectric materials, but tetragonal STO displays a paraelectric behaviour down to very low temperatures due to quantum fluctuations. In this chapter, our prime interest is to study the structural, vibrational, and lattice anharmonic effects in the tetragonal phase of STO. We have also examined the structural, electronic, and vibrational properties in cubic STO structure. In the next section, we describe the structural, electronic, and vibrational properties of cubic STO.

Cubic $SrTiO_3$

Calculated values of the lattice constant, energy band gaps (both direct and indirect), and the bulk modulus of cubic STO are listed in Table. 10.2. Our results are compared with the available theoretical and experimental data. Our results are in reasonable agreement with the literature data.

Table 10.1: Wyckoff positions and phonon symmetry in cubic and tetragonal AFD $SrTiO_3$

$Pm\bar{3}m$ O_h^1 (SG 221)			I4/mcm D_{4h}^{18} (SG 140)	
	Γ	R		Γ
Ti			Ti	
$1a(0,0,0)$			$2c(0,0,0)$	
$O_h, T_{1u}(x,y,z)$	$4^-(T_{1u})$	4^-	$C_{4h}A_u(z)$	$A_{1u}A_{2u}$
			$E'_u(x,y), E''_u(x,y)$	$2E_u$
				$T_{1u} \to A_{2u}E_u$
Sr			Sr	
$1b(0.5,0.5,0.5)$			$2b(0,0.5,0.25)$	
$O_h, T_{1u}(x,y,z)$	$4^-(T_{1u})$	5^+	$D_{2d}B_2(z)$	$A_{2u}B_{2g}$
				$R_{5^+} \to B_{2g}E_g$
			$E(x,y)$	E_gE_u
				$T_{1u} \to A_{2u}E_u$
O			O	
$3d(0.5,0,0)$			$2a(0,0,0.25)$	
$D_{4h}, A_{2u}(z)$	$4^-(T_{1u})$	1^+3^+	$D_4A_2(z)$	$A_{2g}A_{2u}$
$E_u(x,y)$	$4^-(T_{1u})$	4^+5^+	$E(x,y)$	E_gE_u
	$5^-(T_{2u})$			
				$R_{1^+} \to A_{2g}$
				$R_{3^+} \to E_g$
				$T_{1u} \to A_{2u}E_u$
			O	
			$4h(-u+0.5,u,0)$	
			$C_{2v}A_1(z)$	$A_{1g}B_{2g}E_u$
			$B_1(x)$	$A_{1g}A_{2g}E_u$
			$B_2(y)$	$A_{2u}B_{1u}E_g$
				$R_{4^+} \to B_{1g}E_g$
				$R_{5^+} \to B_{2g}E_g$
				$T_{1u} \to A_{2u}E_u$
				$T_{2u} \to B_{1u}E_u$

Table 10.2: Cubic STO basic properties. Theory A and B correspond to the other first-principles calculations.

	PW LDA (This work)	Theory A Ref.[76]	Theory B Ref.[76]	Experimental
Lattice constant a_0 (Å)	3.85	3.96	3.94	3.91 Ref.[217]
Direct (and indirect) band gap (eV)	2.2 (1.9)	2.1 (1.8)	2.1 (1.8)	3.8 (3.3) Ref.[218]
Bulk modulus (GPa)	205	171	169	179[219]

The phonon band dispersion of cubic STO is shown in Fig. 10.1. Imaginary frequencies, shown as negative values in the figure, are found with large magnitudes, specially at the Γ and R points of the BZ. These imaginary frequencies imply the structural instabilities, which are general characteristics of the perovskite materials, as they exhibit interesting ferroelectric properties. Our calculated phonon

frequencies for cubic STO, at each Γ and R points, are shown in Table 10.3 along with the available literature data. As can be seen, our results are reasonably close to the other theoretical calculations and the experimental data.

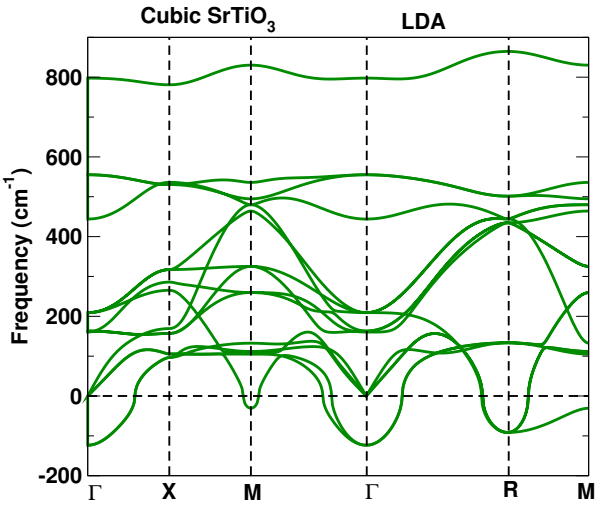

Figure 10.1: Phonon band dispersion of cubic $SrTiO_3$ calculated within the LDA framework.

Table 10.3: Calculated phonon frequencies (cm^{-1}) in cubic STO, compared with the available literature data.

		PW LDA (This work)	LCAO PBE Ref.[76]	PW PBE Ref.[76]	PW PBE Ref.[220]	Expt.
Γ	T_{1u}	$129i$	$71i$	$133i$	$115i$	42 (Ref.[221]), 91 (Ref.[222])
	T_{1u}	163	166	146	147	175 (Ref.[221]), 170 (Ref.[222])
	T_{2u}	206	247	226	234	265 (Ref.[222])
	T_{1u}	555	522	508	512	545 (Ref.[221]), 547(Ref.[222])
R	R_{4+}	$102i$	$16i$	$86i$	$90i$	52 (Ref.[222])
	R_{5+}	134	144	128		145 (Ref.[222])
	R_{4-}	432	432	413		446 (Ref.[222])
	R_{5+}	444	437	419		450 (Ref.[222])
	R_{3+}	502	440	433		474 (Ref.[222])
	R_{1+}	865	804	798		800 (Ref.[223])

Tetragonal $SrTiO_3$

As mentioned earlier, our prime interest is in the study of phonon properties in tetragonal STO. Our plane wave LDA results of the structural properties of the antiferrodistortive (AFD) STO are shown in Table. 10.4. Our calculated values of the structural parameters are in reasonably good agreement with the available theoretical and experimental results.

Our LDA values for the frequencies of Raman active, silent, and Infrared active modes of tetragonal

Table 10.4: AFD STO structural properties.

	PW LDA (This work)	Theory A Ref.[76]	Theory B Ref.[76]	Expt. Ref.[224]
Lattice constant a_0 (Å)	5.426	5.594	5.566	5.507
c (Å)	7.673	7.922	7.908	7.796
Cubic-tetragonal distortion $c/(\sqrt{2}a)$	1.00001	1.0014	1.0046	1.0010
O-atom position, u, fractional un.	0.221	0.245	0.228	0.241
TiO_6-rotation angle arctan $(1-4u)°$	6.6	1.1	4.9	2.0

STO, along with the available theoretical and experimental results are listed in Table. 10.5. As is evident from the results, frequencies of several modes are not consistent among different theoretical calculations. Calculations in Theory A[76] are based on the Perdew-Burke-Ernzerhof (PBE) or the generalized gradient approximation (GGA), but within two different approaches of the basis wavefunctions, i.e. the linear combination of the atomic orbitals (LCAO) and the plane wave (PW), whereas the calculations in Theory B[77] are based on the plane wave LDA. Interestingly, two low frequency Raman active and two low frequency Infrared active modes behave quite unusually in different sets of theoretical calculations. Our calculated values of frequencies for two low frequency Raman active A_{1g} and E_g modes are respectively found to be around 58 and 146 cm^{-1}; in LCAO PBE calculations these are found to be around 29 and 48 cm^{-1}; PW PBE calculations report them to be around 98 and $17i$ cm^{-1}. From our theoretical calculations, it is found that the frequencies of two low frequency Infrared active A_{2u} and E_u modes are respectively found to be around 66 and 82 cm^{-1}; in LCAO PBE calculations these are found to be around 2 and 1 cm^{-1}; in PW PBE these are found to be around $4i$ and $28i$ cm^{-1}; Theory B (PW LDA) report them to be around $90i$ and $96i$ cm^{-1}. Overall, our theoretical values of the frequencies for most of the vibrational modes are in reasonably good agreement with the literature data.

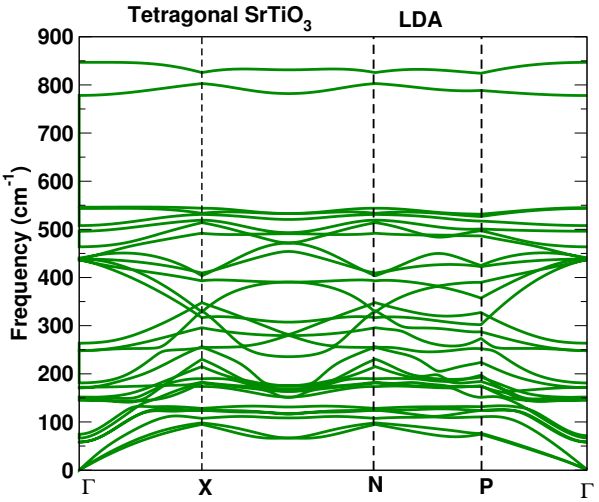

Figure 10.2: Phonon band dispersion of Tetragonal $SrTiO_3$ calculated within the LDA framework.

Table 10.5: Calculated LDA values of frequencies of Raman active, silent, and Infrared active modes in tetragonal STO structure, along with the available theoretical (Theory A[76] and Theory B[77]) and experimental results.

	LDA (This work)	Theory A (LCAO PBE)	Theory A (PW PBE)	Theory B (PW LDA)	Expt.
Raman					
A_{1g}	58	29	98		48 (Ref.[223])
E_g	146	48	17i		15 (Ref.[223])
E_g	151	137	183		143 (Ref.[223])
B_{2g}	152	152	140		235 (Ref.[223])
B_{2g}	438	441	421		
E_g	439	444	425		460 (Ref.[223])
B_{1g}	508	438	437		
Silent					
B_{1u}	264	252	245		
A_{1u}	436	430	410		
A_{2g}	496	440	434		
A_{2g}	847	806	793		
Infrared					
A_{2u}	66	2	4i	90i	
E_u	82	1	28i	96i	
E_u	172	163	183		
A_{2u}	182	180	158	157	185 (Ref.[225])
E_u	248	252	239	240	
E_u	441	433	411	419	450 (Ref.[225])
E_u	543	523	504	515	
A_{2u}	548	526	510		

The phonon band dispersion of tetragonal STO is shown in Fig. 10.2 along the high symmetry directions. It is evident from the spectra that all the modes are found to be real valued across all the symmetry directions of the BZ.

10.4.2 Quasiharmonic calculations in tetragonal $SrTiO_3$

The mode Grüneisen parameter is calculated as

$$\gamma_j = -\frac{\partial \ln \omega_j}{\partial \ln V} = -\frac{V}{\omega_j}\frac{\partial \omega_j}{\partial V} \tag{10.1}$$

where V is the cell volume and ω_j is the frequency of j^{th} phonon mode. As in the earlier chapters, phonon frequencies were calculated for different cell volumes and the derivative of the frequency with respect to the volume was calculated by fitting ω_j-V data with cubic spline polynomials. Calculated values of the mode Grüneisen parameters for several modes are shown in Table 10.6. To the best of our knowledge, there is no experimental or theoretical data available for the mode Grüneisen parameters to compare with our theoretical results.

Within the quasiharmonic approximation, the temperature dependence of frequency shift is obtained

via the temperature dependence of the linear thermal expansion:

$$\Delta_j^{(0)}(T) = \omega_j(0)\left[e^{-3\gamma_j \int_0^T \alpha(T')dT'} - 1\right] \tag{10.2}$$

where $\omega_j(0)$ and γ_j correspond to the frequency and the mode Grüneisen parameter for $(\mathbf{0}j)$ mode at temperature $T = 0$ K. The linear thermal coefficient is written as

$$\alpha = \frac{1}{3BV}\sum_{\boldsymbol{q}j}\left[\gamma_j(\boldsymbol{q})\frac{(\hbar\omega_j(\boldsymbol{q}))^2}{k_B T^2}\frac{e^{\hbar\omega_j(\boldsymbol{q})/k_B T}}{(e^{\hbar\omega_j(\boldsymbol{q})/k_B T}-1)^2}\right] \tag{10.3}$$

where B is the bulk modulus, V the cell-volume, and $\gamma_j(\boldsymbol{q})$ is the mode Grüneisen parameter for $\boldsymbol{q}j$ vibrational mode.

Calculation of the linear thermal expansion coefficient involves the dispersion of the mode Grüneisen parameter, $\gamma_j(\boldsymbol{q})$, which is a bit trickier to calculate. Again, cubic spline polynomial fittings were used to calculate $\gamma_j(\boldsymbol{q})$.

Our calculated result for the linear thermal expansion coefficient as a function of temperature is shown in Fig. 10.3. The temperature dependent quasiharmonic shifts for Raman active, IR active, and silent modes are shown in Fig. 10.4. Two low frequency Raman active modes show a positive shift with increasing temperature, which is because of the negative values of their mode Grüneisen parameters.

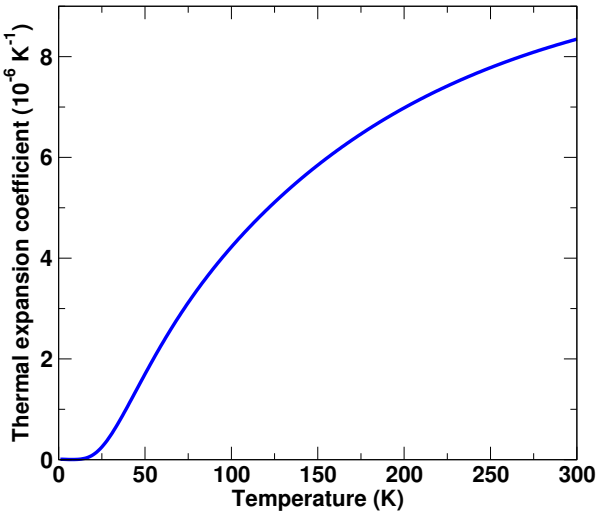

Figure 10.3: Temperature dependence of the linear thermal expansion coefficient of tetragonal STO.

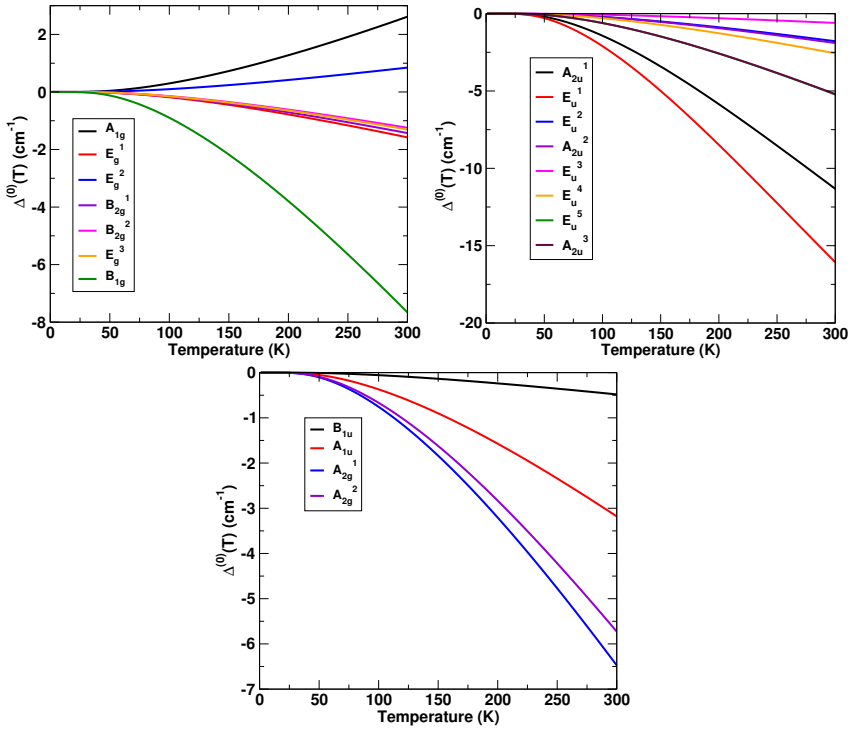

Figure 10.4: Temperature dependence of the Quasiharmonic contribution to Raman active(top left), IR active (top right), and silent (bottom) modes in $SrTiO_3$ perovskite.

10.4.3 Anharmonic results

After neglecting electron-phonon, crystal field-phonon, and spin-phonon contributions, and all the terms beyond the third-order anharmonic corrections, the temperature dependence of the frequency of the j^{th} phonon mode at the centre of the BZ is obtained as

$$\omega_j(T) = \omega_j(0) + \Delta_j^{(0)}(\omega, T) + \Delta_j^{(3)}(\omega, T) \tag{10.4}$$

where $\Delta_j^{(0)}(\omega, T)$ and $\Delta_j^{(3)}(\omega, T)$ are the quasiharmonic and third-order anharmonic shifts, respectively.

As discussed earlier, the phonon lineshifts and the linewidths are calculated as

$$\begin{aligned} \Delta^{(3)}(\omega_j) &= -\frac{18}{\hbar^2} \sum_{\boldsymbol{q}, j_1 j_2} |V^{(3)}(\mathbf{0}j; \boldsymbol{q}j_1; -\boldsymbol{q}j_2)|^2 \\ &\times \mathcal{P}\left[\frac{n_1 + n_2 + 1}{\omega + \omega_1 + \omega_2} - \frac{n_1 + n_2 + 1}{\omega - \omega_1 - \omega_2} + \frac{n_1 - n_2}{\omega - \omega_1 + \omega_2} - \frac{n_1 - n_2}{\omega + \omega_1 - \omega_2}\right] \end{aligned} \tag{10.5}$$

$$\begin{aligned}\Gamma(\omega_j) &= \frac{18\pi}{\hbar^2}\sum_{\boldsymbol{q},j_1 j_2}|V^{(3)}(\mathbf{0}j;\boldsymbol{q}j_1;-\boldsymbol{q}j_2)|^2 \\ &\times [(n_1+n_2+1)\delta(\omega-\omega_1-\omega_2)+2(n_1-n_2)\delta(\omega+\omega_1-\omega_2)] \end{aligned} \quad (10.6)$$

where $\omega_1 = \omega_{j_1}(\boldsymbol{q})$ and $\omega_2 = \omega_{j_2}(-\boldsymbol{q})$. The three phonon coupling constant matrix elements are evaluated using the DFPT and the $2n+1$ theorem by exactly the same procedure as described in Chapter 8, section 8.3.2.

Table 10.6: Calculated phonon frequencies, mode Grüneisen parameters, full width at half maximum at $\boldsymbol{q} = \mathbf{0}$, and phonon lifetimes of tetragonal $SrTiO_3$ perovskite.

Mode	ω (cm^{-1})	γ	$2\Gamma(0)$ (cm^{-1})	τ (ps)
A_{1g}	60	-9.31	0.06	94.7
A_{2u}	66	41.05	0.04	136.0
E_u	67	59.82	0.06	94.7
E_g	146	2.37	0.04	136.0
E_g	151	-1.22	2.04	2.6
B_{2g}	152	2.06	0.11	50.0
E_u	173	2.26	0.23	23.2
A_{2u}	182	2.29	0.20	26.5
E_u	248	0.53	0.87	6.1
B_{1u}	263	0.40	1.18	4.5
A_{1u}	435	1.60	2.33	2.3
B_{2g}	438	0.62	1.57	3.4
E_g	439	0.65	1.27	4.2
E_u	442	1.27	2.56	2.1
A_{2g}	497	2.86	9.20	0.6
B_{1g}	507	3.32	11.78	0.5
E_u	543	2.11	2.89	1.8
A_{2u}	548	2.08	3.29	1.6
A_{2g}	847	1.48	8.58	0.6

The full width at half maximum calculated at the centre of the BZ and at zero temperature ($2\Gamma(0)$) for all the optically active phonon modes, along with their lifetimes, calculated using the above formalism, are listed in Table 10.6. The lifetime has a large variation amongst the modes, wherein the highest lifetime is 136 ps for A_{2u} and E_g vibrational modes and the lowest lifetime is 0.5 ps for B_{1g} vibrational mode.

The temperature variation of the cubic contribution to all the optically active phonons of tetragonal STO is shown in Fig. 10.5. An important point to note is that there are 5 vibrational modes (2 Raman active, 1 IR active, and 2 silent) for which the third order anharmonic shifts increase with increasing temperature, but their values are so small compared with the quasiharmonic contributions (see Fig. 10.4) that when we add all the contributions together with the zeroth order term, the frequency for almost all the modes decreases with increasing temperature (see Fig. 10.6). Thus, our theoretical calculations show no phonon anomaly for any of the vibrational modes. As the tetragonal STO is quite a complex material from the phonons points of view, it is likely that some of the vibrational modes may display anomalous behaviour with cooling. It would be interesting, though challenging to see what happens to the temperature dependent phonon properties when one includes the higher order terms of the lattice potential energy in the calculations.

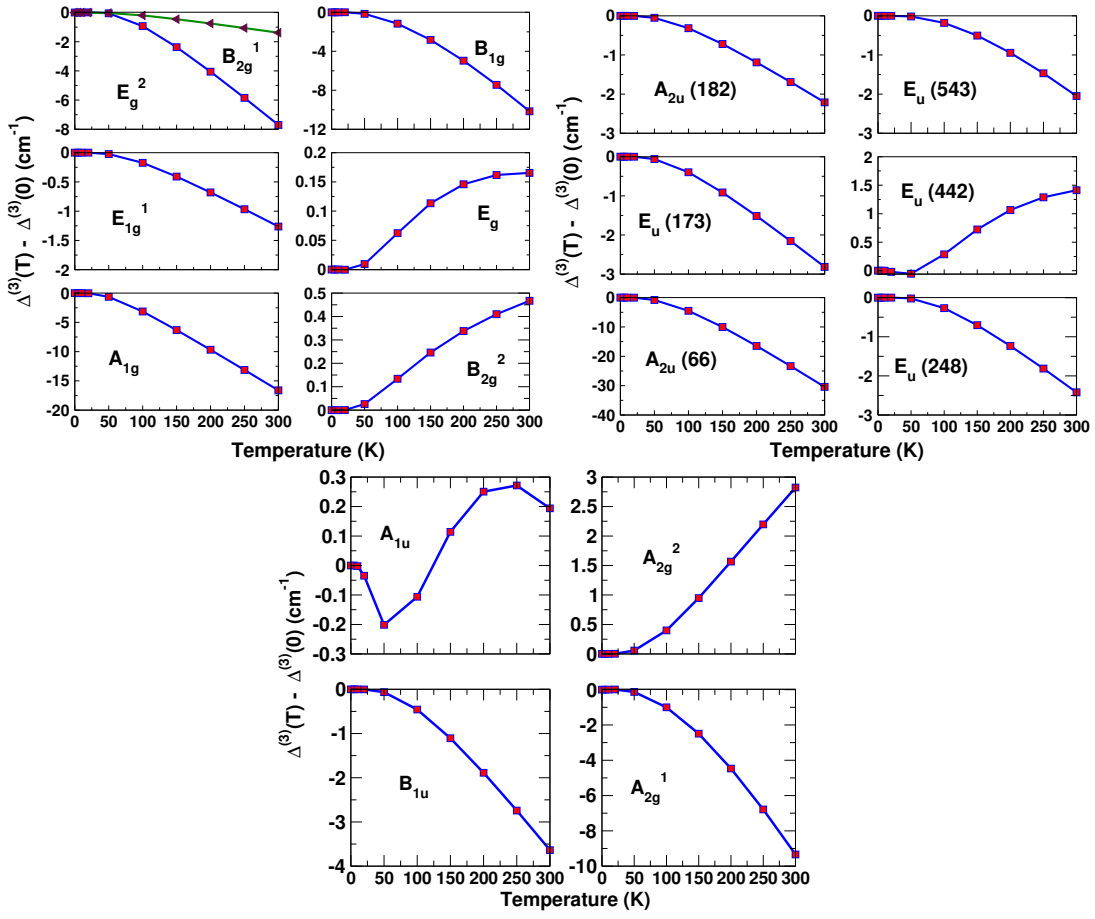

Figure 10.5: Temperature dependence of cubic contribution to Raman active(top left), IR active (top right), and silent (bottom) modes in $SrTiO_3$ perovskite.

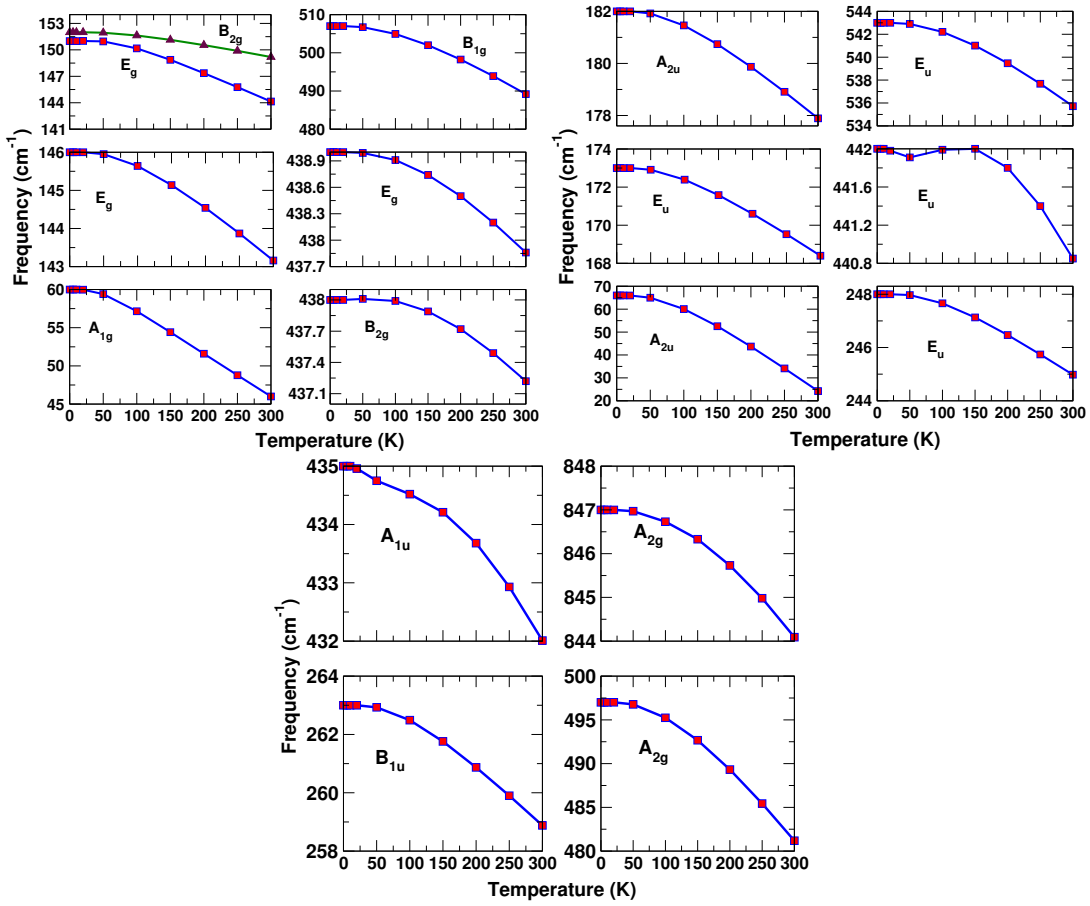

Figure 10.6: Temperature variation of phonon frequencies of Raman active(top left), IR active (top right), and silent (bottom) modes in $SrTiO_3$ perovskite.

The temperature variation of the full width at half maximum (FWHM) or 2Γ for Raman active, IR active, and silent modes calculated at the centre of the BZ is shown in Fig. 10.7. Since the FWHM is directly proportional to the phonon population, its value should increase with increasing the temperature; as the temperature increases, the phonon population in any $\boldsymbol{qj}$ mode also increases. Our theoretical results clearly show such a trend, wherein the FWHM increases for all the modes with increasing temperature. At very low temperatures, they are almost constant for all the modes, while at very high temperatures, they vary linearly with temperature. These behaviours of FWHM can easily be understood in the limiting regimes of temperatures in the same way as discussed in Chapter 8.

At very low temperatures, the contributions from the down conversion processes are significantly larger than the up conversion processes. Thus, after neglecting the up conversion processes, the phonon

linewidth is written as

$$\Gamma(\omega_j) \simeq \frac{18\pi}{\hbar^2} \sum_{\boldsymbol{q},j_1 j_2} |V^{(3)}(\mathbf{0}j;\boldsymbol{q}j_1;-\boldsymbol{q}j_2)|^2 (n_1+n_2+1)\delta(\omega-\omega_1-\omega_2) \tag{10.7}$$

where the phonon occupation number is given as

$$n(\omega_j(\boldsymbol{q})) = \frac{1}{e^{\hbar\omega_j(\boldsymbol{q})/k_BT}-1} \tag{10.8}$$

Since sum over the $\boldsymbol{q}$-grid in Eq. 10.7 excludes the $\boldsymbol{q}=0$ point in the calculations, at very low temperatures $\hbar\omega_j(\boldsymbol{q})/k_BT \gg 1$, and hence the phonon occupation number goes as $n(\omega_j(\boldsymbol{q})) \sim e^{-\hbar\omega_j(\boldsymbol{q})/k_BT}$. Thus, the term (n_1+n_2+1) is almost independent of temperature at very low temperatures; in our case the FWHM remains almost constant for temperatures up-to 50 K.

On the other hand, as the temperature increases, the up conversion process also starts contributing. In this case the linewidth or the FWHM is calculated from Eq. 10.6. At very high temperatures ($T \sim 1000$ K or more), $\hbar\omega_j(\boldsymbol{q})/k_BT \ll 1$, the phonon occupation number is directly proportional to the temperature, i.e. $n(\omega_j(\boldsymbol{q})) \sim k_BT/\hbar\omega_j(\boldsymbol{q})$. Thus, the linewidths at very high temperatures are calculated as

$$\begin{aligned}\Gamma(\omega) &\simeq k_BT\frac{18\pi}{\hbar^2} \sum_{\boldsymbol{q},j_1 j_2} |V^{(3)}(\mathbf{0}j;\boldsymbol{q}j_1;-\boldsymbol{q}j_2)|^2 \\ &\times \left[\left(\frac{1}{\hbar\omega_1}+\frac{1}{\hbar\omega_2}+1\right)\delta(\omega-\omega_1-\omega_2) + 2\left(\frac{1}{\hbar\omega_1}-\frac{1}{\hbar\omega_2}\right)\delta(\omega+\omega_1-\omega_2)\right]\end{aligned} \tag{10.9}$$

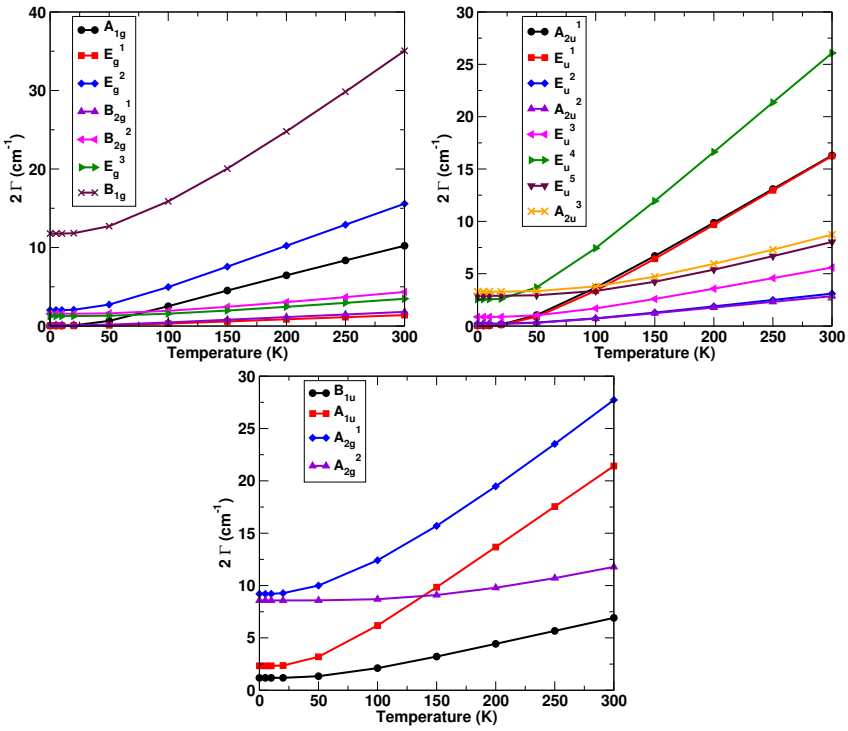

Figure 10.7: Temperature variation of full width at half maximum(FWHM) of Raman active(top left), IR active (top right), and silent (bottom) modes in $SrTiO_3$ perovskite.

10.5 Conclusions

In summary, in this chapter we discussed the temperature dependence of the phonon modes in Tetragonal $SrTiO_3$ perovskite arising from 3rd order anharmonic interactions.

Within the quasiharmonic approximation, we calculated the mode Grüneisen parameters, the temperature dependence of the linear thermal expansion coefficient and frequency shifts for several modes.

The most challenging part in the anharmonic calculations is the ab-initio evaluation of the third-order anharmonic force constant matrix elements. In this chapter, we calculated them using "$2n+1$" theorem as implemented within the density functional linear response theory. Using these, we calculated the third-order frequency shifts as a function of temperature for several phonon modes.

Finally, the temperature dependence of phonon frequencies and the FWHM was studied for several modes. From our calculations, we found that the frequencies of almost all the modes increase with decreasing temperature. Thus, no anomaly for any of the modes is obtained within the theoretical framework we used.

We are aware of an unpublished temperature dependent Raman study of the optical phonons in tetragonal STO from Prof. Ajay K Sood's group, where they find that the frequencies of almost all the

modes behave anomalously with temperature. Any explanation of such anomalies clearly requires the inclusion of effects beyond what we have considered in this chapter.

Chapter 11

Summary and conclusion

In conclusion, in this thesis we presented first-principles studies of various properties in two oxide families, namely the pyrochlores and perovskites. Using DFT and the Green's function formalism, we also explored the temperature dependent phonon properties in some of the pyrochlores and in $SrTiO_3$ perovskite. Below, we summarize our findings and discuss the possible future studies that could be undertaken for a better understanding of the above systems.

In **Chapter 3**, we presented DFT results of the structural, electronic, and vibrational properties in a series of rare-earth $RE_2B_2O_7$ (RE = Sm, Gd, Tb, Dy, Ho, Er, Yb, Lu and B = Ti, Zr, Hf) pyrochlores. We performed a comparative analysis and showed how the structural, electronic, and vibrational properties of pyrochlore depend on the rare-earth and transition metal cations. The interesting findings in the pyrochlore titanate are the anomalous dynamical charges and structural instabilities which manifest as imaginary phonon frequencies. We showed that a small distortion of the atomic positions within the unit cell stabilizes the structure. We briefly explored the contribution of the various force constants to the vibrational modes and presented a comprehensive and comparative analysis of Raman and infrared active modes among various pyrochlore titanates.

In **Chapter 4**, we presented a comparative study of the elastic, mechanical, and thermal properties in rare-earth $RE_2B_2O_7$ (RE = Sm, Gd, Tb, Dy, Ho, Er, Yb, Lu and B = Ti, Zr, Hf) pyrochlores. We have shown the dependence of the bulk modulus, elastic constants, shear modulus, Young's modulus, Poisson's ratio, sound velocities, Debye temperature and the minimum thermal conductivity on the rare-earth and transition metal cations. Here, we also presented a comparative analysis between the LDA and GGA methods.

In **Chapter 5**, we presented pressure-dependent studies of structural, elastic, and phonon properties

in $Dy_2Ti_2O_7$. Both experimental and theoretical results show that the cell-volume, internal structure parameter, elastic moduli, and the vibrational frequencies display a slope change around 9 GPa pressure. The space group remains invariant across the pressures studied, hence the slope change is most likely related to an isostructural phase transition.

In **Chapter 6**, we examined the structural, electronic, vibrational, elastic, mechanical, and thermal properties in yttrium-based pyrochlores, i.e. $Y_2B_2O_7$ (B = Ti, Zr, and Hf). A large anomalous dynamical charge for Ti^{4+} ions was reported. The GGA calculations of $Y_2Ti_2O_7$ displayed large structural instabilities with respect to the phonon calculations, i.e. the frequencies of several of the optical modes were imaginary. A small distortion of the atomic positions in the primitive unit-cell stabilized the structure in the sense that all the frequencies became real valued. When the lighter Ti^{4+} ions were replaced by the heavier ions like, Zr^{4+} or Hf^{4+} ions, no structural instability was found in either of the approaches used.

In **Chapter 7**, we presented temperature dependent phonon studies in $Y_2Ti_2O_7$ using first principles density functional theory calculations and the many-body Green's function approach. Here, we reported the Grüneisen parameter values for various phonon modes, the temperature variation of the linear thermal expansion coefficient, and the temperature dependence of the quasiharmonic contribution to the various normal modes. A calculation of the contribution to the temperature dependent shifts in the phonon frequencies (and the phonon line-widths) arising from the third-order anharmonic interactions requires a knowledge of the third-order interatomic force constant matrix elements. The calculations presented in this chapter were carried out by approximating these matrix elements in terms of an assumed form involving a single coupling constant, which was then used as a fitting parameter. Within this approximation, we performed a comprehensive analysis of the two-phonon density of states, phonon linewidths, and frequency shifts for some of the phonon modes. We found that the results do not completely match experiments, in that while we did find anomalous temperature dependence, they happened only for two high frequency modes, and not for the low frequency modes as seen experimentally.

In **Chapter 8**, Motivated by the results of Chapter 7, we reexamined the temperature-dependent phonon properties in $Y_2B_2O_7$ (B = Ti, Zr) pyrochlores using the same DFT plus Green's function approach, but this time calculating the third-order interatomic force constant matrix elements (IFC3s) ab initio, using the "$2n+1$" theorem, implemented within the density functional linear response theory. The most interesting finding in our calculations in case of $Y_2Ti_2O_7$ was the anomalous behaviour of the same two modes as in the previous calculation. Among these two modes, we found that the F_{1g} mode shows a huge anomaly compared to the other anomalous mode. However, even these more sophisticated

calculations were unable to reproduce the anomalies reported in experiments for the lower frequency modes. On the other hand, when Ti^{4+} ions were replaced by Zr^{4+} ions, no anomaly in any of the phonon modes was found, consistent with the experimental finding in $Sm_2Ti_{2-x}Zr_xO_7$, where the authors found phonon anomalies in $Sm_2Ti_2O_7$, whereas $Sm_2Zr_2O_7$ showed no anomalous behaviour of any phonon modes.

In **Chapter 9**, we presented temperature-dependent phonon studies in rare-earth $RE_2Ti_2O_7$ (RE = Dy, Lu) pyrochlores using the same procedure as in Chapter 7 to get a qualitative understanding of the behaviour of phonons as a function of temperature. We found that the third order anharmonic shift in frequency for some of the phonon modes in these systems showed a positive contribution, which is a likely signature of phonon anomalous behaviour that one will find if one calculates the third order force constant matrix elements exactly.

Future outlook: As briefly described in the thesis, Maczka et al. and Saha et al. have found that their temperature-dependent Raman studies show an anomalous behavior for several low and high frequency optical modes in titanate pyrochlores. They suggested that phonon-phonon interactions are the main cause for these anomalies. In their analysis, they neglected the contributions from spin-phonon, crystal field-phonon, and the electron-phonon interactions (see Chapter 1 for more details). Hence, we considered only the phonon-phonon interactions in our theoretical studies to check whether they are sufficient to explain the observed anomalous nature of various phonon modes in titanate pyrochlores. Since our maximum temperature of interest is only up to 300K, which is smaller than the Debye temperature, Θ_D ($\Theta_D \sim 600$K for the pyrochlores), we considered only up to the third-order terms in the lattice anharmonic potential. From our sophisticated theoretical calculations, we found that a few high frequency phonon modes in titanate pyrochlores behave anomalously with temperature, consistent with the experimental results where also it has been found that a few high frequency modes show anomalous behaviour with cooling. However, we were unable to explain the anomalous behaviour of the low frequency modes as observed in experiments. Thus, it is still an open theoretical problem to explain the phonon anomaly for the low frequency modes. It would be interesting to see what happens when one also includes the higher order terms of the lattice anharmonic potential, other than the leading quasiharmonic and third-order anharmonic corrections. Also, from the dynamical charges it is clear that the titanate pyrochlores are ionic materials; hence the electron-phonon coupling (EPC) (specially for the optical phonons) might be important to include to explain the phonon anomalies in these materials. Thus, it would be interesting to study the effect of EPC on the phonon properties within the density functional theory framework.

In **Chapter 10**, we presented our studies of the temperature-dependent phonons in tetragonal $SrTiO_3$

perovskite. Here, we also presented the vibrational properties in the high temperature cubic phase of $SrTiO_3$, which displays a strong structural instability as indicated by the imaginary frequencies for several of the optical modes. For the tetragonal structure, we calculated the mode Grüneisen parameters, temperature variation of the linear thermal expansion coefficient, and the quasiharmonic frequency shift. Here also we used "$2n+1$" theorem to calculate the IFC3s. Within the third-order anharmonic approach, we studied the two-phonon density of states and temperature dependence of the phonon linewidths as well as the temperature dependence of the shift in frequency and the total frequency for some of the phonon modes. Unlike in the titanate pyrochlores we found that all the modes show a normal behaviour with temperature, i.e. their frequencies harden with cooling, completely unlike the experiments.

Future outlook: As briefly discussed in this chapter, Tetragonal $SrTiO_3$ is quite complex in nature with respect to the phonon calculations, consistent with the earlier reported results in the literature. STO is regarded as almost ferroelectric in the sense that a ferroelectric phase transition is expected at very low temperatures, but has not been found experimentally. The absence of the ferroelectric phase transition has been attributed to quantum fluctuations. For this reason, STO is also known as an incipient-ferroelectric (or quantum paraelectric). Hence, in this material also, it is likely that other terms (other than what we have considered in this thesis, i.e. the quasiharmonic and third-order anharmonic), like the higher order anharmonic effects, electron-phonon coupling, etc. need to be included to get a better picture of temperature-dependent phonon frequencies.

Appendix A

Linear thermal expansion coefficient

The linear thermal expansion coefficient is defined as the relative change of the length with respect to temperature at a fixed pressure

$$\begin{aligned} \alpha(T) &= \frac{1}{l}\left(\frac{\partial l}{\partial T}\right)_P \\ &= \frac{1}{3V}\left(\frac{\partial V}{\partial T}\right)_P \end{aligned} \tag{A.1}$$

where the change in the cell-volume as a function of temperature at a fixed pressure is obtained using the thermodynamics relations as follows

$$\left(\frac{\partial V}{\partial T}\right)_P = -\frac{(\partial P/\partial T)_V}{(\partial P/\partial V)_T} \tag{A.2}$$

Putting the Eq. A.2 into Eq. A.1, and using the definition of the bulk modulus ($B = -V\partial P/\partial V$), we get

$$\alpha(T) = \frac{1}{3B}\left(\partial P/\partial T\right)_V \tag{A.3}$$

Now the task is to evaluate the equation of state within the harmonic approximation. The pressure as a function of temperature is obtained from the Gibbs Free energy:

$$P = -\frac{\partial F}{\partial V} \tag{A.4}$$

where the free energy F is defined as

$$F = U - TS \tag{A.5}$$

where U is the internal energy and S is the entropy of the system. The energy-entropy relation is given as

$$T\left(\frac{\partial S}{\partial T}\right)_V = \left(\frac{\partial U}{\partial T}\right)_V \tag{A.6}$$

The entropy is obtained as $(S(T=0)=0)$

$$S = \int_0^T \frac{dT'}{T'}\frac{\partial U}{\partial T'} \tag{A.7}$$

Therefore, the pressure in terms of the internal energy is written as

$$P = -\frac{\partial}{\partial V}\left[U - T\int_0^T \frac{dT'}{T'}\frac{\partial U}{\partial T'}\right] \tag{A.8}$$

The internal energy of the system within the harmonic approximation is given as[91]

$$U = U^{(0)} + \sum_{\boldsymbol{q}j}\frac{1}{2}\hbar\omega_j(\boldsymbol{q}) + \sum_{\boldsymbol{q}j}\hbar\omega_j(\boldsymbol{q})n_j(\boldsymbol{q}) \tag{A.9}$$

where the first term in Eq. A.9 is the equilibrium energy of the system, the second term is due to the zero-point vibrations, and the third term is the vibrational energy at a finite temperature. The phonon occupation number is given as

$$n_j(\boldsymbol{q}) = \frac{1}{e^{\beta\hbar\omega_j(\boldsymbol{q})}-1} \tag{A.10}$$

Using Eqs. A.8 and A.9, the pressure is obtained as

$$\begin{aligned} P &= -\frac{\partial}{\partial V}\left[U^{(0)} + \sum_{\boldsymbol{q}j}\frac{1}{2}\hbar\omega_j(\boldsymbol{q}) + \sum_{\boldsymbol{q}j}\hbar\omega_j(\boldsymbol{q})n_j(\boldsymbol{q})\right] \\ &- k_BT\left(-\frac{\partial}{\partial V}\right)\left[\sum_{\boldsymbol{q}j}\left(\frac{\hbar\omega_j(\boldsymbol{q})}{k_B}\right)^2\int_0^T\frac{dT'}{T'^3}\frac{e^{\beta'\hbar\omega_j(\boldsymbol{q})}}{\left(e^{\beta'\hbar\omega_j(\boldsymbol{q})}-1\right)^2}\right] \end{aligned} \tag{A.11}$$

Changing the integration variable as $x = \beta\hbar\omega_j(\boldsymbol{q})$, we get

$$\begin{aligned} P &= -\frac{\partial}{\partial V}\left[U^{(0)} + \sum_{\boldsymbol{q}j}\frac{1}{2}\hbar\omega_j(\boldsymbol{q}) + \sum_{\boldsymbol{q}j}\hbar\omega_j(\boldsymbol{q})n_j(\boldsymbol{q})\right] \\ &- Tk_B\left(-\frac{\partial}{\partial V}\right)\left[\sum_{\boldsymbol{q}j}\int_{\beta\hbar\omega_j(\boldsymbol{q})}^{\infty}dx\frac{xe^x}{(e^x-1)^2}\right] \end{aligned} \tag{A.12}$$

After integrating by parts, we get

$$\int_{\beta\hbar\omega_j(\boldsymbol{q})}^{\infty} dx \frac{xe^x}{(e^x-1)^2} = \beta\hbar\omega_j(\boldsymbol{q}) + \frac{\beta\hbar\omega_j(\boldsymbol{q})}{e^{\beta\hbar\omega_j(\boldsymbol{q})}-1} - \ln\left[e^{\beta\hbar\omega_j(\boldsymbol{q})}-1\right] \tag{A.13}$$

Finally, the equation of state is obtained as

$$P = -\frac{\partial}{\partial V}\left[U^{(0)} + \sum_{\boldsymbol{q}j}\frac{1}{2}\hbar\omega_j(\boldsymbol{q})\right] + \sum_{\boldsymbol{q}j}\left(-\frac{\partial}{\partial V}(\hbar\omega_j(\boldsymbol{q}))\right) n_j(\boldsymbol{q}) \tag{A.14}$$

This result has a very simple structure: The first term (which is all that survives at $T = 0$) is the negative volume derivative of the ground-state energy. At nonzero temperatures this must be supplemented with the negative volume derivative of the phonon energies, the contribution of each phonon level being weighted with its mean occupation number.

Thus, the linear thermal expansion coefficient is obtained as:

$$\begin{aligned}
\alpha &= \frac{1}{3B}\left(\frac{\partial P}{\partial T}\right)_V \\
&= \frac{1}{3B}\sum_{\boldsymbol{q}j}\left[\left(-\frac{\hbar\partial\omega_j(\boldsymbol{q})}{\partial V}\right)\frac{\hbar\omega_j(\boldsymbol{q})}{k_BT^2}\frac{e^{\hbar\omega_j(\boldsymbol{q})/k_BT}}{(e^{\hbar\omega_j(\boldsymbol{q})/k_BT}-1)^2}\right] \\
&= \frac{1}{3BV}\sum_{\boldsymbol{q}j}\left[\gamma_j(\boldsymbol{q})\frac{(\hbar\omega_j(\boldsymbol{q}))^2}{k_BT^2}\frac{e^{\hbar\omega_j(\boldsymbol{q})/k_BT}}{(e^{\hbar\omega_j(\boldsymbol{q})/k_BT}-1)^2}\right]
\end{aligned} \tag{A.15}$$

where $\gamma_j(\boldsymbol{q})$ is the mode Grüneisen parameter for a phonon mode j at the wavevector $\boldsymbol{q}$ in the first Brillouin Zone.

Appendix B

Quasiharmonic shift in frequency

The mode Grüneisen parameter is defined as the logarithmic derivative of frequency with respect to the volume

$$\gamma_j = -\frac{\partial \ln \omega_j}{\partial \ln V} = -\frac{V}{\omega_j}\frac{\partial \omega_j}{\partial V} \tag{B.1}$$

After rearranging the terms, we get

$$\frac{\partial \omega_j}{\omega_j} = -\gamma_j \frac{\partial V}{V} = -\frac{\gamma_j}{V}\left(\frac{\partial V}{\partial T}\right)_P \partial T \tag{B.2}$$

Using Eq. A.1, the change in volume with respect to temperature at a fixed pressure is written as

$$\left(\frac{\partial V}{\partial T}\right)_P = 3V\alpha(T) \tag{B.3}$$

where $\alpha(T)$ is the linear thermal expansion coefficient. By putting Eq. B.3 into Eq. B.2, we get

$$\frac{\partial \omega_j}{\omega_j} = -3\gamma_j \alpha(T) \partial T \tag{B.4}$$

After integrating both sides with respect to T, the phonon frequency as a function of temperature within the quasiharmonic approximation is obtained as

$$\omega_j(T) = \omega_j(0) e^{-3\gamma_j \int_0^T \alpha(T')dT'} \tag{B.5}$$

Finally, the quasiharmonic shift in frequency is obtained as

$$\Delta_j^{(qh)} = \omega_j(T) - \omega_j(0) = \omega_j(0)\left[e^{-3\gamma_j \int_0^T \alpha(T')dT'} - 1\right] \tag{B.6}$$

Appendix C

Phonon-Phonon interactions

C.1 Non-zero Temperature Green's function formalism

Our goal is to explain the temperature dependence of phonon behaviour in real materials, so we have to work with the non-zero temperature Green's function formalism. At non-zero temperature, phonon is interacting with a bath of other phonons which have an average energy. The exact state of all other phonons is unknown, since they are fluctuating between different configurations. All that we know is the temperature, which is related to the mean energy. For the Green's function, we have to average over all possible configurations of the system. The phonon Green's function is defined as[226]

$$G(\boldsymbol{q}j, t-t') = \frac{Tre^{-\beta H}A_{\boldsymbol{q}j}(t)A_{-\boldsymbol{q}j}(t')}{Tre^{-\beta H}} \tag{C.1}$$

where β is the inverse temperature function, H is the Hamiltonian operator, and the time evolution of the phonon displacement vector within the Heisenberg representation is given by

$$A_{\boldsymbol{q}j}(t) = e^{itH}A_{\boldsymbol{q}j}e^{-itH} \tag{C.2}$$

Tr in Eq. C.1 stands for the trace which is the summation over some complete set of phonon states.

$$Tr \equiv \sum_{n}\langle n|...|n\rangle \tag{C.3}$$

The Hamiltonian within our study is

$$H = H_0 + V_3 \tag{C.4}$$

where H_0 corresponds to the harmonic part of the Hamiltonian which can be solved exactly and V_3 is the perturbation, cubic phonon-phonon interaction in our case. In the Matsubara approach, time is a

complex quantity. Let $\tau = it$. Green's functions are functions of τ with domain $-\beta \leq \tau \leq \beta$.

According to Fourier transform, if a function $f(\tau)$ is defined over the range $-\beta \leq \tau \leq \beta$, then the Fourier expansion is

$$f(\tau) = \frac{a_0}{2} + \sum_{n=1}^{\infty} \left[a_n \cos\left(\frac{n\pi\tau}{\beta}\right) + b_n \sin\left(\frac{n\pi\tau}{\beta}\right) \right] \tag{C.5}$$

Where

$$a_n = \frac{1}{\beta} \int_{-\infty}^{\infty} d\tau f(\tau) \cos\left(\frac{n\pi\tau}{\beta}\right) \tag{C.6}$$

$$b_n = \frac{1}{\beta} \int_{-\infty}^{\infty} d\tau f(\tau) \sin\left(\frac{n\pi\tau}{\beta}\right) \tag{C.7}$$

Another way to write Fourier transform is to define

$$f(i\omega_n) = \frac{1}{2}\beta(a_n + ib_n) \tag{C.8}$$

hence we have

$$f(\tau) = \frac{1}{\beta} \sum_{n=-\infty}^{\infty} e^{-in\pi\tau/\beta} f(i\omega_n) \tag{C.9}$$

$$f(i\omega_n) = \frac{1}{2} \int_{-\infty}^{\infty} d\tau f(\tau) e^{in\pi\tau/\beta} \tag{C.10}$$

The phonon occupation number is

$$n(\omega_j(\boldsymbol{q})) = \frac{1}{e^{\beta\omega_j(\boldsymbol{q})} - 1} \tag{C.11}$$

$n(\omega_j(\boldsymbol{q}))$ has poles at $\omega_n = \frac{2n\pi}{\beta}$, where $n = 0, \pm 1, \pm 2, \ldots$

C.1.1 Matsubara Green's function

For phonons in the interval $-\beta \leq \tau \leq \beta$, the Green's function is

$$G(\boldsymbol{q}j, \tau - \tau') = -\langle T_\tau A_{\boldsymbol{q}j}(\tau) A_{-\boldsymbol{q}j}(\tau') \rangle \tag{C.12}$$

$$A_{\boldsymbol{q}j}(\tau) = e^{\tau H} \left(a_{\boldsymbol{q}j} + a^\dagger_{-\boldsymbol{q}j} \right) e^{-\tau H} \tag{C.13}$$

$$G(\boldsymbol{q}j, \tau - \tau') = \frac{Tr\left[e^{-\beta H} T_\tau A_{\boldsymbol{q}j}(\tau) A_{-\boldsymbol{q}j}(\tau')\right]}{Tr e^{-\beta H}} \tag{C.14}$$

The factor T_τ is a τ-ordering operator, which arranges operators with earliest τ (closest to -β) to the right. We have to show that the left hand side is exactly a function of $\tau - \tau'$. Defining

$$Z_0 = Tr e^{-\beta H} \tag{C.15}$$

We consider the case for $\tau > \tau'$.

$$\begin{aligned} G(\boldsymbol{q}j, \tau - \tau') &= -\Theta(\tau - \tau')\frac{1}{Z_0} Tr\left[e^{-\beta H} A_{\boldsymbol{q}j}(\tau) A_{-\boldsymbol{q}j}(\tau')\right] \\ &- \Theta(\tau' - \tau)\frac{1}{Z_0} Tr\left[e^{-\beta H} A_{-\boldsymbol{q}j}(\tau') A_{\boldsymbol{q}j}(\tau)\right] \end{aligned} \tag{C.16}$$

As phonons are Bosons, so there is no sign change whenever phonon operators are interchanged.

$$\begin{aligned} G(\boldsymbol{q}j, \tau - \tau') &= -\Theta(\tau - \tau')\frac{1}{Z_0} Tr\left[e^{-\beta H} e^{\tau H}(a_{\boldsymbol{q}j} + a^{\dagger}_{-\boldsymbol{q}j}) e^{-\tau H} e^{\tau' H}(a_{-\boldsymbol{q}j} + a^{\dagger}_{\boldsymbol{q}j}) e^{-\tau' H}\right] \\ &- \Theta(\tau' - \tau)\frac{1}{Z_0} Tr\left[e^{-\beta H} e^{\tau' H}(a_{-\boldsymbol{q}j} + a^{\dagger}_{\boldsymbol{q}j}) e^{-\tau' H} e^{\tau H}(a_{\boldsymbol{q}j} + a^{\dagger}_{-\boldsymbol{q}j}) e^{-\tau H}\right] \end{aligned} \tag{C.17}$$

Using the theorem which states that the trace is invariant by a cyclic change of the operators.

$$Tr(ABC...XYZ) = Tr(BC...XYZA) \tag{C.18}$$

After arranging terms, we get

$$\begin{aligned} G(\boldsymbol{q}j, \tau - \tau') &= -\Theta(\tau - \tau')\frac{1}{Z_0} Tr\left[e^{-\beta H} e^{(\tau - \tau')H}(a_{\boldsymbol{q}j} + a^{\dagger}_{-\boldsymbol{q}j}) e^{-(\tau - \tau')H}(a_{-\boldsymbol{q}j} + a^{\dagger}_{\boldsymbol{q}j})\right] \\ &- \Theta(\tau' - \tau)\frac{1}{Z_0} Tr\left[e^{-\beta H} e^{(\tau' - \tau)H}(a_{-\boldsymbol{q}j} + a^{\dagger}_{\boldsymbol{q}j}) e^{-(\tau' - \tau)H}(a_{\boldsymbol{q}j} + a^{\dagger}_{-\boldsymbol{q}j})\right] \end{aligned} \tag{C.19}$$

The right hand side of this equation is now a function only of the combination $\tau - \tau'$. The Green's function can always be written as a function of this difference. It gives us the freedom to drop one of the time variables since it is unnecessary.

An equivalent definition of the Green's function is

$$\begin{aligned} G(\boldsymbol{q}j, \tau) &= -\langle T_\tau A_{\boldsymbol{q}j}(\tau) A_{-\boldsymbol{q}j}(0)\rangle \\ &= -\frac{1}{Z_0} Tr\left[e^{-\beta H} T_\tau e^{\tau H}(a_{\boldsymbol{q}j} + a^{\dagger}_{-\boldsymbol{q}j}) e^{-\tau H}(a_{-\boldsymbol{q}j} + a^{\dagger}_{\boldsymbol{q}j})\right] \end{aligned} \tag{C.20}$$

behaviour for $\tau < 0$,

$$\begin{aligned} G(\boldsymbol{q}j, \tau) &= -\langle A_{-\boldsymbol{q}j}(0) A_{\boldsymbol{q}j}(\tau)\rangle \\ &= -\frac{1}{Z_0} Tr\left[e^{-\beta H} A_{-\boldsymbol{q}j} e^{\tau H} A_{\boldsymbol{q}j} e^{-\tau H}\right] \end{aligned} \tag{C.21}$$

Using the cyclic permutations of the trace turn the trace into

$$\begin{aligned} G(\boldsymbol{q}j,\tau) &= -\frac{1}{Z_0}Tr\left[e^{\tau H}A_{\boldsymbol{q}j}e^{-(\tau+\beta)H}A_{-\boldsymbol{q}j}\right] \\ &= -\frac{1}{Z_0}Tr\left[e^{-\beta H}e^{(\tau+\beta)H}A_{\boldsymbol{q}j}e^{-(\tau+\beta)H}A_{-\boldsymbol{q}j}\right] \end{aligned} \tag{C.22}$$

Which proves

$$-\beta < \tau < 0: \quad G(\boldsymbol{q}j,\tau) = G(\boldsymbol{q}j,\tau+\beta) \tag{C.23}$$

The Fourier transform,

$$\begin{aligned} G(\boldsymbol{q}j,i\omega_n) &= \int_0^\beta e^{i\omega_n\tau}G(\boldsymbol{q}j,\tau) \\ G(\boldsymbol{q}j,\tau) &= \frac{1}{\beta}\sum_n e^{-i\omega_n\tau}G(\boldsymbol{q}j,i\omega_n) \\ \omega_n &= 2n\pi k_BT \end{aligned} \tag{C.24}$$

The non-interacting phonon Green's function is obtained by taking

$$H = H_0 = \sum_{\boldsymbol{q}j}\omega_j(\boldsymbol{q})a^\dagger_{\boldsymbol{q}j}a_{\boldsymbol{q}j} \tag{C.25}$$

$$a_{\boldsymbol{q}j}(\tau) = e^{\tau H_0}a_{\boldsymbol{q}j}e^{-\tau H_0} = e^{-\tau\omega_j(\boldsymbol{q})}a_{\boldsymbol{q}j} \tag{C.26}$$

$$a^\dagger_{\boldsymbol{q}j}(\tau) = e^{\tau H_0}a^\dagger_{\boldsymbol{q}j}e^{-\tau H_0} = e^{\tau\omega_j(\boldsymbol{q})}a^\dagger_{\boldsymbol{q}j} \tag{C.27}$$

$$\tag{C.28}$$

$$\begin{aligned} G^{(0)}(\boldsymbol{q}j,\tau) &= -\Theta(\tau)\langle(a_{\boldsymbol{q}j}e^{-\tau\omega_j(\boldsymbol{q})}+a^\dagger_{-\boldsymbol{q}j}e^{\tau\omega_j(\boldsymbol{q})})(a_{-\boldsymbol{q}j}+a^\dagger_{\boldsymbol{q}j})\rangle \\ &- \Theta(-\tau)\langle(a_{-\boldsymbol{q}j}+a^\dagger_{\boldsymbol{q}j})(a_{\boldsymbol{q}j}e^{-\tau\omega_j(\boldsymbol{q})}+a^\dagger_{-\boldsymbol{q}j}e^{\tau\omega_j(\boldsymbol{q})})\rangle \end{aligned} \tag{C.29}$$

The mean within the harmonic eigenstates: $\langle a^\dagger_{\boldsymbol{q}j}a_{\boldsymbol{q}j}\rangle = n_{\boldsymbol{q}j}; \langle a_{\boldsymbol{q}j}a^\dagger_{\boldsymbol{q}j}\rangle = n_{\boldsymbol{q}j}+1; \langle a_{\boldsymbol{q}j}a_{\boldsymbol{q}j}\rangle = 0; \langle a^\dagger_{\boldsymbol{q}j}a^\dagger_{\boldsymbol{q}j}\rangle = 0$

The Green's function of frequency is

$$\begin{aligned} G^{(0)}(\boldsymbol{q}j,i\omega_n) &= \int_0^\beta d\tau e^{i\omega_n\tau}G^{(0)}(\boldsymbol{q}j,\tau) \\ &= -\left[(n_{\boldsymbol{q}j}+1)\frac{e^{\beta(i\omega_n-\omega_j(\boldsymbol{q}))}-1}{i\omega_n-\omega_j(\boldsymbol{q})}+n_{\boldsymbol{q}j}\frac{e^{\beta(i\omega_n+\omega_j(\boldsymbol{q}))}-1}{i\omega_n+\omega_j(\boldsymbol{q})}\right] \end{aligned} \tag{C.30}$$

Now we have

$$
\begin{aligned}
e^{i\omega_n\beta} &= 1 && \text{(C.31)}\\
(n_{\boldsymbol{q}j}+1)(e^{-\beta\omega_j(\boldsymbol{q})}-1) &= -1 && \text{(C.32)}\\
(n_{\boldsymbol{q}j})(e^{\beta\omega_j(\boldsymbol{q})}-1) &= 1 && \text{(C.33)}\\
& && \text{(C.34)}
\end{aligned}
$$

Finally, the non-interacting phonon Green's function of frequency is obtained as

$$
\begin{aligned}
G^{(0)}(\boldsymbol{q}j,i\omega_n) &= \frac{1}{i\omega_n-\omega_j(\boldsymbol{q})}-\frac{1}{i\omega_n+\omega_j(\boldsymbol{q})}\\
&= -\frac{2\omega_j(\boldsymbol{q})}{\omega^2+\omega_j^2(\boldsymbol{q})} && \text{(C.35)}
\end{aligned}
$$

C.1.2 Dyson's equation

Phonon Green's function:

$$
\begin{aligned}
G(\boldsymbol{q}j,\tau) &= -\frac{1}{Z_0}Tr\left[e^{-\beta H}e^{\tau H}A_{\boldsymbol{q}j}e^{-\tau H}A_{-\boldsymbol{q}j}\right] && \text{(C.36)}\\
H &= H_0+V_3 && \text{(C.37)}
\end{aligned}
$$

H_0 can be solved exactly, so that we know its complete set of states. Consider the operators in the interaction representation. The Unitary and phonon displacement operators are written as

$$
\begin{aligned}
U(\tau) &= e^{\tau H_0}e^{-\tau H} && \text{(C.38)}\\
U^{-1}(\tau) &= e^{\tau H}e^{-\tau H_0} && \text{(C.39)}\\
\hat{A}_{\boldsymbol{q}j}(\tau) &= e^{\tau H_0}A_{\boldsymbol{q}j}e^{-\tau H_0}=e^{-\tau\omega_j(\boldsymbol{q})}A_{\boldsymbol{q}j} && \text{(C.40)}
\end{aligned}
$$

The Green's function for $\tau>0$,

$$
G(\boldsymbol{q}j,\tau)=-\frac{1}{Z_0}Tr\left[e^{-\beta H_0}(e^{\beta H_0}e^{-\beta H})(e^{\tau H}e^{-\tau H_0})(e^{\tau H_0}A_{\boldsymbol{q}j}e^{-\tau H_0})(e^{\tau H_0}e^{-\tau H})A_{-\boldsymbol{q}j}\right] \quad \text{(C.41)}
$$

$$
Z_0=Tre^{-\beta H}=Tr\left[e^{-\beta H_0}(e^{\beta H_0}e^{-\beta H})\right]=Tr\left[e^{-\beta H_0}U(\beta)\right] \quad \text{(C.42)}
$$

$$
G(\boldsymbol{q}j,\tau)=-\frac{1}{Z_0}Tr\left[e^{-\beta H_0}U(\beta)U^{-1}(\tau)\hat{A}_{\boldsymbol{q}j}(\tau)U(\tau)\hat{A}_{-\boldsymbol{q}j}\right] \quad \text{(C.43)}
$$

The operator $U(\tau)$ can be solved in terms of τ-ordered products. The derivative in the interaction representation is expressed as

$$\frac{\partial}{\partial\tau}U(\tau) = -\hat{V}_3(\tau)U(\tau) \tag{C.44}$$

This equation for $U(\tau)$ may be solved, at least formally, by repeated integrations and using $U(0) = 1$:

$$\begin{aligned} U(\tau) &= 1 - \int_0^\tau d\tau_1 \hat{V}_3(\tau_1)U(\tau_1) \\ &= \sum_{n=0}^{\infty}(-1)^n \int_0^\tau d\tau_1 ... \int_0^{\tau_{n-1}} d\tau_n \hat{V}_3(\tau_1)...\hat{V}_3(\tau_n) \\ &= \sum_{n=0}^{\infty}\frac{(-1)^n}{n!} \int_0^\tau d\tau_1 ... \int_0^\tau d\tau_n \left[T_\tau \hat{V}_3(\tau_1)...\hat{V}_3(\tau_n)\right] \\ &= T_\tau \exp\left[-\int_0^\tau d\tau_1 \hat{V}_3(\tau_1)\right] \end{aligned} \tag{C.45}$$

S-matrix is defined

$$S(\tau_1,\tau_2) = T_\tau \exp\left[-\int_{\tau_1}^{\tau_2} d\tau_1 \hat{V}_3(\tau_1)\right] \tag{C.46}$$

S-matrix identities:

$$S(\tau) = U(\tau) \tag{C.47}$$

$$S(\tau_1,\tau_2) = U(\tau_2)U^{-1}(\tau_1) \tag{C.48}$$

$$S(\tau_3,\tau_2)S(\tau_2,\tau_1) = S(\tau_3,\tau_1) \tag{C.49}$$

In this notation the Green's function (Eq. C.43) may be rewritten for $\tau > 0$ as

$$G(\boldsymbol{q}j,\tau) = -\frac{Tr\left[e^{-\beta H_0}T_\tau S(\beta,\tau)\hat{A}_{\boldsymbol{q}j}(\tau)S(\tau)\hat{A}_{-\boldsymbol{q}j}(0)\right]}{Tr\left[e^{-\beta H_0}S(\beta)\right]} \tag{C.50}$$

Using the above properties of $S(\beta,\tau)$ and taking advantage of the freedom to rearrange terms within the τ-ordering operator, we can write

$$G(\boldsymbol{q}j,\tau) = -\frac{Tr\left[e^{-\beta H_0}T_\tau S(\beta)\hat{A}_{\boldsymbol{q}j}(\tau)\hat{A}_{-\boldsymbol{q}j}(0)\right]}{Tr\left[e^{-\beta H_0}S(\beta)\right]} \tag{C.51}$$

Writing

$$Tre^{-\beta H_0} = \langle\hat{O}\rangle_0 \tag{C.52}$$

$\hat{O}$ is any operator. The Green's function is

$$G(\boldsymbol{q}j,\tau) = -\frac{\langle T_\tau S(\beta)\hat{A}_{\boldsymbol{q}j}(\tau)\hat{A}_{-\boldsymbol{q}j}(0)\rangle_0}{\langle S(\beta)\rangle_0} \tag{C.53}$$

The Green's function is evaluated by expanding S-matrix in the numerator,

$$\langle T_\tau S(\beta)\hat{A}_{\boldsymbol{q}j}(\tau)\hat{A}_{-\boldsymbol{q}j}(0)\rangle_0 = \sum_{n=0}^{\infty}\frac{(-1)^n}{n!}\int_0^\beta d\tau_1 ... \int_0^\beta d\tau_n \langle T_\tau \hat{A}_{\boldsymbol{q}j}(\tau)\hat{V}_3(\tau_1)...\hat{V}_3(\tau_n)\hat{A}_{-\boldsymbol{q}j}(0) \tag{C.54}$$

Each of the nth terms are evaluated by applying Wick's theorem to the brackets and thereby expressing the brackets as combinations of the non-interacting Green's functions $G^{(0)}$.

$$\begin{aligned}\langle T_\tau \hat{A}_{\boldsymbol{q}j}(\tau)\hat{A}_{\boldsymbol{q}_1 j_1}(\tau_1)\hat{A}_{\boldsymbol{q}_2 j_2}(\tau_1)\hat{A}_{-\boldsymbol{q}j}(0)\rangle_0 &= \delta_{\boldsymbol{q}+\boldsymbol{q}_1}\delta_{\boldsymbol{q}_2+\boldsymbol{q}}\delta_{j,j_1}\delta_{j_2,j}G^{(0)}(\boldsymbol{q}j,\tau-\tau_1)G^{(0)}(\boldsymbol{q}j,\tau_1) \\ &+ \delta_{\boldsymbol{q}_1+\boldsymbol{q}_2}\delta_{\boldsymbol{q}_1-\boldsymbol{q}}\delta_{j,j_2}\delta_{j_1,j}G^{(0)}(\boldsymbol{q}j,\tau-\tau_1)G^{(0)}(\boldsymbol{q}j,\tau) \\ &+ \delta_{\boldsymbol{q}_1+\boldsymbol{q}_2}\delta_{j_1,j_2}G^{(0)}(\boldsymbol{q}j,\tau)n_{\boldsymbol{q}_1 j_1}\end{aligned} \tag{C.55}$$

Diagrams in the S-matrix are connected or disconnected. Only connected diagrams are retained since the disconnected diagrams are cancelled by the vacuum polarization diagrams (see Ref.[226] for more details). From Matsubara Green's functions, the vacuum polarization graphs come from the denominator of Eq. C.53,

$$Z_0 = \langle S(\beta)\rangle_0 = \sum_{n=0}^{\infty}\frac{(-1)^n}{n!}\int_0^\beta d\tau_1 ... \int_0^\beta d\tau_n \langle T_\tau \hat{V}_3(\tau_1)...\hat{V}_3(\tau_n)\rangle_0 \tag{C.56}$$

The expansion of Z_0 produces a series of diagrams which just cancel the disconnected parts from the numerator of Eq. C.53. Finally, we are left with only different connected diagrams

$$G(\boldsymbol{q}j,\tau) = -\sum_{n=0}^{\infty}(-1)^n\int_0^\beta d\tau_1 ... \int_0^\beta d\tau_n \langle T_\tau \hat{A}_{\boldsymbol{q}j}(\tau)\hat{V}_3(\tau_1)...\hat{V}_3(\tau_n)\hat{A}_{-\boldsymbol{q}j}(0) \text{ (different connected)} \tag{C.57}$$

The Green's function of frequency

$$G(\boldsymbol{q}j,i\omega_n) = \int_0^\beta d\tau e^{i\omega_n\tau}G(\boldsymbol{q}j,\tau) \tag{C.58}$$

Where $\omega_n = 2n\pi k_B T$

The terms yield self-energy diagrams which may be collected into Dyson's equation

$$G(\boldsymbol{q}j, i\omega_n) = \frac{G^{(0)}(\boldsymbol{q}j, i\omega_n)}{1 - \Sigma(\boldsymbol{q}j, i\omega_n)G^{(0)}(\boldsymbol{q}j, i\omega_n)} \tag{C.59}$$

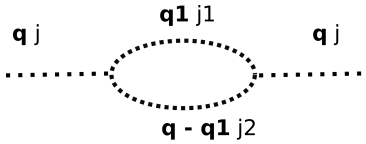

Figure C.1: Self energy diagram in second order perturbation theory

$$V_3 = \sum_{\boldsymbol{q_1},\boldsymbol{q_2}j_1,j_2,j_3} V^{(3)}(\boldsymbol{q}_1 j_1; \boldsymbol{q}_2 j_2; \boldsymbol{q} - \boldsymbol{q_1} j_3) A_{\boldsymbol{q}_1 j_1} A_{\boldsymbol{q}_2 j_2} A_{\boldsymbol{q}-\boldsymbol{q}_1 j_3} \tag{C.60}$$

For $n = 2$ the only connected diagram contribution is (see Fig. C.1)

$$\begin{aligned} G(\boldsymbol{q}j, \tau) &= -18 \sum_{\boldsymbol{q}_1, j_1, j_2} |V^{(3)}(\boldsymbol{q}j; \boldsymbol{q}_1 j_1; \boldsymbol{q} - \boldsymbol{q_1} j_2)|^2 \int_0^\beta d\tau_1 \int_0^\beta d\tau_2 G^{(0)}(\boldsymbol{q}j, \tau - \tau_1) G^{(0)}(\boldsymbol{q}_1 j_1, \tau_1 - \tau_2) \\ &\times \quad G^{(0)}(\boldsymbol{q} - \boldsymbol{q_1} j_2, \tau_1 - \tau_2) G^{(0)}(\boldsymbol{q}j, \tau_2) \end{aligned} \tag{C.61}$$

The factor of 18 multiplying the sums in Eq. C.61 arises from the fact that in Fig. C.1 the phonon $(\boldsymbol{q}j)$ can pair with any of three phonons at the left vertex, and also the phonon $(\boldsymbol{q}j)$ at right side can pair with any of three phonons at the right vertex. The two remaining phonons at the left vertex can pair with the two remaining phonons at the right vertex in two ways. Each of these 18 pairing schemes contributes equally to $G(\boldsymbol{q}j, \tau)$.

The τ integrals are done by using the expansion given below([226])

$$G^{(0)}(\boldsymbol{q}_1 j_1, \tau_1 - \tau_2) = \frac{1}{\beta} \sum_{\omega_n} e^{-i\omega_n(\tau_1 - \tau_2)} G^{(0)}(\boldsymbol{q}_1 j_1, i\omega_n) \tag{C.62}$$

so that

$$\begin{aligned} G(\boldsymbol{q}j, i\omega_n) &= -\frac{18}{\beta^4} \sum_{\boldsymbol{q}_1, j_1, j_2} |V^{(3)}(\boldsymbol{q}j; \boldsymbol{q}_1 j_1; \boldsymbol{q} - \boldsymbol{q_1} j_2)|^2 \\ &\times \sum_{mnn'n''} G^{(0)}(\boldsymbol{q}j, i\omega_m) G^{(0)}(\boldsymbol{q}_1 j_1, i\omega_n') G^{(0)}(\boldsymbol{q} - \boldsymbol{q_1} j_2, i\omega_n'') G^{(0)}(\boldsymbol{q}j, i\omega_n''') \\ &\times \int_0^\beta d\tau \int_0^\beta d\tau_1 \int_0^\beta d\tau_2 e^{i\omega_n \tau} e^{-i\omega_m(\tau - \tau_1)} e^{-i\omega_n'(\tau_1 - \tau_2)} e^{-i\omega_n''(\tau_1 - \tau_2)} e^{-i\omega_n''' \tau_2} \end{aligned} \tag{C.63}$$

All three τ integrals are of the form

$$\begin{aligned}\frac{1}{\beta}\int_0^\beta d\tau e^{i\tau(\omega_n-\omega_m)} &= \frac{1}{i\beta(\omega_n-\omega_m)}\left(e^{i\beta(\omega_n-\omega_m)}-1\right)\\ &= \frac{1}{2\pi i(n-m)}\left(e^{2\pi i(n-m)}-1\right)\\ &= \delta_{nm} \end{aligned} \tag{C.64}$$

which are written in the shorthand notation

$$\frac{1}{\beta}\int_0^\beta d\tau e^{i\tau(\omega_n-\omega_m)} = \delta_{\omega_n=\omega_m} \tag{C.65}$$

$$\frac{1}{\beta}\int_0^\beta d\tau_1 e^{i\tau_1(\omega_m-\omega_n'-\omega_n'')} = \delta_{\omega_m=\omega_n'+\omega_n''} \tag{C.66}$$

$$\frac{1}{\beta}\int_0^\beta d\tau_2 e^{i\tau_2(\omega_n'+\omega_n''-\omega_n''')} = \delta_{\omega_n'=\omega_n'''-\omega_n''} \tag{C.67}$$

$$\tag{C.68}$$

Combining these results yields the final result

$$\begin{aligned} G(\boldsymbol{q}j,i\omega_n) &= -\frac{18}{\beta}\sum_{\boldsymbol{q}_1,j_1,j_2}|V^{(3)}(\boldsymbol{q}j;\boldsymbol{q}_1j_1;\boldsymbol{q}-\boldsymbol{q}_1j_2)|^2 G^{(0)}(\boldsymbol{q}j,i\omega_n)\sum_{n'}G^{(0)}(\boldsymbol{q}_1j_1,i\omega_n')\\ &\times\ G^{(0)}(\boldsymbol{q}-\boldsymbol{q_1}j_2,i\omega_n-i\omega_n')G^{(0)}(\boldsymbol{q}j,i\omega_n)\\ &= G^{(0)}(\boldsymbol{q}j,i\omega_n)^2\Sigma(\boldsymbol{q}j,i\omega_n) \end{aligned} \tag{C.69}$$

Where the one-particle phonon self energy term is

$$\Sigma(\boldsymbol{q}j,i\omega_n) = -\frac{18}{\beta}\sum_{\boldsymbol{q}_1,j_1,j_2}|V^{(3)}(\boldsymbol{q}j;\boldsymbol{q}_1j_1;\boldsymbol{q}-\boldsymbol{q}_1j_2)|^2\sum_{\omega_m}G^{(0)}(\boldsymbol{q}_1j_1,i\omega_m)G^{(0)}(\boldsymbol{q}-\boldsymbol{q_1}j_2,i\omega_n-i\omega_m) \tag{C.70}$$

C.1.3 Frequency summations

When using the Matsubara Green's functions, one must often evaluate frequency summations over combinations of unperturbed Green's functions.

Considering the frequency summation part

$$\begin{aligned} S &= -\frac{1}{\beta}\sum_m G^{(0)}(\boldsymbol{q}_1j_1,i\omega_m)G^{(0)}(\boldsymbol{q}-\boldsymbol{q_1}j_2,i\omega_n-i\omega_m)\\ &= -\frac{1}{\beta}\sum_m \frac{2\omega_{j_1}(\boldsymbol{q}_1)}{\omega_m^2+\omega_{j_1}^2(\boldsymbol{q}_1)}\times\frac{2\omega_{j_2}(\boldsymbol{q}-\boldsymbol{q}_1)}{(\omega_n-\omega_m)^2+\omega_{j_2}^2(\boldsymbol{q}-\boldsymbol{q_1})} \end{aligned} \tag{C.71}$$

Writing this equation as

$$S = -\frac{1}{\beta}\sum_{m} f(i\omega_m) \tag{C.72}$$

where $f(i\omega_m)$ is the product of Green's functions in Eq. C.71. This summation can be evaluated using contour integration. The integral has the form

$$I = \lim_{R\to\infty} \oint \frac{dz}{2\pi i} f(z)n(z) \tag{C.73}$$

where the contour is a large circle of radius R in the limit as $R \to \infty$. The function $n(z)$ is chosen to generate poles at the points $i\omega_m$ for all even integer m. The function which does this is

$$n(z) = \frac{1}{e^{\beta z} - 1} \tag{C.74}$$

The poles of $n(z)$ are at the points $i2\pi m k_B T$ for all positive and negative integer m and $m = 0$. the residue at these poles is $1/\beta$. In Fig. C.2 ,these poles are shown as $\times$ marks which are evenly spaced on the vertical axis. The large circle is the contour of integration, which is a circle of radius R.

The function $f(z)$ is

$$f(z) = \frac{2\omega_{j_1}(\boldsymbol{q}_1)}{z^2 - \omega^2_{j_1}(\boldsymbol{q}_1)} \times \frac{2\omega_{j_2}(\boldsymbol{q}-\boldsymbol{q}_1)}{(i\omega_n - z)^2 - \omega^2_{j_2}(\boldsymbol{q}-\boldsymbol{q}_1)} \tag{C.75}$$

It has poles at the points $\pm\omega_{j_1}(\boldsymbol{q}_1)$ and $i\omega_n \pm \omega_{j_2}(\boldsymbol{q}-\boldsymbol{q}_1)$. The poles, and their residues, of the integral

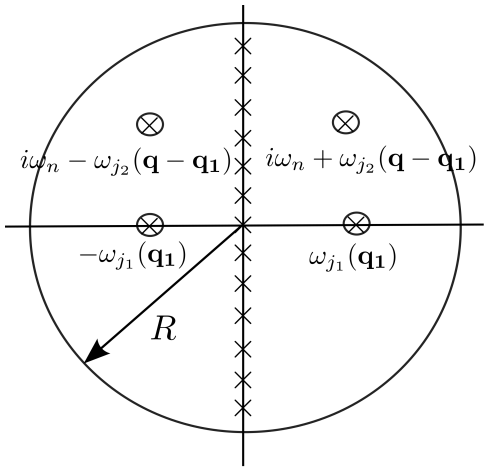

Figure C.2: Contour of evaluation of frequency sums

I in Eq. C.73 are

$$\begin{aligned}
z_m &= \frac{i2\pi m}{\beta}\ ,\ \ R_i = \frac{1}{\beta} f(i\omega_m) \\
z_1 &= \omega_{j_1}(\boldsymbol{q}_1)\ ,\ \ R_1 = \frac{n(\omega_{j_1}(\boldsymbol{q}_1))2\omega_{j_2}(\boldsymbol{q}-\boldsymbol{q_1})}{(i\omega_n - \omega_{j_1}(\boldsymbol{q}_1))^2 - \omega_{j_2}(\boldsymbol{q}-\boldsymbol{q_1})^2} \\
z_2 &= -\omega_{j_1}(\boldsymbol{q}_1)\ ,\ \ R_2 = -\frac{n(-\omega_{j_1}(\boldsymbol{q}_1))2\omega_{j_2}(\boldsymbol{q}-\boldsymbol{q_1})}{(i\omega_n + \omega_{j_1}(\boldsymbol{q}_1))^2 - \omega_{j_2}(\boldsymbol{q}-\boldsymbol{q_1})^2} \\
z_3 &= i\omega_n + \omega_{j_2}(\boldsymbol{q}-\boldsymbol{q_1})\ ,\ \ R_3 = \frac{n(\omega_{j_2}(\boldsymbol{q}-\boldsymbol{q_1}) + i\omega_n)2\omega_{j_1}(\boldsymbol{q_1})}{(i\omega_n + \omega_{j_2}(\boldsymbol{q}-\boldsymbol{q_1}))^2 - \omega_{j_1}(\boldsymbol{q_1})^2} \\
z_4 &= i\omega_n - \omega_{j_2}(\boldsymbol{q}-\boldsymbol{q_1})\ ,\ \ R_4 = \frac{n(i\omega_n - \omega_{j_2}(\boldsymbol{q}-\boldsymbol{q_1}))2\omega_{j_1}(\boldsymbol{q_1})}{(i\omega_n - \omega_{j_2}(\boldsymbol{q}-\boldsymbol{q_1}))^2 - \omega_{j_1}(\boldsymbol{q_1})^2}
\end{aligned} \tag{C.76}$$

We have

$$n(-\omega_{j_1}(\boldsymbol{q}_1)) = -\left[n(\omega_{j_1}(\boldsymbol{q}_1)) + 1\right];\quad e^{\beta i\omega_n} = 1 \tag{C.77}$$

Finally , the residues are written as

$$\begin{aligned}
R_1 &= \frac{n(\omega_{j_1}(\boldsymbol{q}_1))}{i\omega_n - \omega_{j_1}(\boldsymbol{q}_1) - \omega_{j_2}(\boldsymbol{q}-\boldsymbol{q_1})} - \frac{n(\omega_{j_1}(\boldsymbol{q}_1))}{i\omega_n - \omega_{j_1}(\boldsymbol{q}_1) + \omega_{j_2}(\boldsymbol{q}-\boldsymbol{q_1})} \\
R_2 &= \frac{n(\omega_{j_1}(\boldsymbol{q}_1)) + 1}{i\omega_n + \omega_{j_1}(\boldsymbol{q}_1) - \omega_{j_2}(\boldsymbol{q}-\boldsymbol{q_1})} - \frac{n(\omega_{j_1}(\boldsymbol{q}_1)) + 1}{i\omega_n + \omega_{j_1}(\boldsymbol{q}_1) + \omega_{j_2}(\boldsymbol{q}-\boldsymbol{q_1})} \\
R_3 &= -\frac{n(\omega_{j_2}(\boldsymbol{q}-\boldsymbol{q_1}))}{i\omega_n + \omega_{j_1}(\boldsymbol{q}_1) + \omega_{j_2}(\boldsymbol{q}-\boldsymbol{q_1})} + \frac{n(\omega_{j_2}(\boldsymbol{q}-\boldsymbol{q_1}))}{i\omega_n - \omega_{j_1}(\boldsymbol{q}_1) + \omega_{j_2}(\boldsymbol{q}-\boldsymbol{q_1})} \\
R_4 &= -\frac{n(\omega_{j_2}(\boldsymbol{q}-\boldsymbol{q_1})) + 1}{i\omega_n + \omega_{j_1}(\boldsymbol{q}_1) - \omega_{j_2}(\boldsymbol{q}-\boldsymbol{q_1})} + \frac{n(\omega_{j_2}(\boldsymbol{q}-\boldsymbol{q_1})) + 1}{i\omega_n - \omega_{j_1}(\boldsymbol{q}_1) - \omega_{j_2}(\boldsymbol{q}-\boldsymbol{q_1})}
\end{aligned} \tag{C.78}$$

The integral is evaluated by adding all these residues:

$$I = \frac{1}{\beta}\sum_m f(i\omega_m) + R_1 + R_2 + R_3 + R_4 \tag{C.79}$$

The integral vanishes ($I = 0$) in the limit that $R \to \infty$, finally we have

$$S = -\frac{1}{\beta}\sum_m f(i\omega_m) = R_1 + R_2 + R_3 + R_4 \tag{C.80}$$

After adding up all the residues we get

$$\begin{aligned}
S &= \left[n(\omega_{j_1}(\boldsymbol{q}_1)) + n(\omega_{j_2}(\boldsymbol{q}-\boldsymbol{q_1})) + 1\right]\left[\frac{1}{i\omega_n - \omega_{j_1}(\boldsymbol{q}_1) - \omega_{j_2}(\boldsymbol{q}-\boldsymbol{q_1})} - \frac{1}{i\omega_n + \omega_{j_1}(\boldsymbol{q}_1) + \omega_{j_2}(\boldsymbol{q}-\boldsymbol{q_1})}\right] \\
&+ \left[n(\omega_{j_1}(\boldsymbol{q}_1)) - n(\omega_{j_2}(\boldsymbol{q}-\boldsymbol{q_1}))\right] \\
&\times \left[\frac{1}{i\omega_n + \omega_{j_1}(\boldsymbol{q}_1) - \omega_{j_2}(\boldsymbol{q}-\boldsymbol{q_1})} - \frac{1}{i\omega_n - \omega_{j_1}(\boldsymbol{q}_1) + \omega_{j_2}(\boldsymbol{q}-\boldsymbol{q_1})}\right]
\end{aligned} \tag{C.81}$$

The Phonon self-energy obtained as

$$\begin{aligned}\Sigma(\boldsymbol{q}j, i\omega_n) &= 18\sum_{\boldsymbol{q_1},j_1,j_2}|V^{(3)}(\boldsymbol{q}j;\boldsymbol{q_1}j_1;\boldsymbol{q}-\boldsymbol{q_1}j_2)|^2\Big\{\left[n(\omega_{j_1}(\boldsymbol{q_1}))+n(\omega_{j_2}(\boldsymbol{q}-\boldsymbol{q_1}))+1\right]\\ &\times \left(\frac{1}{i\omega_n-\omega_{j_1}(\boldsymbol{q_1})-\omega_{j_2}(\boldsymbol{q}-\boldsymbol{q_1})}-\frac{1}{i\omega_n+\omega_{j_1}(\boldsymbol{q_1})+\omega_{j_2}(\boldsymbol{q}-\boldsymbol{q_1})}\right)\\ &+ \left[n(\omega_{j_1}(\boldsymbol{q_1}))-n(\omega_{j_2}(\boldsymbol{q}-\boldsymbol{q_1}))\right]\\ &\times \left(\frac{1}{i\omega_n+\omega_{j_1}(\boldsymbol{q_1})-\omega_{j_2}(\boldsymbol{q}-\boldsymbol{q_1})}-\frac{1}{i\omega_n-\omega_{j_1}(\boldsymbol{q_1})+\omega_{j_2}(\boldsymbol{q}-\boldsymbol{q_1})}\right)\Big\}\end{aligned} \tag{C.82}$$

Letting $i\omega_n = \omega + i\delta$ and $\omega_1 = \omega_{j_1}(\boldsymbol{q_1}), \omega_2 = \omega_{j_2}(\boldsymbol{q}-\boldsymbol{q_1}), n_1 = n(\omega_{j_1}(\boldsymbol{q_1})), n_2 = n(\omega_{j_2}(\boldsymbol{q}-\boldsymbol{q_1}))$. The phonon self-energy is written as

$$\begin{aligned}\Sigma(\boldsymbol{q}j, \omega_n) &= 18\sum_{\boldsymbol{q_1},j_1,j_2}|V^{(3)}(\boldsymbol{q}j;\boldsymbol{q_1}j_1;\boldsymbol{q}-\boldsymbol{q_1}j_2)|^2\Big\{(n_1+n_2+1)\left(\frac{1}{\omega-\omega_1-\omega_2+i\delta}-\frac{1}{\omega+\omega_1+\omega_2+i\delta}\right)\\ &+ (n_1-n_2)\left(\frac{1}{\omega+\omega_1-\omega_2+i\delta}-\frac{1}{\omega-\omega_1+\omega_2+i\delta}\right)\Big\}\end{aligned} \tag{C.83}$$

Using the relation:

$$\frac{1}{\omega+i\delta} = \mathcal{P}\frac{1}{\omega} - i\pi\delta(\omega) \tag{C.84}$$

where $\mathcal{P}$ stands for the Cauchy principal value. Taking only the complex part of the self energy, the linewidth of a phonon mode $\boldsymbol{q}j$ is obtained as

$$\begin{aligned}\Gamma(\boldsymbol{q}j, \omega) &= 18\pi\sum_{\boldsymbol{q_1},j_1,j_2}|V^{(3)}(\boldsymbol{q}j;\boldsymbol{q_1}j_1;\boldsymbol{q}-\boldsymbol{q_1}j_2)|^2\Big\{(n_1+n_2+1)\left[\delta(\omega-\omega_1-\omega_2)-\delta(\omega+\omega_1+\omega_2)\right]\\ &+ (n_1-n_2)\left[\delta(\omega+\omega_1-\omega_2)-\delta(\omega-\omega_1+\omega_2)\right]\Big\}\end{aligned} \tag{C.85}$$

Since the experiments are performed at the Γ-point ($\boldsymbol{q}=\boldsymbol{0}$) of the Brillouin zone, therefore, the phonon linewidth at the zone-centre of the Brillouin zone is written as

$$\begin{aligned}\Gamma(\omega_j, T) &= 18\pi\sum_{\boldsymbol{q},j_1,j_2}|V^{(3)}(\boldsymbol{0}j;\boldsymbol{q}j_1;-\boldsymbol{q}j_2)|^2\\ &\times \Big\{\left[n(\omega_{j_1}(\boldsymbol{q}))+n(\omega_{j_2}(-\boldsymbol{q}))+1\right]\left[\delta(\omega-\omega_{j_1}(\boldsymbol{q})-\omega_{j_2}(-\boldsymbol{q}))-\delta(\omega+\omega_{j_1}(\boldsymbol{q})+\omega_{j_2}(-\boldsymbol{q}))\right]\\ &+ \left[n(\omega_{j_1}(\boldsymbol{q}))-n(\omega_{j_2}(-\boldsymbol{q}))\right]\left[\delta(\omega+\omega_{j_1}(\boldsymbol{q})-\omega_{j_2}(-\boldsymbol{q}))-\delta(\omega-\omega_{j_1}(\boldsymbol{q})+\omega_{j_2}(-\boldsymbol{q}))\right]\Big\}\end{aligned} \tag{C.86}$$

So far in our calculations we have taken $\hbar = 1$, after introducing $\hbar$ in all our calculations, the phonon

linewidth is written as,

$$\begin{aligned}\Gamma(\omega_j,T) &= \frac{18\pi}{\hbar^2}\sum_{\boldsymbol{q},j_1,j_2}|V^{(3)}(\mathbf{0}j;\boldsymbol{q}j_1;-\boldsymbol{q}j_2)|^2 \\ &\times \Big\{[n(\omega_{j_1}(\boldsymbol{q}))+n(\omega_{j_2}(-\boldsymbol{q}))+1]\,[\delta(\omega-\omega_{j_1}(\boldsymbol{q})-\omega_{j_2}(-\boldsymbol{q}))-\delta(\omega+\omega_{j_1}(\boldsymbol{q})+\omega_{j_2}(-\boldsymbol{q}))] \\ &+ [n(\omega_{j_1}(\boldsymbol{q}))-n(\omega_{j_2}(-\boldsymbol{q}))]\,[\delta(\omega+\omega_{j_1}(\boldsymbol{q})-\omega_{j_2}(-\boldsymbol{q}))-\delta(\omega-\omega_{j_1}(\boldsymbol{q})+\omega_{j_2}(-\boldsymbol{q}))]\Big\} \quad \text{(C.87)}\end{aligned}$$

This expression of the phonon linewidth is used in all the calculations in this thesis. Since the self-energy is a complex quantity, and generally is written as $\Sigma(\omega_j,T)=\Delta(\omega_j,T)-i\Gamma(\omega_j,T)$, where the real part of it, $\Delta(\omega_j,T)$, represents the shift in frequency, whereas the imaginary part, $\Gamma(\omega_j,T)$, represents the linewidth of a jth phonon mode at temperature T. If we know the imaginary part, then the real part can be calculated easily by utilizing the Kramers-Krönig relation.

$$\Delta(\omega_j,T)=-\frac{1}{\pi}\mathcal{P}\int_{-\infty}^{\infty}\frac{d\omega'\Gamma(\omega',T)}{\omega'-\omega_j} \quad \text{(C.88)}$$

where $\mathcal{P}$ represents the Cauchy principal value integral.

Appendix D

Theory of elasticity in the cubic crystals

D.1 Stress-strain dependence

The relation between strain and stress is given by using the Hook's law of elasticity which states that the amount by which a material body is deformed (the strain) is linearly related to the force causing the deformation (the stress). The most general relationship between stress and strain can be written as

$$\sigma_{ij} = C_{ijkl}\epsilon_{ij} \tag{D.1}$$

Where C_{ijkl} is fourth order elastic stiffness tensor comprising 81 coefficients. However, depending on the symmetry of the crystal, the number of coefficients can be reduced.

D.2 The relation between elastic energy, strain and elastic constants within the harmonic approximation

The potential energy within the harmonic approximation is written as ([91])

$$U^{harm} = -\frac{1}{4}\sum_{\boldsymbol{R},\boldsymbol{R'}}[\boldsymbol{u}(\boldsymbol{R'}) - \boldsymbol{u}(\boldsymbol{R})]\boldsymbol{D}(\boldsymbol{R} - \boldsymbol{R'})[\boldsymbol{u}(\boldsymbol{R'}) - \boldsymbol{u}(\boldsymbol{R})] \tag{D.2}$$

where $\boldsymbol{u}$ represent the ionic displacement vectors and $\boldsymbol{D}$ correspond to the second-order force constant matrix elements. If $\boldsymbol{u}(\boldsymbol{R})$ varies little over the range of $\boldsymbol{D}(\boldsymbol{R} - \boldsymbol{R'})$, then to an excellent approximation

(which becomes exact in the limit of very long-wavelength disturbances) we can make the replacement

$$u(\boldsymbol{R'}) = u(\boldsymbol{R}) + (\boldsymbol{R'} - \boldsymbol{R}).\boldsymbol{\Delta} u(\boldsymbol{r})|_{\boldsymbol{r}=\boldsymbol{R}} \tag{D.3}$$

Then we have

$$\begin{aligned} U^{harm} &= -\frac{1}{4}\sum_{\boldsymbol{R},\boldsymbol{R'}} [(\boldsymbol{R'} - \boldsymbol{R}).\boldsymbol{\Delta} u(\boldsymbol{r})|_{\boldsymbol{r}=\boldsymbol{R}} \boldsymbol{D}(\boldsymbol{R'} - \boldsymbol{R}).\boldsymbol{\Delta} u(\boldsymbol{r})|_{\boldsymbol{r}=\boldsymbol{R}}] \\ &= -\frac{1}{4}\sum_{\boldsymbol{R},\boldsymbol{R'},\mu\nu\sigma\tau} R_\sigma \frac{\partial}{\partial x_\sigma} u_\mu(\boldsymbol{R}) D_{\mu\nu}(\boldsymbol{R}) R_\tau \frac{\partial}{\partial x_\tau} u_\nu(\boldsymbol{R}) \end{aligned} \tag{D.4}$$

Harmonic potential energy can be written as

$$U^{harm} = \frac{1}{2}\sum_{\boldsymbol{R},\mu\nu\sigma\tau} \left(\frac{\partial}{\partial x_\sigma} u_\mu(\boldsymbol{R})\right)\left(\frac{\partial}{\partial x_\tau} u_\nu(\boldsymbol{R})\right) E_{\sigma\mu\tau\nu} \tag{D.5}$$

Where $E_{\sigma\mu\tau\nu}$ is a fourth rank tensor quantity and is given as

$$E_{\sigma\mu\tau\nu} = -\frac{1}{2}\sum_{\boldsymbol{R}} R_\sigma D_{\mu\nu}(\boldsymbol{R}) R_\tau \tag{D.6}$$

As $u(\boldsymbol{r})$ are slowly varying functions, we can write summation as integral,

$$U^{harm} = \frac{1}{2}\sum_{\sigma\tau\mu\nu} \int d\boldsymbol{r} \left(\frac{\partial}{\partial x_\sigma} u_\mu(\boldsymbol{R})\right)\left(\frac{\partial}{\partial x_\tau} u_\nu(\boldsymbol{R})\right) \bar{E}_{\sigma\mu\tau\nu} \tag{D.7}$$

where

$$\bar{E}_{\sigma\mu\tau\nu} = \frac{1}{v} E_{\sigma\mu\tau\nu} \tag{D.8}$$

v is the volume of the primitive cell.

Based on symmetries, we can see that $E_{\sigma\mu\tau\nu}$ is invariant by the interchange $\mu \leftrightarrow \nu$ or the interchange $\sigma \leftrightarrow \tau$. Thus it is enough to specify the values of $E_{\sigma\mu\tau\nu}$ for the six values xx, yy, zz, yz, zx, xy for the pair $\mu\nu$, and the same six values of the pair $\sigma\tau$. Therefore, in total 36 independent numbers are required to specify the energy for a given deformation.

D.2.1 Further reduction in the number of independent elastic constants

The energy of a crystal is unaffected by a rigid rotation. However, a rotation through the infinitesimal angle $\delta\omega$ about an axis $\hat{n}$ passing through the origin, each Bravais lattice vector will be shifted by

$$\boldsymbol{u}(\boldsymbol{R}) = \delta\boldsymbol{\omega} \times \boldsymbol{R} \tag{D.9}$$

where, $\delta\boldsymbol{\omega} = \delta\omega\hat{n}$. For arbitrary $\delta\omega$, $U^{harm} = 0$, we get strain tensor as[91]

$$\epsilon_{\sigma\mu} = \frac{1}{2}\left(\frac{\partial}{\partial x_\sigma}u_\mu + \frac{\partial}{\partial x_\mu}u_\sigma\right) \tag{D.10}$$

Harmonic potential energy can also be written as

$$\begin{aligned} U^{harm} &= \frac{1}{2}\int d\boldsymbol{r} \sum_{\sigma\mu\tau\nu} \frac{1}{2}\left(\frac{\partial}{\partial x_\sigma}u_\mu + \frac{\partial}{\partial x_\mu}u_\sigma\right)\frac{1}{2}\left(\frac{\partial}{\partial x_\tau}u_\nu + \frac{\partial}{\partial x_\nu}u_\tau\right) \\ &\times \left(-\frac{1}{8v}\sum_{\boldsymbol{R}}(R_\sigma D_{\mu\nu}R_\tau + R_\mu D_{\sigma\nu}R_\tau + R_\sigma D_{\mu\tau}R_\nu + R_\mu D_{\sigma\tau}R_\nu)\right) \\ &= \frac{1}{2}\int d\boldsymbol{r} \sum_{\sigma\mu,\tau\nu} \epsilon_{\sigma\mu}C_{\sigma\mu\tau\nu}\epsilon_{\tau\nu} \end{aligned} \tag{D.11}$$

where

$$C_{\sigma\mu\tau\nu} = -\frac{1}{8v}\sum_{\boldsymbol{R}}[R_\sigma D_{\mu\nu}R_\tau + R_\mu D_{\sigma\nu}R_\tau + R_\sigma D_{\mu\tau}R_\nu + R_\mu D_{\sigma\tau}R_\nu] \tag{D.12}$$

$C_{\sigma\mu\tau\nu}$ is invariant under $\sigma\mu \leftrightarrow \tau\nu$. It is also invariant under $\sigma \leftrightarrow \mu$ or $\tau \leftrightarrow \nu$. Therefore, the total independent components of $C_{\sigma\mu\tau\nu}$ are 36 - 15 = 21.

Another way of defining the strain tensors is

$$\begin{aligned} e_{\mu\nu} &= \epsilon_{\mu\nu}, \qquad \mu = \nu \\ &= 2\epsilon_{\mu\nu}, \qquad \mu \neq \nu \end{aligned} \tag{D.13}$$

which are in turn, simplified to $e_\alpha, \alpha = 1, ...6.$ where $xx \to 1, yy \to 2, zz \to 3, yz \to 4, zx \to 5, xy \to 6.$

Thus, the total energy in terms of strain and elastic constants is written as

$$U^{harm} = \frac{1}{2}\sum_{\alpha\beta}\int d\boldsymbol{r} e_\alpha C_{\alpha\beta}e_\beta \tag{D.14}$$

where $C_{\alpha\beta} = C_{\sigma\mu\tau\nu}$, $\alpha \leftrightarrow \sigma\mu$, and $\beta \leftrightarrow \tau\nu$.

$C_{\alpha\beta}$ are called elastic stiffness constants or elastic moduli.

The elastic energy density is written as

$$U = \frac{1}{2}\sum_{\alpha=1}^{6}\sum_{\beta=1}^{6} C_{\alpha\beta}e_{\alpha}e_{\beta} \tag{D.15}$$

The stress component σ_{xx} is given as

$$\sigma_{xx} = \frac{\partial U}{\partial e_{xx}} = \frac{\partial U}{\partial e_1} = C_{11}e_1 + \frac{1}{2}\sum_{\beta=2}^{6}(C_{1\beta} + C_{\beta 1})e_{\beta} \tag{D.16}$$

Only the combination $\frac{1}{2}(C_{1\beta} + C_{\beta 1})$ enters the stress-strain relations. Therefore, elastic stiffness constants are symmetrical.

$$C_{\alpha\beta} = C_{\beta\alpha} \tag{D.17}$$

D.2.2 Elastic stiffness constants of cubic crystals

The minimum symmetry requirements for a cubic structure is the existence of four three-fold rotation axes. The axes are in the [111] and equivalent directions (Fig. D.1). The effect of a rotation of $2\pi/3$ about these four axes is to interchange the x, y, z axes according to the schemes.

$$\begin{aligned} x \to y \to z \to x; \qquad & -x \to z \to -y \to -x \\ x \to z \to -y \to x; \qquad & -x \to y \to z \to -x \end{aligned} \tag{D.18}$$

according to the axis chosen. Under first of these symmetry schemes ($x \to y \to z \to x$), we have

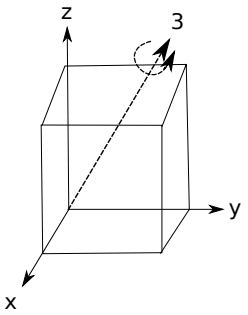

Figure D.1: Rotation by $2\pi/3$ about the axis marked 3 changes $x \to y; y \to z;$ and $z \to x$.

$C_{11} = C_{22} = C_{33}; C_{44} = C_{55} = C_{66}; C_{12} = C_{13} = C_{23}; C_{14} = C_{25} = C_{36}; C_{15} = C_{26} = C_{34}; C_{16} = C_{24} =$

$C_{35}; C_{45} = C_{56}; C_{46} = C_{54}$. The elastic energy density is written as

$$U = \frac{1}{2}\begin{pmatrix} e_{xx} & e_{yy} & e_{zz} & e_{yz} & e_{zx} & e_{xy} \end{pmatrix} \begin{pmatrix} C_{11} & C_{12} & C_{12} & C_{14} & C_{15} & C_{16} \\ C_{12} & C_{11} & C_{12} & C_{24} & C_{25} & C_{26} \\ C_{12} & C_{12} & C_{11} & C_{34} & C_{35} & C_{36} \\ C_{14} & C_{24} & C_{34} & C_{44} & C_{45} & C_{46} \\ C_{15} & C_{25} & C_{35} & C_{45} & C_{44} & C_{56} \\ C_{16} & C_{26} & C_{36} & C_{46} & C_{56} & C_{44} \end{pmatrix} \begin{pmatrix} e_{xx} \\ e_{yy} \\ e_{zz} \\ e_{yz} \\ e_{zx} \\ e_{xy} \end{pmatrix} \tag{D.19}$$

After taking the symmetries of elastic stiffness constants we get the energy density as

$$\begin{aligned} U &= \frac{1}{2}C_{11}\left[e_{xx}^2 + e_{yy}^2 + e_{zz}^2\right] + \frac{1}{2}C_{44}\left[e_{yz}^2 + e_{zx}^2 + e_{xy}^2\right] + C_{12}\left[e_{xx}e_{yy} + e_{yy}e_{zz} + e_{zz}e_{xx}\right] \\ &+ C_{14}\left[e_{xx}e_{yz} + e_{yy}e_{zx} + e_{zz}e_{xy}\right] + C_{15}\left[e_{xx}e_{zx} + e_{yy}e_{xy} + e_{zz}e_{yz}\right] + C_{16}\left[e_{xx}e_{xy} + e_{yy}e_{yz} + e_{zz}e_{zx}\right] \\ &+ C_{45}\left[e_{yz}e_{zx} + e_{zx}e_{xy}\right] + C_{46}e_{yz}e_{xy} \end{aligned} \tag{D.20}$$

First three terms are invariant under the symmetry schemes listed above. For example,under first scheme, $e_{xx}^2 + e_{yy}^2 + e_{zz}^2 \rightarrow e_{yy}^2 + e_{zz}^2 + e_{xx}^2$. Similarly, we can show that first three terms of energy density are invariant under all four symmetry schemes considered above. Last five terms are odd in one or more indices and a rotation among four symmetry schemes will change the sign of the term, because $e_{xy} = -e_{x(-y)}$, for example. Thus these terms are not invariant under the required operations.

Hence the elastic energy density for a cubic crystal is written as

$$U = \frac{1}{2}C_{11}\left[e_{xx}^2 + e_{yy}^2 + e_{zz}^2\right] + \frac{1}{2}C_{44}\left[e_{yz}^2 + e_{zx}^2 + e_{xy}^2\right] + C_{12}\left[e_{xx}e_{yy} + e_{yy}e_{zz} + e_{zz}e_{xx}\right] \tag{D.21}$$

The stress components in terms of elastic constants and strain tensors are written as

$$\begin{aligned} \sigma_{xx} &= C_{11}e_{xx} + C_{12}e_{yy} + C_{13}e_{zz} + C_{14}e_{yz} + C_{15}e_{zx} + C_{16}e_{xy} \\ \sigma_{yy} &= C_{21}e_{xx} + C_{22}e_{yy} + C_{23}e_{zz} + C_{24}e_{yz} + C_{25}e_{zx} + C_{26}e_{xy} \\ \sigma_{zz} &= C_{31}e_{xx} + C_{32}e_{yy} + C_{33}e_{zz} + C_{34}e_{yz} + C_{35}e_{zx} + C_{36}e_{xy} \\ \sigma_{yz} &= C_{41}e_{xx} + C_{42}e_{yy} + C_{43}e_{zz} + C_{44}e_{yz} + C_{45}e_{zx} + C_{46}e_{xy} \\ \sigma_{zx} &= C_{51}e_{xx} + C_{52}e_{yy} + C_{53}e_{zz} + C_{54}e_{yz} + C_{55}e_{zx} + C_{56}e_{xy} \\ \sigma_{xy} &= C_{61}e_{xx} + C_{62}e_{yy} + C_{63}e_{zz} + C_{64}e_{yz} + C_{65}e_{zx} + C_{66}e_{xy} \end{aligned} \tag{D.22}$$

The stress tensors can also be obtained from the energy density. For cubic crystal,

$$\sigma_{xx} = \frac{\partial U}{\partial e_{xx}} = C_{11}e_{xx} + C_{12}(e_{zz} + e_{yy}) \tag{D.23}$$

Comparing Eq. D.23 with the σ_{xx} of Eq. D.22, we get

$$C_{12} = C_{13}; \qquad C_{14} = C_{15} = C_{16} = 0 \tag{D.24}$$

$$\sigma_{xy} = \frac{\partial U}{\partial e_{xy}} = C_{44} e_{xy}; \tag{D.25}$$

on comparison with Eq. D.22 we have

$$C_{61} = C_{62} = C_{63} = C_{64} = C_{65} = 0; \qquad C_{66} = C_{44} \tag{D.26}$$

Thus based on the symmetry schemes considered we find that the array of values of elastic stiffness constants is reduced for a cubic crystal to the matrix form

$$C = \begin{pmatrix} C_{11} & C_{12} & C_{12} & 0 & 0 & 0 \\ C_{12} & C_{11} & C_{12} & 0 & 0 & 0 \\ C_{12} & C_{12} & C_{11} & 0 & 0 & 0 \\ 0 & 0 & 0 & C_{44} & 0 & 0 \\ 0 & 0 & 0 & 0 & C_{44} & 0 \\ 0 & 0 & 0 & 0 & 0 & C_{44} \end{pmatrix} \tag{D.27}$$

D.3 Calculation of elastic constants

D.3.1 Hydrostatic deformation of fcc lattice

The lattice parameters for the unstrained fcc lattice are $a = b = c = a_0$. The cell parameters in matrix form are given as

$$R^{fcc} = \frac{a_0}{2} \begin{pmatrix} -1 & 0 & 1 \\ 0 & 1 & 1 \\ -1 & 1 & 0 \end{pmatrix} \tag{D.28}$$

In the hydrostatic deformation, we change the lattice parameters in such a way that the lattice experiences an isotropic pressure along all three axes. If we deform the lattice parameters by a small amount ϵ, where within the elastic limit, the maximum value of ϵ is taken to be $\|0.04\|$. The deformed lattice

parameter matrix is given as

$$D_{hydro} = a_0 \begin{pmatrix} 1+\epsilon & 0 & 0 \\ 0 & 1+\epsilon & 0 \\ 0 & 0 & 1+\epsilon \end{pmatrix} \tag{D.29}$$

The cell parameters after the deformation are given as

$$R^{fcc}_{hydro} = \frac{a_0+\epsilon}{2} \begin{pmatrix} -1 & 0 & 1 \\ 0 & 1 & 1 \\ -1 & 1 & 0 \end{pmatrix} \tag{D.30}$$

For the hydrostatic deformation, the strain components are given as $e_{xx} = e_{yy} = e_{zz} = \epsilon; e_{xy} = e_{yz} = e_{zx} = 0$ The elastic energy is obtained as,

$$E = \frac{3}{2} V_0 (C_{11} + 2C_{12}) \epsilon^2 \tag{D.31}$$

D.3.2 Uniaxial or tetragonal deformation

The uniaxial deformations are also called the tetragonal deformation where we give strain along one axis. In cubic lattice, all the axes are symmetrically equivalent. So the application of stress along the z-axis is symmetrically equivalent as giving the strain along either x or y-axis. If we apply the stress along the z-direction, the deformed lattice parameters are given as

$$D_{uniaxial} = a_0 \begin{pmatrix} 1 & 0 & 0 \\ 0 & 1 & 0 \\ 0 & 0 & 1+\epsilon \end{pmatrix} \tag{D.32}$$

The cell parameters are reduced to

$$R^{fcc}_{uniaxial} = \frac{1}{2} \begin{pmatrix} -a_0 & 0 & (a_0+\epsilon) \\ 0 & a_0 & (a_0+\epsilon) \\ -a_0 & a_0 & 0 \end{pmatrix} \tag{D.33}$$

Within the uniaxial strain, the components of strain tensor are given as

$$\epsilon_{xx} = \epsilon_{yy} = 0; \epsilon_{zz} = \epsilon; \epsilon_{xy} = \epsilon_{yz} = \epsilon_{zx} = 0 \tag{D.34}$$

The elastic energy in the case of uniaxial deformation is reduced to

$$E = \frac{1}{2} V_0 C_{11} \epsilon^2 \tag{D.35}$$

D.3.3 Shear deformation

The lattice parameters under the shear deformation are given as

$$D_{shear} = \begin{pmatrix} a_0 & \epsilon & \epsilon \\ \epsilon & a_0 & \epsilon \\ \epsilon & \epsilon & a_0 \end{pmatrix} \tag{D.36}$$

The cell parameters for the shear deformation are

$$R^{fcc}_{uniaxial} = \frac{1}{2} \begin{pmatrix} -(a_0 - \epsilon) & 0 & (a_0 - \epsilon) \\ 2\epsilon & (a_0 + \epsilon) & (a_0 + \epsilon) \\ -(a_0 - \epsilon) & (a_0 - \epsilon) & 0 \end{pmatrix} \tag{D.37}$$

strain tensor components are given as

$$\epsilon_{xy} = \epsilon_{yz} = \epsilon_{zx} = \epsilon; \epsilon_{xx} = \epsilon_{yy} = \epsilon_{zz} = 0 \tag{D.38}$$

the shear deformed elastic energy is given as

$$E = \frac{3}{2} V_0 C_{44} \epsilon^2 \tag{D.39}$$

Bibliography

[1] Jason S. Gardner, Michel J. P. Gingras, and John E. Greedan. Magnetic pyrochlore oxides. *Rev. Mod. Phys.*, 82:53–107, 2010.

[2] M.A. Subramanian, G. Aravamudan, and G.V. Subba Rao. Oxide pyrochlores a review. *Progress in Solid State Chemistry*, 15:55–143, 1983.

[3] John E. Greedan. Geometrically frustrated magnetic materials. *J. Mater. Chem.*, 11:37–53, 2001.

[4] J. H. Zhao, H. P. Kunkel, X. Z. Zhou, Gwyn Williams, and M. A. Subramanian. Critical behavior of the magnetoresistive pyrochlore $tl_2mn_2O_7$. *Phys. Rev. Lett.*, 83:219–222, 1999.

[5] Surajit Saha. Phonon anomalies and phase transitions in pyrochlore titanates, boron nitride nanotubes and multiferroic $bifeo_3$: Temperature and pressure-dependent raman studies. *PhD diss., Indian Institute of Science*, 2010.

[6] Andrew Harrison. First catch your hare: the design and synthesis of frustrated magnets. *Journal of Physics: Condensed Matter*, 16:S553, 2004.

[7] G. Toulouse. Theory of the frustration effect in spin glasses i. *Commun Phys*, 2:115, 1977.

[8] J Villain. Spin glass with non-random interactions. *Journal of Physics C: Solid State Physics*, 10: 1717, 1977.

[9] J. A. Hodges, P. Bonville, A. Forget, A. Yaouanc, P. Dalmas de Réotier, G. André, M. Rams, K. Królas, C. Ritter, P. C. M. Gubbens, C. T. Kaiser, P. J. C. King, and C. Baines. First-order transition in the spin dynamics of geometrically frustrated $yb_2ti_2O_7$. *Phys. Rev. Lett.*, 88:077204, 2002.

[10] S. Nakatsuji, Y. Machida, Y. Maeno, T. Tayama, T. Sakakibara, J. van Duijn, L. Balicas, J. N. Millican, R. T. Macaluso, and Julia Y. Chan. Metallic spin-liquid behavior of the geometrically frustrated kondo lattice $pr_2ir_2o_7$. *Phys. Rev. Lett.*, 96:087204, 2006.

[11] J. S. Gardner, S. R. Dunsiger, B. D. Gaulin, M. J. P. Gingras, J. E. Greedan, R. F. Kiefl, M. D. Lumsden, W. A. MacFarlane, N. P. Raju, J. E. Sonier, I. Swainson, and Z. Tun. Cooperative paramagnetism in the geometrically frustrated pyrochlore antiferromagnet $tb_2ti_2o_7$. *Phys. Rev. Lett.*, 82:1012–1015, 1999.

[12] A P Ramirez. Strongly geometrically frustrated magnets. *Annual Review of Materials Science*, 24:453–480, 1994.

[13] M. J. P. Gingras, C. V. Stager, N. P. Raju, B. D. Gaulin, and J. E. Greedan. Static critical behavior of the spin-freezing transition in the geometrically frustrated pyrochlore antiferromagnet $y_2mo_2o_7$. *Phys. Rev. Lett.*, 78:947–950, 1997.

[14] J. S. Gardner, B. D. Gaulin, S.-H. Lee, C. Broholm, N. P. Raju, and J. E. Greedan. Glassy statics and dynamics in the chemically ordered pyrochlore antiferromagnet $Y_2mo_2O_7$. *Phys. Rev. Lett.*, 83:211–214, 1999.

[15] M. J. Harris, S. T. Bramwell, D. F. McMorrow, T. Zeiske, and K. W. Godfrey. Geometrical frustration in the ferromagnetic pyrochlore $ho_2ti_2O_7$. *Phys. Rev. Lett.*, 79:2554–2557, 1997.

[16] J. N. Reimers, A. J. Berlinsky, and A.-C. Shi. Mean-field approach to magnetic ordering in highly frustrated pyrochlores. *Phys. Rev. B*, 43:865–878, 1991.

[17] N. P. Raju, M. Dion, M. J. P. Gingras, T. E. Mason, and J. E. Greedan. Transition to long-range magnetic order in the highly frustrated insulating pyrochlore antiferromagnet $gd_2ti_2o_7$. *Phys. Rev. B*, 59:14489–14498, 1999.

[18] S. E. Palmer and J. T. Chalker. Order induced by dipolar interactions in a geometrically frustrated antiferromagnet. *Phys. Rev. B*, 62:488–492, 2000.

[19] Maged Elhajal, Benjamin Canals, Raimon Sunyer, and Claudine Lacroix. Ordering in the pyrochlore antiferromagnet due to dzyaloshinsky-moriya interactions. *Phys. Rev. B*, 71:094420, 2005.

[20] Oleg Tchernyshyov, R. Moessner, and S. L. Sondhi. Spin-peierls phases in pyrochlore antiferromagnets. *Phys. Rev. B*, 66:064403, 2002.

[21] E. F. Shender, V. B. Cherepanov, P. C. W. Holdsworth, and A. J. Berlinsky. Kagomé antiferromagnet with defects: Satisfaction, frustration, and spin folding in a random spin system. *Phys. Rev. Lett.*, 70:3812–3815, 1993.

[22] R. Moessner and A. J. Berlinsky. Magnetic susceptibility of diluted pyrochlore and $srcr_{9-9x}ga_{3+9x}O_{19}$ antiferromagnets. *Phys. Rev. Lett.*, 83:3293–3296, 1999.

[23] T. E. Saunders and J. T. Chalker. Spin freezing in geometrically frustrated antiferromagnets with weak disorder. *Phys. Rev. Lett.*, 98:157201, 2007.

[24] N. P. Raju, E. Gmelin, and R. K. Kremer. Magnetic-susceptibility and specific-heat studies of spin-glass-like ordering in the pyrochlore compounds $r_2mo_2o_7$ (r=y, sm, or gd). *Phys. Rev. B*, 46: 5405–5411, 1992.

[25] J. E. Greedan, J. N. Reimers, S. L. Penny, and C. V. Stager. Shortrange ordering in a threedimensionally frustrated magnet, tb2mo2o7, by wide and smallangle neutron diffraction. *Journal of Applied Physics*, 67:5967–5969, 1990.

[26] B. D. Gaulin, J. N. Reimers, T. E. Mason, J. E. Greedan, and Z. Tun. Spin freezing in the geometrically frustrated pyrochlore antiferromagnet $tb_2mo_2o_7$. *Phys. Rev. Lett.*, 69:3244–3247, 1992.

[27] J. D. M. Champion, M. J. Harris, P. C. W. Holdsworth, A. S. Wills, G. Balakrishnan, S. T. Bramwell, E. Čižmár, T. Fennell, J. S. Gardner, J. Lago, D. F. McMorrow, M. Orendáč, A. Orendáčová, D. McK. Paul, R. I. Smith, M. T. F. Telling, and A. Wildes. $er_2ti_2o_7$: evidence of quantum order by disorder in a frustrated antiferromagnet. *Phys. Rev. B*, 68:020401, 2003.

[28] I. Mirebeau, I. N. Goncharenko, P. Cadavez-Peres, S. T. Bramwell, M. J. P. Gingras, and J. S. Gardner. Pressure-induced crystallization of a spin liquid. *Nature*, 420:54–57, 2002.

[29] K. C. Rule, J. P. C. Ruff, B. D. Gaulin, S. R. Dunsiger, J. S. Gardner, J. P. Clancy, M. J. Lewis, H. A. Dabkowska, I. Mirebeau, P. Manuel, Y. Qiu, and J. R. D. Copley. Field-induced order and spin waves in the pyrochlore antiferromagnet $tb_2ti_2o_7$. *Phys. Rev. Lett.*, 96:177201, 2006.

[30] A. P. Ramirez, B. S. Shastry, A. Hayashi, J. J. Krajewski, D. A. Huse, and R. J. Cava. Multiple field-induced phase transitions in the geometrically frustrated dipolar magnet: $gd_2ti_2o_7$. *Phys. Rev. Lett.*, 89:067202, 2002.

[31] M P Zinkin, M J Harris, Z Tun, R A Cowley, and B M Wanklyn. Lifting of the ground-state degeneracy by crystal-field interactions in the pyrochlore. *Journal of Physics: Condensed Matter*, 8:193–197, 1996.

[32] Y. Taguchi, Y. Oohara, H. Yoshizawa, N. Nagaosa, and Y. Tokura. Spin chirality, berry phase, and anomalous hall effect in a frustrated ferromagnet. *Science*, 291:2573–2576, 2001.

[33] Surjeet Singh, R. Suryanarayanan, R. Tackett, G. Lawes, A. K. Sood, P. Berthet, and A. Revcolevschi. Ordered spin-ice state in the geometrically frustrated metallic ferromagnet $sm_2mo_2o_7$. *Phys. Rev. B*, 77:020406, 2008.

[34] K Matsuhira, Z Hiroi, T Tayama, S Takagi, and T Sakakibara. A new macroscopically degenerate ground state in the spin ice compound dy 2 ti 2 o 7 under a magnetic field. *Journal of Physics: Condensed Matter*, 14:L559, 2002.

[35] K Matsuhira, Y Hinatsu, K Tenya, and T Sakakibara. Low temperature magnetic properties of frustrated pyrochlore ferromagnets ho 2 sn 2 o 7 and ho 2 ti 2 o 7. *Journal of Physics: Condensed Matter*, 12:L649, 2000.

[36] A.P. Ramirez, A. Hayashi, R.J. Cava, R. Siddharthan, and B.S. Shastry. Zero-point entropy in 'spin ice'. *Nature*, 399:333–335, 1999.

[37] Hironori Sakai, Kazuyoshi Yoshimura, Hiroyuki Ohno, Harukazu Kato, Shinsaku Kambe, Russell E Walstedt, Tatsuma D Matsuda, Yoshinori Haga, and Yoshichika Onuki. Superconductivity in a pyrochlore oxide, cd 2 re 2 o 7. *Journal of Physics: Condensed Matter*, 13:L785, 2001.

[38] O. Vyaselev, K. Arai, K. Kobayashi, J. Yamazaki, K. Kodama, M. Takigawa, M. Hanawa, and Z. Hiroi. Superconductivity and magnetic fluctuations in $cd_2re_2O_7$ via cd nuclear magnetic resonance and re nuclear quadrupole resonance. *Phys. Rev. Lett.*, 89:017001, 2002.

[39] T. Fennell, P. P. Deen, A. R. Wildes, K. Schmalzl, D. Prabhakaran, A. T. Boothroyd, R. J. Aldus, D. F. McMorrow, and S. T. Bramwell. Magnetic coulomb phase in the spin ice ho2ti2o7. *Science*, 326:415–417, 2009.

[40] D. J. P. Morris, D. A. Tennant, S. A. Grigera, B. Klemke, C. Castelnovo, R. Moessner, C. Czternasty, M. Meissner, K. C. Rule, J.-U. Hoffmann, K. Kiefer, S. Gerischer, D. Slobinsky, and R. S. Perry. Dirac strings and magnetic monopoles in the spin ice dy2ti2o7. *Science*, 326:411–414, 2009.

[41] S. Kumar and H.C. Gupta. First principles study of zone centre phonons in rare-earth pyrochlore titanates, re2ti2o7 (re=gd, dy, ho, er, lu; y). *Vibrational Spectroscopy*, 62:180–187, 2012.

[42] Franois Brisse and Osvald Knop. Pyrochlores. iii. x-ray, neutron, infrared, and dielectric studies of a2sn2o7 stannates. *Canadian Journal of Chemistry*, 46:859–873, 1968.

[43] Osvald Knop, Franois Brisse, and Lotte Castelliz. Pyrochlores. v. thermoanalytic, x-ray, neutron, infrared, and dielectric studies of a2ti2o7 titanates. *Canadian Journal of Chemistry*, 47:971–990, 1969.

[44] John F. McCaffrey, Neil T. McDevitt, and Conrad M. Phillippi. Infrared lattice spectra of rare-earth stannate and titanate pyrochlores. *J. Opt. Soc. Am.*, 61:209–212, 1971.

[45] M. T. Vandenborre, E. Husson, J. P. Chatry, and D. Michel. Rare-earth titanates and stannates of pyrochlore structure; vibrational spectra and force fields. *Journal of Raman Spectroscopy*, 14: 63–71, 1983.

[46] H. C. Gupta, Sonal Brown, Neelima Rani, and V. B. Gohel. Lattice dynamic investigation of the zone center wavenumbers of the cubic a2ti2o7 pyrochlores. *Journal of Raman Spectroscopy*, 32: 41–44, 2001.

[47] F.X. Zhang and S.K. Saxena. Structural changes and pressure-induced amorphization in rare earth titanates re2ti2o7 (re: Gd, sm) with pyrochlore structure. *Chemical Physics Letters*, 413: 248–251, 2005.

[48] F. X. Zhang, B. Manoun, S. K. Saxena, and C. S. Zha. Structure change of pyrochlore sm2ti2o7 at high pressures. *Applied Physics Letters*, 86:181906, 2005.

[49] Surajit Saha, D. V. S. Muthu, C. Pascanut, N. Dragoe, R. Suryanarayanan, G. Dhalenne, A. Revcolevschi, Sukanta Karmakar, Surinder M. Sharma, and A. K. Sood. High-pressure raman and x-ray study of the spin-frustrated pyrochlore $gd_2ti_2o_7$. *Phys. Rev. B*, 74:064109, 2006.

[50] F.X. Zhang, B. Manoun, and S.K. Saxena. Pressure-induced orderdisorder transitions in pyrochlore re2ti2o7 (re=y, gd). *Materials Letters*, 60:2773–2776, 2006.

[51] T. T. A. Lummen, I. P. Handayani, M. C. Donker, D. Fausti, G. Dhalenne, P. Berthet, A. Revcolevschi, and P. H. M. van Loosdrecht. Phonon and crystal field excitations in geometrically frustrated rare earth titanates. *Phys. Rev. B*, 77:214310, 2008.

[52] M. Maczka, J. Hanuza, K. Hermanowicz, A. F. Fuentes, K. Matsuhira, and Z. Hiroi. Temperature-dependent raman scattering studies of the geometrically frustrated pyrochlores dy2ti2o7, gd2ti2o7 and er2ti2o7. *Journal of Raman Spectroscopy*, 39:537–544, 2008.

[53] M. Maczka, M. L. Sanjuán, A. F. Fuentes, K. Hermanowicz, and J. Hanuza. Temperature-dependent raman study of the spin-liquid pyrochlore $tb_2ti_2o_7$. *Phys. Rev. B*, 78:134420, 2008.

[54] Surajit Saha, Surjeet Singh, B. Dkhil, S. Dhar, R. Suryanarayanan, G. Dhalenne, A. Revcolevschi, and A. K. Sood. Temperature-dependent raman and x-ray studies of the spin-ice pyrochlore $dy_2ti_2o_7$ and nonmagnetic pyrochlore $lu_2ti_2o_7$. *Phys. Rev. B*, 78:214102, 2008.

[55] Surjeet Singh, Surajit Saha, S. K. Dhar, R. Suryanarayanan, A. K. Sood, and A. Revcolevschi. Manifestation of geometric frustration on magnetic and thermodynamic properties of the pyrochlores $sm_2X_2o_7$ ($x = \mathrm{Ti}, \mathrm{Zr}$). *Phys. Rev. B*, 77:054408, 2008.

[56] Surajit Saha, D. V. S Muthu, Surjeet Singh, B. Dkhil, R. Suryanarayanan, G. Dhalenne, H. K. Poswal, S. Karmakar, Surinder M. Sharma, A. Revcolevschi, and A. K. Sood. Low-temperature and high-pressure raman and x-ray studies of pyrochlore $tb_2ti_2o_7$: Phonon anomalies and possible phase transition. *Phys. Rev. B*, 79:134112, 2009.

[57] M. Maczka, M. L. Sanjuán, A. F. Fuentes, L. Macalik, J. Hanuza, K. Matsuhira, and Z. Hiroi. Temperature-dependent studies of the geometrically frustrated pyrochlores $ho_2ti_2o_7$ and $dy_2ti_2o_7$. *Phys. Rev. B*, 79:214437, 2009.

[58] C Z Bi, J Y Ma, B R Zhao, Z Tang, D Yin, C Z Li, D Z Yao, J Shi, and X G Qiu. Far infrared optical properties of the pyrochlore spin ice compound dy2ti2o7. *Journal of Physics: Condensed Matter*, 17:5225–5233, 2005.

[59] J. S. Gardner, B. D. Gaulin, A. J. Berlinsky, P. Waldron, S. R. Dunsiger, N. P. Raju, and J. E. Greedan. Neutron scattering studies of the cooperative paramagnet pyrochlore $tb_2ti_2o_7$. *Phys. Rev. B*, 64:224416, 2001.

[60] James A. Noland. Optical absorption of single-crystal strontium titanate. *Phys. Rev.*, 94:724–724, 1954.

[61] R. Moos, W. Menesklou, and K. H. Härdtl. Hall mobility of undoped n-type conducting strontium titanate single crystals between 19 k and 1373 k. *Applied Physics A*, 61:389–395, 1995.

[62] J. Gerblinger and H. Meixner. Fast oxygen sensors based on sputtered strontium titanate. *Sensors and Actuators B: Chemical*, 4:99–102, 1991.

[63] Farrel W. Lytle. Xray diffractometry of lowtemperature phase transformations in strontium titanate. *Journal of Applied Physics*, 35:2212–2215, 1964.

[64] M. A. Saifi and L. E. Cross. Dielectric properties of strontium titanate at low temperature. *Phys. Rev. B*, 2:677–684, 1970.

[65] K. A. Müller and W. Berlinger. Static critical exponents at structural phase transitions. *Phys. Rev. Lett.*, 26:13–16, 1971.

[66] Alastair George Hartley Smith. Structural and defect properties of strontium titanate. *PhD diss., University College London*, 2011.

[67] K. A. Müller and H. Burkard. $Srtio_3$: An intrinsic quantum paraelectric below 4 k. *Phys. Rev. B*, 19:3593–3602, 1979.

[68] V. Železný, Eric Cockayne, J. Petzelt, M. F. Limonov, D. E. Usvyat, V. V. Lemanov, and A. A. Volkov. Temperature dependence of infrared-active phonons in $catio_3$: a combined spectroscopic and first-principles study. *Phys. Rev. B*, 66:224303, 2002.

[69] Chen Ang, A. S. Bhalla, and L. E. Cross. Dielectric behavior of paraelectric $ktao_3$, $catio_3$, and $(Ln_{1/2}na_{1/2})tio_3$ under a dc electric field. *Phys. Rev. B*, 64:184104, 2001.

[70] C. H. Perry and T. F. McNelly. Ferroelectric "soft" mode in $ktao_3$. *Phys. Rev.*, 154:456–458, 1967.

[71] G. A. Samara and B. Morosin. Anharmonic effects in $ktao_3$: Ferroelectric mode, thermal expansion,and compressibility. *Phys. Rev. B*, 8:1256–1264, 1973.

[72] G. Shirane and Y. Yamada. Lattice-dynamical study of the 110 k phase transition in $srtio_3$. *Phys. Rev.*, 177:858–863, 1969.

[73] P A Fleury. The effects of soft modes on the structure and properties of materials. *Annual Review of Materials Science*, 6:157–180, 1976.

[74] G. Venkataraman. Soft modes and structural phase transitions. *Bulletin of Materials Science*, 1: 129–170, 1979.

[75] G. Shirane. Neutron scattering studies of structural phase transitions at brookhaven. *Rev. Mod. Phys.*, 46:437–449, 1974.

[76] Robert A. Evarestov, Evgeny Blokhin, Denis Gryaznov, Eugene A. Kotomin, and Joachim Maier. Phonon calculations in cubic and tetragonal phases of $srtio_3$: A comparative lcao and plane-wave study. *Phys. Rev. B*, 83:134108, 2011.

[77] Na Sai and David Vanderbilt. First-principles study of ferroelectric and antiferrodistortive instabilities in tetragonal $srtio_3$. *Phys. Rev. B*, 62:13942–13950, 2000.

[78] Narayani Choudhury, Eric J. Walter, Alexander I. Kolesnikov, and Chun-Keung Loong. Large phonon band gap in $SrTio_3$ and the vibrational signatures of ferroelectricity in $aTio_3$ perovskites: First-principles lattice dynamics and inelastic neutron scattering. *Phys. Rev. B*, 77:134111, 2008.

[79] Terumasa Tadano and Shinji Tsuneyuki. Self-consistent phonon calculations of lattice dynamical properties in cubic $srtio_3$ with first-principles anharmonic force constants. *Phys. Rev. B*, 92:054301, 2015.

[80] M. Born and K. Huang. Dynamical theory of crystal lattices. 1954.

[81] Robert M. Pick, Morrel H. Cohen, and Richard M. Martin. Microscopic theory of force constants in the adiabatic approximation. *Phys. Rev. B*, 1:910–920, 1970.

[82] Richard M. Martin. Electronic structure:basic theory and practical methods. 2004.

[83] P. Hohenberg and W. Kohn. Inhomogeneous electron gas. *Phys. Rev.*, 136:B864–B871, 1964.

[84] W. Kohn and L. J. Sham. Self-consistent equations including exchange and correlation effects. *Phys. Rev.*, 140:A1133–A1138, 1965.

[85] J. F. Janak. Proof that $\frac{\partial e}{\partial n_i} = \epsilon$ in density-functional theory. *Phys. Rev. B*, 18:7165–7168, 1978.

[86] D. M. Ceperley and B. J. Alder. Ground state of the electron gas by a stochastic method. *Phys. Rev. Lett.*, 45:566–569, 1980.

[87] E. Wigner. Effects of the electron interaction on the energy levels of electrons in metals. *Trans. Faraday Soc.*, 34:678–685, 1938.

[88] L Hedin and B I Lundqvist. Explicit local exchange-correlation potentials. *Journal of Physics C: Solid State Physics*, 4:2064, 1971.

[89] S. H. Vosko, L. Wilk, and M. Nusair. Accurate spin-dependent electron liquid correlation energies for local spin density calculations: a critical analysis. *Canadian Journal of Physics*, 58:1200–1211, 1980.

[90] J. P. Perdew and Alex Zunger. Self-interaction correction to density-functional approximations for many-electron systems. *Phys. Rev. B*, 23:5048–5079, 1981.

[91] N. W. Ashcroft and N. D. Mermin. Solid state physics. page 133, 1976.

[92] D. J. Chadi and Marvin L. Cohen. Special points in the brillouin zone. *Phys. Rev. B*, 8:5747–5753, 1973.

[93] J D Joannopoulos and M L Cohen. Electronic charge densities for zns in the wurtzite and zincblende structures. *Journal of Physics C: Solid State Physics*, 6:1572, 1973.

[94] Hendrik J. Monkhorst and James D. Pack. Special points for brillouin-zone integrations. *Phys. Rev. B*, 13:5188–5192, 1976.

[95] R. A. Evarestov and V. P. Smirnov. Special points of the brillouin zone and their use in the solid state theory. *physica status solidi (b)*, 119:9–40, 1983.

[96] James C. Phillips. Energy-band interpolation scheme based on a pseudopotential. *Phys. Rev.*, 112:685–695, 1958.

[97] M. T. Yin and Marvin L. Cohen. Theory of ab initio pseudopotential calculations. *Phys. Rev. B*, 25:7403–7412, 1982.

[98] R. P. Feynman. Forces in molecules. *Phys. Rev.*, 56:340–343, 1939.

[99] John D. Head and Michael C. Zerner. A broydenfletchergoldfarbshanno optimization procedure for molecular geometries. *Chemical Physics Letters*, 122:264–270, 1985.

[100] O. H. Nielsen and Richard M. Martin. First-principles calculation of stress. *Phys. Rev. Lett.*, 50: 697–700, 1983.

[101] A. A. Maradudin and A. E. Fein. Scattering of neutrons by an anharmonic crystal. *Phys. Rev.*, 128:2589–2608, 1962.

[102] Stefano Baroni, Stefano de Gironcoli, Andrea Dal Corso, and Paolo Giannozzi. Phonons and related crystal properties from density-functional perturbation theory. *Rev. Mod. Phys.*, 73:515–562, 2001.

[103] M. T. Yin and Marvin L. Cohen. Theory of lattice-dynamical properties of solids: Application to si and ge. *Phys. Rev. B*, 26:3259–3272, 1982.

[104] Stefano Baroni, Paolo Giannozzi, and Andrea Testa. Green's-function approach to linear response in solids. *Phys. Rev. Lett.*, 58:1861–1864, 1987.

[105] Charles Kittel. Introduction to solid state physics. 2004.

[106] J. M. Pruneda and Emilio Artacho. First-principles study of structural, elastic, and bonding properties of pyrochlores. *Phys. Rev. B*, 72:085107, 2005.

[107] A.M. Srivastava and M.G. Brik. Comparative ab initio study of electronic, optical and chemical bonding properties of pyrochlores, y2b2o7 (b=ti4+, sn4+). *Journal of Luminescence*, 130:2368–2376, 2010.

[108] J. Matt Farmer, Lynn A. Boatner, Bryan C. Chakoumakos, Mao-Hua Du, Michael J. Lance, Claudia J. Rawn, and Jeff C. Bryan. Structural and crystal chemical properties of rare-earth titanate pyrochlores. *Journal of Alloys and Compounds*, 605:63–70, 2014.

[109] Lan Yang, Changhua Zhu, Ye Sheng, Hongqiang Nian, Qian Li, Peng Song, Wencong Lu, Jiong Yang, and Bin Liu. Investigation of mechanical and thermal properties of rare earth pyrochlore oxides by first-principles calculations. *Journal of the American Ceramic Society*, 102:2830–2840, 2019.

[110] Paolo Giannozzi, Stefano Baroni, Nicola Bonini, Matteo Calandra, Roberto Car, Carlo Cavazzoni, Davide Ceresoli, Guido L Chiarotti, Matteo Cococcioni, Ismaila Dabo, Andrea Dal Corso, Stefano de Gironcoli, Stefano Fabris, Guido Fratesi, Ralph Gebauer, Uwe Gerstmann, Christos Gougoussis, Anton Kokalj, Michele Lazzeri, Layla Martin-Samos, Nicola Marzari, Francesco Mauri, Riccardo Mazzarello, Stefano Paolini, Alfredo Pasquarello, Lorenzo Paulatto, Carlo Sbraccia, Sandro Scandolo, Gabriele Sclauzero, Ari P Seitsonen, Alexander Smogunov, Paolo Umari, and Renata M Wentzcovitch. Quantum espresso: a modular and open-source software project for quantum simulations of materials. *Journal of Physics: Condensed Matter*, 21:395502, 2009.

[111] James D. Pack and Hendrik J. Monkhorst. "special points for brillouin-zone integrations"—a reply. *Phys. Rev. B*, 16:1748–1749, 1977.

[112] Bernd G. Pfrommer, Michel Ct, Steven G. Louie, and Marvin L. Cohen. Relaxation of crystals with the quasi-newton method. *Journal of Computational Physics*, 131:233–240, 1997.

[113] Jie Lian, Jian Chen, L. M. Wang, Rodney C. Ewing, J. Matt Farmer, Lynn A. Boatner, and K. B. Helean. Radiation-induced amorphization of rare-earth titanate pyrochlores. *Phys. Rev. B*, 68: 134107, 2003.

[114] A. V. Shlyakhtina, I. V. Kolbanev, A. V. Knotko, M. V. Boguslavskii, S. Yu. Stefanovich, O. K. Karyagina, and L. G. Shcherbakova. Ionic conductivity of ln2 + xzr2 xo7 x/2 (ln = sm-gd) solid solutions. *Inorganic Materials*, 41:854–863, 2005.

[115] Marinus van Dijk, Anthonie Burggraaf, Alastair N. Cormack, and C. R. A. Catlow. Defect structures and migration mechanisms in oxide pyrochlores. 1985.

[116] B.P. Mandal, Nandini Garg, Surinder M. Sharma, and A.K. Tyagi. Preparation, xrd and raman spectroscopic studies on new compounds re2hf2o7 (re=dy, ho, er, tm, lu, y): Pyrochlores or defect-fluorite? *Journal of Solid State Chemistry*, 179:1990–1994, 2006.

[117] R. D. Shannon. Revised effective ionic radii and systematic studies of interatomic distances in halides and chalcogenides. *Acta Crystallographica Section A*, 32:751–767, 1976.

[118] R. D. Shannon and C. T. Prewitt. Effective ionic radii in oxides and fluorides. *Acta Crystallographica Section B*, 25:925–946, 1969.

[119] R.D. Shannon and C.T. Prewitt. Effective ionic radii and crystal chemistry. *Journal of Inorganic and Nuclear Chemistry*, 32:1427–1441, 1970.

[120] Linus Pauling. The sizes of ions and the structure of ionic crystals. *Journal of the American Chemical Society*, 49:765–790, 1927.

[121] J. C. Slater. Atomic radii in crystals. *The Journal of Chemical Physics*, 41:3199–3204, 1964.

[122] G.R. Lumpkin, R.C. Ewing, and E.M. Foltyn. Thermal recrystallization of alpha-recoil damaged minerals of the pyrochlore structure type. *Journal of Nuclear Materials*, 139:113–120, 1986.

[123] L. H. Brixner. Preparation and properties of the ln2ti2o7-type rare earth titanate. *Inorganic Chemistry*, 3:1065–1067, 1964.

[124] Bryan C. Chakoumakos. Systematics of the pyrochlore structure type, ideal a2b2x6y. *Journal of Solid State Chemistry*, 53:120–129, 1984.

[125] B.P. Mandal, Ankita Banerji, Vasant Sathe, S.K. Deb, and A.K. Tyagi. Orderdisorder transition in nd2ygdyzr2o7 pyrochlore solid solution: An x-ray diffraction and raman spectroscopic study. *Journal of Solid State Chemistry*, 180:2643–2648, 2007.

[126] S Zhang, H B. Zhang, F A. Zhao, Meiren Jiang, H Y. Xiao, Zi-Jiang Liu, and X T. Zu. Impact of isovalent and aliovalent substitution on the mechanical and thermal properties of gd2zr2o7. *Scientific Reports*, 7, 2017.

[127] Farheen N. Sayed, V. Grover, K. Bhattacharyya, D. Jain, A. Arya, C. G. S. Pillai, and A. K. Tyagi. Sm2xdyxzr2o7 pyrochlores: Probing orderdisorder dynamics and multifunctionality. *Inorganic Chemistry*, 50:2354–2365, 2011.

[128] M. Posternak, R. Resta, and A. Baldereschi. Role of covalent bonding in the polarization of perovskite oxides: The case of $knbo_3$. *Phys. Rev. B*, 50:8911–8914, 1994.

[129] Ph. Ghosez, J.-P. Michenaud, and X. Gonze. Dynamical atomic charges: The case of ABo_3 compounds. *Phys. Rev. B*, 58:6224–6240, 1998.

[130] Paolo Giannozzi, Stefano de Gironcoli, Pasquale Pavone, and Stefano Baroni. Ab initio calculation of phonon dispersions in semiconductors. *Phys. Rev. B*, 43:7231–7242, 1991.

[131] D. C. Wallace. Thermodynamics of crystals. 1998.

[132] Sonal Brown, H. C. Gupta, J. A. Alonso, and M. J. Martinez-Lope. Vibrational spectra and force field calculation of a2mn2o7 (a = y, dy, er, yb) pyrochlores. *Journal of Raman Spectroscopy*, 34: 240–243, 2003.

[133] Masashi Mori, Geoff M Tompsett, Nigel M Sammes, Eisaku Suda, and Yasuo Takeda. Compatibility of gdxti2o7 pyrochlores (1.72x2.0) as electrolytes in high-temperature solid oxide fuel cells. *Solid State Ionics*, 158:79–90, 2003.

[134] N. J. Hess, B. D. Begg, S. D. Conradson, D. E. McCready, P. L. Gassman, and W. J. Weber. Spectroscopic investigations of the structural phase transition in gd2(ti1-yzry)2o7 pyrochlores. *The Journal of Physical Chemistry B*, 106:4663–4677, 2002.

[135] M.T. Vandenborre and E. Husson. Comparison of the force field in various pyrochlore families. i. the a2b2o7 oxides. *Journal of Solid State Chemistry*, 50:362–371, 1983.

[136] Michael Fischer, Thomas Malcherek, Ulrich Bismayer, Peter Blaha, and Karlheinz Schwarz. Structure and stability of $cd_2nb_2o_7$ and $cd_2ta_2o_7$ explored by ab initio calculations. *Phys. Rev. B*, 78: 014108, 2008.

[137] A. Garbout, A. Rubbens, R. N. Vannier, S. Bouattour, and A. W. Kolsi. Raman scattering and x-ray diffraction on ybiti2o7 prepared at low temperature. *Journal of Raman Spectroscopy*, 39: 1469–1474, 2008.

[138] Charles H. Patterson. First-principles calculation of the structure and dielectric properties of $bi_2ti_2o_7$. *Phys. Rev. B*, 82:155103, 2010.

[139] Antonio F. Fuentes, Khalid Boulahya, Miroslaw Maczka, Jerzy Hanuza, and Ulises Amador. Synthesis of disordered pyrochlores, a2ti2o7 (a=y, gd and dy), by mechanical milling of constituent oxides. *Solid State Sciences*, 7(4):343–353, 2005.

[140] Robert Vassen, Xueqiang Cao, Frank Tietz, Debabrata Basu, and Detlev Stver. Zirconates as new materials for thermal barrier coatings. *Journal of the American Ceramic Society*, 83:2023–2028, 2000.

[141] David P. Cann, Clive A. Randall, and Thomas R. Shrout. Investigation of the dielectric properties of bismuth pyrochlores. *Solid State Communications*, 100:529–534, 1996.

[142] Rodney C. Ewing, William J. Weber, and Jie Lian. Nuclear waste disposalpyrochlore (a2b2o7): Nuclear waste form for the immobilization of plutonium and minor actinides. *Journal of Applied Physics*, 95:5949–5971, 2004.

[143] Stefan J. Korf, Harry J. A. Koopmans, Bernard C. Lippens, Anthonie J. Burggraaf, and Paul J. Gellings. Electrical and catalytic properties of some oxides with the fluorite or pyrochlore structure. co oxidation on some compounds derived from gd2zr2o7. *J. Chem. Soc., Faraday Trans. 1*, 83: 1485–1491, 1987.

[144] K. E. Sickafus, L. Minervini, R. W. Grimes, J. A. Valdez, M. Ishimaru, F. Li, K. J. McClellan, and T. Hartmann. Radiation tolerance of complex oxides. *Science*, 289:748–751, 2000.

[145] P. K. Schelling, S. R. Phillpot, and R. W. Grimes. Optimum pyrochlore compositions for low thermal conductivity. *Philosophical Magazine Letters*, 84:127–137, 2004.

[146] Licia Minervini, Robin W. Grimes, and Kurt E. Sickafus. Disorder in pyrochlore oxides. *Journal of the American Ceramic Society*, 83:1873–1878, 2000.

[147] Beverly Brooks Hinojosa, Juan C. Nino, and Aravind Asthagiri. First-principles study of cubic bi pyrochlores. *Phys. Rev. B*, 77:104123, 2008.

[148] Wendy R. Panero, Lars Stixrude, and Rodney C. Ewing. First-principles calculation of defect-formation energies in the $y_2(\mathrm{Ti}, \mathrm{Sn}, \mathrm{Zr})_2o_7$ pyrochlore. *Phys. Rev. B*, 70:054110, 2004.

[149] H Y Xiao, L M Wang, X T Zu, Jie Lian, and Rodney C Ewing. Theoretical investigation of structural, energetic and electronic properties of titanate pyrochlores. *Journal of Physics: Condensed Matter*, 19:346203, 2007.

[150] D. Liu, K. Tse, and J. Robertson. Electronic structure and defects of high dielectric constant gate oxide la2hf2o7. *Applied Physics Letters*, 90:062901, 2007.

[151] B. Liu, J.Y. Wang, F.Z. Li, and Y.C. Zhou. Theoretical elastic stiffness, structural stability and thermal conductivity of la2t2o7 (t=ge, ti, sn, zr, hf) pyrochlore. *Acta Materialia*, 58:4369–4377, 2010.

[152] David Vanderbilt. Soft self-consistent pseudopotentials in a generalized eigenvalue formalism. *Phys. Rev. B*, 41:7892–7895, 1990.

[153] S. Boucetta and F. Zegrar. Density functional study of elastic, mechanical and thermodynamic properties of mgcu with a cscl-type structure. *Journal of Magnesium and Alloys*, 1:128–133, 2013.

[154] M. Sanati, R. C. Albers, T. Lookman, and A. Saxena. Elastic constants, phonon density of states, and thermal properties of uo_2. *Phys. Rev. B*, 84:014116, 2011.

[155] Francis Birch. Finite strain isotherm and velocities for single-crystal and polycrystalline nacl at high pressures and 300k. *Journal of Geophysical Research: Solid Earth*, 83:1257–1268, 1978.

[156] Zhi-jian Wu, Er-jun Zhao, Hong-ping Xiang, Xian-feng Hao, Xiao-juan Liu, and Jian Meng. Crystal structures and elastic properties of superhard Irn_2 and Irn_3 from first principles. *Phys. Rev. B*, 76:054115, 2007.

[157] Yanbing Luan. Elastic properties of complex transition metal oxides studied by resonant ultrasound spectroscopy. *PhD diss., University of Tennessee*, 2011.

[158] J. Feng, B. Xiao, C.L. Wan, Z.X. Qu, Z.C. Huang, J.C. Chen, R. Zhou, and W. Pan. Electronic structure, mechanical properties and thermal conductivity of ln2zr2o7 (ln=la, pr, nd, sm, eu and gd) pyrochlore. *Acta Materialia*, 59:1742–1760, 2011.

[159] Guoqiang Lan, Bin Ouyang, and Jun Song. The role of low-lying optical phonons in lattice thermal conductance of rare-earth pyrochlores: A first-principle study. *Acta Materialia*, 91:304–317, 2015.

[160] X.J. Wang, H.Y. Xiao, X.T. Zu, and W.J. Weber. Study of cerium solubility in gd2zr2o7 by dft+u calculations. *Journal of Nuclear Materials*, 419:105–111, 2011.

[161] W. Voigt. Lehrbuch de kristallphysik (terubner). leipzig. 1928.

[162] A. Reuss. Berechnung der fliegrenze von mischkristallen auf grund der plastizittsbedingung fr einkristalle . *ZAMM - Journal of Applied Mathematics and Mechanics / Zeitschrift fr Angewandte Mathematik und Mechanik*, 9:49–58, 1929.

[163] R Hill. The elastic behaviour of a crystalline aggregate. *Proceedings of the Physical Society. Section A*, 65:349–354, 1952.

[164] N. Soga E. Schreiber, O. L. Anderson. Elastic constants and their measurements. 1973.

[165] S.F. Pugh. Xcii. relations between the elastic moduli and the plastic properties of polycrystalline pure metals. *The London, Edinburgh, and Dublin Philosophical Magazine and Journal of Science*, 45:823–843, 1954.

[166] Varshney, D., Shriya, S., and Varshney, M. Study of pressure induced structural phase transition and elastic properties of lanthanum pnictides. *Eur. Phys. J. B*, 85:241, 2012.

[167] Orson L. Anderson. A simplified method for calculating the debye temperature from elastic constants. *Journal of Physics and Chemistry of Solids*, 24:909–917, 1963.

[168] Jie Wu, Xuezheng Wei, Nitin P. Padture, Paul G. Klemens, Maurice Gell, Eugenio Garca, Pilar Miranzo, and Maria I. Osendi. Low-thermal-conductivity rare-earth zirconates for potential thermal-barrier-coating applications. *Journal of the American Ceramic Society*, 85:3031–3035, 2002.

[169] David R. Clarke and Simon R. Phillpot. Thermal barrier coating materials. *Materials Today*, 8: 22–29, 2005.

[170] David G. Cahill, S. K. Watson, and R. O. Pohl. Lower limit to the thermal conductivity of disordered crystals. *Phys. Rev. B*, 46:6131–6140, 1992.

[171] B. Liu, J.Y. Wang, Y.C. Zhou, T. Liao, and F.Z. Li. Theoretical elastic stiffness, structure stability and thermal conductivity of la2zr2o7 pyrochlore. *Acta Materialia*, 55:2949–2957, 2007.

[172] Ravhi S. Kumar, Andrew L. Cornelius, Malcolm F. Nicol, Kinson C. Kam, Anthony K. Cheetham, and Jason S. Gardner. Pressure-induced structural transitions in tb-pyrochlore oxides. *Applied Physics Letters*, 88:031903, 2006.

[173] F. X. Zhang, J. Lian, U. Becker, R. C. Ewing, Jingzhu Hu, and S. K. Saxena. High-pressure structural changes in the $gd_2zr_2o_7$ pyrochlore. *Phys. Rev. B*, 76:214104, 2007.

[174] F. X. Zhang, J. Lian, U. Becker, R. C. Ewing, L. M. Wang, L. A. Boatner, Jingzhu Hu, and S. K. Saxena. Pressure-induced structural transitions and phase decomposition in the $cd_2nb_2o_7$ pyrochlore. *Phys. Rev. B*, 74:174116, 2006.

[175] N.R. Sanjay Kumar, N.V. Chandra Shekar, and P.Ch. Sahu. Pressure induced structural transformation of pyrochlore gd2zr2o7. *Solid State Communications*, 147:357–359, 2008.

[176] H. Y. Xiao, Fei Gao, and W. J. Weber. Ab initio investigation of phase stability of $y_2ti_2o_7$ and $y_2zr_2o_7$ under high pressure. *Phys. Rev. B*, 80:212102, 2009.

[177] J. Lian, L. Wang, J. Chen, K. Sun, R.C. Ewing, J. Matt Farmer, and L.A. Boatner. The orderdisorder transition in ion-irradiated pyrochlore. *Acta Materialia*, 51:1493–1502, 2003.

[178] Unpublished data kindly provided by the experimental group of prof. a k sood, department of physics, iisc.

[179] R. Terki, G. Bertrand, H. Aourag, and C. Coddet. Ab initio calculations of structural and electronic properties of y2ti2o7 and cd2nb2o7. *Physica B: Condensed Matter*, 392:341–347, 2007.

[180] Yong Jiang, John R. Smith, and G. Robert Odette. Prediction of structural, electronic and elastic properties of y2ti2o7 and y2tio5. *Acta Materialia*, 58:1536–1543, 2010.

[181] T. Danielson, E. Tea, and C. Hin. Ab initio investigation of helium in y2ti2o7: Mobility and effects on mechanical properties. *Journal of Nuclear Materials*, 477:215–221, 2016.

[182] A.K. Pandit, T.H. Ansari, M. Prasad, R.A. Singh, and B.M. Wanklyn. On the electrical conductivity, thermoelectric power and dielectric constant of y2ti2o7 single crystals. *Materials Letters*, 12:77–83, 1991.

[183] Alberto Debernardi. Phonon linewidth in iii-v semiconductors from density-functional perturbation theory. *Phys. Rev. B*, 57:12847–12858, 1998.

[184] I. P. Ipatova, A. A. Maradudin, and R. F. Wallis. Temperature dependence of the width of the fundamental lattice-vibration absorption peak in ionic crystals. ii. approximate numerical results. *Phys. Rev.*, 155:882–895, 1967.

[185] Tian Lan, Xiaoli Tang, and Brent Fultz. Phonon anharmonicity of rutile tio_2 studied by raman spectrometry and molecular dynamics simulations. *Phys. Rev. B*, 85:094305, 2012.

[186] Tian Lan, Chen W. Li, and Brent Fultz. Phonon anharmonicity of rutile sno_2 studied by raman spectrometry and first principles calculations of the kinematics of phonon-phonon interactions. *Phys. Rev. B*, 86:134302, 2012.

[187] Anthony J. C. Ladd, Bill Moran, and William G. Hoover. Lattice thermal conductivity: A comparison of molecular dynamics and anharmonic lattice dynamics. *Phys. Rev. B*, 34:5058–5064, 1986.

[188] L. Bohlin and T. Hgberg. Anharmonic phonon shifts and widths for a centro symmetrical potential. *Journal of Physics and Chemistry of Solids*, 29:1805–1810, 1968.

[189] R.A. Cowley. Raman scattering from crystals of the diamond structure. *J. Phys. France*, 26: 659–667, 1965.

[190] E. Haro, M. Balkanski, R. F. Wallis, and K. H. Wanser. Theory of the anharmonic damping and shift of the raman mode in silicon. *Phys. Rev. B*, 34:5358–5367, 1986.

[191] David Vanderbilt, Steven G. Louie, and Marvin L. Cohen. Calculation of anharmonic phonon couplings in c, si, and ge. *Phys. Rev. B*, 33:8740–8747, 1986.

[192] Alberto Debernardi, Stefano Baroni, and Elisa Molinari. Anharmonic phonon lifetimes in semiconductors from density-functional perturbation theory. *Phys. Rev. Lett.*, 75:1819–1822, 1995.

[193] G. Lang, K. Karch, M. Schmitt, P. Pavone, A. P. Mayer, R. K. Wehner, and D. Strauch. Anharmonic line shift and linewidth of the raman mode in covalent semiconductors. *Phys. Rev. B*, 59: 6182–6188, 1999.

[194] A. Debernardi, C. Ulrich, K. Syassen, and M. Cardona. Raman linewidths of optical phonons in $3c-$SiC under pressure: First-principles calculations and experimental results. *Phys. Rev. B*, 59: 6774–6783, 1999.

[195] Shobhana Narasimhan and David Vanderbilt. Anharmonic self-energies of phonons in silicon. *Phys. Rev. B*, 43:4541–4544, 1991.

[196] G. Deinzer, G. Birner, and D. Strauch. Ab initio calculation of the linewidth of various phonon modes in germanium and silicon. *Phys. Rev. B*, 67:144304, 2003.

[197] Xiaoli Tang and Jianjun Dong. Pressure dependence of harmonic and anharmonic lattice dynamics in mgo: A first-principles calculation and implications for lattice thermal conductivity. *Physics of the Earth and Planetary Interiors*, 174:33–38, 2009.

[198] Xiaoli Tang and Jianjun Dong. Lattice thermal conductivity of mgo at conditions of earth's interior. *Proceedings of the National Academy of Sciences*, 107:4539–4543, 2010.

[199] Xiaoli Tang, Chen W. Li, and B. Fultz. Anharmonicity-induced phonon broadening in aluminum at high temperatures. *Phys. Rev. B*, 82:184301, 2010.

[200] Laurent Chaput, Atsushi Togo, Isao Tanaka, and Gilles Hug. Phonon-phonon interactions in transition metals. *Phys. Rev. B*, 84:094302, 2011.

[201] Terumasa Tadano and Shinji Tsuneyuki. First-principles lattice dynamics method for strongly anharmonic crystals. *Journal of the Physical Society of Japan*, 87:041015, 2018.

[202] Atsushi Togo, Laurent Chaput, and Isao Tanaka. Distributions of phonon lifetimes in brillouin zones. *Phys. Rev. B*, 91:094306, 2015.

[203] Fabrice Vallée. Time-resolved investigation of coherent lo-phonon relaxation in iii-v semiconductors. *Phys. Rev. B*, 49:2460–2468, 1994.

[204] José Menéndez and Manuel Cardona. Temperature dependence of the first-order raman scattering by phonons in si, ge, and $\alpha - \mathrm{Sn}$: Anharmonic effects. *Phys. Rev. B*, 29:2051–2059, 1984.

[205] B.A. Weinstein. Pressure dependent optical phonon anharmonicity in gap. *Solid State Communications*, 20:999–1003, 1976.

[206] X. Gonze and J.-P. Vigneron. Density-functional approach to nonlinear-response coefficients of solids. *Phys. Rev. B*, 39:13120–13128, 1989.

[207] Alberto Debernardi and Stefano Baroni. Third-order density-functional perturbation theory: A practical implementation with applications to anharmonic couplings in si. *Solid State Communications*, 91:813–816, 1994.

[208] C. Ulrich, E. Anastassakis, K. Syassen, A. Debernardi, and M. Cardona. Lifetime of phonons in semiconductors under pressure. *Phys. Rev. Lett.*, 78:1283–1286, 1997.

[209] Lorenzo Paulatto, Francesco Mauri, and Michele Lazzeri. Anharmonic properties from a generalized third-order ab initio approach: Theory and applications to graphite and graphene. *Phys. Rev. B*, 87:214303, 2013.

[210] D. C. Wallace. Thermodynamics of crystals. 1972.

[211] A. Ward, D. A. Broido, Derek A. Stewart, and G. Deinzer. Ab initio theory of the lattice thermal conductivity in diamond. *Phys. Rev. B*, 80:125203, 2009.

[212] L. Lindsay, D. A. Broido, and Natalio Mingo. Flexural phonons and thermal transport in graphene. *Phys. Rev. B*, 82:115427, 2010.

[213] Li Dong Zhao, Shih Han Lo, Yongsheng Zhang, Hui Sun, Gangjian Tan, Ctirad Uher, Christopher M Wolverton, Vinayak P Dravid, and Mercouri Kanatzidis. Ultralow thermal conductivity and high thermoelectric figure of merit in snse crystals. *Nature*, 508:373–377, 2014.

[214] Toshiro Takabatake, Koichiro Suekuni, Tsuneyoshi Nakayama, and Eiji Kaneshita. Phonon-glass electron-crystal thermoelectric clathrates: Experiments and theory. *Rev. Mod. Phys.*, 86:669–716, 2014.

[215] Keivan Esfarjani and Harold T. Stokes. Method to extract anharmonic force constants from first principles calculations. *Phys. Rev. B*, 77:144112, 2008.

[216] Zhiting Tian, Jivtesh Garg, Keivan Esfarjani, Takuma Shiga, Junichiro Shiomi, and Gang Chen. Phonon conduction in pbse, pbte, and $pbte_{1-x}se_x$ from first-principles calculations. *Phys. Rev. B*, 85:184303, 2012.

[217] Lixin Cao, E. Sozontov, and J. Zegenhagen. Cubic to tetragonal phase transition of srtio3 under epitaxial stress: An x-ray backscattering study. *physica status solidi (a)*, 181:387–404, 2000.

[218] K. van Benthem, C. Elssser, and R. H. French. Bulk electronic structure of srtio3: Experiment and theory. *Journal of Applied Physics*, 90:6156–6164, 2001.

[219] George J. Fischer, Zichao Wang, and Shun-ichiro Karato. Elasticity of catio3, srtio3 and batio3 perovskites up to 3.0 gpa: the effect of crystallographic structure. *Physics and Chemistry of Minerals*, 20:97–103, 1993.

[220] Roman Wahl, Doris Vogtenhuber, and Georg Kresse. $srtio_3$ and $batio_3$ revisited using the projector augmented wave method: Performance of hybrid and semilocal functionals. *Phys. Rev. B*, 78: 104116, 2008.

[221] J. L. Servoin, Y. Luspin, and F. Gervais. Infrared dispersion in $srtio_3$ at high temperature. *Phys. Rev. B*, 22:5501–5506, 1980.

[222] W G Stirling. Neutron inelastic scattering study of the lattice dynamics of strontium titanate: harmonic models. *Journal of Physics C: Solid State Physics*, 5:2711–2730, 1972.

[223] P. A. Fleury, J. F. Scott, and J. M. Worlock. Soft phonon modes and the 110 k phase transition in $srtio_3$. *Phys. Rev. Lett.*, 21:16–19, 1968.

[224] W. Jauch and A. Palmer. Anomalous zero-point motion in $srtio_3$: results from γ-ray diffraction. *Phys. Rev. B*, 60:2961–2963, 1999.

[225] J.C. Galzerani and R.S. Katiyar. The infrared reflectivity in srtio3 and the antidistortive transition. *Solid State Communications*, 41:515–519, 1982.

[226] Gerald D. Mahan. Many-particle physics. 2000.